DEVELOPMENT OF BISPECIFIC PROSTATE-SPECIFIC MEMBRANE ANTIGEN/FIBROBLAST ACTIVATION PROTEIN (PSMA/FAP) – TARGETING RADIOTRACERS FOR PROSTATE CANCER IMAGING

by

Arsyangela Verena

B.Sc., National Taiwan University, 2017

A THESIS SUBMITTED IN PARTIAL FULFILLMENT OF

THE REQUIREMENTS FOR THE DEGREE OF

MASTER OF SCIENCE

in

THE FACULTY OF GRADUATE AND POSTDOCTORAL STUDIES

(Interdisciplinary Oncology)

THE UNIVERSITY OF BRITISH COLUMBIA

(Vancouver)

December 2023

The following individuals certify that they have read, and recommend to the Faculty of Graduate and Postdoctoral Studies for acceptance, the thesis entitled:

Development of Bispecific Prostate-Specific Membrane Antigen/Fibroblast Activation Protein (PSMA/FAP) - Targeting Radiotracers For Prostate Cancer Imaging

submitted by Arsyangela Verena in partial fulfillment of the requirements for

the degree of Master of Science

in Interdisciplinary Oncology

Examining Committee:

Dr. Kuo-Shyan Lin, Associate Professor, Department of Radiology, Faculty of Medicine, UBC

Supervisor

Dr. François Bénard, Professor, Department of Radiology, Faculty of Medicine, UBC

Supervisory Committee Member

Dr. Joseph Lau, Assistant Professor, Department of Radiology, UBC

Additional Examiner

Additional Supervisory Committee Members:

Dr. Urs Häfeli, Professor, Faculty of Pharmaceutical Sciences, UBC

Supervisory Committee Member

Abstract

Oncology practice is rapidly shifting toward personalize cancer diagnosis and treatment by utilizing targeted therapies or probes against the specific molecular drivers of tumors in individual patients. Molecular imaging has been playing a major role in personalized cancer management, including detection, staging, and treatment response assessment. However, tumor heterogeneity limits the utility of monospecific radiotracers in prostate cancer diagnosis and therapy. Utilizing heterodimeric radiotracers to target different proteins overexpressed in tumor has been shown to be a promising strategy to overcome these limitations and improve lesion detection.

Previous studies evinced that prostate-specific membrane antigen (PSMA) and fibroblast activation protein (FAP) are overexpressed in prostate cancer, and their expressions are associated with poor prognosis. Therefore, both PSMA and FAP are promising biomarkers of prostate cancer and many PSMA- and FAP-targeting radioligands have been developed for imaging and therapy. Despite many effective PSMA-targeting radiotherapeutic agents being developed, patients with low to no PSMA expression are not eligible for these PSMA-targeted radioligand therapies and have very limited treatment options. Since FAP and PSMA are concomitantly expressed in prostate cancer**,** the use of bispecific PSMA/FAP-targeting radioligands is expected to increase lesion detection sensitivity in this patient cohort.

We hypothesize that the bispecific PSMA/FAP-targeting radiotracers will have comparable or even higher tumor uptake than the monospecific radiotracers. In this thesis, we synthesized several bispecific PSMA/FAP-targeting radiotracers, evaluated their binding affinity in vitro using cell-based competitive binding assays, imaging potential and biodistribution in tumor-bearing mice, and compared their data with the monospecific PSMA- and FAP- targeting radiotracers. Here, we also describe the work of developing pyridine-based FAP-targeted

pharmacophore which we hypothesized to be more hydrophilic than the quinoline-based pharmacophore, resulting in higher tumor-to-background contrast ratio of the derived radiotracers. Lastly, we synthesized two bispecific PSMA/FAP-targeting tracers containing the pyridine-based FAP-targeted pharmacophore. Overall, this research demonstrates the feasibility of designing PSMA/FAP-targeting radiotracers and how linker selection, length, pharmacophore selection and modification, and hydrophilicity of the compounds affect the binding affinity, tumor uptake, tumor-to-background contrast ratio of the bispecific PSMA/FAP-targeting radiotracers. This can give insights on parameters to consider in designing PSMA/FAP bispecific radiotracers.

Lay Summary

Molecular probes labelled with a radioactive material (radiotracers) can bind to target proteins that are overexpressed in tumor and help detect tumor lesions in cancer patients. Heterogeneous expression of different biomarkers in tumor lesions (tumor heterogeneity) limits the efficiency and reliability of monospecific radiotracers in prostate cancer diagnosis and therapy. Previous studies have shown the potential of bispecific radiotracers to target different proteins overexpressed in tumor to overcome these limitations and improve lesion detection. It is evident that prostate-specific membrane antigen (PSMA) and fibroblast activation protein (FAP) are concomitantly overexpressed in prostate tumor, and their expressions are associated with poor prognosis. Therefore, the use of bispecific PSMA/FAP-targeting radiotracer is expected to increase lesion detection sensitivity. In this thesis, our goal was to synthesize and evaluate novel bispecific PSMA/FAP radiotracers by comparing their binding affinity, tumor uptake, and the imaging potential with the monospecific PSMA- or FAP-targeting radiotracers.

Preface

A version of Chapter 2 has been published in *Molecules* [**A Verena**., Z Zhang, H-T Kuo, H Merkens, J Zeisler, R Wilson, S Bendre, A A W L Wong, F Bénard, K-S Lin. Synthesis and Preclinical Evaluation of Three Novel ^{68}Ga-Labeled Bispecific PSMA/FAP-Targeting Tracers for Prostate Cancer Imaging]. I was the lead investigator in this project and was responsible for data collection and analysis, as well as the manuscript composition. I performed the peptide synthesis, purification using HPLC, identification using LC/MS, cell culture, plate-based competition binding assays, and biodistribution studies. K-S Lin performed the organic synthesis and synthesized the FAP-targeting ligand. Z Zhang trained me to perform solid phase peptide synthesis and purification, and was responsible for tracer radiosynthesis. H-T Kuo synthesized one of the compounds in this paper. H Merkens trained me to do cell culture,the binding affinity assay, and performed the tumor inoculation. J Zeisler and S Bendre produced the transfected cell line used in this paper. S Bendre designed and trained me how to do one of the enzymatic binding assay. A A W L Wong performed and analyzed the NMR data. N Colpo performed the PET/CT image acquisitions. H Merkens and R Wilson aided in biodistribution studies. F Bénard and K-S Lin were the supervisory authors and were involved throughout the project in concept formation and manuscript composition.

A version of Chapter 3 has been published in *Pharmaceuticals* [**A Verena**, H-T Kuo, H Merkens, J Zeisler, S Bendre, A A W L Wong; F Bénard; K-S Lin. Novel ^{68}Ga-Labeled Pyridine-Based Fibroblast Activation Protein-Targeted Tracers with High Tumor-to-Background Contrast.]. I was the lead investigator, responsible for all major areas of data collection and analysis, as well as the manuscript composition. I performed the organic synthesis, purification using HPLC, identification using LC/MS, cell culture, cell-based competition binding assays, and

biodistribution studies. H-T Kuo was responsible for tracer radiosynthesis. H Merkens and I performed the tumor inoculation. J Zeisler and S Bendre produced the transfected cell line used in this paper. S Bendre designed the enzymatic binding assay. A A W L Wong performed and analyzed the NMR data. N Colpo performed the PET/CT image acquisitions. H Merkens and H-T Kuo aided in biodistribution studies. F Bénard and K-S Lin were the supervisory authors and were involved throughout the project in concept formation and manuscript composition.

For Chapter 4, I was the lead researcher, responsible for all major areas of concept formation, data collection and analysis, as well as the manuscript composition. I performed the organic synthesis, purification using HPLC, identification using LC/MS, cell culture, cell-based competition binding assays, tumor inoculation, and biodistribution studies. H-T Kuo, C-C Chen, D Chaple, and I performed the tracer radiosynthesis. A A W L Wong performed and analyzed the NMR data. N Colpo and L Wang performed the PET/CT image acquisitions. P Ng and S Bendre aided in biodistribution studies. F Bénard and K-S Lin were the supervisory member and were involved throughout the project in concept formation and manuscript composition.

Experimental work in this thesis was performed at British Columbia Cancer Research Centre (BCCRC). All the animal studies performed in this thesis were under animal protocol A20-0113 (Preclinical Evaluation of Radiotracers for Cancer) that was approved by the Institutional Animal Care Committee of the University of British Columbia and were performed in compliance with the Canadian Council on Animal Care Guidelines.

Table of Contents

List of Tables

List of Figures

List of Symbols

$	Dollar
%	Percentage
°	Degree
℃	Degree Celcius
P	P value
$t_{1/2}$	Half-life
v/v	Volume per volume
α	Alpha
β^-	Beta
β^+	Positron
γ	Gamma

List of Abbreviations

%ID/g	Percent injected dose per gram
[^{18}F]FDG	^{18}F-Fluorodeoxyglucose
µM	micromolar
2D	2-Dimensional
2-Nal	3-(2-Naphthyl)-*L*-alanine
3D	3-Dimensional
^{68}Ga	Gallium-68
^{68}Ge	Germanium-68
bl	Urinary bladder
boroPro	2-pyrrolidinylboronic acid
CAF	Cancer associated fibroblast
CT	Computed tomography
DCM	Dichloromethane
DGA	N,N,N',N'-tetra-n-octyldiglycolamide
DIAD	Diisopropyl azodicarboxylate
DIC	*N,N'*-Diisopropylcarbodiimide
DIEA	N,N-Diisopropylethylamine
DMEM	Dulbecco Modified Eagle Medium
DMF	*N,N*-dimethylformamide
DOTA	1,4,7,10-tetraazacyclododecane- 1,4,7,10- tetraacetic acid
DPPIV	Dipeptidyl peptidase IV
DRE	Digital rectal examination
DTPA	Diethylenetriaminepentaacetic acid
EDTA	Ethylenediaminetetraacetic acid
Et_3SiH	Triethylsilane
FAP	Fibroblast activation protein
FAPI	Fibroblast activation protein inhibitor
FBS	Fetal bovine serum
FOLH1	Folate hydrolase 1
g	Gram(s)
GBq	Gigabequerel
GCPII	Glutamate carboxypeptidase II
h	Hour
HATU	Hexafluorophosphate azabenzotriazole tetramethyl uronium
HEPES	4-(2-Hydroxyethyl)-1-piperazineethanesulfonic acid
HER2	Human epidermal growth factor receptor 2
HPLC	High-performance liquid chromatography
IC_{50}	Half maximal inhibitory concentration
kD	Kilodalton
keV	kilo-electronvolt
LogD	The logarithm of the n-octanol/water distribution coefficient
$LogD_{7.4}$	n-octanol/buffer solution distribution coefficient at pH = 7.4
M	Molar (concentration)

MBq	Megabequerel
mCRPC	Metatastic castration-resistant prostate cancer
mg	Milligram
MHz	Megahertz
min	Minute(s)
mL	Milliliters
mm	Millimeters
mmol	Millimole
mpMRI	Multiparametric magnetic resonance imaging
MRI	Magnetic resonance imaging
MS	Mass spectrometry
NAAG	N-acetyl-aspartyl-glutamate
NaI	Sodium iodide
NaOAc	Sodium acetate
nM	Nanomolar
nm	Nanometer
NMR	Nuclear magnetic resonance
NOTA	1,4,7- triazacyclononane-1,4,7- triacetic acid
NPY	Neuropeptide Y
NRG	NOD.Cg-*Rag1*^{tm1Mom} *Il2rg*^{tm1Wjl}/SzJ
PBS	Phosphate-buffered saline (pH 7.4 unless otherwise stated)
PCa	Prostate cancer
PD	Pharmacodynamics
PET	Positron emission tomography
PK	Pharmacokinetics
pM	Picomolar
PREP	Prolyl olligopeptidase
PSA	Prostate specific antigen
PSMA	Prostate-specific membrane antigen
PYY	Pancreatic peptide YY
QC	Quality control
RLT	Radioligand therapy
RPMI	Roswell Park Memorial Institute
SD	Standard deviation
SPECT	Single photon emission computed tomography
TBTA	Tris(benzyltriazolylmethyl)amine
TFP	2,3,5,6-Tetrafluorophenol
THF	Tetrahydrofuran
TIS	Triisopropylsilane
TRUS	Transrectal ultrasound
US FDA	The United States Food and Drug Administration
UV	Ultraviolet

List of Schemes

Acknowledgements

First and foremost, I would like to offer my sincere gratitude to my supervisor, Dr. Kuo-Shyan Lin, who gave me the opportunity to come to Canada and pursue my graduate degree in such interdisciplinary research group with motivated and welcoming people whom I had pleasure working with. Thank you Dr. Lin for all of your guidance, insights, and patience throughout my journey, also for always encouraging me even when the experiment fails and answering all of my questions. Your extensive knowledge and passion for research continue to inspire me to continue pursuing my dream.

I would also like to thank the other members of my supervisory committee. Dr. François Bénard, thank you for all of your advices during our weekly meetings and enhancing my understanding in techniques I can learn and use in radiopharmaceutical development. Thank you, Dr. Urs Häfeli for your insights during the committee meetings and for giving me in depth knowledge of nuclear medicine during and the course you taught.

Moreover, I would like to express my gratitude to all of our past and current Bénard-Lin lab members, who have supported me along my journey. Big thank you to Dr. Zhengxing Zhang (Johnson) for taking me under your wing and mentoring me at the beginning, even throughout the first year of my research, and for helping me labeling most of my first compounds. Thank you Helen Merkens for showing me how to do most of the biological assays and helping me perform couple of tumor inoculation and biodistribution studies. Thank you Dr. Hsiou-Ting Kuo for teaching me how to do ^{68}Ga-labeling, also for labeling the compounds for my first and second manuscripts, also for performing some of the PET scans. I would like to thank Dr. Jutta Zeisler and Shreya Bendre for providing me with the transfected cell line needed for my experiments and helping take care of my cells when I wasn't able to. Thank you Shreya Bendre for designing and

teaching me how to do the enzymatic binding assay. I would like to thank Ryan Wilson and Pauline Ng for helping me do most of the biodistribution studies. I would like to give thanks to Nadine Colpo who helped me with the majority of PET scan and animal studies. Thank you to our postdoctoral fellows, Dr. Devon Chapple and Dr. Chao-Cheng Chen (Jimmy) for labeling my compounds for my final project. Also, to Dr. Lei Wang, who helped me do the PET scan for my final project. Lastly, thanks to Antonio Wong for doing all the NMR experiments and analysis, also for sharing your extensive knowledge in chemistry.

To those who are not directly involved in my projects, I would like to thank everyone else in our lab for their friendship and support. Graduate school can be stressful at times, and our conversation and laughs during lunch times and after work really help me keep pushing through the tough times.

I would also like to acknowledge the members of the BCCRC Animal Resource Centre (ARC), and BC Cancer (Vancouver) cyclotron facility for their support in making all my studies possible. Lastly, I would like to acknowledge all the mice that were sacrificed in the name of science for this thesis. The work presented herein was funded by the Canadian Institute of Health Research.

Dedication

To my parents – I would not have gotten this far in my career without all your sacrifices. Thank you for your support throughout the years of my education abroad, and for always encouraging me to be the best version of myself and strive for excellence. Thank you for being always ready to listen and give suggestions to my problems.

And to my best friend and partner, Pranata – Thank you for always being there for me throughout the ups and down my degree, for answering all my phone calls even late at night. Thank you for always trusting me and keeping me calm, sane, and feel loved and supported even from miles apart.

Chapter 1 : Introduction

1.1 Molecular Imaging in Nuclear Medicine

Nuclear medicine is a specialized field that utilizes radioactive isotopes and their emitted radiation to diagnose, stage, and treat various diseases, including cancer[1]. Molecular imaging is an emerging multidiscipline which realizes noninvasive and real time visualization of *in vivo* physiological or pathological process at cellular or molecular level[2,3]. This entails administering small amounts of radioactive substances, known as radiopharmaceuticals, into patients through injection, ingestion or inhalation, and acquiring images using high resolution and high sensitive instruments. These radiopharmaceuticals can be used either for diagnostic (referred as radiotracers) by incorporating gamma rays or positron (β^+)-emitting radioisotopes, and for targeted radionuclide therapy or theranostic purposes by incorporating alpha- (α) or beta- (β^-) emitting radioisotopes[4]. In comparison to the conventional imaging modalities, like X-ray or CT scan, that provide information on morphological differences, molecular imaging can reveal the physiological activities or expression status of specific molecules within tissue by utilizing molecular probes. Molecular imaging has aided physicians in evaluating therapeutic responses, prognosis prediction, and selecting disease- and patient-specific therapeutic treatment (personalized medicine).

1.2 Molecular Imaging in Nuclear Medicine

Two main imaging modalities currently used for molecular imaging are single photon emission computed tomography (SPECT) and positron emission tomography (PET) (Table 1.1). Both of these imaging modalities are usually paired with computed tomography (CT) or magnetic resonance imaging (MRI) to provide high-resolution anatomical information in image overlays[5]. These molecular imaging techniques aid physicians in disease detection, diagnosis and

management, in particular PET, which has become an indispensable tool for drug development and discovery, cancer treatment, staging, and detection of recurrent diseases due to its high sensitivity of 10^{-11}-10^{-12} mol/L.

Table 1.1 Comparison of PET and SPECT. Adapted from Lu FM, Yuan Z. PET/SPECT Molecular Imaging in Clinical Neuroscience: Recent Advances in the Investigation of CNS Diseases. *Quant. Imaging Med. Surg*. 2015; 5 (3): 433–4477[6] and Hwang BH, Kim MH, Chang K. Molecular Imaging of High-Risk Atherosclerotic Plaques: Is It Clinically Translatable? *Korean Circ J*. 2011;41(9):497[7].

	PET	**SPECT**
Spatial Resolution[a]	4-6 mm	8-12 mm
Temporal resolution[b]	Seconds-Minutes	Minutes-hours
Sensitivity[c]	10^{-11}-10^{-12}	10^{-10}-10^{-11}
Advantages	High sensitivity; no tissue penetrating limit; whole-body imaging; higher resolution	High sensitivity; no tissue penetrating limit; no need for cyclotron
Disadvantages	High cost of cyclotron needed; radiation risk	radiation risk; hard to quantify
Probe quantity	nanogram	nanogram
Priced	$2.5M for PET/CT	$750k for SPECT or $1-1.2M for SPECT/CT

[a]Spatial resolution expresses in millimeters, refers to the minimum distance that the imaging modality can differentiate two independently measured objects; [b]temporal resolution, refers to the duration of time needed to acquire enough events to form an image of a dynamic process; [c]sensitivity, refers to the ability to distinguish a molecular probe from the background, the unit is mole per liter; [d]cost is based on purchase price of imaging systems in Canada (in Canadian dollars ($))[8].

Compared to SPECT, PET imaging has the advantage of exhibiting a higher sensitivity by approximately two orders of magnitude. This is due to the need of collimators in SPECT to restrict the angular range of the photon being detected to provide the positional information, which in turn

lowering the geometric efficiency or sensitivity[9]. Moreover, PET also has better spatial resolution. On the other hand, SPECT scans are more affordable than PET scans, partly due to cheaper scanner, ease of radiolabeling, and the nuclides used in SPECT are readily available and have longer half-life[6].

1.2.1 Positron emission Tomography (PET)

Positron emission tomography (PET) is a non-invasive three-dimensional diagnostic imaging tool to measure the physiological function in the body[10]. It has been extensively used in clinical oncology since it's combined with the multislice helical CT (PET/CT) in 2001 enabling integrated functional and high-resolution morphologic imaging[11].

In PET imaging, a radiotracer is administered to the patient, which consists of a positron-emitting radionuclide, including but not limited to ^{11}C, ^{13}N, ^{15}O, ^{18}F, and ^{68}Ga, which emit positrons upon decay[12,13]. Once injected, the radiotracer distributes throughout the body, accumulates in tissues of interest, and emits positrons. The emitted positron travels a short distance before colliding with an electron, known as annihilation event, resulting in the production of two photons or gamma rays with 511 keV energy in opposite directions (Figure 1.1). These gamma rays are detected by a ring of detectors surrounding the patient, allowing for the precise localization and quantification of the radiotracer distribution in three-dimensional space[14,15].

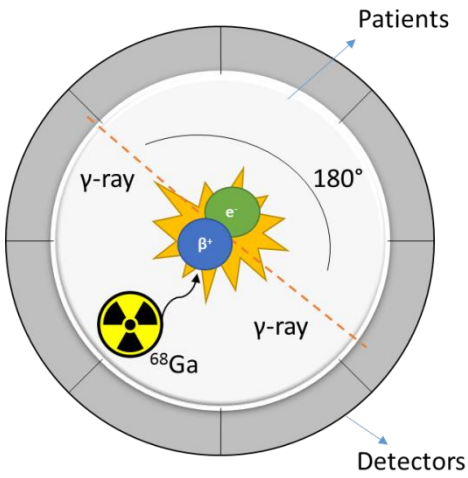

Figure 1.1 Schematic representation of the detection of PET radiotracer injected into a patient. ^{68}Ga is an example radionuclide used to illustrate the positron-electron annihilation event.

PET is the most established modality in oncologic imaging, and used in diagnosis, staging, and follow-up of various tumors[16]. The gold standard of PET radiopharmaceutical is ^{18}F-2-fluoro-2-deoxyglucose ([^{18}F]FDG). [^{18}F]FDG works through the Warburg effect, in which tumor cells have much higher metabolic and glycolytic rate, causing [^{18}F]FDG to be accumulated in tumor cell[13]. Despite its promising applications[17–19], the pitfall of [^{18}F]FDG is that it is not specific for the tumor cell as its uptake is also observed in the infection and inflammation site[20]. Hence, many different radiopharmaceuticals have been developed for various tumors with improved specificity[21–23].

1.2.1.1 Gallium-68 (^{68}Ga) in Medical Imaging

To date, fluorine-18, in particular [^{18}F]FDG is the most widely used radioisotope for PET imaging. However, its production is dependent on the availability of a cyclotron facility, which is more costly and not available in most places, especially developing countries. Therefore, generator-based radioisotopes are attractive alternatives for PET imaging.

Gallium-68 (^{68}Ga) was among the first generator-based PET radioisotopes to be used in nuclear medicine. ^{68}Ga can be produced from a ^{68}Ge/^{68}Ga generator which has been available since the early 1960s[24]. The long-lived parent isotope, germanium-68 (^{68}Ge) ($t_{1/2}$=271 days), allows for convenient generator distribution, while the short-lived ^{68}Ga ($t_{1/2}$=68 min) has decay characteristics that are appropriate for PET imaging[25]. ^{68}Ga decays 87.68% through positron emission with a maximum energy of 1.9 MeV, mean 0.89 MeV (Figure 1.2). ^{68}Ga emits positrons with a higher kinetic energy than those of ^{18}F (maximum energy of 0.63 MeV, mean 0.25 MeV), causing it to have a lower imaging spatial resolution than ^{18}F[26].

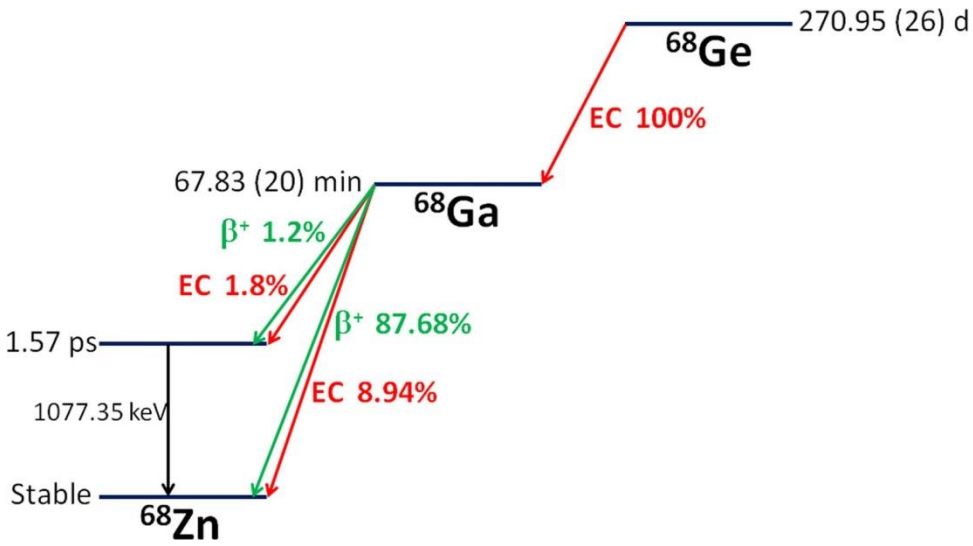

Figure 1.2 Simplified representation of decay scheme of nuclide chain ^{68}Ge/^{68}Ga. Reprinted with permission from Marganiec-Gałązka, J et al.. Activity Determination of ^{68}Ge/^{68}Ga by Means of 4πβ(Č)-γ Coincidence Counting. Appl. Radiat. Isot. 2018, 134, 240–244[27].

The short-lived ^{68}Ga is best suited for use in combination with small molecules or peptides that have short biological half-life and are metabolized and cleared rapidly from the blood pool. ^{68}Ga is incorporated by complexation of the $^{68}Ga^{3+}$ ion with specific chelators that are linked to the targeting ligands. The most extensively adopted chelators are DOTA (1,4,7,10-tetraazacyclododecane-1,4,7,10-tetraacetic acid), NOTA (1,4,7-triazacyclononane-1,4,7- triacetic

acid), EDTA (ethylenediaminetetraacetic acid), and DTPA (diethylenetriaminepentaacetic acid)[28]. Compared to NOTA, Ga-DOTA complex has relatively lower thermodynamic stability and slower formation kinetics, and it requires longer and higher temperature for labeling. However, DOTA is effective for labeling with many diagnostic radioisotopes (such as ^{68}Ga, ^{152}Tb, and ^{111}In) and radiotherapeutic radionuclides (such as ^{149}Tb, ^{90}Y, and ^{177}Lu), enabling a wider theranostic approach than NOTA, hence it is also referred as the "universal chelator". Moreover, several bio-conjugates containing ^{68}Ga-DOTA moiety showed very promising results in vivo and in vitro[29]. Therefore DOTA and its derivatives have become an important class of chelators for clinical diagnostic imaging.

1.2.2 Single Photon Emission Computed Tomography (SPECT)

Similar to PET, Single Photon Emission Computed Tomography (SPECT) also utilizes radiopharmaceuticals for detection. However, SPECT only detects radiopharmaceuticals tagged with single photon (gamma, γ) emitting radioisotopes. The most common radioisotopes for SPECT imaging are ^{99m}Tc ($t_{1/2}$ =6 hours), ^{123}I ($t_{1/2}$ =13.3 hours), and ^{111}In ($t_{1/2}$ =2.8 days). One advantage SPECT has over PET scan is that it is able to distinguish different radioisotopes from the different γ-ray energies exhibited, hence enabling dual-isotope imaging simultaneously.[6]

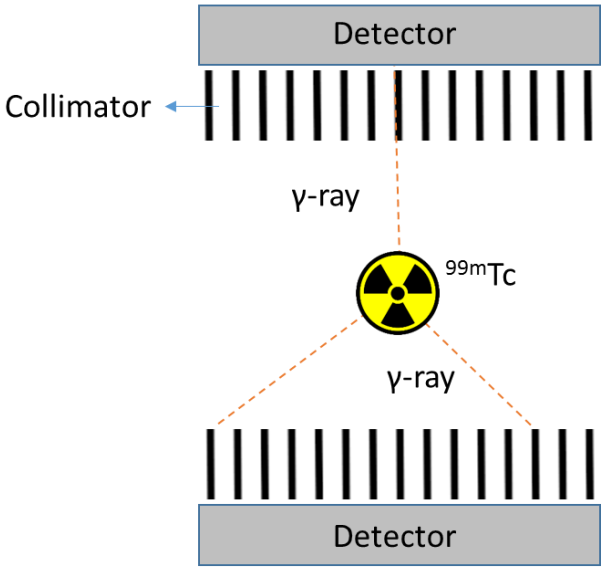

Figure 1.3 Schematic representation of the detection of SPECT radiotracer injected into a patient. ^{99m}Tc is an example radionuclide used to illustrate the detection of grammar rays.

To acquire SPECT image, tracers are usually injected intravenously, then the photons that emitted from the gamma decay of the tracer are filtered by the collimator or multi-hole aperture, which allows only photons that are parallel to the detector through (Figure 1.3). These photons are then captured by the rotating multi-headed gamma camera or detector. The camera takes planar scan (2D) images every 3 to 6 degrees which then are processed and reconstructed to get 3D image representation. These images are usually combined with CT scan images for anatomical information. The disadvantage of using a collimator is that most of the photons are absorbed by the collimator, which affects the resolution and sensitivity of the final image.[30]

1.3 Role of Molecular Imaging in Oncology

Nowadays molecular imaging plays a central role in diagnosis and treatment of a range of diseases, such as neurodegeneration, infection, cardiovascular disease, and cancer[3]. In oncology, PET and SPECT are widely used in clinical practice for detecting lesions or lymph nodes in cancer

patients and for evaluating the efficacy of anticancer treatments[31–33]. These imaging modalities require the injection of tumor-specific imaging probes which consist of positron emitting radioisotopes for PET imaging or a γ-ray emitting radioisotopes for SPECT imaging. These radioisotopes are chelated or bound to a molecular probe that binds to a specific target overexpressed in cancer cells or tumor microenvironment. The molecular probe can be in the form of small molecules, peptides, antibodies, or peptidomimetics[22,34,35]. A linker may be added in between the radioisotope and molecular probe to optimize the utility of the imaging probes.

Furthermore, molecular imaging plays a critical role in personalized cancer treatment, as it is able to help assess tumors based on molecular alteration, identify heterogeneity in primary and distant metastatic lesions, monitor disease progression and identify treatment responses in patients[36,37]. Noninvasive and repetitive measurements of biological tumor characteristics have the potential to predict which patients will benefit from a particular treatment and enable more specific patient selection[38,39]. In the clinic, PET tracers, such as [^{18}F]FDG, provide high accuracy for staging of small-cell lung cancer, thyroid cancer, head and neck cancer, melanoma and lymphoma[11]. Moreover, molecular imaging also aids in evaluation of therapeutic responses, for example, radiolabeled antibody targeting human epidermal growth factor receptor 2 (HER2) in breast cancer, such as ^{68}Ga-DOTA-F(ab')$_2$-trastuzumab[40] and ^{124}I-trastuzumab were able to detect and differentiate HER2-positive and -negative lesions, and this might help in evaluating the effectiveness of HER2-targeted treatment in each patient. In addition, Gebhart et al.[41] observed that ^{89}Zr-trastuzumab PET/CT combined with FDG-PET was able to predict HER2-positive breast cancer patients response to treatment with trastuzumab emtansine (T-DM1) with 100% negative predictive value. Molecular imaging also has a substantial role in the early drug discovery process by enabling non-invasive study of substrate-target interaction, pharmacokinetics (PK) and

pharmacodynamics (PD) of investigational drugs[42]. The examples described above demonstrate the critical and potential roles of molecular imaging in cancer diagnosis, treatment, and drug discovery, therefore further exploration can be pursued to expand its application in cancer care.

1.4 Tumor Heterogeneity and Bispecific-targeting Radiotracers

Many PET radiotracers for oncologic imaging have been developed, and several have been approved by the US FDA, such as [^{68}Ga]Ga-PSMA-11 for prostate cancer imaging and [^{18}F]fluoroestradiol for estrogen receptor-positive breast cancer imaging[43–45]. Although the monospecific radiotracers have shown promising results in the clinic, most tumor and metastatic lesions, such as in prostate cancer, have heterogeneous expression level of cancer-associated proteins intra- and inter-patients[46,47]. In Figure 1.4, two metastatic castration-resistant prostate cancer (mCRPC) patients were imaged with three different radiotracers: PSMA-targeted tracer, FDG, and FAP-targeted tracer[47]. The patient on Figure 1.4.a has many FAP-positive metastatic lesions and very few PSMA-positive lesions shown by high uptake of [^{18}F]FDG (B) and [^{68}Ga]Ga-FAPI-04 (C) and low uptake of [^{68}Ga]Ga-PSMA (A). Whereas The patient on Figure 1.4.b has more PSMA-positive lesions compared to FAP-positive lesions shown by high uptake of [^{68}Ga]Ga-PSMA (A) and very minimal uptake of the other two tracers. Patients with PSMA-negative lesions are not eligible to receive PSMA-targeted radioligand therapy and have very limited treatment options. Moreover, heterogeneous expression of FAP and PSMA in each patient can cause some lesions not being detected when injected with only one monospecific radiotracer, which can lead to misdiagnosis in the clinic.

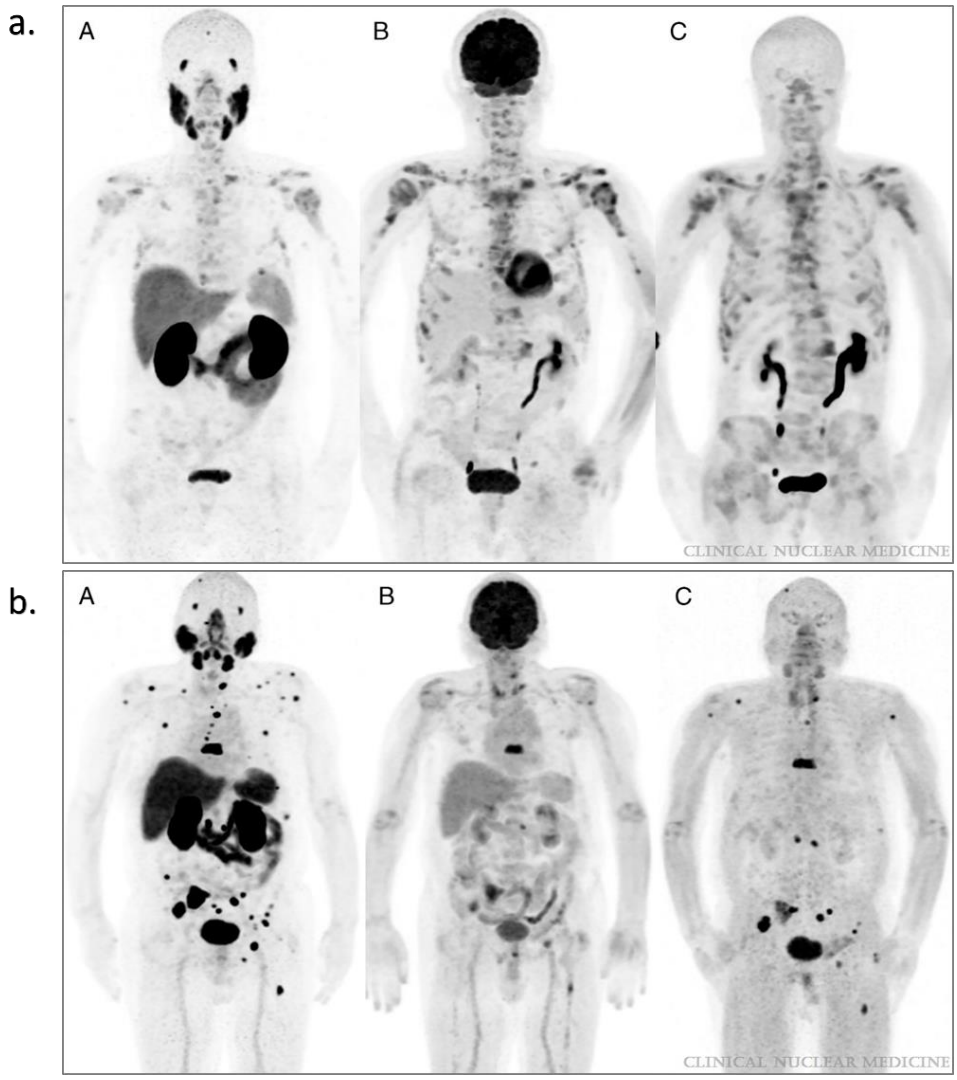

Figure 1.4 PET/CT imaging of metastatic castration-resistant prostate cancer (mCRPC) patients injected with (A) [^{68}Ga]Ga-PSMA, (B) [^{18}F]FDG and (C)[^{68}Ga]Ga-FAPI-04. (**a**) A 69-year-old man with mCRPC and has FAPI-positive/PSMA-negative metastatic bone lesions. (**b**) A 74-year-old man with mCRPC and has FAPI-negative/PSMA-positive metastatic bone lesions. Reprinted with permission from Isik, E. G.; Has-Simsek, D.; Sanli, O.; Sanli, Y.; Kuyumcu, S. Fibroblast Activation Protein–Targeted PET Imaging of Metastatic Castration-Resistant Prostate Cancer Compared With ^{68}Ga-PSMA and ^{18}F-FDG PET/CT. *Clin. Nucl. Med.* **2022**, *47* (1), e54[46].

One way to overcome this problem is by utilizing heterodimeric/bispecific radioligands that can bind to more than one target. Previous studies showed the potential of using bispecific radioligands to improve detection sensitivity and tumor uptake. For example, a bispecific radiotracer targeting prostate-specific membrane antigen (PSMA) and gastrin-releasing peptide

receptor (GRPR) was developed to improve tumor targeting and increase the detection sensitivity of prostate cancer imaging[48]. Moreover, Li group designed and evaluated gastrin-releasing peptide receptor (GRPR) and integrin $\alpha_v\beta_3$ bispecific radiotracers for imaging prostate cancer[49]. Their results showed that the GRPR/integrin $\alpha_v\beta_3$ bispecific tracer ([^{18}F]FB-BBN-RGD) achieved higher tumor uptake and tumor-to-background contrast ratios than both of its corresponding monospecific tracers ([^{18}F]FB-BBN for GRPR and [^{18}F]FB-RGD for integrin $\alpha_v\beta_3$).

Compared to the administration of a cocktail of two radiotracers with different targets, a single heterodimeric agent would likely have a more uniform dosimetry and pharmacokinetics, making it more feasible for clinical translation. In addition, it should be noted that the same diagnostic information obtained from the use of a bispecific tracer could be obtained by two separate scans using its corresponding monospecific tracers. However, the use of a bispecific tracer would save the time and overall cost by reducing two procedures (hospital visit, tracer preparation, tracer injection, PET scan, scan reading, and report writing) to one, and reduce patients' absorbed radiation dose from PET scanning. It should also be noted that compared to its corresponding monospecific tracers, a bispecific tracer would have a larger molecular size, and combining two different targeting vectors into a single molecule could potentially negatively impact both its pharmacokinetic properties and receptor binding affinities. However, with thorough investigations on the selection of targeting vectors, linkers, and potentially pharmacokinetic modifiers, it may be possible to identify an optimized bispecific tracer with higher tumor uptake and even higher tumor-to-background contrast ratios than both of its corresponding monospecific tracers.

1.5 Target of Interest

1.5.1 Prostate Cancer

Prostate cancer (PCa) is the second most common cancer and the fifth leading cause of cancer death in men worldwide, with and estimation of 1,410,000 new cancer cases and 375,304 deaths in 2020.[50] Based on the recent cancer statistic by Siegel, R.L. et al[51], the 5-year relative survival rates of localized and regional prostate cancer is >99%, however it decreases significantly to 32% for metastatic prostate cancer patients. Therefore, early and accurate detection is important to further improve the survival rates of PCa patients.

The current gold standard for early detection of prostate cancer is a digital rectal examination (DRE) and prostate specific antigen (PSA) measurement. DRE is a physical palpation of prostate to assess gland enlargement and texture. It has been shown to have high negative predictive value, however it has moderate sensitivity and low positive predictive value[52]. Therefore, it is commonly complemented with other tests, such as blood-serum test and ultrasound. If a DRE result is suspicious and complemented with elevated PSA level (from 3 to 10 ng/mL), transrectal ultrasound scan (TRUS)-guided biopsies are implemented for systematic sampling of 10-12 cores for histopathological diagnosis. However, TRUS biopsies tend to miss the anteriorly located tumours[53]. Therefore, multiparametric magnetic resonance imaging (mpMRI)-guided biopsies are preferred and recommended world-wide due to its better sensitivity and ability to visualize anterior tumors, increasing the detection rate and accuracy. Nevertheless, these biopsies are subjected to risk of infectious complications, hematospermia, haematuria lasting >1 d, and rectal bleeding[54]; therefore, non-invasive prostate cancer diagnosis, such nuclear imaging, has become an attractive alternative.

In recent years, PET tracers are being increasingly recognized as a powerful tool for diagnosis, staging, and disease management of PCa, and it is shown that utilizing PET tracers, such as ^{68}Ga-PSMA, has significantly impacted clinical decision-making, especially for the high-risk PCa cohort[55]. Zhou et al.[55] observed that the diagnostic performance of ^{68}Ga-PSMA PET/CT was superior to mpMRI in the high-risk PCa cohort. In addition, ^{68}Ga-PSMA PET also has better sensitivity and specificity in detecting skeletal metastases compared to other methods (i.e. bone scintigraphy and MRI)[57,58]. Hence, more molecular targets in PCa are being analyzed and more radiotracers are being developed to further improve PCa diagnosis. One of the most common targets for prostate cancer diagnosis and therapy is prostate-specific membrane antigen (PSMA).

1.5.2 Prostate-specific Membrane Antigen (PSMA)

Prostate-specific membrane antigen (PSMA) is a 750-residue type II transmembrane glycoprotein, also known as glutamate carboxypeptidase II (GCPII), N-acetyl-aspartyl-glutamate (NAAG) peptidase or folate hydrolase 1, which has enzymatic functions to cleave terminal glutamate[59–61]. It is found to be expressed at low levels in normal prostate tissue, kidney, and colon tissues, and is highly overexpressed in prostate tumors and the neovasculature of other cancers, such as renal, colon and breast carcinomas[62–64]. By using the PSMA-targeted antibody 7E11-C5, Wright Jr, G. L. et al.[65] found that PSMA expression in prostate cancer is positively correlated with tumor grade. Ross et al. also reported that PSMA overexpression in the primary tumor independently predicts prostate cancer recurrence and prognosis[66]. Therefore, PSMA has become an attractive tumor marker for a targeted prostate cancer diagnosis and therapy.

Apart from being a tumor marker, PSMA also has been shown to have a functional role in normal tissue and disease progression. One of its major roles is in processing and uptake of folate

as it removes the γ-linked glutamates from folate, providing deglutamated folate for absorption and nutrition; hence, the official gene name of PSMA is folate hydrolase 1 (*FOLH1*). This function might be responsible for the increased invasiveness and poorer prognosis of PSMA-expressing prostate cancers, as this increases cell folate uptake, an important component in nucleic acid synthesis[67]. It was observed that the release of glutamate from glutamated folate (vitamin B9) by PSMA enzymatic activity activates the PI3K-Akt signaling and promotes cancer proliferation[68]. Moreover, Gordon et al. demonstrated that PSMA may support angiogenesis by increasing folate levels which induce endothelial nitric oxide synthase (eNOS) regeneration[69].

PSMA imaging was initially based on an anti-PSMA antibody, ^{111}Indium (In) capromab pendetide (ProstaScint™) which was approved by the US FDA in 1996[70]. However, as it binds to the intracellular component of PSMA[71], it has limited ability to localize living cancer cells, which led to a poor specificity and high intra-reader variability in the clinic[72]. In the last few years, there are many PSMA-targeted radiopharmaceuticals that have been developed, four of them has been approved by the US FDA: [^{18}F]DCFPyL[35], [^{68}Ga]Ga-PSMA-11[43] and [^{18}F]rhPSMA-7.3[73,74] for prostate cancer imaging and [^{177}Lu]Lu-PSMA-617 for metastatic castration-resistant prostate cancer (mCRPC) radioligand therapy[33].

Most current PSMA-targeted radioligands are in the form of small molecule peptidomimetics, as they offer more advantages over large-molecule monoclonal antibodies, including increased permeability to solid tumors, more rapid tissue distribution and clearance. The glutamate-urea-lysine (Glu-urea-Lys)-based PSMA targeted ligands, such as in PSMA-11 and PSMA-617 have been shown to have high affinity to PSMA[75,76]. Moreover, the 2-naphthyl-L-alanine and tranexamic acid linker moieties in PSMA-617 were shown to improve the pharmacokinetic profile, high internalization ratio and high-contrast PET image[77]. Hence, many

emerging PSMA-targeted ligands are an analogue or derived from the Glu-urea-Lys pharmacophore, such as [^{177}Lu]Lu-PSMA-I&T[78] and [^{18}F]PSMA-1007[79].

Despite the potential benefit and positive clinical results of these PSMA-targeted theranostic approach[33,80,81], there are patients with low to no expression of PSMA who are unable to benefit from these treatments[47,82] Moreover, it was observed that PSMA-negative lesions, such as neuroendocrine prostate cancer (NEPC), are prone to being more aggressive and metabolically active, shown by high [^{18}F]FDG uptake, which led to worse prognosis[83]. Therefore, new strategies should be considered to improve lesion detection for this patient cohort, such as utilizing bispecific tracers that can target PSMA and other proteins overexpressed in prostate cancer.

1.5.3 Fibroblast Activation Protein (FAP)

Fibroblast activation protein (FAP) is a 97-kD type II transmembrane serine protease and a member of the prolyl peptidase family. Among this family, FAP is mostly similar to dipeptidyl peptidase 4 (DPPIV), as it shares 68% sequence identity in the putative catalytic region[84] and contains a catalytic triad of serine, aspartic acid, and histidine.[85] Both proteins have a dipeptidylpeptidase activity, in which the serine acts as a nucleophile to hydrolyze the post-proline bonds from the N-terminus of substrates[86,86,87]. Moreover, differing from the DPPIV, FAP has an endopeptidase activity, favoring cleavage after Gly-Pro-X, and is most effective where X is Phe or Met and least effective when X is His or Glu[88,89]. This endopeptidase activity has been used as the basis for FAP-specific detection methods and FAP-specific inhibitory molecules.

Not only sharing some common substrate to DPPIV, such as neuropeptide Y (NPY) in the brain, peptide YY (PYY) produced by the gastrointestinal tract, substance P (neurotransmitter) and B-type natriuretic peptide 32[90], FAP also has distinct natural substrate, including denatured

type 1 collagen[86,91], α_2-antiplasmin[92,93], and fibroblast growth factor 21[94]. FAP was observed to digest the denatured human collagen I and plays a role in collagen turnover by accelerating the intermediate-sized collagen fragment degradation and clearance from mice lungs[95], hence its endopeptidase activity also known as collagenase o gelatinase activity.

In contrast to DPPIV, FAP is almost absent in the normal cells[96] and are mostly expressed in sites of tissue remodeling and activated stroma, such as during wound healing[97]. Moreover, studies found that FAP is overexpressed in cancer-associated fibroblast (CAFs) in more than 90% of epithelial cancers, such as breast, colorectal, pancreatic, and prostate cancer[98–101]. CAFs occupy the tumor microenvironment[102,103], and its overexpression has been associated with tumor growth[104], angiogenesis[105], and metastasis[106], leading to poor prognosis. Moreover, Henry et al.[107] observed colon cancer patients with a high level of stromal FAP expression in their tumor are more likely to have an aggressive disease progression and higher potential to develop metastasis. Futhermore a study by Kesch et al.[101] showed that there is a significant rise in FAP expression throughout the progression of prostate cancer, in which men with advanced CRPC have the highest number of FAP-positive lesions. Therefore, FAP has become a promising target for targeted cancer diagnosis and therapy.

Many FAP inhibitors have been developed as potential anticancer agents, in the form of small molecule, antibody[108–110]. For small molecule-based FAP inhibitors (FAPI), there are two major groups based on the binding motif, which are 2-cyanopyrrolidine derivatives and 2-pyrrolidinylboronic acid derivatives (boroPro). For the first group, Jansen et al synthesized and compared several (4-quinolinoyl)glycyl-2-cyanopyrrolidine derivatives as FAP inhibitors[111,112]. They observed that difluoro substitution at the 4-position of 2-cyanopyrrolidine ring improved FAP binding affinity, and substituting glycine with other amino acids decreased binding affinity.

Hence, they identified (4-quinolinoyl)glycyl-(4,4-difluoro-2-cyanopyrrolidine) as the optimized pharmacophore for FAP-targeting. Several boroPro derivatives were discovered and compared by Poplawski et al.[113]. They found that (pyridine-4-carbonyl)-Gly-boroPro had the highest binding affinity (IC_{50}(FAP) = 0.47 nM), and replacing the pyridine-4-carbonyl moiety with a pyridine-3-carbonyl moiety led to derivatives with reduced FAP binding affinity. Therefore, most of the current FAP-targeted radiopharmaceuticals are the derivatives of these two pharmacophores.

For imaging purposes, [^{68}Ga]Ga-FAPI-04, with a (4-quinolinoyl)glycyl-(4,4-difluoro-2-cyanopyrrolidine) binding motif attached to a DOTA chelator is the most widely used FAP-targeted tracer and has been shown to have good uptake in several malignancies[114]. Compared to the widely used [^{18}F]FDG, [^{68}Ga]Ga-FAPI-04 has been shown to have a comparable or even better biodistribution, tumor-to-background contrast, and faster kinetics[115]. Despite the promising utilities of [^{68}Ga]Ga-FAPI-04, it has a relatively short tumor retention, making it unsuitable for theranostic purposes. Therefore, many other FAP-targeted radioligands are being developed to improve the tumor retention and uptake, such as [^{177}Lu]Lu-FAP-2286[116], [^{68}Ga]Ga-FAPI-46[117], and [^{177}Lu]Lu-DOTA.SA.FAPi[118].

1.6 Thesis Theme

Radiopharmaceuticals are radioactive compounds that have been widely used in the clinic for cancer diagnosis and therapy. Many clinical trials have shown the benefit and utility of these compounds to improve cancer patients' outcomes. Most of the clinically available tracers are monospecific, meaning they only bind to one target molecule, which are usually overexpressed in patients' tumors. However, studies have found that different tumors lesions in a patient can have different expression levels of cancer-related proteins. This phenomenon is known as tumor

heterogeneity and can limit the efficiency and reliability of the current monospecific tracers, because it might lead to some tumor lesions diagnosed as false-negative, and lead to potential relapse post radioligand therapy (RLT).

Studies have shown that prostate-specific membrane antigen (PSMA) and fibroblast activation protein (FAP) are concomitantly overexpressed in prostate cancer. Hence, this thesis aims to describe the development and evaluation of novel bispecific PSMA/FAP-targeting radiotracers. This is a proof-of-concept study to demonstrate the potential of the bispecific radiotracers in overcoming the limitation of monospecific tracers due to the heterogeneous biomarker expression in patient's tumor.

1.7 Hypothesis and Aims

Hypothesis: The bispecific PSMA/FAP-targeting radiotracers can bind to both PSMA and FAP, and have comparable or even higher binding affinity and tumor uptake than the respective monospecific radiotracers.

Aim 1: Design, synthesis, and evaluation of novel bispecific PSMA/FAP-targeting radiotracers for prostate cancer imaging including their binding affinity to PSMA and FAP, and imaging and biodistribution studies in tumor-bearing mice.

Aim 2: Comparison of the bispecific PSMA/FAP-targeting radiotracers with the respective monospecific radiotracers including their binding affinity to PSMA and FAP, and imaging and biodistribution studies in tumor-bearing mice.

Chapter 2 : Synthesis and Preclinical Evaluation of Three Novel ^{68}Ga-Labeled Bispecific PSMA/FAP-Targeting Tracers for Prostate Cancer Imaging

The following chapter is an adaption of the following published paper: Verena, A.; Zhang, Z.; Kuo, H.-T.; Merkens, H.; Zeisler, J.; Wilson, R.; Bendre, S.; Wong, A.A.W.L.; Bénard, F.; Lin, K.-S. Synthesis and Preclinical Evaluation of Three Novel ^{68}Ga-Labeled Bispecific PSMA/FAP-Targeting Tracers for Prostate Cancer Imaging. *Molecules* **2023**, *28*, 1088. https://doi.org/10.3390/molecules28031088

2.1 Introduction

Previous studies have shown the potential of using bispecific radioligands targeting PSMA and other overexpressed proteins, such as gastrin-releasing peptide receptor (GRPR), to improve tumor targeting and increase the detection sensitivity of prostate cancer imaging[48,119]. Here, our goal is to develop PSMA/FAP bispecific radioligands with comparable or even higher tumor uptake compared to the PSMA- and FAP-targeting monospecific tracers. Previously, Boinapally et al.[120] reported two ^{64}Cu-labeled PSMA/FAP bispecific tracers, [^{64}Cu]Cu-FP-L1 and [^{64}Cu]Cu-FP-L2 (Figure 2.1A), which showed high and specific uptake in both FAP- and PSMA-expressing tumor models. However, no head-to-head comparison of their bispecific tracers with the FAP- or PSMA-targeting monospecific tracer was reported. Hu et al. [121]reported the development of two ^{18}F-labeled PSMA/FAP bispecific tracers, [^{18}F]AlF-PSMA-FAPI-01 and [^{18}F]AlF-PSMA-FAPI-02 (Figure 2.1B), and both showed higher uptake in PSMA- and FAP-expressing tumor models when compared with the PSMA- and FAP-targeting monospecific tracers, respectively. Although promising results were obtained from these two reports, their use of NOTA as the radioisotope chelator excludes the labeling of these reported PSMA/FAP bispecific ligands with the commonly used radiotherapeutic metals such as ^{177}Lu and ^{90}Y.

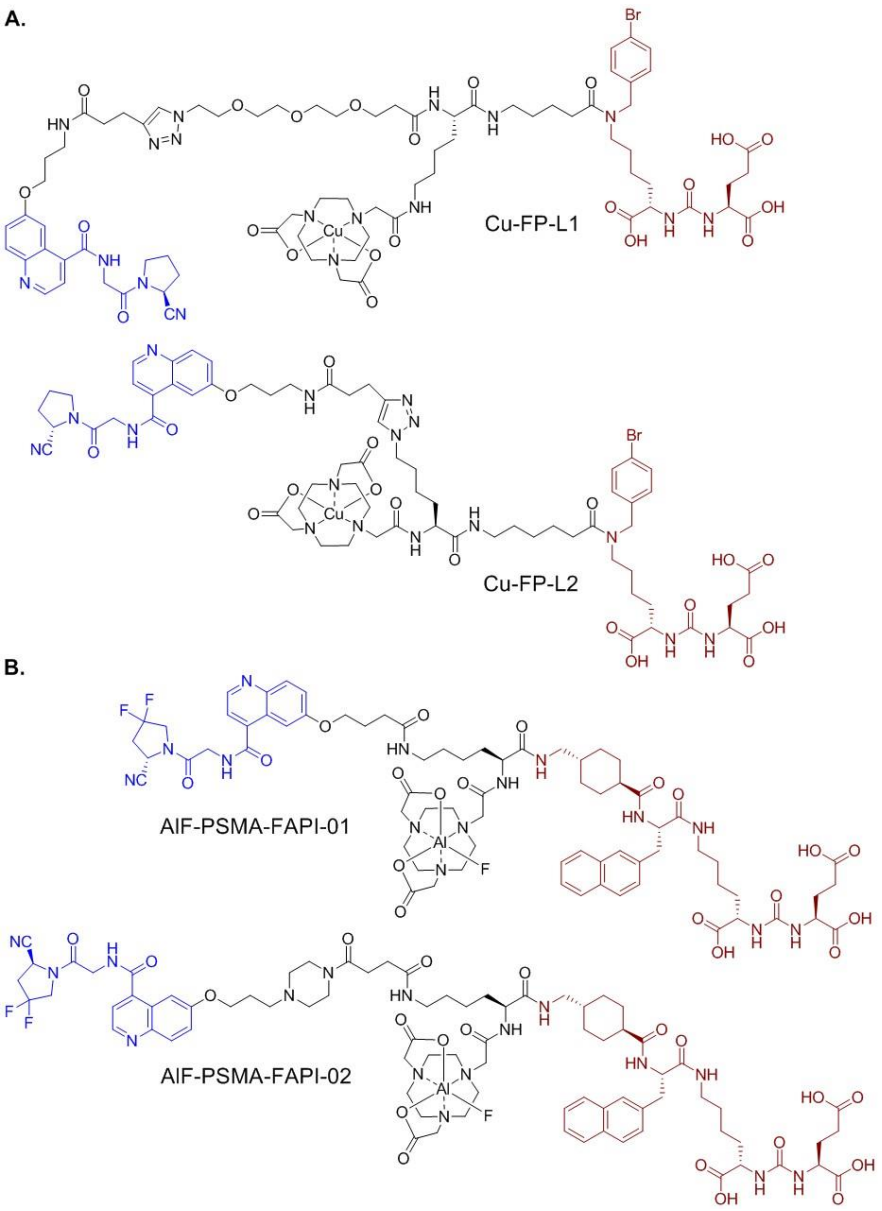

Figure 2.1 Chemical structures of (A) Cu-FP-L1 and Cu-FP-L2, and (B) AlF-PSMA-FAPI-01 and AlF-PSMA-FAPI-02. The PSMA- and FAP-targeting pharmacophores are shown in brown and blue, respectively.

To expand the potential usage of bispecific PSMA/FAP-targeting ligands for radiotherapeutic applications, we chose DOTA as our chelator, which has theranostic capabilities to label both diagnostic isotopes, such as ^{68}Ga, and therapeutic isotopes, such as ^{177}Lu. This will enable us to use the same ligands for diagnostic applications and ensure the pharmacokinetics of

diagnostic and radiotherapeutic agents are comparable as they are derived from the same PSMA/FAP-targeting ligands.

Here we report the design, synthesis, and evaluation of three ^{68}Ga-labeled DOTA conjugated bispecific PSMA/FAP tracers (Figure 2.2). The PSMA binding motif of AV01017, AV01030, and AV01038 was based on our previously reported [^{68}Ga]Ga-HTK03041[122], and their FAP-targeting motif was derived from [^{68}Ga]Ga-FAPI-04. The difference between these three tracers is the length of their linker between the quinoline and the triazole with ring null, -O-CH_2-, and -O-$(CH_2)_3$- for ^{68}Ga-labeled AV01030, AV01038, and AV01017, respectively. The potential of the tracers for prostate cancer imaging was evaluated by an in vitro competition binding assay, PET imaging, and ex vivo biodistribution studies in preclinical PSMA-expressing LNCaP and FAP-expressing HEK293T:hFAP tumor models

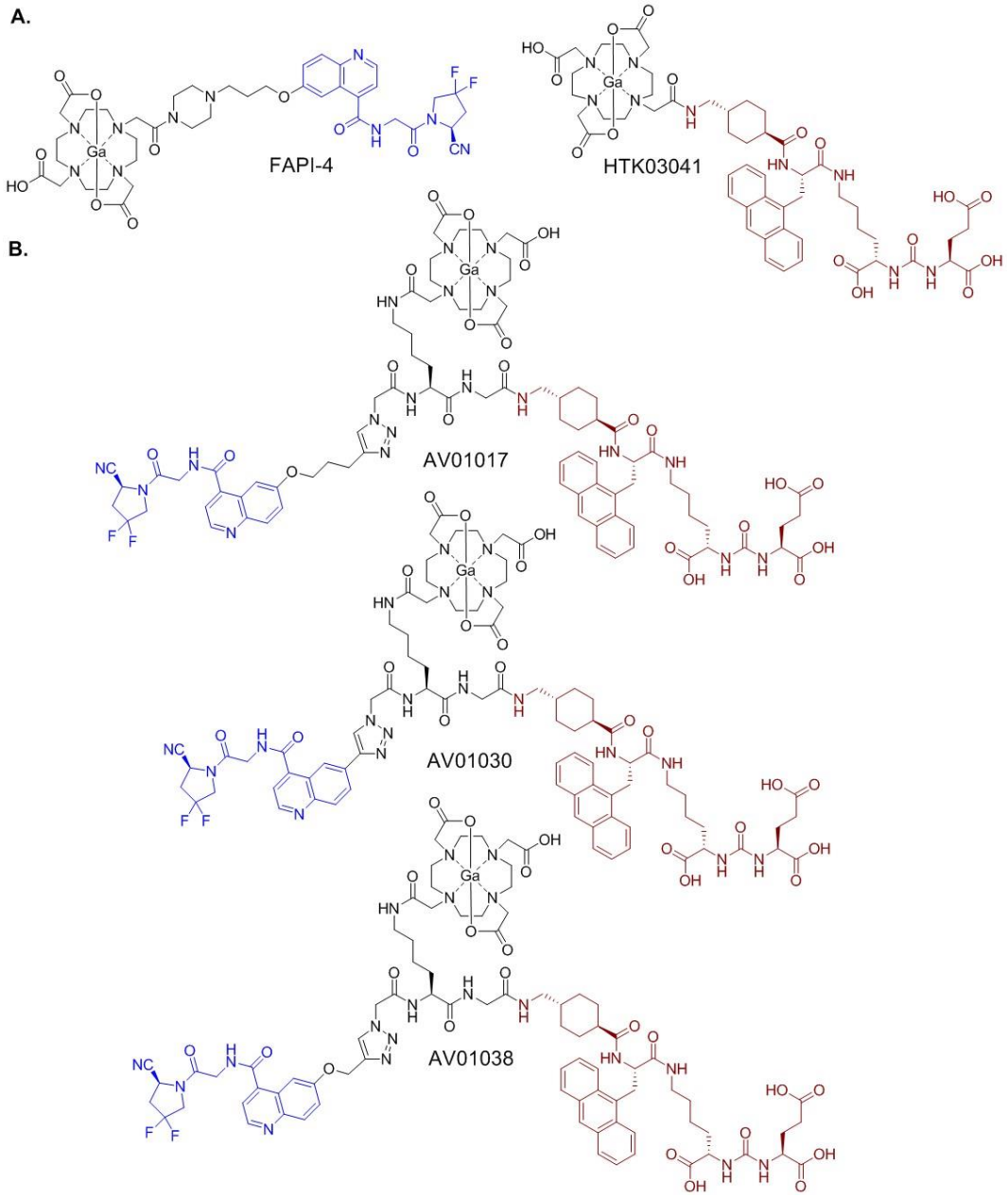

Figure 2.2 Chemical structures of (A) PSMA-targeting [^{68}Ga]Ga-HTK03041 and FAP-targeting [^{68}Ga]Ga-FAPI-04; and (B) bispecific PSMA/FAP-targeting ^{68}Ga-labeled AV01017, AV01030, and AV01038. The PSMA- and FAP-targeting pharmacophores are shown in brown and blue, respectively

2.2 Materials and Methods

2.2.1 General Method

Methyl-6-bromoquinoline-4-carboxylate, (*S*)-1-(2-aminoacetyl)-4,4-difluoropyrrolidine-2-carbonitrile-4-methylbenzenesulfonate, FAPI-04, HTK03041, Ga-HTK03041 and [^{68}Ga]Ga-HTK03041 were synthesized following literature procedures[22,111,123,124]. All other chemicals and solvents were obtained from commercial sources and used without further purification. DOTA-conjugated PSMA/FAP bispecific ligands were synthesized via SPPH with an AAPPTec (Louisville, KY) Endeavor 90 peptide synthesizer. Purification and quality control of DOTA-conjugated ligands and their ^{nat}Ga/^{68}Ga-complexed analogs were performed on Agilent (Santa Clara, CA) HPLC systems equipped with a model 1200 quaternary pump, a model 1200 UV absorbance detector (220 nm), and a Bioscan (Washington, DC) NaI scintillation detector. The HPLC columns used were a semi-preparative column (Luna C18, 5 μm, 250 × 10 mm) and an analytical column (Luna C18, 5 μm, 250 × 4.6 mm) purchased from Phenomenex (Torrance, CA). The collected HPLC eluates containing the desired peptides were lyophilized using a Labconco (Kansas City, MO) FreeZone 4.5 Plus freeze-drier. MS analyses were conducted using the Waters (Milford, MA) Acquity QDa mass spectrometer with the equipped 2489 UV/Vis detector and e2695 Separations module. C18 Sep-Pak cartridges (1 cm^3, 50 mg) were purchased from Waters (Milford, MA). ^{68}Ga was eluted from an ITM Medical Isotopes GmbH (Munich, Germany) generator, and purified according to the previously published procedures using a DGA resin column from Eichrom Technologies LLC (Lisle, IL)[125]. The radioactivity of ^{68}Ga-labeled tracers was measured using a Capintec (Ramsey, NJ) CRC®-25R/W dose calibrator and the radioactivity of mouse tissues collected from biodistribution studies were counted using a Perkin Elmer (Waltham, MA) Wizard2 2480 automatic gamma counter.

2.2.2 FAP-targeted Ligands Syntheses

2.2.2.1 Synthesis of (S)-*N*-(2-(2-cyano-4,4-difluoropyrrolidin-1-yl)-2-oxoethyl)-6-(pent-4-yn-1-yloxy)quinoline-4-carboxamide (5)

Compound **5** was synthesized following the steps depicted in Scheme 2.1.

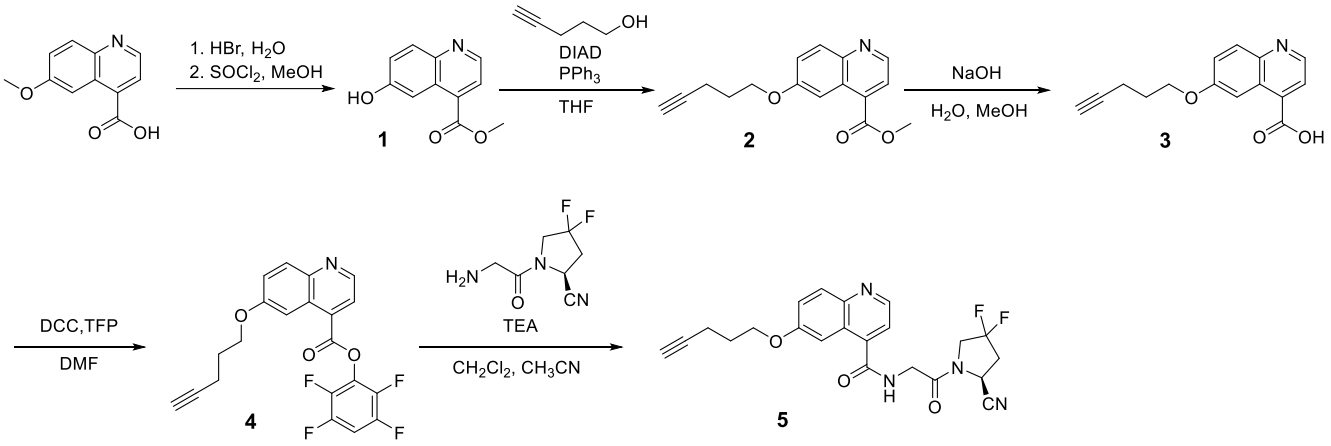

Scheme 2.1 Synthesis of (S)-N-(2-(2-cyano-4,4-difluoropyrrolidin-1-yl)-2-oxoethyl)-6-(pent-4-yn-1-yloxy)quinoline-4-carboxamide (**5**)

2.2.2.1.1 Synthesis of methyl 6-hydroxyquinoline-4-carboxylate (1)

A solution of quininic acid (5.0 g, 24.6 mmol) in mixture of hydrogen bromide (48%, 100 mL) and ethanol (25 mL) was stirred for 72 h at 115 °C. The solution was evaporated under reduced pressure and dissolved in methanol (80 mL). The solution was added thionyl chloride (5 mL) and stirred at 60 °C. After stirred for 22 h, the solution was evaporated, dissolved in saturated sodium bicarbonate (80 mL), and extracted with water (100 mL × 3). The organic phases were combined, dried over anhydrous $MgSO_4$, filtered, and evaporated under reduced pressure to yield compound **1** as a yellow solid (2.32 g, 47% yield). MS (ESI) calculated for $C_{16}H_{15}NO_3$ 203.10, found $[M+H]^+$ 204.04. ^1H NMR (300 MHz, DMSO) δ 10.40 (s, 1H), 8.79 (d, J = 4.4 Hz, 1H), 7.98

(d, *J* = 6.4 Hz, 1H), 7.96 (s, 1H), 7.86 (d, *J* = 4.4 Hz, 1H), 7.39 (dd, *J* = 9.1, 2.7 Hz, 1H), 3.95 (s, 3H).

2.2.2.1.2 Synthesis of methyl 6-(pent-4-yn-1-yloxy)quinoline-4-carboxylate (2)

To a solution of methyl 6-hydroxyquinoline-4-carboxylate **1** (1.73 g, 8.5 mmol), 4-pentyn-1-ol (7.57 g, 9 mmol) and triphenylphosphine (2.36 g, 9 mmol) in THF (50 mL) cooled in an ice/water bath was added diisopropyl azodicarboxylate (DIAD) (1.82 g, 9 mmol) dropwise. After stirring for 20 h, the resulting solution was evaporated, dissolved in DCM and purified using silica gel flash column chromatography eluted with 3:7 (v/v) ethyl acetate/hexanes. The collected product eluate fractions were combined, evaporated and dried under reduced pressure to yield **2** as a white powder (2.28 g, 100% yield). MS (ESI) calculated for $C_{16}H_{15}NO_3$ 269.11, found $[M+H]^+$ 270.09. ^{1}H NMR (300 MHz, DMSO) δ 8.89 (d, *J* = 4.5 Hz, 2H), 8.12 – 8.00 (m, 2H), 7.95 (d, *J* = 4.5 Hz, 1H), 7.53 (dd, *J* = 9.2, 2.8 Hz, 1H), 4.20 (t, *J* = 6.2 Hz, 2H), 3.98 (s, 3H), 2.40 (td, *J* = 7.1, 2.7 Hz, 2H), 1.99 (p, *J* = 6.6 Hz, 2H).

2.2.2.1.3 Synthesis of 6-(pent-4-yn-1-yloxy)quinoline-4-carboxylic acid (3)

A solution of compound **2** (2.28 g, 8.5 mmol) and sodium hydroxide (2.4 g, 61 mmol) in a mixture of methanol (25 mL) and water (20 mL) was stirred for 16 h. The solution was evaporated under reduced pressure and the residue was dissolved in water (80 mL). The aqueous solution was acidified with concentrated HCl to pH 3. The resulting white precipitates were collected by filtration and dried under reduced pressure to yield compound **3** as a white powder (1.61 g, 74% yield). MS (ESI) calculated for $C_{15}H_{13}NO_3$ 255.09, found $[M+H]^+$ 256.10. ^{1}H NMR (300 MHz, DMSO) δ 8.87 (d, *J* = 4.4 Hz, 1H), 8.17 (d, *J* = 2.8 Hz, 1H), 8.03 (d, *J* = 9.2 Hz, 1H), 7.93 (d, *J* =

4.4 Hz, 1H), 7.50 (dd, *J* = 9.2, 2.8 Hz, 1H), 4.18 (t, *J* = 6.2 Hz, 2H), 2.82 (t, *J* = 2.6 Hz, 1H), 2.40 (td, *J* = 7.1, 2.7 Hz, 2H), 1.99 (p, *J* = 6.6 Hz, 2H).

2.2.2.1.4 Synthesis of 2,3,5,6-tetrafluorophenyl 6-(pent-4-yn-1-yloxy)quinoline-4-carboxylate (4)

To a solution of compound **3** (1.56 g, 6.1 mmol) and 2,3,5,6-tetrafluorophenol (1.22 g, 7.3 mmol) in DMF (25 mL) cooled in an ice/water bath was added *N*,*N'*-dicyclohexylcarbodiimide (DCC, 1.26 g, 6.1 mmol) in DMF (25 mL) dropwise. After stirring for 72 h at room temperature, the resulting solution was filtered through celite and the organic solvent was evaporated under reduced pressure. The residue was purified by silica gel flash column chromatography eluted with 1:3 (v/v) ethyl acetate/hexanes. The collected product eluate fractions were combined, evaporated and dried under reduced pressure to yield **4** as a light yellow solid (1.77 g, 72% yield). MS (ESI) calculated for $C_{21}H_{13}F_4NO_3$ 403.08, found $[M+H]^+$ 404.16. ^{1}H NMR (300 MHz, DMSO) δ 8.86 (d, *J* = 4.4 Hz, 1H), 8.17 (d, *J* = 2.8 Hz, 1H), 8.02 (d, *J* = 9.2 Hz, 1H), 7.92 (d, *J* = 4.4 Hz, 1H), 7.50 (dd, *J* = 9.2, 2.8 Hz, 1H), 7.19 (tt, *J* = 10.9, 7.2 Hz, 1H), 4.18 (t, *J* = 6.2 Hz, 2H), 2.82 (t, *J* = 2.6 Hz, 1H), 2.40 (td, *J* = 7.1, 2.7 Hz, 2H), 1.99 (p, *J* = 6.6 Hz, 2H).

2.2.2.1.5 Synthesis of (S)-N-(2-(2-cyano-4,4-difluoropyrrolidin-1-yl)-2-oxoethyl)-6-(pent-4-yn-1-yloxy)quinoline-4-carboxamide (5)

A solution of compound **4** (403 mg, 1 mmol), (*S*)-1-(2-aminoacetyl)-4,4-difluoropyrrolidine-2-carbonitrile 4-methylbenzenesulfonate (1 mmol) and triethylamine (202 g, 2 mmol) in mixture of CH_2Cl_2 (8 mL) and CH_3CN (8 mL) was stirred at 50 °C for 23 h. The resulting solution was evaporated under reduced procedure and the residue was purified through

silica gel flash column chromatography eluted with 1:5 (v/v) methanol/ethyl acetate. The collected product eluate fractions were combined, evaporated and dried under reduced pressure to yield **5** as a light yellow solid (415 mg, 97% yield). MS (ESI) calculated for $C_{22}H_{20}F_2N_4O_3$ 426.15, found $[M+H]^+$ 427.22. ^1H NMR (300 MHz, DMSO) δ 9.10 (t, *J* = 6.0 Hz, 1H), 8.81 (d, *J* = 4.3 Hz, 1H), 7.99 (d, *J* = 9.2 Hz, 1H), 7.51 (d, *J* = 4.3 Hz, 1H), 7.47 (dd, *J* = 9.2, 2.7 Hz, 1H), 5.14 (dd, *J* = 9.1, 3.0 Hz, 1H), 4.50 – 4.02 (m, 6H), 2.80 (t, *J* = 2.6 Hz, 1H), 2.38 (td, *J* = 7.1, 2.7 Hz, 2H), 1.98 (m, *J* = 6.7 Hz, 2H).

2.2.2.2 Synthesis of (*S*)-*N*-(2-(2-cyano-4,4-difluoropyrrolidin-1-yl)-2-oxoethyl)-6-ethynylquinoline-4-carboxamide (9)

Compound **9** was synthesized following the steps depicted in Scheme 2.2.

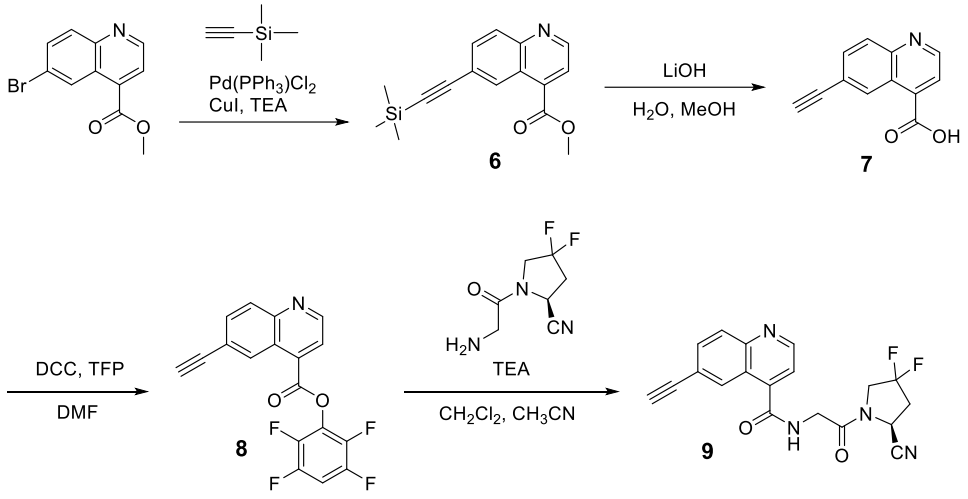

Scheme Error! No text of specified style in document.**2** Synthesis of (*S*)-*N*-(2-(2-cyano-4,4-difluoropyrrolidin-1-yl)-2-oxoethyl)-6-ethynylquinoline-4-carboxamide (**9**)

2.2.2.2.1 Synthesis of methyl 6-(2-(trimethylsilyl)ethynyl)quinoline-4-carboxylate (6)

A solution of methyl 6-bromoquinoline-4-carboxylate (1.33 g, 5 mmol), tetrakis(triphenylphosphine)palladium(0) (175 mg, 0.25 mmol), copper (I) iodide (95 mg, 0.5 mmol) and ethynyltrimethylsilane (982 mg, 10 mmol) in TEA (12 mL) was stirred at 90 °C for 18 h. The solution was diluted with water (100 mL) and then filtered through celite. The filtered aqueous solution was extracted with ethyl acetate (100 mL × 3). The organic phases were combined, dried over anhydrous $MgSO_4$, filtered, and evaporated under reduced pressure. The residue was purified with silica gel flash column chromatography eluted with 1:1 (v/v) diethyl ether/hexanes. The product eluate fractions were combined and evaporated under reduced pressure to yield **6** as a yellow oil (880 mg, 62% yield). MS (ESI) calculated for $C_{16}H_{17}NO_2Si$ 283.10, found $[M+H]^+$ 284.08. ^1H NMR (300 MHz, DMSO) δ 9.09 (d, *J* = 4.4 Hz, 1H), 8.74 (d, *J* = 1.8 Hz, 1H), 8.11 (d, *J* = 8.7 Hz, 1H), 8.00 (d, *J* = 4.4 Hz, 1H), 7.84 (dd, *J* = 8.7, 1.9 Hz, 1H), 3.99 (s, 3H).

2.2.2.2.2 Synthesis of 6-ethynylquinoline-4-carboxylic acid (7)

A solution of compound **6** (880 mg, 3.1 mmol) and lithium hydroxide (30 mmol) in a mixture of water (25 mL) and methanol (25 mL) was stirred at 60 °C for 3 h. After evaporation, the residue was dissolved in water (40 mL), and washed with diethyl ether (80 ml). The aqueous phase was then acidified using concentrated HCl to pH 3. The resulting precipitates were collected and dried under reduced pressure to yield **7** as a yellow powder (509 mg, 83% yield). MS (ESI) calculated for $C_{12}H_7NO_3$ 197.05, found $[M+H]^+$ 198.11. ^1H NMR (300 MHz, DMSO) δ 9.15 (d, *J* = 4.3 Hz, 1H), 8.98 (d, *J* = 1.8 Hz, 1H), 8.20 (d, *J* = 8.7 Hz, 1H), 8.07 (d, *J* = 4.4 Hz, 1H), 7.93 (dd, *J* = 8.7, 1.6 Hz, 1H), 4.51 (s, 1H).

2.2.2.2.3 Synthesis of 2,3,5,6-tetrafluorophenyl 6-ethynylquinoline-4-carboxylate (8)

To a solution of compound **7** (495 mg, 2.51 mmol) and 2,3,5,6-tetrafluorophenol (540 mg, 3.2 mmol) in DMF (20 mL) cooled in an ice/water bath was added dropwise a solution of DCC (660 mg, 3.2 mmol) in DMF (10 mL). The resulting solution was stirred for 21 h at room temperature, filtered, and the filtrate was evaporated under reduced pressure. The residue was purified using silica gel flash column chromatography eluted with 2:3 (v/v) diethyl ether/hexanes. The product eluate fractions were combined, evaporated and dried under reduced pressure to yield **8** as a light yellow solid (615 mg, 70.9% yield). MS (ESI) calculated for $C_{18}H_7F_4NO_3$ 345.04, found $[M+H]^+$ 346.06. ^{1}H NMR (300 MHz, DMSO) δ 9.07 (d, *J* = 4.4 Hz, 1H), 8.89 (d, *J* = 1.8 Hz, 1H), 8.11 (d, *J* = 8.7 Hz, 1H), 8.00 (d, *J* = 4.4 Hz, 1H), 7.85 (dd, *J* = 8.7, 1.9 Hz, 1H), 7.30 – 7.11 (m, 1H), 4.42 (s, 1H).

2.2.2.2.4 Synthesis of (*S*)-*N*-(2-(2-cyano-4,4-difluoropyrrolidin-1-yl)-2-oxoethyl)-6-ethynylquinoline-4-carboxamide (9)

A solution of compound **8** (605 mg, 1.75 mmol), (*S*)-1-(2-aminoacetyl)-4,4-difluoropyrrolidine-2-carbonitrile 4-methylbenzenesulfonate (2.1 g, 2.1 mmol) and TEA (606 g, 6 mmol) in a mixture of CH_2Cl_2 (15 mL) and CH_3CN (15 mL) was stirred at 50 °C for 19 h. The solution was then evaporated and purified through silica gel flash column chromatography eluted with 1:9 (v/v) methanol/ethyl acetate. The product eluate fractions were combined, evaporated and dried under reduced pressure to yield **9** as a white solid (644 mg, 100% yield). MS (ESI) calculated for $C_{19}H_{14}F_2N_4O_2$ 368.11, found $[M+H]^+$ 369.16. ^{1}H NMR (300 MHz, DMSO) δ 9.20 (t, *J* = 5.9 Hz, 1H), 9.03 (d, *J* = 4.3 Hz, 1H), 8.46 (d, *J* = 1.8 Hz, 1H), 8.09 (d, *J* = 8.7 Hz, 1H), 7.84 (dd, *J* = 8.7, 1.9 Hz, 1H), 7.63 (d, *J* = 4.3 Hz, 1H), 5.19 (dd, *J* = 9.1, 2.8 Hz, 1H), 4.35 – 4.05 (m, 2H), 3.05 – 2.78 (m, 2H).

2.2.2.3 Synthesis of (*S*)-*N*-(2-(2-cyano-4,4-difluoropyrrolidin-1-yl)-2-oxoethyl)-6-(prop-2-yn-1-yloxy)quinoline-4-carboxamide (13)

Compound **13** was synthesized following the steps depicted in Scheme 2.3.

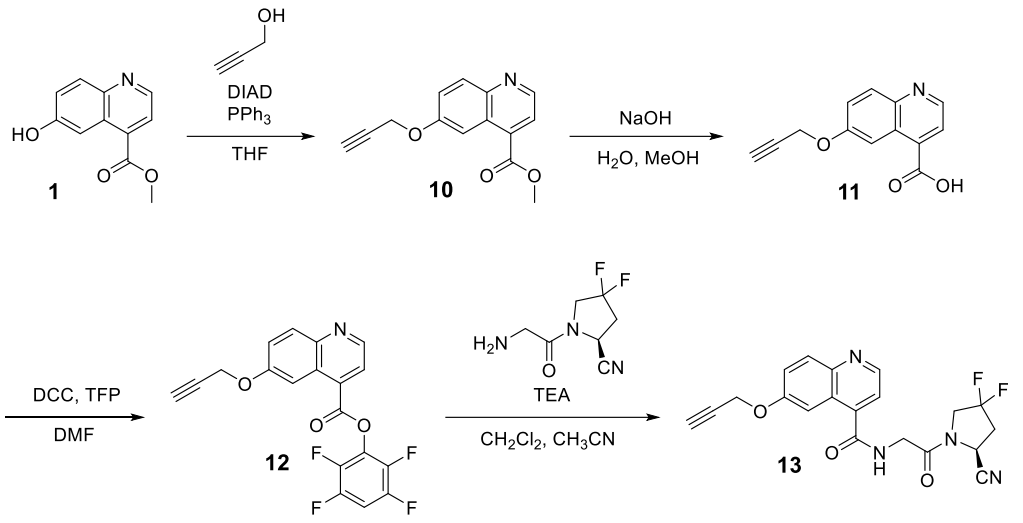

Scheme 2.3 Synthesis of (S)-N-(2-(2-cyano-4,4-difluoropyrrolidin-1-yl)-2-oxoethyl)-6-(prop-2-yn-1-yloxy)quinoline-4-carboxamide (**13**)

2.2.2.3.1 Synthesis of methyl 6-(prop-2-yn-1-yloxy)quinoline-4-carboxylate (10)

To a solution of methyl 6-hydroxyquinoline-4-carboxylate **1** (1.13 g, 5.6 mmol), 2-propyn-1-ol (348 mg, 6.2 mmol) and triphenylphosphine (1.63 g, 6.2 mmol) in THF (30 mL) cooled in an ice/water bath was added dropwise a solution of DIAD (1.25 g, 6.2 mmol) in THF (10 mL). The resulting solution was stirred for 20 h at room temperature. The solution was then evaporated and purified through silica gel flash column chromatography eluted with 6:4 (v/v) ethyl acetate:hexanes. The product eluate fractions were combined, evaporated and dried under reduced pressure to yield **10** as a white powder (1.35 g, 100% yield). MS (ESI) calculated for $C_{14}H_{11}NO_3$ 241.07, found $[M+H]^+$ 242.05. ^{1}H NMR (300 MHz, DMSO) δ 8.92 (d, *J* = 4.5 Hz, 1H), 8.19 (d, *J*

= 2.8 Hz, 1H), 8.08 (d, *J* = 9.2 Hz, 1H), 7.95 (d, *J* = 4.5 Hz, 1H), 7.56 (dd, *J* = 9.2, 2.8 Hz, 1H), 4.97 (d, *J* = 2.4 Hz, 2H), 3.99 (s, 3H), 3.64 (t, *J* = 2.4 Hz, 1H).

2.2.2.3.2 Synthesis of 6-(prop-2-yn-1-yloxy)quinoline-4-carboxylic acid (11)

A solution of compound **10** (1.35 g, 5.6 mmol) and sodium hydroxide (2.52 g, 63 mmol) in a mixture of water (20 mL) and methanol (25 mmol) was stirred for 17 h. After evaporation, the residue was dissolved in water and the resulting solution was acidified with concentrated HCl to pH 3. The resulting white precipitates were collected by filtration and dried under reduced pressure to yield **11** as a yellow solid (927 mg, 73% yield). MS (ESI) calculated for $C_{13}H_9NO_3$ 227.06, found $[M+H]^+$ 228.08. ^{1}H NMR (300 MHz, DMSO) δ 8.89 (d, *J* = 4.4 Hz, 1H), 8.27 (d, *J* = 2.9 Hz, 1H), 8.06 (d, *J* = 9.2 Hz, 1H), 7.93 (d, *J* = 4.4 Hz, 1H), 7.54 (dd, *J* = 9.2, 2.9 Hz, 1H), 4.95 (d, *J* = 2.4 Hz, 2H), 3.62 (t, *J* = 2.4 Hz, 1H).

2.2.2.3.3 Synthesis of 2,3,5,6-tetrafluorophenyl 6-(prop-2-yn-1-yloxy)quinoline-4-carboxylate (12)

To a solution of compound **11** (900 mg, 4 mmol) and 2,3,5,6-tetrafluorophenol (830 mg, 5 mmol) in DMF (20 mL) cooled in an ice/water bath was added dropwise a solution of DCC (825 mg, 4 mmoL) in DMF (20 mL). The resulting solution was stirred for 22 h and then filtered. The filtrate was evaluated under reduced pressure and the residue was purified through silica gel flash column chromatography eluted with 4:6 (v/v) diethyl ether/hexanes. The product eluate fractions were combined, evaporated and dried under reduced pressure to yield **12** as a yellow solid (1.02 g, 68% yield). MS (ESI) calculated for $C_{19}H_9F_4NO_3$ 375.05, found $[M+H]^+$ 376.08. ^{1}H NMR (300 MHz, DMSO) δ 8.89 (d, *J* = 4.4 Hz, 1H), 8.28 (d, *J* = 2.8 Hz, 1H), 8.06 (d, *J* = 9.2 Hz, 1H), 7.94

(d, *J* = 4.4 Hz, 1H), 7.54 (dd, *J* = 9.2, 2.9 Hz, 1H), 7.22 (q, *J* = 8.4 Hz, 1H), 4.95 (s, 2H), 3.62 (d, *J* = 4.5 Hz, 1H).

2.2.2.3.4 Synthesis of (*S*)-*N*-(2-(2-cyano-4,4-difluoropyrrolidin-1-yl)-2-oxoethyl)-6-(prop-2-yn-1-yloxy)quinoline-4-carboxamide (13)

A solution of compound **12** (500 mg, 1.33 mmol), (*S*)-1-(2-aminoacetyl)-4,4-difluoropyrrolidine-2-carbonitrile 4-methylbenzenesulfonate (481 mg, 1.33 mmol) and TEA (3 mmol, 304 mg) in a mixture of CH_2Cl_2 (8 mL) and CH_3CN (8 mL) was stirred at 50 °C for 22 h. The solution was then evaporated under reduced pressure and the residue was purified using silica gel flash column chromatography eluted with 1:5 (v/v) methanol/ethyl acetate. The product eluate fractions were collected, combined, evaporated and dried under reduced pressure to yield **13** as a white solid (528 mg, 100% yield). MS (ESI) calculated for $C_{20}H_{16}F_2N_4O_3$ 398.12, found $[M+H]^+$ 399.24. ^{1}H NMR (300 MHz, DMSO) δ 9.09 (t, *J* = 6.0 Hz, 1H), 8.83 (dd, *J* = 10.2, 4.4 Hz, 1H), 8.02 (t, *J* = 9.8 Hz, 1H), 7.88 (d, *J* = 2.9 Hz, 1H), 7.59 – 7.45 (m, 1H), 5.16 (dd, *J* = 9.2, 2.9 Hz, 1H), 4.41 – 4.02 (m, 4H), 3.06 – 2.74 (m, 3H).

2.2.3 Synthesis of DOTA-conjugated Peptides

AV01017, AV01030, and AV01038 were synthesized on solid phase using Fmoc peptide chemistry. Fmoc-Lys(ivDde)-Wang resin (0.05 mmol, 0.081 mg) was treated with 20% piperidine in DMF to remove the Fmoc protecting group. The isocyanate derivative (3 eq.) of Glu(tBu)-OtBu was synthesized following previously published procedures[126] and was added to the lysine-immobilized resin, with *N*,*N*-diisopropylethylamine (DIEA, 2 eq.) as the base and reacted for 16 h to form the Lys-urea-Glu moiety. The ivDde-protecting group was then removed with 2%

hydrazine in DMF (5 × 5 min). Fmoc-Ala(9-Anth)-OH (3 eq.), Fmoc-tranexamic acid (3 eq.), Fmoc-Gly-OH, and Fmoc-Lys(ivDde)-OH were pre-activated with HATU (3 eq.) and DIEA (3 eq.) before being sequentially coupled to the resin. Following the removal of Fmoc protecting group, azidoacetic acid (2 eq.) was pre-activated with DIC (3 eq.) and DIEA (3 eq.) and coupled to the α-amino group of lysine. A click reaction was then performed between the alkyne-containing FAPI-targeting moiety (compound **5**, **9** or **13**, 2 eq.) and the azido group on resin in the presence of $CuSO_4$ (1 M, 10 µL), tris(benzyltriazolylmethyl)amine (TBTA, 3eq.) and ascorbic acid (1 M, 100 uL) for 48 h. Finally, the ivDde-protecting group on lysine was removed and coupled with DOTA-tris(*t*-butyl)ester activated with HATU (3 eq.) and DIEA (7 eq.)

The peptides were deprotected and simultaneously cleaved from the resin with a mixture of trifluoroacetic acid (TFA, 95%), triisopropylsilane (TIS 2.5%) and water (2.5%) for 4 h at room temperature. The cleaved peptides were filtrated and then precipitated by adding cold diethyl ether. The crude peptides were collected by centrifugation and purified with HPLC (semi-preparative column; flow rate: 4.5 mL/min). The eluates containing the desired peptides were collected and lyophilized. The HPLC conditions, retention times, isolated yields and MS confirmations of DOTA-conjugated peptides are provided in Table 2.1.

2.2.4 Synthesis of Nonradioactive Ga-complexed Standards

The nonradioactive Ga-complexed standards were prepared by reacting the DOTA-conjugated precursor with $GaCl_3$ (5 eq.) in NaOAc buffer (0.1 M, 500 µL, pH 4.2 – 4.5) at 80 °C for 15 min. The reaction mixture was then purified via HPLC (semi-preparative column, flow rate: 4.5 mL/min). The HPLC eluates containing the desired peptide were collected and lyophilized.

The HPLC conditions, retention times, isolated yields and MS confirmations of these nonradioactive Ga-complexed standards are provided in Table 2.2.

2.2.5 Synthesis of ^{68}Ga-labeled Compounds

The radiolabeling experiments were performed according to previously published procedures [126,127] Purified $^{68}GaCl_3$ in 0.5 mL water was added to a 4-mL glass vial preloaded with 0.7 mL of HEPES buffer (2 M, pH 5.0) and 10 μL precursor solution (1 mM). The radiolabeling reaction was carried out under microwave heating for 1 min, followed by purification using HPLC semi-preparative column. The eluate fraction containing the radiolabeled product was collected, diluted with water (50 mL), and passed through a C18 Sep-Pak cartridge that was pre-washed with ethanol (10 mL) and water (10 mL). The C18 Sep-Pak cartridge was washed with water (10 mL), and the ^{68}Ga-labeled product was eluted off the cartridge with ethanol (0.4 mL). The eluted product was diluted with PBS for imaging and biodistribution studies. Quality control was performed using the analytical column. The HPLC conditions and retention times are provided in Table 2.3. The tracers were obtained in 43-60% decay-corrected radiochemical yields with >74 GBq/μmol molar activity and >99% radiochemical purity.

Table 2.1 HPLC purification conditions and MS characterizations of DOTA-conjugated precursors.

Compound name	HPLC conditions	Retention time (min)	Yield (%)	Calculated mass (m/z)	Found (m/z)
AV01017	29% CH_3CN and 0.1% TFA in H_2O	8.3	1.5	$[M+2H]^{2+}$ 893.9	$[M+2H]^{2+}$ 893.6
AV01030	29% CH_3CN and 0.1% TFA in H_2O	11.3	4.0	$[M+2H]^{2+}$ 864.9	$[M+2H]^{2+}$ 865.4
AV01038	28% CH_3CN and 0.1% TFA in H_2O	13.5	1.3	$[M+2H]^{2+}$ 879.9	$[M+2H]^{2+}$ 880.2

Table 2.2 HPLC purification conditions and MS characterizations of nonradioactive Ga-complexed standards.

Compound name	HPLC conditions	Retention time (min)	Yield (%)	Calculated mass (m/z)	Found (m/z)
Ga-AV01017	30% CH_3CN and 0.1% TFA in H_2O	7.5	24.8	$[M+2H]^{2+}$ 928.4	$[M+2H]^{2+}$ 927.7
Ga-AV01030	30% CH_3CN and 0.1% TFA in H_2O	11.5	24.5	$[M+2H]^{2+}$ 899.3	$[M+2H]^{2+}$ 899.8
Ga-AV01038	28% CH_3CN and 0.1% TFA in H_2O	15.9	88.9	$[M+2H]^{2+}$ 914.4	$[M+2H]^{2+}$ 913.5
Ga-FAPI-04	10% CH_3CN and 0.1% TFA in H_2O	10.5	8.7	$[M+2H]^{2+}$ 471.65	$[M+2H]^{2+}$ 470.29

Table 2.3 HPLC conditions for the purification and quality control of ^{68}Ga-labeled AV01017, AV01030 and AV01038. FA: formic acid. TFA: Trifluoroacetic acid

Compound name	HPLC conditions	Retention time (min)

[^{68}Ga]Ga-AV01017	Semi-Prep	29% CH_3CN and 0.1% FA in H_2O; flow rate 4.5 mL/min	17.0
	QC	31% CH_3CN and 0.1% FA in H_2O; flow rate 2 mL/min	5.1
[^{68}Ga]Ga-AV01030	Semi-Prep	29% CH_3CN and 0.1% FA in H_2O; flow rate 4.5 mL/min	16.2
	QC	31% CH_3CN and 0.1% FA in H_2O; flow rate 2 mL/min	6.0
[^{68}Ga]Ga-AV01038	Semi-Prep	31% CH_3CN and 0.1% FA in H_2O; flow rate 4.5 mL/min	10.3
	QC	30% CH_3CN and 0.1% FA in H_2O; flow rate 2 mL/min	5.8
[^{68}Ga]Ga-FAPI-04	Semi-Prep	11% CH_3CN and 0.1% TFA in H_2O; flow rate 4.5 mL/min	24.5
	QC	16% CH_3CN and 0.1% TFA in H_2O; flow rate 2 mL/min	5.2

2.2.6 Molar Activity Calculation

To determine the molar activity, 4 different amounts (0.01, 0.05, 0.1, and 0.2 nmole) of the Ga-complexed standards were injected to the analytical column to generate the standard curve. The amount of ^{68}Ga-labeled injected was calculated from the standard curve equation $y = mx + b$, where y is the absorbance detected by the HPLC and x is the amount of radiotracer injected. The molar activity (GBq/µmole) was calculated by dividing the radioactivity injected by the amount of radiotracer injected.

2.2.7 Cell Culture

The LNCaP cells obtained from ATCC (via Cedarlane, Burlington, Canada) were cultured in RPMI 1640 medium supplemented with 10% FBS, penicillin (100 U/mL) and streptomycin (100 µg/mL) at 37 °C in a Panasonic Healthcare (Tokyo, Japan) MCO-19AIC humidified incubator containing 5% CO_2. The cells were confirmed to be pathogen-free by the IMPACT Rodent Pathogen Test (IDEXX BioAnalytics). Cells were grown until 80-90% confluence and

washed with sterile phosphate-buffered saline (PBS, pH 7.4) and collected after 1 min trypsinization. The cell concentration was counted in triplicate using a hemocytometer and a manual laboratory counter.

2.2.8 Cell Transfection

The HEK293T cells were obtained from ATCC. The FAP-expressing vector was constructed using Genome-CRISPRTM Human AAVS1 Safe Harbor Gene Knock-in Kits (GeneCopoeaiaTM) by inserting FAP-expressing gene into the AAVS1 vector. The cells were then transfected by the FAP-expressing vector following the EndofectinTM Transfection Reagent protocol. The cells undergone 3 serial dilutions and were sorted using fluorescence activated cell sorting (FACS) to obtain FAP-expressing monoclonal colonies. HEK293T:hFAP cells were cultured in DMEM GlutaMAX™ medium supplemented with 10% FBS, penicillin (100 U/mL) and streptomycin (100 μg/mL) at 37 °C in a Panasonic Healthcare (Tokyo, Japan) MCO-19AIC humidified incubator containing 5% CO_2. Cells were grown until 80-90% confluence and washed with sterile PBS (pH 7.4) and collected.

2.2.9 In Vitro PSMA Competition Binding Assay

The PSMA binding assays were conducted following previously published procedures using LNCaP cells and [^{18}F]DCFPyL as the radioligand[122,123,128]. Data analyses of IC_{50} were performed using the nonlinear regression algorithm of GraphPad Prism 7 (San Diego, CA) software. Briefly, LNCaP cells (400,000/well) were plated onto a 24-well poly-D-lysine coated plate for 48 h. Growth media was removed and replaced with HEPES buffered saline (50 mM HEPES, pH 7.5, 0.9% sodium chloride), and the cells were incubated for 1 h at 37 °C.

[^{18}F]DCFPyL (0.1 nM) was added to each well (in triplicate) containing various concentrations (10 mM−0.5 pM) of tested compounds (Ga-AV01017, Ga-AV01030, and Ga-AV01038). Nonspecific binding was determined in the presence of 10 μM nonradiolabeled DCFPyL. The assay mixtures were further incubated for 1 h at 37 °C with gentle agitation. Then, the buffer and hot ligand were removed, and cells were washed twice with cold HEPES buffered saline. To harvest the cells, 400 μL of 0.25% trypsin solution was added to each well. Radioactivity was measured on a PerkinElmer (Waltham, MA) Wizard2 2480 automatic gamma counter. Nonlinear regression analyses and IC_{50} calculations were performed using the GraphPad Prism 7 software.

2.2.10 In Vitro FAP Fluorescence Assay

The half maximal inhibitory concentration (IC_{50}) values of the tested compounds for FAP were measured by in vitro enzymatic assay. The recombinant human FAP (Biolegend; 0.2 μg/mL, 50 μL) was added into costar 96-well plate. PBS and varied concentrations (0.2 pM to 2 μM) of tested nonradioactive Ga-complexed standards were added to each wells (in duplicate) containing the recombinant human FAP. After being incubated for 30 min at 37 °C, 50 μL of Suc-Gly-Pro-AMC (2 μM, Bachem) was added to each well. The fluorescent signals were acquired at 15, 30, 45, and 60 min using FlexStation 3 Multi-Mode Microplate Reader with excitation at 380 nm and emission at 460 nm. The IC_{50}(FAP) was calculated using “nonlinear fit model” built-in model in GraphPad Prism 7.02 software.

2.2.11 Ex Vivo Biodistribution and PET/CT Imaging Studies

Imaging and biodistribution studies were performed using male NOD.Cg-Rag1tm1Mom Il2rgtm1Wjl/SzJ (NRG) mice following previously published procedures[129,130]. The experiments

were conducted according to the guidelines established by the Canadian Council on Animal Care and approved by Animal Ethics Committee of the University of British Columbia. The mice were briefly sedated by inhalation of 2.5% isoflurane in oxygen, and 100 µL LNCaP (8×10^6 cells) or HEK293T:hFAP (8.5×10^6 cells) cells were inoculated subcutaneously behind the left shoulder. When the tumor grew to 5-8 mm in diameter over 3-4 weeks and 4-5 weeks for HEK293T:hFAP and LNCaP tumors, respectively, the mice were used for PET/CT imaging and biodistribution studies.

PET/CT imaging experiments were carried out using a Siemens (Knoxville, TN) Inveon micro PET/CT scanner. Each tumor-bearing mouse was injected with ~4-6 MBq of ^{68}Ga-labeled tracer through a lateral caudal tail vein under 2.5% isoflurane in oxygen anesthesia, followed by recovery and roaming freely in its cage during the uptake period. At 50 min post-injection, a 10-min CT scan was conducted first for localization and attenuation correction after segmentation for reconstructing the PET images, followed by a 10-min static PET imaging acquisition.

For biodistribution studies, the mice were injected with the radiotracer (~2-4 MBq) as described above. At 1 h post-injection, the mice were euthanized by CO_2 inhalation. Blood was withdrawn by cardiac puncture, and organs/tissues of interest were collected, weighed and counted using a Perkin Elmer (Waltham, MA) Wizard2 2480 automatic gamma counter.

2.2.12 Statistical Analysis

Data were analyzed with the GraphPad Prism, version 7.02 and Microsoft (Redmond, WA) Excel software. One way ANOVA and multiple t tests were performed for all organs in the biodistribution studies of [^{68}Ga]Ga-AV01017, [^{68}Ga]Ga-AV01030, [^{68}Ga]Ga-AV01038, [^{68}Ga]Ga-HTK03041, [^{68}Ga]Ga-FAPI-04 in LNCaP and HEK293T:hFAP tumor models. A

statistically significant difference was considered present when the adjusted *P* value was less than 0.05 using the Holm–Sidak method.

2.3 Results

2.3.1 Synthesis of PSMA/FAP bispecific ligands

The syntheses of compounds **5**, **9** and **13** are depicted in Schemes 2.1-2.3, respectively. For the preparation of compound **5** (Scheme 2.1), quininic acid was demethylated in 48% HBr solution, followed by esterification in methanol in the presence of thionyl chloride to obtain **1** in 47% yield. Mitsunobu coupling between compound **1** and 4-pentyn-1-ol resulted in **2** in 100% yield. Compound **3** was obtained in 74% yield by the hydrolysis of **2** with NaOH in a mixture of water and methanol. Esterification of compound **3** with tetrafluorphenol (TFP) led to compound **4** in 72% yield. Compound **5** was obtained in 97% yield by coupling the activated ester **4** with (*S*)-1-(2-aminoacetyl)-4,4-difluoropyrrolidine-2-carbonitrile.

The synthesis of compound **9** is depicted in Scheme 2.2. Sonogashira reaction was performed for coupling methyl 6-bromoquinoline-4-carboxylate and ethynyltrimethylsilane to obtain compound **6** in 62% yield. Silane deprotection and ester hydrolysis were performed simultaneously with LiOH in a mixture of water and methanol to afford compound **7** in 83% yield. Compound **7** was subsequently activated with tetrafluorophenol to afford the activated ester **8** in 71% yield. The desired compound **9** was obtained in 100% yield by coupling the activated ester **8** with (*S*)-1-(2-aminoacetyl)-4,4-difluoropyrrolidine-2-carbonitrile.

The synthetic procedures for the preparation of compound **13** are provided in Scheme 2.3. Mitsunobu coupling of compound **1** and 2-propyn-1-ol resulted in **10** in 100% yield. Compound

10 was hydrolyzed with NaOH in a mixture of water and methanol to obtain compound **11** in 73% yield. Activation of compound **11** with tetrafluorophenol resulted in compound **12** in 68% yield. Compound **13** was obtained in 100% yield by coupling the activated ester **12** with (*S*)-1-(2-aminoacetyl)-4,4-difluoropyrrolidine-2-carbonitrile.

AV01017, AV01030 and AV01038 were synthesized on solid phase. Detailed synthetic procedures and characterizations are provided in the method section (Table 2.1). Briefly, Lys(azidoacetic acid-Lys(ivDde)-Gly-tranexamic acid-Ala(9-Anth))-urea-Glu(OtBu)-OtBu was first constructed on solid phase, followed by the click addition of the alkyne-containing FAP-targeting motif: compound **5** for AV01017, Compound **9** for AV01030 and compound **13** for AV01038. The amino group at Lys side chain was then deprotected and coupled with the DOTA chelator. The DOTA-conjugated ligands were then cleaved off from resin and purified by HPLC.

Detailed syntheses and characterizations of nonradioactive Ga- and ^{68}Ga-complexed AV01017, AV01030 and AV01038 are provided in the method section (Table 2.2–2.3). Nonradioactive Ga-complexed AV01017, AV01030 and AV01038 were obtained in 25-89% yields, and their ^{68}Ga-labeled analogs were obtained in 43 – 60% decay-corrected radiochemical yields with >74 GBq/μmol molar activity and >99% radiochemical purity.

2.3.2 Binding Affinity

The binding affinities of Ga-AV01017, Ga-AV01030, Ga-AV01038, Ga-HTK03041 and Ga-FAPI-04 to PSMA were measured by a cell-based binding assay using PSMA-expressing LNCaP prostate cancer cells. The nonradioactive Ga-complexed standards inhibited the binding of [^{18}F]DCFPyL to LNCaP cells in a dose-dependent manner except Ga-FAPI-04 (Figure 2.3A). The calculated IC_{50}(PSMA) values for Ga-AV01017, Ga-AV01030, Ga-AV01038, Ga-

HTK03041, and Ga-FAPI-04 were 25.2±10.7, 71.6±23.0, 29.4±25.2, 0.76±0.12 and >1,000 nM, respectively (n = 3).

The binding affinities of Ga-AV01017, Ga-AV01030, Ga-AV01038, Ga-HTK03041 and Ga-FAPI-04 to human FAP were measure by an enzyme inhibition assay using Suc-Gly-Pro-AMC as the FAP substrate. The human FAP enzymatic activity on the substrate was inhibited by Ga-complexed standards in a dose dependent-manner (Figure 2.3B). The calculated IC_{50}(FAP) values for Ga-AV01017, Ga-AV01030, Ga-AV01038, Ga-HTK03041, and Ga-FAPI-04 were 1.25±0.39, 2.74±0.33, 2.31±0.13, 2,010±585 and 1.03±0.4 nM, respectively (n = 3).

2.3.3 PET Imaging and Biodistribution Studies

Representative PET images acquired at 1 h post-injection using [^{68}Ga]Ga-AV01017, [^{68}Ga]Ga-AV01030, [^{68}Ga]Ga-AV01038, [^{68}Ga]Ga-HTK03041, and [^{68}Ga]Ga-FAPI-04 are provided in Figure 2.4. All of the radiotracers were excreted primarily through the renal pathway. All the bispecific tracers ([^{68}Ga]Ga-AV01017, [^{68}Ga]Ga-AV01030 and [^{68}Ga]Ga-AV01038) had significantly higher background and heart uptake compared to the monospecific tracers ([^{68}Ga]Ga-HTK03041 and [^{68}Ga]Ga-FAPI-04). LNCaP tumor xenografts were clearly visualized by [^{68}Ga]Ga-HTK03041 with an excellent contrast, barely visualized by the bispecific tracers ([^{68}Ga]Ga-AV01017, [^{68}Ga]Ga-AV01030, [^{68}Ga]Ga-AV01038), and not visualized by [^{68}Ga]Ga-FAPI-04 (Figure 2.4A). For HEK293T:hFAP tumor xenografts, they were clearly visualized by [^{68}Ga]Ga-FAPI-4 with an excellent contrast and by [^{68}Ga]Ga-AV01030 with a good contrast, barely visualized by [^{68}Ga]Ga-AV01017 and [^{68}Ga]Ga-AV01038, and not visualized by [^{68}Ga]Ga-HTK03041 (Figure 2.4B). All tracers, except [^{68}Ga]Ga-HTK03041 have bone and joint uptake, which is commonly observed for FAP-targeting tracers. High thyroid uptake was also observed in [^{68}Ga]Ga-AV01017, [^{68}Ga]Ga-AV01030, [^{68}Ga]Ga-AV01038 PET images. There was a high

kidney uptake in mice injected with the bispecific tracers and [^{68}Ga]Ga-HTK03041, but not in mice injected with [^{68}Ga]Ga-FAPI-04.

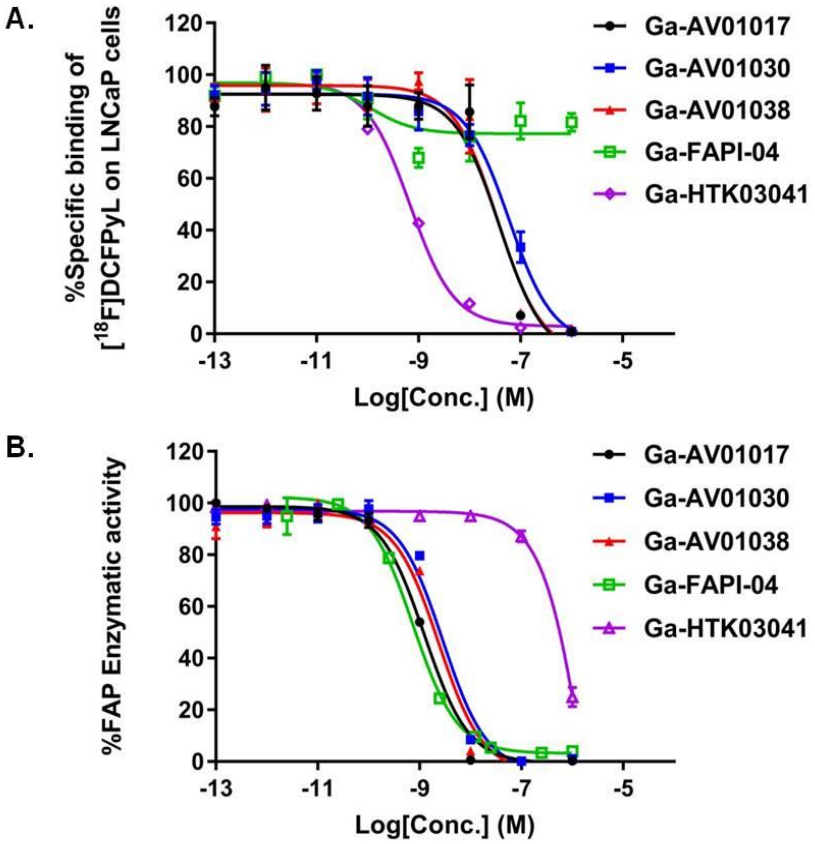

Figure 2.3 (A) Displacement curves of [^{18}F]DCFPyL by Ga-AV01017, Ga-AV01030, Ga-AV01038, Ga-FAPI-04, and Ga-HTK03041 generated using PSMA-expressing LNCaP cells; (B) Fluorescence curve of FAP enzymatic activity on Suc-Gly-Pro-AMC substrate with inhibition by Ga-AV01017, Ga-AV01030, Ga-AV01038, Ga-FAPI-04, and Ga-HTK03041.

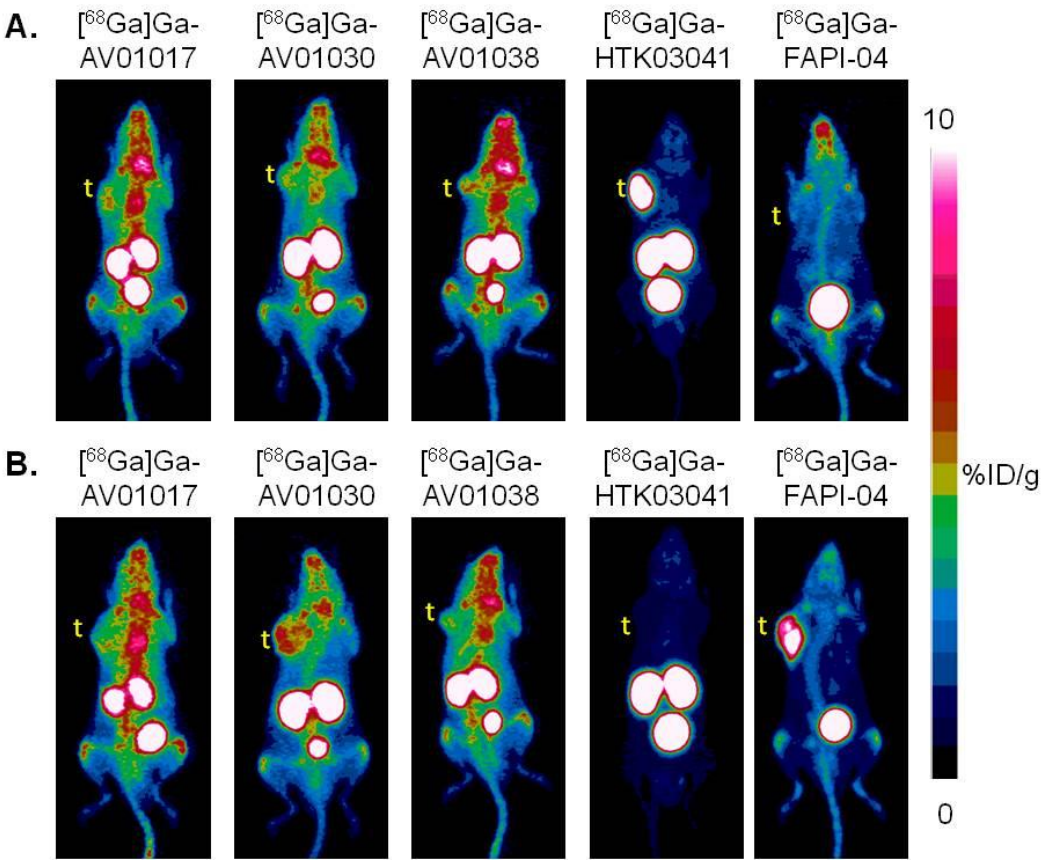

Figure 2.4 Representative maximum intensity projection PET images of [^{68}Ga]Ga-AV01017, [^{68}Ga]Ga-AV01030, [^{68}Ga]Ga-AV01038, [^{68}Ga]Ga-HTK03041, and [^{68}Ga]Ga-FAPI-04 acquired at 1 h post-injection in mice bearing (A) LNCaP tumor xenografts and (B) HEK293T:hFAP tumor xenografts. t:tumor.

Biodistribution studies were conducted at 1 h post-injection with ^{68}Ga-labeled AV01017, AV01030, AV01038, HTK03041, and FAPI-04 in LNCaP tumor-bearing mice (Figure 2.5 and Table 2.4). The results were consistent with the observation from their PET images. Tumor uptake values for [^{68}Ga]Ga-AV01017, [^{68}Ga]Ga-AV01030, [^{68}Ga]Ga-AV01038, [^{68}Ga]Ga-HTK03041, [^{68}Ga]Ga-FAPI-04 were 4.38±0.55, 5.17±0.51, 4.25±0.86, 23.1±6.11, and 3.15±1.43 %ID/g, respectively. All the bispecific tracers have statistically significant higher heart and blood uptake than the monospecific [^{68}Ga]Ga-HTK03041 and [^{68}Ga]Ga-FAPI-04 (blood uptake: 5.75 – 9.24 vs

1.43 – 2.16 %ID/g, P <0.05; heart uptake: 2.41 – 4.04 vs 0.70 – 1.82 %ID/g, P <0.05). Although not statistically significant, the bispecific tracers with a longer linker tend to have a higher blood uptake value (9.24±1.55 %ID/g for [^{68}Ga]Ga-AV01017; 7.07±0.31 %ID/g for [^{68}Ga]Ga-AV01038; 5.75±0.59 %ID/g for [^{68}Ga]Ga-AV01030) and a lower tumor-to-blood ratio (0.48±0.11 for [^{68}Ga]Ga-AV01017; 0.60±0.13 for [^{68}Ga]Ga-AV01038; 0.89±0.03 for [^{68}Ga]Ga-AV01030). The bispecific tracers also had significantly higher uptake values in muscle and thyroid when compared to those of monospecific radiotracers (P <0.05).

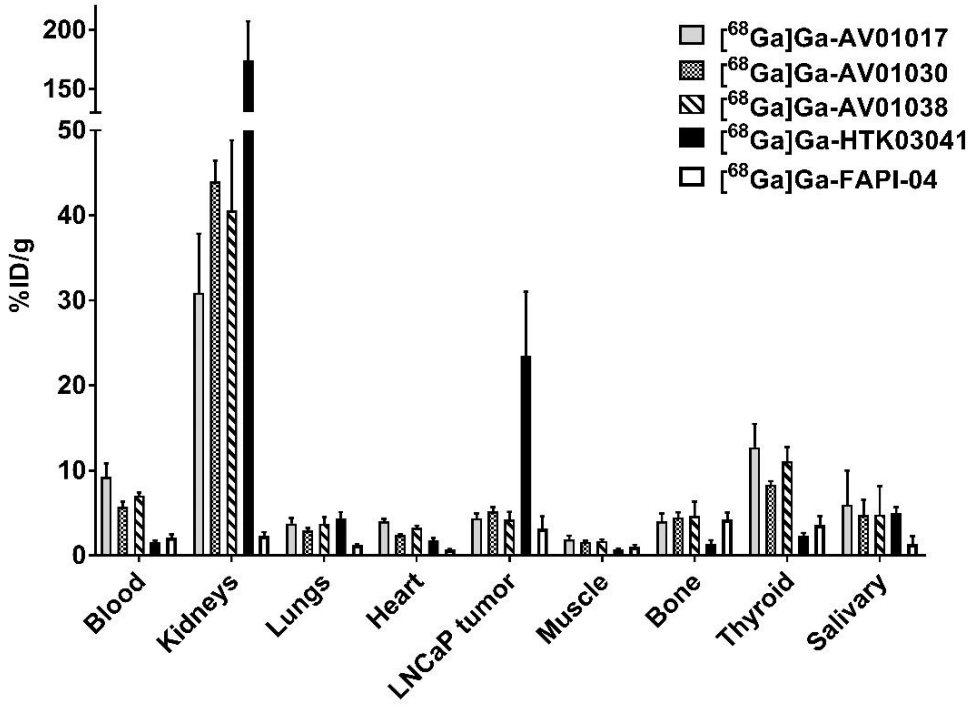

Figure 2.5 Biodistribution of [^{68}Ga]Ga-AV01017, [^{68}Ga]Ga-AV01030, [^{68}Ga]Ga-AV01038, [^{68}Ga]Ga-HTK03041 and [^{68}Ga]Ga-FAPI-04 in LNCaP tumor-bearing mice.

Biodistribution studies were also conducted at 1 h post-injection with [^{68}Ga]Ga-AV01017, [^{68}Ga]Ga-AV01030, [^{68}Ga]Ga-AV01038, [^{68}Ga]Ga-HTK03041, [^{68}Ga]Ga-FAPI-04 in HEK293T:hFAP tumor-bearing mice (Figure 2.6 and Table 2.5). Tumor uptake values for

[^{68}Ga]Ga-AV01017, [^{68}Ga]Ga-AV01030, [^{68}Ga]Ga-AV01038, [^{68}Ga]Ga-HTK03041, and [^{68}Ga]Ga-FAPI-04 were 2.99±0.37, 3.69±0.81, 3.64±0.83, 0.62±0.19, and 12.5±2.00 %ID/g, respectively. There was a very low tumor uptake in mice injected with [^{68}Ga]Ga-HTK03041, showing very minimal PSMA expression in this tumor model. The uptake levels of these tracers on the major organs and tissues are consistent with the trends observed in the LNCaP tumor-bearing mice (Figure 2.6 and Table 2.5).

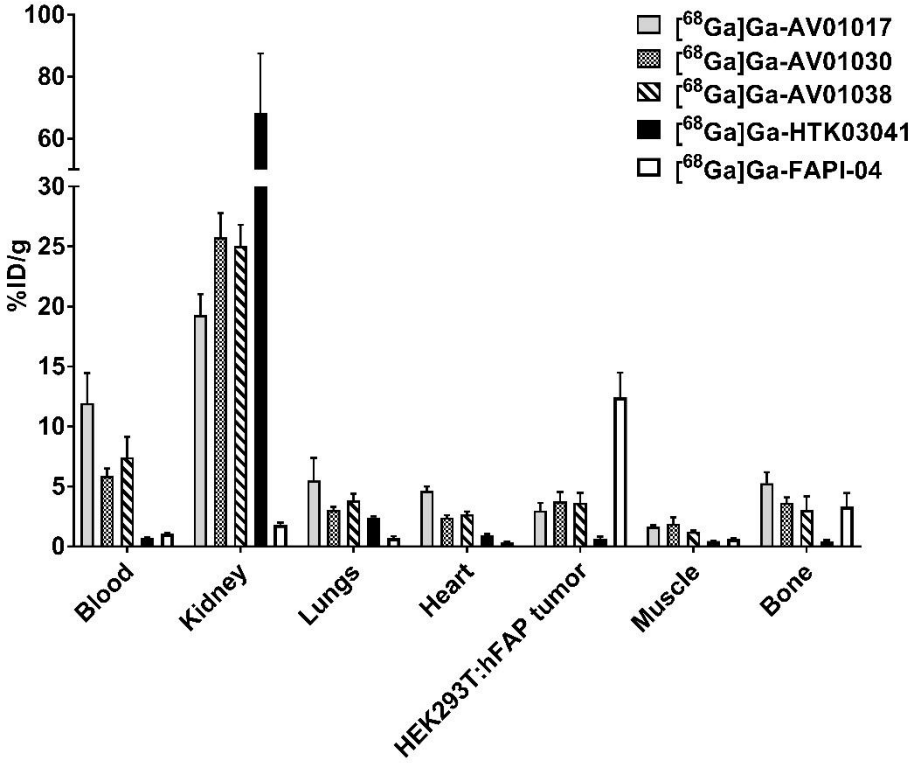

Figure 2.6 Biodistribution of [^{68}Ga]Ga-AV01017, [^{68}Ga]Ga-AV01030, [^{68}Ga]Ga-AV01038, [^{68}Ga]Ga-HTK03041 and [^{68}Ga]Ga-FAPI-04 in HEK293T:hFAP tumor-bearing mice.

Table 2.4 Biodistribution (mean ± SD, n = 4) and uptake ratios of ^{68}Ga-labeled PSMA/FAP-dual targeting tracers, HTK03041, and FAPI-04 in LNCaP tumor-bearing mice.

Tissue (%ID/g)	[^{68}Ga]Ga-AV01017	[^{68}Ga]Ga-AV01030	[^{68}Ga]Ga-AV01038	[^{68}Ga]Ga-HTK03041*	[^{68}Ga]Ga-FAPI-04
	1 h	1 h	1 h	1 h	1 h
Blood	9.24 ± 1.55	5.75 ± 0.59	7.07 ± 0.31	1.43 ± 0.30	2.16 ± 0.33
Fat	1.01 ± 0.48	0.68 ± 0.12	1.01 ± 0.28	2.06 ± 0.59	0.55 ± 0.47
Seminal vesicle	1.12 ± 0.21	1.04 ± 0.13	1.51 ± 0.08	-	3.72 ± 5.09
Testes	0.69 ± 0.06	0.70 ± 0.08	1.04 ± 0.10	1.34 ± 0.22	0.42 ± 0.04
Small Intestine	2.47 ± 0.48	1.58 ± 0.13	2.12 ± 0.24	1.14 ± 0.18	0.74 ± 0.12
Large Intestine	1.76 ± 0.21	1.32 ± 0.29	1.65 ± 0.31	-	0.73 ± 0.09
Stomach	0.64 ± 0.11	0.44 ± 0.07	0.64 ± 0.11	0.41 ± 0.11	0.26 ± 0.04
Spleen	3.73 ± 1.19	6.50 ± 1.37	6.77 ± 4.86	8.95 ± 3.22	0.67 ± 0.11
Liver	2.24 ± 0.34	1.43 ± 0.26	2.06 ± 0.13	1.38 ± 0.25	0.76 ± 0.08
Pancreas	5.38 ± 1.29	3.63 ± 0.29	3.91 ± 0.20	1.47 ± 0.16	0.99 ± 0.25
Adrenal glands	6.24 ± 2.31	3.13 ± 1.25	3.69 ± 2.54	-	2.16 ± 1.08
Kidneys	30.9 ± 6.89	44.0 ± 2.42	40.5 ± 8.26	170 ± 26.4	2.36 ± 0.38
Lungs	3.76 ± 0.66	2.93 ± 0.28	3.74 ± 0.78	4.32 ± 4.32	1.23 ± 0.07
Heart	4.04 ± 0.28	2.41 ± 0.13	3.26 ± 0.24	1.82 ± 0.62	0.70 ± 0.04
LNCaP tumor	4.38 ± 0.55	5.17 ± 0.51	4.25 ± 0.86	23.1 ± 6.11	3.15 ± 1.43
Muscle	1.91 ± 0.43	1.59 ± 0.14	1.68 ± 0.21	0.75 ± 0.09	1.04 ± 0.20
Bone	4.05 ± 0.86	4.48 ± 0.59	4.64 ± 1.70	1.29 ± 0.45	4.27 ± 0.74
Brain	0.18 ± 0.01	0.12 ± 0.01	0.15 ± 0.02	0.10 ± 0.05	0.06 ± 0.00
Thyroid	12.7 ± 2.72	8.33 ± 0.41	11.1 ± 1.62	2.48 ± 0.44	3.62 ± 1.01
Salivary glands	5.98 ± 4.00	4.76 ± 1.79	6.41 ± 1.19	-	1.36 ± 0.92
Lacrimal glands	0.13 ± 0.27	0.44 ± 0.68	0.06 ± 0.13	-	0.06 ± 0.07
Tumor/bone	1.10 ± 0.15	1.17 ± 0.26	0.97 ± 0.30	20.1 ± 9.48	0.51 ± 0.28
Tumor/muscle	2.35 ± 0.35	3.25 ± 0.39	2.52 ± 0.33	31.6 ± 12.1	2.30 ± 0.79
Tumor/blood	0.48 ± 0.11	0.89 ± 0.03	0.60 ± 0.13	17.3 ± 7.24	1.04 ± 0.42
Tumor/kidney	0.14 ± 0.03	0.11 ± 0.00	0.10 ± 0.02	0.14 ± 0.04	0.90 ± 0.28

*The biodistribution of [^{68}Ga]Ga-HTK03041 has been reported previously[122]

Table 2.5 Biodistribution (mean ± SD, n = 4) and uptake ratios of ^{68}Ga-labeled PSMA/FAP-dual targeting tracers, HTK03041, and FAPI-04 in HEK293T:hFAP tumor-bearing mice.

Tissue (%ID/g)	[^{68}Ga]Ga-AV01017	[^{68}Ga]Ga-AV01030	[^{68}Ga]Ga-AV01038	[^{68}Ga]Ga-HTK03041	[^{68}Ga]Ga-FAPI-04
	1 h	1 h	1 h	1 h	1 h
Blood	11.9 ± 3.37	5.68 ± 0.72	7.45 ± 1.70	0.71 ± 0.07	1.07 ± 0.08
Fat	0.61 ± 0.13	0.63 ± 0.20	0.53 ± 0.10	0.55 ± 0.12	0.10 ± 0.01
Seminal vesicle	1.15 ± 0.33	0.64 ± 0.15	1.15 ± 0.69	0.32 ± 0.03	0.15 ± 0.04
Testes	1.15 ± 0.86	0.66 ± 0.08	0.74 ± 0.09	0.60 ± 0.41	0.28 ± 0.04
Small Intestine	2.14 ± 0.65	1.23 ± 0.16	1.70 ± 0.19	0.71 ± 0.01	0.36 ± 0.08
Large Intestine	1.44 ± 0.20	1.15 ± 0.10	0.99 ± 0.17	0.43 ± 0.04	-
Stomach	0.63 ± 0.08	0.42 ± 0.04	0.60 ± 0.18	0.22 ± 0.04	0.07 ± 0.01
Spleen	3.63 ± 3.60	7.41 ± 1.75	5.47 ± 1.03	8.09 ± 2.37	0.56 ± 0.11
Liver	3.40 ± 0.64	1.51 ± 0.33	2.16 ± 0.33	0.72 ± 0.06	0.36 ± 0.02
Pancreas	3.80 ± 0.25	3.26 ± 0.82	3.82 ± 1.29	0.71 ± 0.07	0.37 ± 0.05
Adrenal glands	4.06 ± 0.27	3.15 ± 0.39	6.14 ± 3.79	4.18 ± 0.48	1.07 ± 0.32
Kidneys	19.3 ± 2.25	30.0 ± 8.71	25.0 ± 1.76	68.4 ± 19.2	1.83 ± 0.16
Lungs	5.50 ± 1.26	3.02 ± 0.25	3.83 ± 0.55	2.43 ± 0.08	0.74 ± 0.11
Heart	4.63 ± 0.42	2.20 ± 0.46	2.69 ± 0.22	0.98 ± 0.07	0.34 ± 0.04
HEK293T:hFAP tumor	2.99 ± 0.37	3.69 ± 0.81	3.64 ± 0.83	0.62 ± 0.19	12.5 ± 2.00
Muscle	1.63 ± 0.06	1.78 ± 0.58	1.23 ± 0.11	0.47 ± 0.03	0.67 ± 0.05
Bone	5.26 ± 0.32	3.59 ± 0.44	3.03 ± 1.12	0.42 ± 0.11	3.36 ± 1.09
Brain	0.21 ± 0.07	0.12 ± 0.02	0.13 ± 0.02	0.03 ± 0.00	0.04 ± 0.00
Thyroid	10.7 ± 2.15	7.70 ± 1.08	6.51 ± 1.07	1.38 ± 0.10	-
Salivary glands	6.43 ± 1.03	7.01 ± 2.25	4.02 ± 0.69	2.29 ± 0.16	-
Lacrimal gland	1.34 ± 0.50	0.20 ± 0.24	0.22 ± 0.16	0.25 ± 0.33	-
Tumor/bone	0.44 ± 0.12	1.04 ± 0.31	1.17 ± 0.40	1.39 ± 0.58	3.93 ± 1.16
Tumor/muscle	1.25 ± 0.17	2.12 ± 0.30	2.21 ± 0.17	1.22 ± 0.73	18.8 ± 4.09
Tumor/blood	0.18 ± 0.08	0.65 ± 0.15	0.49 ± 0.37	0.83 ± 0.54	11.7 ± 2.04
Tumor/kidney	0.11 ± 0.03	0.64 ± 0.65	0.11 ± 0.02	0.01 ± 0.01	6.85 ± 1.33

2.4 Discussions

Both PSMA and FAP are promising biomarkers of prostate cancer and many radioligands have been developed to target these two membrane proteins for imaging and therapy. However, the detection sensitivities of these radiotracers are strongly dependent on the expression levels and heterogeneities of these two biomarkers in different disease stages and between individuals[47,82]. Despite many effective PSMA-targeting radiotherapeutic agents being developed, patients with low to no PSMA expression are not eligible for these emerging PSMA-targeted radioligand therapies and still have very limited treatment options. Since FAP and PSMA are both expressed in prostate cancer and other cancers such as pancreatic cancer[101,131–134], the use of PSMA/FAP bispecific radioligands is expected to increase lesion detection sensitivity and treatment efficacy. Our ultimate goal of this reported research is to develop ^{68}Ga-labeled PSMA/FAP bispecific tracers with comparable or higher tumor uptake when compared to the monospecific tracers, [^{68}Ga]Ga-FAPI-04 and [^{68}Ga]Ga-HTK03041, a PSMA-targeting tracer previously reported by our group[122].

To date there have been only two reports on the development of PSMA/FAP bispecific tracers for imaging (Figure 2.1)[120,121]. Both of them used the NOTA chelator for radioisotope complexation: one for ^{64}Cu and the other for Al^{18}F. To the best of our knowledge, there has been no report on the development of ^{68}Ga-labeled PSMA/FAP bispecific tracers despite the growing popularity and increased accessibility of clinical ^{68}Ga generators. Although NOTA can be used for labeling ^{68}Ga as well, it cannot be used for labeling the common and effective radiotherapeutic nuclides such as ^{90}Y, and ^{177}Lu. Therefore, for this reported research, we chose DOTA as the chelator for ^{68}Ga labeling as DOTA is a universal chelator and is effective for labeling with many diagnostic (such as ^{68}Ga, ^{152}Tb and ^{111}In) and radiotherapeutic radionuclides (such as ^{149}Tb, ^{90}Y, and ^{177}Lu).

We selected the pharmacophores of [^{68}Ga]Ga-FAPI-04 (in blue, Figure 2.2) and [^{68}Ga]Ga-HTK03041 (in brown, Figure 2.2) for the design of our PSMA/FAP bispecific tracers as they have high affinity for FAP and PSMA, respectively[122,135]. These two pharmacophores are separated by an azidoacetic-Lys-Gly linker (Figure 2.2) to minimize the interaction of both pharmacophores as such interaction might interfere the bindings of both pharmacophores to their respective targets. The PSMA-targeting pharmacophore (Lys(tranexamic acid-Ala(9-Anth))-urea-Glu and the linker (azidoacetic acid-Lys-Gly) was constructed directly on solid phase using the commercially available amino acids. While the DOTA chelator was coupled to the amino group on the Lys side chain, the alkyne-containing FAP-targeting motif was coupled to the azido group via the formation of a triazole ring by click chemistry. For AV01030, the triazole ring is directly linked to the quinoline ring of the FAP-targeting pharmacophore. For AV01038 and AV01017, there are additional -O-CH_2- and -O-$(CH_2)_3$-, respectively, to separate the triazole ring and the quinoline ring of the FAP-targeting pharmacophore. This allowed us to investigate the effect of the additional linker and its length on the binding affinity and pharmacokinetics of the resulting bispecific tracers.

The enzymatic assay (Figure 2.3B) confirmed that FAP binding affinities of our bispecific ligands (IC_{50} = 1.25 – 2.74 nM) were comparable to that of Ga-FAPI-04 (IC_{50} = 1.03 nM). To investigate if the PSMA-targeting pharmacophore has any effect on the overall FAP binding of our bispecific ligands, we also measured the FAP binding affinity of Ga-HTK03041. The very weak binding affinity of Ga-HTK03041 (IC_{50} = 2,010±585 nM) suggests that the potent FAP binding affinity of our bispecific ligands is contributed mainly from the FAPI-04 pharmacophore.

Unlike the comparable FAP binding affinity of bispecific ligands and the monospecific Ga-FAPI-4, the PSMA binding affinities of bispecific ligands (IC_{50} = 25.2 – 71.6 nM) were much inferior to that of Ga-HTK03041 (IC_{50} = 0.76 nM). Although Ga-FAPI-04 has minimal binding

affinity to PSMA (IC_{50} > 1,000 nM), the addition of its pharmacophore and a linker clearly interferes the overall binding of the bispecific ligands to PSMA. Such interference seems to reduce with the increased linker length between the triazole ring and the FAP-targeting pharmacophore as the IC_{50}(PSMA) values for Ga-AV01030, Ga-AV01038 and Ga-AV01017 are 71.6, 29.4 and 25.2 nM, respectively.

PET imaging and biodistribution studies (Figures 2.4-2.6 and Tables 2.4-2.5) revealed that the bispecific tracers retained the characteristics of the monospecific tracers as high uptake was observed in common off-targets of PSMA-targeting (kidneys and salivary glands) and FAP-targeting tracers (joints and salivary glands). However, the bispecific tracers showed much lower uptake values in LNCaP and HEK293T:hFAP tumor xenografts when compared to those of the monospecific tracers, [^{68}Ga]Ga-HTK03041 and [^{68}Ga]Ga-FAPI-04, respectively. Unlike the fast blood clearance of the monospecific tracers, the bispecific tracers had a much longer retention in blood. Besides, it seems that the blood retention was positively correlated to the length of linker between the triazole ring and the FAP-targeting pharmacophore as the blood uptake values for Ga-AV01030, Ga-AV01038 and Ga-AV01017 are 5.68-5.75, 7.07-7.45 and 9.24-11.9 %ID/g, respectively. A longer blood retention would prevent fast binding of the bispecific tracers to its targets: PSMA in the LNCaP tumor xenografts and FAP in the HEK293T:hFAP tumor xenografts. This is evident by the observations that with no additional linker between the triazole ring and the FAP-targeting pharmacophore, [^{68}Ga]Ga-AV01030 showed relatively higher tumor uptake and tumor-to-background (bone, muscle and blood) contrast ratios in both tested tumor models than those of [^{68}Ga]Ga-AV01017 and [^{68}Ga]Ga-AV01038.

It should be noted that evaluation by imaging and/or biodistribution studies in tumor-bearing mice as in this report is a common practice in the development of radiopharmaceuticals.

However, the obtained high tumor-to-background contrast either from imaging or biodistribution data might not be observed in the clinic especially for ^{68}Ga-labeled tracers. This is because compared with other positron emitters, ^{68}Ga has a higher average positron energy (^{68}Ga, 0.829 MeV; ^{18}F, 0.250 MeV; ^{64}Cu, 0.288 MeV; ^{89}Zr, 0.396 MeV), leading to poorer spatial resolution and difficulty in the visualization of small lesions (a few millimeters in size). In addition, the tumor xenografts used in the imaging and biodistribution studies are often derived from (genetically-modified) cancer cell lines overexpressing the targeted cancer markers, which might not be representative of cancer lesions encountered in the clinic.

Directly comparing the performance of our bispecific tracers with those reported previously is difficult as different tumor models were used for evaluation: PSMA-expressing LNCaP tumors and FAP-expressing HEK293T:hFAP tumors used in this report; PSMA-expressing PC3-PIP tumors and FAP-expressing U87 tumors used by Boinapally et al.[120]; PSMA-expressing 22Rv1 tumors and FAP-expressing A549-FAP tumors used by Hu et al.[121]. However, comparing the pharmacokinetics of our tracers and those reported previously shows that our tracers had significantly high blood retention at 1 h post-injection. The longer blood retention of our tracers could be due to the increased lipophilicity[136], which could be resulted from (1) the replacement of 2-Nal with a more lipophilic Ala(9-Anth) in the PSMA-targeting pharmacophore; (2) the deletion of the hydrophilic piperazine linker in the FAP-targeting pharmacophore of FAPI-04; and/or (3) the use of click reaction for coupling the FAP-targeting pharmacophore as this forms a relatively lipophilic triazole ring instead of a hydrophilic amide bond.

Further modifications are needed to improve the binding affinities, pharmacokinetics and tumor uptake of ^{68}Ga-labeled PSMA/FAP bispecific tracers by considering the linker's length, lipophilicity and the use of less lipophilic PSMA- and/or FAP-targeting pharmacophores. This can

be accomplished by the use of less lipophilic linkers such as PEG linkers and well as piperazine-based linkers which have been shown to be important for maintaining good tumor uptake of FAP-targeting tracers[137]. Similarly, the use of potent and less lipophilic pharmacophores should also be investigated such as (1) replacing Ala(9-Anth) in the PSMA-targeting pharmacophore with 2-Nal, (2) replacing the quinoline motif in the FAP-targeting pharmacophore with a more hydrophilic pyridine motif, and/or (3) replacing the 2-pyrrolidinecarbonitrile motif in the FAP-targeting pharmacophore with a more hydrophilic pyrrolidin-2-ylboronic acid.

2.5 Conclusions

Three novel ^{68}Ga-labeled PSMA/FAP bispecific tracers were designed, synthesized, and confirmed to have the ability to bind both PSMA and FAP in vitro and in vivo. Compared with the monospecific tracers, the bispecific tracers have decreased binding affinities towards PSMA, but retain comparable binding affinities towards FAP. The bispecific tracers have lower tumor uptake values compared to the monospecific tracers, in which the tracer with a longer linker tends to have a lower tumor uptake. This might be caused by the longer blood retention of the bispecific tracers. Further modifications will be explored to improve the binding affinity, pharmacokinetics and tumor uptake to generate promising PSMA/FAP bispecific radioligands for imaging and radioligand therapy of mCRPC.

Chapter 3 : Novel ^{68}Ga-labeled Pyridine-based Fibroblast Activation Protein-targeted Tracers with High Tumor-to-background Contrast: Comparison with [^{68}Ga]Ga-FAPI-04

The following chapter is an adaption of the following published paper: Verena, A.; Kuo, H.-T.; Merkens, H.; Zeisler, J.; Bendre, S.; Wong, A.A.W.L.; Bénard, F.; Lin, K.-S. Novel ^{68}Ga-Labeled Pyridine-Based Fibroblast Activation Protein-Targeted Tracers with High Tumor-to-Background Contrast. Pharmaceuticals **2023**, 16, 449. https://doi.org/10.3390/ph16030449

3.1 Introduction

Despite promising utilities, there are some pitfalls in FAP-targeted tracers, as non-tumor related uptake of [^{68}Ga]Ga-FAPI-04 and [^{68}Ga]Ga-FAPI-46 by degenerative lesions associated with joints and vertebral bones, muscles, scars, head-and-neck, and mammary glands has been reported[138]. Therefore, there might be unspecific and off-target uptake of quinoline-based tracers, which can increase background uptake level and lower the image contrast, thus interfering the identification of FAP-positive tumor lesions and even leading to false diagnosis[139]. To improve the tumor-to-background image contrast, we need to develop tracers that can be rapidly excreted from the body, but specifically bind to and be retained in FAP-expressing tumors. Currently, the development of FAP-targeted radioligands focuses on the use of quinoline-based pharmacophores such as the one in ^{68}Ga-FAPI-04 and ^{68}Ga-FAPI-46 (Figure 3.1). Compared with quinoline, pyridine is smaller, more hydrophilic, and could have a faster pharmacokinetics in vivo. Hence, we hypothesized that the pyridine-based FAP-targeted tracers might have faster background clearance and better imaging contrast than the current clinically used quinoline-based FAP-targeted tracers.

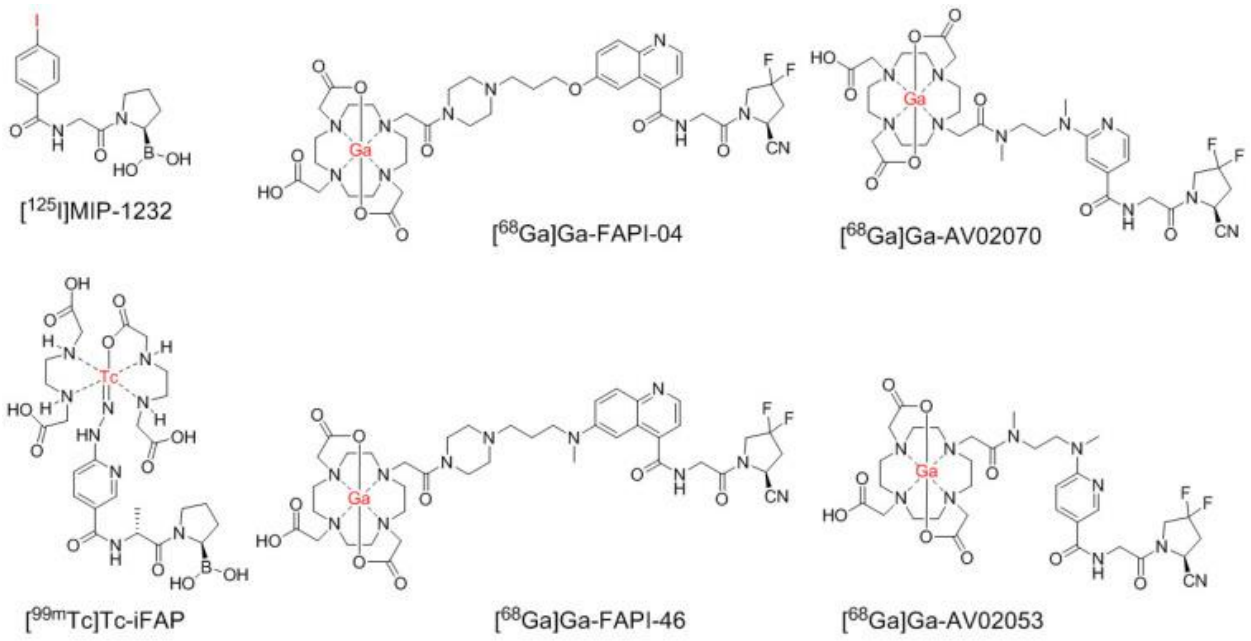

Figure 3.1 Chemical Structures of 68Ga-labeled AV02053 and AV02070, and previously reported [125I]MIP-1232, [99mTc]Tc-iFAP and 68Ga-labeled FAPI-04 and FAPI-46

Previously, Trujillo-Benítez and co-workers developed a ^{99m}Tc-labeled boroPro-based tracer, [^{99m}Tc]Tc-HYNIC-D-alanine-boroPro ([^{99m}Tc]Tc-iFAP) (Figure 3.1) which has minimal background (blood, muscle and bone) uptake and good uptake (5.18±0.82 %ID/g) in Hep-G2 tumor xenografts at 2 h post-injection[140]. This demonstrates that a pyridine-based FAP-targeted tracer has the potential to achieve good tumor uptake, low background, and improved tumor-to-background contrast.

In Chapter 2, we described the work on developing three novel bispecific PSMA/FAP-targeting radiotracers, and we observed high blood uptake that results in lower tumor uptake than the respective monospecific radiotracers. To solve this issue, one of the solutions we proposed was to select a more hydrophilic pharmacophores, such as changing the quinoline-based FAP-targeted ligand to a pyridine-based FAP-targeted ligand. However, there are very few pyridine-based FAP-targeted radioligands that have been developed. Therefore, in this chapter, we report the design, synthesis and evaluation of two pyridine-based FAP-targeted tracers, [^{68}Ga]Ga-AV02053 and

[^{68}Ga]Ga-AV02070 (Figure 3.1), based on the 4,4-difluoro-2-cyanopyrrolidine pharmacophore. Instead of boroPro in [^{99m}Tc]Tc-iFAP, we chose the 4,4-difluoro-2-cyanopyrrolidine pharmacophore as it is easier to synthesize. Instead of D-Ala in [^{99m}Tc]Tc-iFAP, we chose Gly as it led to derivatives with a higher binding affinity[113]. The tertiary amine linkage between the linker and pyridine in [^{68}Ga]Ga-AV02053 and [^{68}Ga]Ga-AV02070 was to mimic the hydrazine group in [^{99m}Tc]Tc-iFAP, in which the nitrogens in hydrazine were reported to interact with FAP and improve binding affinity. The difference between the chemical structures of [^{68}Ga]Ga-AV02053 and [^{68}Ga]Ga-AV02070 is the position of the carbonyl group to the pyridine nitrogen, which is at the meta position for [^{68}Ga]Ga-AV02053 and the para position for [^{68}Ga]Ga-AV02070 (Figure 3.1). The potential of [^{68}Ga]Ga-AV02053 and [^{68}Ga]Ga-AV02070 for cancer imaging was evaluated by in vitro enzymatic assay, PET imaging, and ex vivo biodistribution studies using a preclinical tumor model, HEK293T:hFAP[141]. The results were then compared with those previously obtained using [^{68}Ga]Ga-FAPI-04[141].

3.2 Materials and Methods

3.2.1 General Methods

(*S*)-1-(2-aminoacetyl)-4,4-difluoropyrrolidine-2-carbonitrile 4-methylbenzenesulfonate was synthesized following literature procedure[111]. All other chemicals and solvents were obtained from commercial sources and used without further purification. Purification and quality control of DOTA-conjugated ligands and their ^{nat}Ga/^{68}Ga-complexed analogs were performed on Agilent (Santa Clara, CA) HPLC systems equipped with a model 1200 quaternary pump, a model 1200 UV absorbance detector (220 nm), and a Bioscan (Washington, DC) NaI scintillation detector. The HPLC columns used were a semi-preparative column (Luna C18, 5 μm, 250 × 10 mm) and an analytical column (Luna C18, 5 μm, 250 × 4.6 mm) purchased from Phenomenex (Torrance, CA).

The collected HPLC eluates containing the desired small molecules were lyophilized using a Labconco (Kansas City, MO) FreeZone 4.5 Plus freeze-drier. MS analyses were conducted using the Waters (Milford, MA) Acquity QDa mass spectrometer with the equipped 2489 UV/Vis detector and e2695 Separations module. C18 Sep-Pak cartridges (1 cm^3, 50 mg) were purchased from Waters (Milford, MA). ^{68}Ga was eluted from an ITM Medical Isotopes GmbH (Munich, Germany) generator, and purified according to the previously published procedures using a DGA resin column from Eichrom Technologies LLC (Lisle, IL)[125]. The radioactivity of ^{68}Ga-labeled tracers was measured using a Capintec (Ramsey, NJ) CRC®-25R/W dose calibrator and the radioactivity of mouse tissues collected from biodistribution studies were counted using a Perkin Elmer (Waltham, MA) Wizard2 2480 automatic gamma counter.

3.2.2 DOTA-conjugated Ligands Syntheses

AV02053 and AV02070 was synthesized following the steps depicted in scheme 3.1 and scheme 3.2, respectively

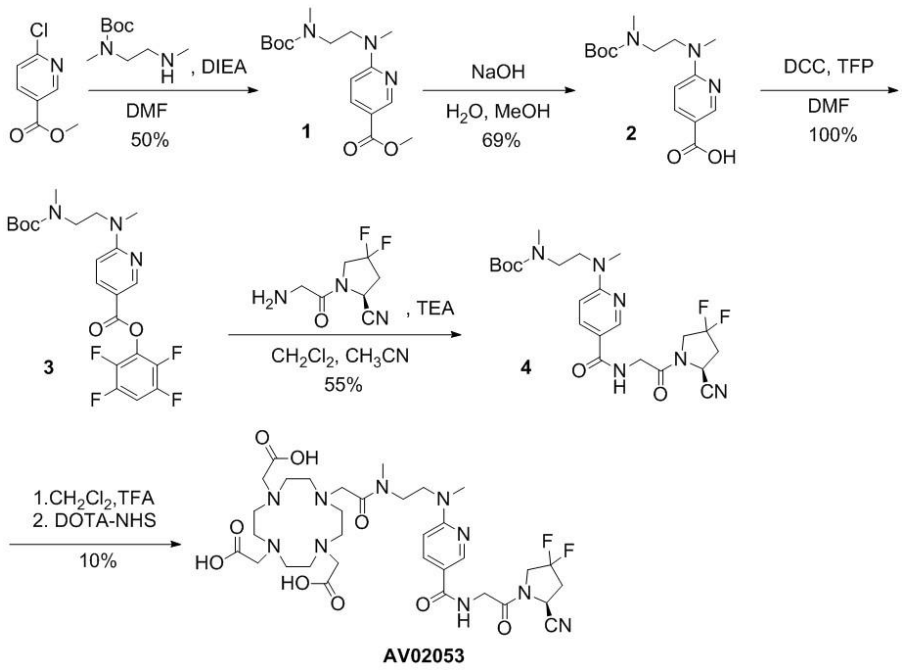

Scheme Error! No text of specified style in document.**1** Synthesis of AV02053.

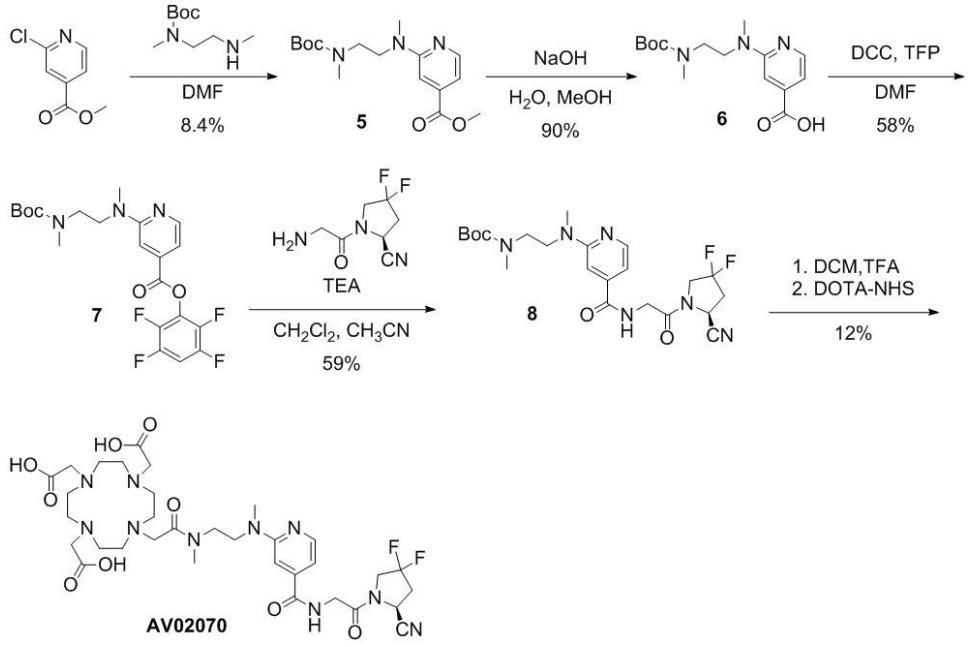

Scheme 3.2 Synthesis of AV02070.

3.2.2.1 Synthesis of methyl 6-[[2-[[(tert-butoxy)carbonyl]methylamino]ethyl]methylamino] pyridine-3- carboxylate (1)

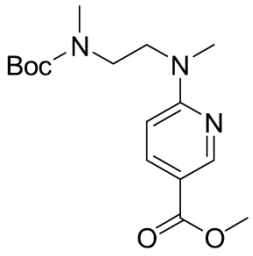

A solution of methyl 6-chloronicotinate (855 mg, 5.0 mmol), *N*-Boc-*N,N'*-dimethyl-1,2-diaminoethane (1.88 g, 10 mmol), and *N,N*-diisopropylethylamine (DIEA, 1.29 g, 10 mmol) in *N,N*-dimethylformamide (DMF, 50 mL) was stirred at 100 °C for 48 h. After evaporation, the residue was dissolved in diethyl ether (100 mL) and washed with water (100 mL). The organic phase was collected, dried over anhydrous $MgSO_4$, filtered, and evaporated under reduced pressure. The residue was purified with silica gel flash column chromatography eluted with 3:7 (v/v) ethyl acetate/hexanes. The product eluate fractions were combined, evaporated and dried under reduced pressure to yield **1** as a brown solid (803 mg, 50% yield). MS (ESI) calculated for $C_{16}H_{25}N_3O_4$ 323.2, found $[M+H]^+$ 324.2. ^{1}H NMR (300 MHz, $CDCl_3$) δ 8.78 (d, *J* = 2.3 Hz, 1H), 7.99 (d, *J* = 8.9 Hz, 1H), 6.46 (d, *J* = 9.0 Hz, 1H), 3.86 (s, 3H), 3.84 – 3.69 (m, 2H), 3.43 (t, *J* = 6.3 Hz, 2H), 3.11 (s, 3H), 2.86 (d, *J* = 17.7 Hz, 3H), 1.38 (s, 9H).

3.2.2.2 Synthesis of 6-[[2-[[(*tert*-butoxy)carbonyl]methylamino]ethyl]methylamino]pyridine -3-carboxylic acid (2)

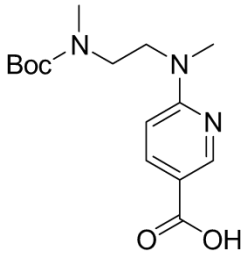

A solution of compound **1** (700 mg, 2.2 mmol) and sodium hydroxide (1.30 g, 32.3 mmol) in a mixture of water (15 mL) and methanol (20 mL) was stirred for 17 h. After evaporation, the residue was dissolved in water and the resulting solution was acidified with concentrated HCl to pH 3. The resulting white precipitate was filtered and dried under reduced pressure to yield **2** as a white powder (465 mg, 69% yield). MS (ESI) calculated for $C_{15}H_{23}N_3O_4$ 309.2, found $[M+H]^+$ 310.1. ^{1}H NMR (300 MHz, DMSO) δ 8.59 (d, *J* = 1.9 Hz, 1H), 7.89 (d, *J* = 8.8 Hz, 1H), 6.63 (t, *J* = 10.2 Hz, 1H), 3.72 (s, 2H), 3.04 (s, 2H), 2.75 (d, *J* = 13.2 Hz, 3H), 2.53 – 2.47 (m, 3H), 1.31 – 1.15 (m, 9H).

3.2.2.3 Synthesis of 2,3,5,6-tetrafluorophenyl 6-[[2-[[(*tert*-butoxy)carbonyl]methylamino] ethyl]methylamino]pyridine-3-carboxylate (3)

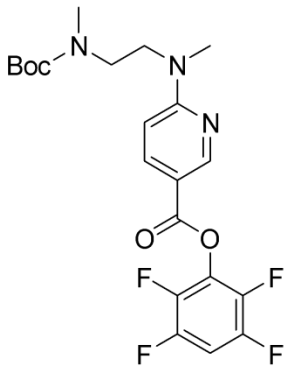

A solution of EDC·HCl (299 mg, 1.6 mmol) in DCM (12 mL) was added dropwise to a solution of compound 2 (440 mg, 1.4 mmol) and 2,3,5,6-tetrafluorophenol (307 mg, 1.9 mmol) in dichloromethane (DCM, 80 mL) cooled in an ice/water bath. The resulting mixture was stirred for 22 h. The solution was evaporated under reduced pressure and the residue was purified through silica gel flash column chromatography eluted with ethyl acetate. The product eluate fractions were combined, evaporated and dried under reduced pressure to yield **3** as a yellow oil (649 mg, 100% yield). MS (ESI) calculated for $C_{21}H_{23}F_4N_3O_4$ 457.2, found $[M+H]^+$ 458.2. ^{1}H NMR (300 MHz, $CDCl_3$) δ 8.92 (d, *J* = 5.2 Hz, 1H), 8.11 (t, *J* = 9.5 Hz, 1H), 7.01 (tt, *J* = 9.9, 7.0 Hz, 1H), 6.60 (s, 1H), 3.83 (dt, *J* = 15.4, 6.5 Hz, 2H), 3.50 (d, *J* = 6.6 Hz, 2H), 3.17 (s, 3H), 2.90 (d, *J* = 9.0 Hz, 3H), 1.40 (s, 9H).

3.2.2.4 Synthesis of (S)-N-(2-(2-cyano-4,4-difluoropyrrolidin-1-yl)-2-oxoethyl)-6-[[2-[[(*tert*-butoxy)-carbonyl]methylamino]ethyl]methylamino]pyridine-3-carboxamide (4)

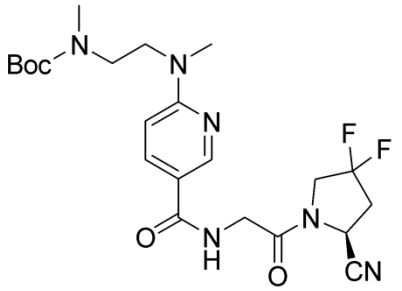

A solution of compound **3** (600 mg, 1.3 mmol), (*S*)-1-(2-aminoacetyl)-4,4-difluoropyrrolidine-2-carbonitrile 4-methylbenzenesulfonate (473 mg, 1.3 mmol) and triethylamine (TEA, 2.6 mmol, 265 mg) in acetonitrile (CH_3CN, 12 mL) was stirred at 50 °C for 22 h. The solution was then evaporated under reduced pressure and the residue was purified using silica gel flash column chromatography eluted with 1:9 (v/v) methanol/ethyl acetate. The product eluate fractions were collected, combined, evaporated and dried under reduced pressure to yield **4**

as a light brown solid (365 mg, 55% yield). MS (ESI) calculated for $C_{22}H_{30}F_2N_6O_4$ 480.2, found $[M+H]^+$ 481.2. ^1H NMR (300 MHz, $CDCl_3$) δ 8.62 (d, *J* = 2.5 Hz, 1H), 7.86 (d, *J* = 8.7 Hz, 1H), 7,28(s, 1H), 6.43 (d, *J* = 9.0 Hz, 1H), 4.97 (t, *J* = 6.6 Hz, 1H), 4.38 (dd, *J* = 17.6, 5.5 Hz, 1H), 4.10 – 3.87 (m, 4H), 3.74 (m, 2H), 3.42 (t, *J* = 6.4 Hz, 2H), 3.11 (d, *J* = 8.6 Hz, 3H), 2.82 – 2.70 (m, 3H), 1.38 (s, 9H).

3.2.2.5 Synthesis of AV02053

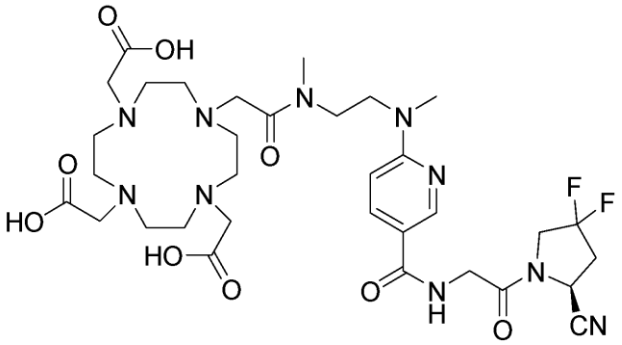

Trifluoroacetic acid (TFA, 1 mL) was added to a solution of compound **4** (21 mg, 44 µmol) in DCM (1 mL), and the resulting solution was stirred at room temperature for 2 h. The solution was then evaporated and the residue was dissolved in water (2 mL). DOTA-NHS-ester (40 mg, 53 µmol) was added, the pH of the resulting solution was adjusted to 8-9 with DIEA, and then the solution was stirred for 40 h. The crude solution was purified using HPLC and the eluted product fraction was collected and lyophilized to obtain AV02053 as a white powder (3.4 mg, 10% yield). MS (ESI) calculated for $C_{33}H_{48}F_2N_{10}O_9$ 766.4, found $[M+H]^+$ 767.2. The HPLC conditions and retention time for the purification of AV02053 are provided in Table 3.1.

3.2.2.6 Synthesis of methyl 2-[[2-[[(*tert*-butoxy)carbonyl]methylamino]ethyl]methylamino] pyridine-4-carboxylate (5)

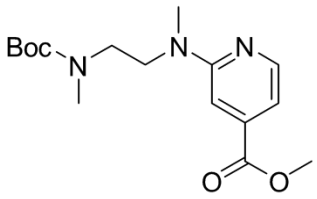

A solution of methyl 2-chloroisonicotinate (1.71 g, 10 mmol), *N*-Boc-*N,N'*-dimethyl-1,2-diaminoethane (3.25 g, 17 mmol), and DIEA (3.5 mL, 20 mmol) in DMF (60 mL) was stirred at 110 °C for 24 h. After evaporation, the residue was dissolved in diethyl ether (100 mL) and washed with water (100 mL). The organic phase was collected, dried over anhydrous $MgSO_4$, filtered, and evaporated under reduced pressure. The crude product was purified with silica gel flash column chromatography eluted with 1:3 (v/v) ethyl acetate/hexanes (1.6 L) followed by ethyl acetate (0.8 L). The product eluate fractions were combined, evaporated and dried under reduced pressure to yield **5** as a white solid (270 mg, 8.4% yield). MS (ESI) calculated for $C_{16}H_{25}N_3O_4$ 323.2, found $[M+H]^+$ 324.2. ^1H NMR (300 MHz, $CDCl_3$) δ 8.23 (d, *J* = 5.4 Hz, 1H), 7.04 (d, *J* = 5.4 Hz, 2H), 3.91 (s, 3H), 3.74 (dd, *J* = 15.0, 8.3 Hz, 2H), 3.42 (t, *J* = 6.3 Hz, 2H), 3.09 (s, 3H), 2.91 – 2.80 (m, 3H), 1.37 (d, *J* = 4.6 Hz, 9H).

3.2.2.7 Synthesis of 2-[[2-[[(*tert*-butoxy)carbonyl]methylamino]ethyl]methylamino]pyridine-4-carboxylic acid (6)

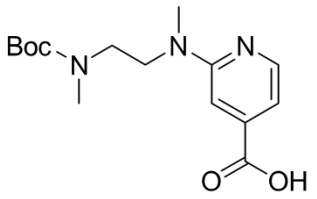

A solution of compound **5** (255 mg, 0.79 mmol) and sodium hydroxide (475 mg, 12 mmol) in a mixture of water (25 mL) and methanol (30 mL) was stirred for 20 h. After evaporation, the residue was dissolved in water and the resulting solution was acidified with concentrated HCl to pH 3. The resulting precipitates were collected by filtration and dried under reduced pressure to yield **6** as a light brown powder (220 mg, 90% yield). MS (ESI) calculated for $C_{15}H_{23}N_3O_4$ 309.2, found $[M+H]^+$ 310.1. ^{1}H NMR (300 MHz, $CDCl_3$) δ 8.20 (d, *J* = 5.01 Hz, 1H), 7.9 (d, *J* = 6.79 Hz, 2H), 3.39 (m, 2H), 3.04(s, 3H), 2.80 (d, J = 14.23 Hz, 2H), 2.11 (s, 3H), 1.31 (m, 9H).

3.2.2.8 Synthesis of 2,3,5,6-tetrafluorophenyl 2-[[2-[[(tert-butoxy)carbonyl]methylamino] ethyl]methylamino]pyridine-4-carboxylate (7)

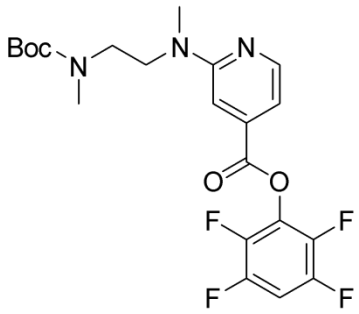

A solution of EDC·HCl (136 mg, 0.71 mmol) in DCM (10 mL) was added dropwise to a solution of compound **6** (200 mg, 0.65 mmol) and 2,3,5,6-tetrafluorophenol (139 mg, 0.84 mmol) in a mixture of DCM (30 mL) and DMF (10 mL) cooled in an ice/water bath. The resulting solution was stirred for 24 h and then evaporated. The residue was purified through silica gel flash column chromatography eluted with 1:2 (v/v) ethyl acetate/hexanes. The product eluate fractions were combined, evaporated and dried under reduced pressure to yield **7** as a yellow solid (170 mg, 58% yield). MS (ESI) calculated for $C_{21}H_{23}F_4N_3O_4$ 457.2, found $[M+H]^+$ 458.1.^{1}H NMR (300 MHz, $CDCl_3$) δ 8.32 (d, *J* = 5.2 Hz, 1H), 7.21 (d, *J* = 5.9 Hz, 2H), 7.06 (tt, *J* = 9.8, 7.0 Hz, 1H), 3.87 – 3.75 (m, 2H), 3.47 (t, *J* = 6.2 Hz, 2H), 3.14 (s, 3H), 2.91 – 2.89 (m, 3H), 1.37 (s, 9H).

3.2.2.9 Synthesis of (S)-N-(2-(2-cyano-4,4-difluoropyrrolidin-1-yl)-2-oxoethyl)-2-[[2-[[(*tert*-butoxy)-carbonyl]methylamino]ethyl]methylamino]pyridine-4-carboxamide (8)

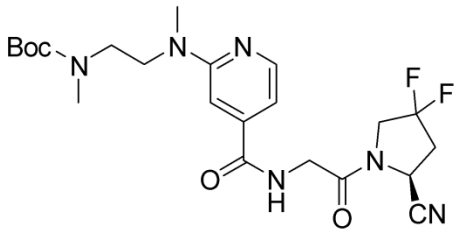

A solution of compound **7** (200 mg, 0.44 mmol), (*S*)-1-(2-aminoacetyl)-4,4-difluoropyrrolidine-2-carbonitrile 4-methylbenzenesulfonate (158 mg, 0.44 µmol) and TEA (88 mg, 0.88 mmol) in CH_3CN (5 mL) was stirred at 50 °C for 22 h. The solution was then evaporated under reduced pressure and the residue was purified using silica gel flash column chromatography eluted with 1:9 (v/v) methanol/ethyl acetate. The product eluate fractions were collected, combined, evaporated and dried under reduced pressure to yield **8** as a yellow solid (124 mg, 59% yield). MS (ESI) calculated for $C_{22}H_{30}F_2N_6O_4$ 480.2, found $[M+H]^+$ 481.2. ^{1}H NMR (300 MHz, $CDCl_3$) δ 8.12 (d, *J* = 5.0 Hz, 1H),), 7.23 (d, *J* = 20.8 Hz, 2H), 6.75 (d, *J* = 20.3 Hz, 1H), 4.91 (t, *J* = 6.6 Hz, 1H), 4.32 (d, *J* = 17.9 Hz, 1H), 3.97 (dd, *J* = 25.6, 13.1 Hz, 3H), 3.64 (t, *J* = 5.9 Hz, 2H), 3.42 – 3.28 (m, 2H), 2.99 (t, *J* = 19.4 Hz, 3H), 2.83 – 2.57 (m, 3H), 1.44 – 1.27 (m, 9H).

3.2.2.10 Synthesis of AV02070

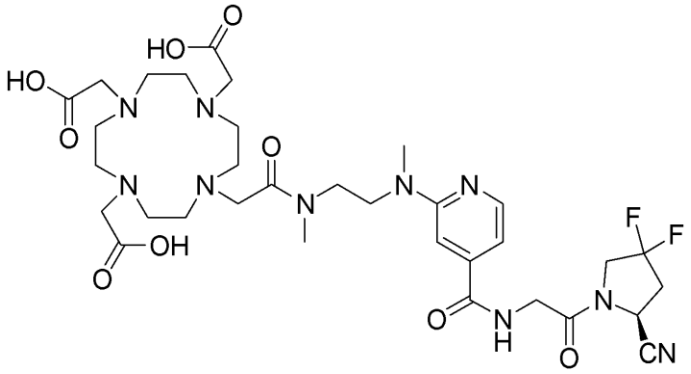

A solution of compound **8** (25 mg, 52 µmol) in DCM (1 mL) was added TFA and stirred at room temperature for 2 h. DOTA-NHS-ester (48 mg, 62 µmol) was added into the solution, the pH of the resulting solution was adjusted to 8-9 with DIEA, and then the solution was stirred for 40 h. The crude solution was purified using HPLC and the eluted product fraction was collected and lyophilized to obtain AV02070 as a white powder (4.6 mg, 12% yield). MS (ESI) calculated for $C_{33}H_{48}F_2N_{10}O_9$ 766.4, found $[M+H]^+$ 767.2. The HPLC conditions and retention time for the purification of AV02070 are provided in Table 3.1.

3.2.3 Synthesis of Nonradioactive Ga-complexed Standards

The nonradioactive Ga-complexed standards were prepared by reacting the DOTA-conjugated precursors with $GaCl_3$ (5 eq.) in NaOAc buffer (0.1 M, 500 µL, pH 4.2 – 4.5) at 80 °C for 15 min. The reaction mixture was then purified via HPLC (semi-preparative column, flow rate: 4.5 mL/min). The HPLC eluates containing the desired products were collected and lyophilized. The HPLC conditions, retention times, isolated yields and MS confirmations of these nonradioactive Ga-complexed standards are provided in Table 3.2.

3.2.4 Synthesis of ^{68}Ga-labeled Compounds

The radiolabeling experiments were performed according to previously published procedures[126,127]. Purified $^{68}GaCl_3$ in 0.5 mL water was added to a 4-mL glass vial preloaded with 0.7 mL of HEPES buffer (2 M, pH 5.0) and 10 µL precursor solution (1 mM). The radiolabeling reaction was carried out under microwave heating for 1 min, followed by purification using the semi-preparative HPLC column. The eluate fraction containing the radiolabeled product was collected, diluted with water (50 mL), and passed through a C18 Sep-Pak cartridge that was pre-washed with ethanol (10 mL) and water (10 mL). The C18 Sep-Pak cartridge was washed with

water (10 mL), and the ^{68}Ga-labeled product was eluted off the cartridge with ethanol (0.4 mL). The eluted product was diluted with PBS for imaging and biodistribution studies. Quality control was performed using the analytical column. The HPLC conditions and retention times are provided in Table 3.3. The tracers were obtained in 33-64% decay-corrected radiochemical yields with ≥44 GBq/μmol molar activity and >95% radiochemical purity.

Table 3.1 HPLC purification conditions and MS characterizations of DOTA-conjugated precursors.

Compound name	HPLC conditions	Retention time (min)	Yield (%)	Calculated mass (m/z)	Found (m/z)
AV02053	15% CH_3CN and 0.1% TFA in H_2O	8.7	10	$[M+H]^+$ 767.4	$[M+H]^+$ 767.2
AV02070	14% CH_3CN and 0.1% TFA in H_2O	8.4	12	$[M+H]^+$ 767.4	$[M+H]^+$ 767.2

Table 3.2 HPLC purification conditions and MS characterizations of nonradioactive Ga-complexed standards.

Compound name	HPLC conditions	Retention time (min)	Yield (%)	Calculated mass (m/z)	Found (m/z)
Ga-AV02053	15% CH_3CN and 0.1% TFA in H_2O	7.2	42	$[M+2H]^{2+}$ 417.1	$[M+2H]^{2+}$ 417.3
Ga-AV02070	14% CH_3CN and 0.1% TFA in H_2O	6.8	22	$[M+2H]^{2+}$ 417.1	$[M+2H]^{2+}$ 417.4

Table 3.3 HPLC conditions for the purification and quality control of ^{68}Ga-labeled tracers.

Compound name	HPLC conditions		Retention time (min)
[^{68}Ga]Ga-AV02053	Semi-Prep	14% CH_3CN and 0.1% TFA in H_2O; flow rate 4.5 mL/min	13.4
	QC	15% CH_3CN and 0.1% TFA in H_2O; flow rate 2.0 mL/min	7.9
[^{68}Ga]Ga-AV02070	Semi-Prep	13% CH_3CN and 0.1% TFA in H_2O; flow rate 4.5 mL/min	15.5
	QC	16% CH_3CN and 0.1% TFA in H_2O; flow rate 2.0 mL/min	8.2

3.2.5 Cell Culture

The HEK293T:hFAP cells generated in our lab[141] were cultured in DMEM GlutaMAX™ medium supplemented with 10% FBS, penicillin (100 U/mL) and streptomycin (100 µg/mL) at 37 °C in a Panasonic Healthcare (Tokyo, Japan) MCO-19AIC humidified incubator containing 5% CO_2. Cells were grown until 80-90% confluence and washed with sterile phosphate-buffered saline (PBS, pH 7.4) and collected after 1 min trypsinization. The cell concentration was counted in triplicate using a hemocytometer and a manual laboratory counter.

3.2.6 In Vitro FAP Fluorescence Assay

The half maximal inhibitory concentration (IC_{50}) values of the tested compounds for FAP were measured by in vitro enzymatic assay. The recombinant human FAP (Bio-legend; 0.2 µg/mL, 50 µL) was added into costar 96-well plate. PBS and varied concentrations (0.2 pM to 2 µM) of tested nonradioactive Ga-complexed standards were added to each wells (in duplicate) containing the recombinant human FAP. After being incubated for 30 min at 37 °C, 50 µL of Suc-Gly-Pro-AMC (2 µM, Bachem) was added to each well. The fluorescent signals were acquired at 15, 30, 45, and 60 min using FlexStation 3 Multi-Mode Microplate Reader with excitation at 380 nm and

emission at 460 nm. The IC_{50} (FAP) values were calculated using "nonlinear fit model" built-in model in GraphPad Prism 7.02 software.

3.2.7 $LogD_{7.4}$ Measurement

The lipophilicity characteristics of the ^{68}Ga-labeled pyridine-based FAPIs were determined by calculating the logarithm of the distribution coefficient (logD) in n-octanol/phosphate-buffered saline (PBS) of pH 7.4. Purified ^{68}Ga-labeled tracer (50 µL) was added into a test tube containing 3 mL n-octanol and 3 mL PBS. The mixture was vortexed and followed by centrifugation for 5 min at 3000 rpm. 1 mL fractions of each layers were then collected separately and the radioactivity was counted using a Perkin Elmer (Waltham, MA) Wizard2 2480 automatic gamma counter. After adjusting the counts to background and calculating the ratio (D) of the activity of the organic to that of the aqueous phase, the logD values were then calculated.

3.2.8 Ex Vivo Biodistribution and PET/CT Imaging Studies

Imaging and biodistribution studies were performed using male NOD.Cg-Rag1tm1Mom Il2rgtm1Wjl/SzJ (NRG) mice following previously published procedures[129,130]. The experiments were conducted according to the guidelines established by the Canadian Council on Animal Care and approved by Animal Ethics Committee of the University of British Columbia. The mice were briefly sedated by inhalation of 2.5% isoflurane in oxygen, and HEK293T:hFAP cells (8.5×10^6 cells) were inoculated subcutaneously behind the left shoulder. When the tumor grew to 5-8 mm in diameter over 3-4 weeks, the mice were used for PET/CT imaging and biodistribution studies.

PET/CT imaging experiments were carried out using a Siemens (Knoxville, TN) Inveon micro PET/CT scanner. Each tumor-bearing mouse was injected with ~4-6 MBq of ^{68}Ga-labeled

tracer through a lateral caudal tail vein under 2.5% isoflurane in oxygen anesthesia, followed by recovery and roaming freely in its cage during the uptake period. At 50 min post-injection, a 10-min CT scan was conducted first for localization and attenuation correction after segmentation for reconstructing the PET images, followed by a 10-min static PET imaging acquisition.

For biodistribution studies, the mice were injected with the radiotracer (~2-4 MBq) as described above. For blocking study the mice were co-injected with 250 μg of FAPI-04. At 1 h post-injection, the mice were euthanized by CO_2 inhalation. Blood was withdrawn by cardiac puncture, and organs/tissues of interest were collected, weighed and counted using a Perkin Elmer (Waltham, MA) Wizard2 2480 automatic gamma counter.

3.2.9 Statistical Analysis

Data were analyzed with the GraphPad Prism, version 7.02 and Microsoft (Redmond, WA) Excel software. One way ANOVA and multiple t tests were performed for all organs in the biodistribution studies of [^{68}Ga]Ga-AV02053, [^{68}Ga]Ga-AV02070, and [^{68}Ga]Ga-FAPI-04 in HEK293T:hFAP tumor models. A statistically significant difference was considered present when the adjusted *P* value was less than 0.05 using the Holm–Sidak method.

3.3 Results

3.3.1 Synthesis of ^{68}Ga/^{nat}Ga-Labeled FOTA-Conjugated FAP-Targeted Agents Based on Pyridine-Based Pharmacophores

The syntheses of DOTA-conjugated AV02053 and AV02070 are depicted in Schemes 3.1 and Scheme 3.2, respectively. For the preparation of AV02053 (Scheme 3.1), methyl 6-chloronicotinate was coupled with *N*-Boc-*N*,*N'*-dimethyl-1,2-diaminoethane via nucleophilic

substitution to obtain **1** in 50% yield. Compound **2** was obtained in 69% yield by the hydrolysis of the methyl ester in compound **1** with NaOH in a mixture of water and methanol. Esterification of compound **2** with 2,3,5,6-tetrafluorophenol (TFP) led to compound **3** in 100% yield. Compound **4** was obtained in 55% yield by coupling the activated ester **3** with (*S*)-1-(2-aminoacetyl)-4,4-difluoropyrrolidine-2-carbonitrile[111]. *Tert*-butyloxycarbonyl (Boc) protecting group was removed using trifluoroacetic acid (TFA) and the deprotected compound **4** was coupled with the DOTA chelator. The crude product was purified using HPLC and the product eluate fraction was collected and lyophilized to obtain AV02053 in 10% yield (Table 3.1).

For the preparation of AV02070 (scheme 3.2), commercially available methyl 2-chloroisoncotinate was coupled with *N*-Boc-*N,N'*-dimethyl-1,2-diaminoethane via nucleophilic substitution to obtain **5** in 8.4% yield. The methyl ester group in **5** was hydrolyzed with NaOH in a mixture of water and methanol, leading to compound **6** in 90% yield. Compound **7** was obtained in 58% yield via esterification of compound **6** with TFP. The activated compound **7** was coupled with (*S*)-1-(2-aminoacetyl)-4,4-difluoropyrrolidine-2-carbonitrile to obtain compound **8** in 59% yield. Boc in compound **8** was removed using TFA, followed by coupling of the deprotected compound **8** with the DOTA chelator. The crude product was purified using HPLC and the product eluate fraction was collected and lyophilized to obtain AV02070 in 12% yield (Table 3.1).

Ga complexation of AV02053 and AV02070 was conducted in NaOAc buffer (0.1 M, pH 4.2-4.5) for nonradioactive standards and in HEPES buffer (2 M, pH 5.0) for ^{68}Ga labeling as previously reported (Table 3.2-3.3)[126,127]. Ga-AV02053 and Ga-AV02070 were obtained in 42 and 22% yields, respectively. ^{68}Ga-labeled AV02053 and AV02070 were obtained in 33-64% decay-corrected radiochemical yield with > 50 GBq/μmol molar activity and > 95% radiochemical purity.

3.3.2 Binding Affinity and Lipophilicity

The binding affinities of Ga-AV02053 and Ga-AV02070 to human FAP were measured by an enzyme inhibition assay using Suc-Gly-Pro-AMC as the FAP substrate. The human FAP enzymatic activity on the substrate was inhibited by Ga-AV02053 and Ga-AV02070 in a dose dependent-manner (Figure 3.2). The calculated IC_{50} values for Ga-AV02053 and Ga-AV02070 were 187±52.0 and 17.1±4.60 nM, respectively. For comparison, the previously reported IC_{50} value for Ga-FAPI-04 under the same assay conditions was 1.03±0.44 nM (Figure 3.2)[141].

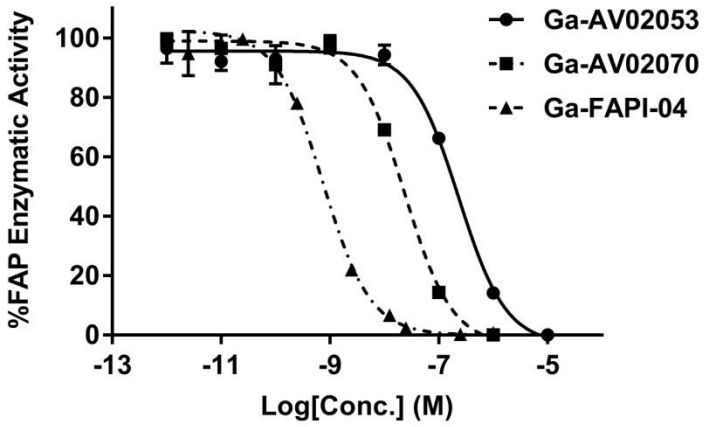

Figure 3.2 Inhibition of FAP enzymatic activity on Suc-Gly-Pro-AMC substrate by Ga-AV02053 and Ga-AV02070, and comparison with the data obtained previously using Ga-FAPI-04[141]. The enzymatic activity represents the fluorescence of AMC which was cleaved by human FAP enzyme. The half-maximal inhibitory concentration (IC_{50}) of the Ga-complex ligands was calculated, with Ga-FAPI-04 showing the lowest value, followed by Ga-AV02070 and Ga-AV02053, respectively. Error bars indicate standard deviation

The lipophilicity of ^{68}Ga-labeled AV02053, AV02070, and FAPI-04 were estimated by measuring their $LogD_{7.4}$ values using the shake flask method with n-octanol and phosphate-buffered saline (pH 7.4). The $LogD_{7.4}$ values of [^{68}Ga]Ga-AV02053, [^{68}Ga]Ga-AV02070, and [^{68}Ga]Ga-FAPI-04 were -3.75±0.16, -3.45±0.10, and -1.02±0.35, respectively. The values indicate

that these ^{68}Ga-labeled tracers are hydrophilic, and the pyridine-based FAP-targeted tracers, [^{68}Ga]Ga-AV02053 and [^{68}Ga]Ga-AV02070, are more hydrophilic than [^{68}Ga]Ga-FAPI-04.

3.3.2 PET Imaging, Ex Vivo Biodistribution, and Blocking Study

Imaging studies showed that the HEK293T:hFAP tumor xenografts were clearly visualized in PET images acquired at 1 h post-injection using both [^{68}Ga]Ga-AV02053 and [^{68}Ga]Ga-AV02070 (Figure 3.3). Both tracers were excreted primarily through the renal pathway and had very low background uptake in normal organs/tissues. Although [^{68}Ga]Ga-AV02053 and [^{68}Ga]Ga-AV02070 had lower tumor uptake than that of previously reported [^{68}Ga]Ga-FAPI-04, both of them had much lower background uptake, resulting in better tumor-to-background contrast than that of [^{68}Ga]Ga-FAPI-04 (Figure 3.3). Co-injection of [^{68}Ga]Ga-AV02053 and [^{68}Ga]Ga-AV02070 with FAPI-04 (250 µg) reduced the uptake of [^{68}Ga]Ga-AV02053 and [^{68}Ga]Ga-AV02070 in HEK293T:hFAP tumor xenografts to almost background level, confirming the uptake of both tracers is FAP mediated.

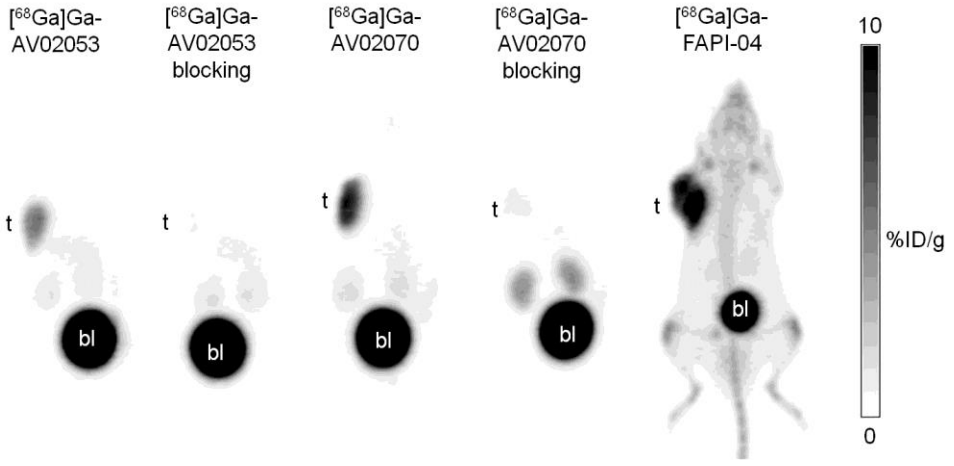

Figure 3.3 Representative maximum intensity projection PET images of [^{68}Ga]Ga-AV02053 and [^{68}Ga]Ga-AV02070 acquired at 1 h post-injection in mice bearing HEK293T:hFAP tumor xenografts. The image of [^{68}Ga]Ga-FAPI-04 has been reported previously[141] and is displayed here

for comparison. Despite having lower tumor uptake, [^{68}Ga]Ga-AV02053 and [^{68}Ga]Ga-AV02070 shown to have better contrast compared to [^{68}Ga]Ga-FAPI-04. The blocking with FAPI-04 decreased the tumor uptake to background level. t: tumor; bl: urinary bladder.

Biodistribution studies were conducted at 1 h post-injection with [^{68}Ga]Ga-AV02053 and [^{68}Ga]Ga-AV02070 in HEK293T:hFAP tumor-bearing mice, and the data are compared with those obtained previously using [^{68}Ga]Ga-FAPI-04 (Figures 3.4-3.5 and Table 3.4). The results are consistent with the observations from their PET images. Except tumor and kidneys (1.35 – 1.85 %ID/g), the average uptake values of [^{68}Ga]Ga-AV02053 and [^{68}Ga]Ga-AV02070 in all other collected organs/tissues were < 0.6 %ID/g. The tumor uptake values of [^{68}Ga]Ga-AV02053, [^{68}Ga]Ga-AV02070, and [^{68}Ga]Ga-FAPI-04 were 5.60±1.12, 7.93±1.88, and 12.5±2.00 %ID/g, respectively. Despite having a higher tumor uptake, [^{68}Ga]Ga-FAPI-04 also had significantly higher blood, muscle, and bone uptake (1.07±0.08, 0.67±0.05 and 3.36±1.09 %ID/g, respectively) compared to those of [^{68}Ga]Ga-AV02053 (0.22±0.04, 0.12±0.05 and 0.14±0.02 %ID/g, respectively) and [^{68}Ga]Ga-AV02070 (0.36±0.05, 0.19±0.10 and 0.23±0.06 %ID/g, respectively). This also led to higher tumor-to-blood, tumor-to-muscle and tumor-to-bone uptake ratios for [^{68}Ga]Ga-AV02053 (25.2±1.97, 51.2±19.8 and 38.1±5.03, respectively) and [^{68}Ga]Ga-AV02070 (22.9±10.1, 45.7±9.88 and 34.3±7.35, respectively) than [^{68}Ga]Ga-FAPI-04 (11.7±2.04, 18.8±4.09 and 3.93±1.16, respectively) ($P < 0.05$).

Co-injection of FAPI-04 reduced the average uptake of [^{68}Ga]Ga-AV02053 and [^{68}Ga]Ga-AV02070 in HEK293T:hFAP tumor xenografts by 95% (5.60 %ID/g down to 0.30 %ID/g at 1 h post-injection) and 97% (7.93 %ID/g down to 0.21 %ID/g at 1 h post-injection), respectively, confirming the specific uptake of both tracers in tumors. On the contrary, there was no significant difference on the average uptake values of [^{68}Ga]Ga-AV02053 and [^{68}Ga]Ga-AV02070 in other

major organs at 1 h post-injection with the co-injection of FAPI-04 (Figures 3.3-3.4 and Table 3.4).

Table 3.4 Biodistribution (mean ± SD, n = 4) and uptake ratios of ^{68}Ga-labeled FAP-targeted tracers in HEK293T:hFAP tumor-bearing mice. The mice in the blocked group were co-injected with FAPI-04 (250 µg).

Tissue (%ID/g)	[^{68}Ga]Ga-AV02053		[^{68}Ga]Ga-AV02070		[^{68}Ga]Ga-FAPI-04*
	1 h	1 h blocked	1 h	1 h blocked	1 h
Blood	0.22 ± 0.04	0.15 ± 0.08	0.36 ± 0.05	0.16 ± 0.14	1.07 ± 0.08
Testes	0.10 ± 0.03	0.14 ± 0.11	0.17 ± 0.07	0.06 ± 0.05	0.28 ± 0.04
Small intestine	0.28 ± 0.07	0.27 ± 0.16	0.42 ± 0.13	0.35 ± 0.21	0.36 ± 0.08
Large intestine	0.08 ± 0.02	0.08 ± 0.06	0.30 ± 0.38	0.04 ± 0.03	-
Stomach	0.05 ± 0.02	0.03 ± 0.02	0.08 ± 0.04	0.06 ± 0.06	0.07 ± 0.01
Spleen	0.17 ± 0.06	0.14 ± 0.13	0.25 ± 0.12	0.07 ± 0.06	0.56 ± 0.11
Liver	0.52 ± 0.12	0.43 ± 0.24	0.39 ± 0.05	0.25 ± 0.14	0.36 ± 0.02
Pancreas	0.13 ± 0.04	0.10 ± 0.09	0.34 ± 0.45	0.05 ± 0.04	0.37 ± 0.05
Kidney	1.35 ± 0.29	1.35 ± 0.75	1.85 ± 0.21	2.01 ± 2.20	1.83 ± 0.16
Lungs	0.23 ± 0.04	0.20 ± 0.10	0.34 ± 0.06	0.17 ± 0.11	0.74 ± 0.11
Heart	0.07 ± 0.01	0.06 ± 0.03	0.12 ± 0.03	0.06 ± 0.05	0.34 ± 0.04
Tumor	5.60 ± 1.12	0.30 ± 0.20	7.93 ± 1.88	0.21 ± 0.15	12.5 ± 2.00
Muscle	0.12 ± 0.05	0.11 ± 0.08	0.19 ± 0.10	0.08 ± 0.07	0.67 ± 0.05
Bone	0.14 ± 0.02	0.08 ± 0.06	0.23 ± 0.06	0.10 ± 0.09	3.36 ± 1.09
Brain	0.01 ± 0.00	0.01 ± 0.00	0.02 ± 0.02	0.01 ± 0.00	0.04 ± 0.00
Thyroid	0.12 ± 0.02	0.11 ± 0.12	0.22 ± 0.02	0.06 ± 0.04	-
Salivary glands	0.15 ± 0.07	0.12 ± 0.12	0.19 ± 0.06	0.11 ± 0.05	-
Tumor/bone	38.1 ± 5.03	4.18 ± 4.17	34.3 ± 7.35	2.15 ± 0.89	3.93 ± 1.16
Tumor/muscle	51.2 ± 19.8	2.97 ± 2.40	45.7 ± 9.88	2.59 ± 1.17	18.8 ± 4.09
Tumor/blood	25.2 ± 1.97	1.78 ± 0.73	22.9 ± 10.1	1.32 ± 0.41	11.7 ± 2.04
Tumor/kidney	4.19 ± 0.65	0.21 ± 0.09	4.34 ± 1.36	0.13 ± 0.04	6.85 ± 1.33

*****The biodistribution data of [^{68}Ga]Ga-FAPI-04 have been reported previously[141]

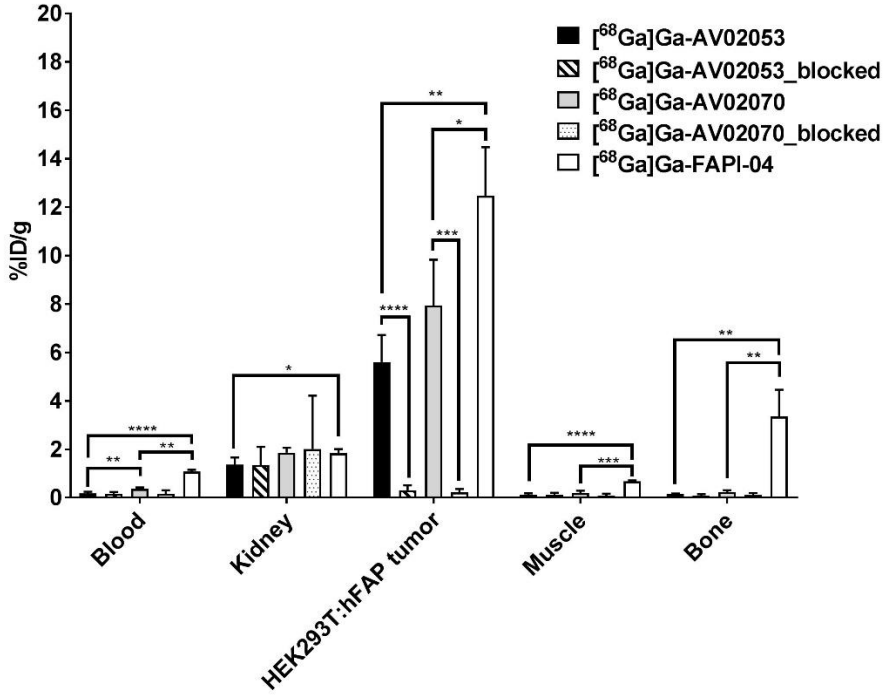

Figure 3.4 Biodistribution of [^{68}Ga]Ga-AV02053 and [^{68}Ga]Ga-AV02070 in HEK293T:hFAP tumor-bearing mice (n = 4) at 1 h post-injection with/without co-injection of FAPI-04 (250 µg). The biodistribution data for [^{68}Ga]Ga-FAPI-04 have been reported previously[141]. Error bars indicate standard deviation. Statistical significance was calculated using unpaired two-tailed *t*-test with Holm-Sidak method. * $p < 0.05$ ** $p < 0.01$ *** $p < 0.001$**** $p < 0.0001$.

3.4 Discussions

Both AV02053 and AV02070 were prepared by multi-step organic synthesis approach, with overall unoptimized yields of 1.90% and 0.31%, respectively. We observed that the difference in the overall yield between AV02053 and AV02070 was mainly contributed by the efficiency of nucleophilic substitution of *N*-Boc-*N,N'*-dimethyl-1,2-diaminoethane with methyl 6-chloronicotinate (for the preparation of AV02053) and methyl 2-chloroisoncotinate (for the preparation of AV02070). The substitution of chloride in methyl 6-chloronicotinate (50% yield for compound **1**) is more efficient compared to methyl 2-chloroisoncotinate (8.4% yield for compound

5). This is because the carbonyl group on the pyridine ring has better electron-withdrawing effect at the para position to chloride (in methyl 6-chloronicotinate) than at the meta position (in methyl 2-chloroisoncotinate).

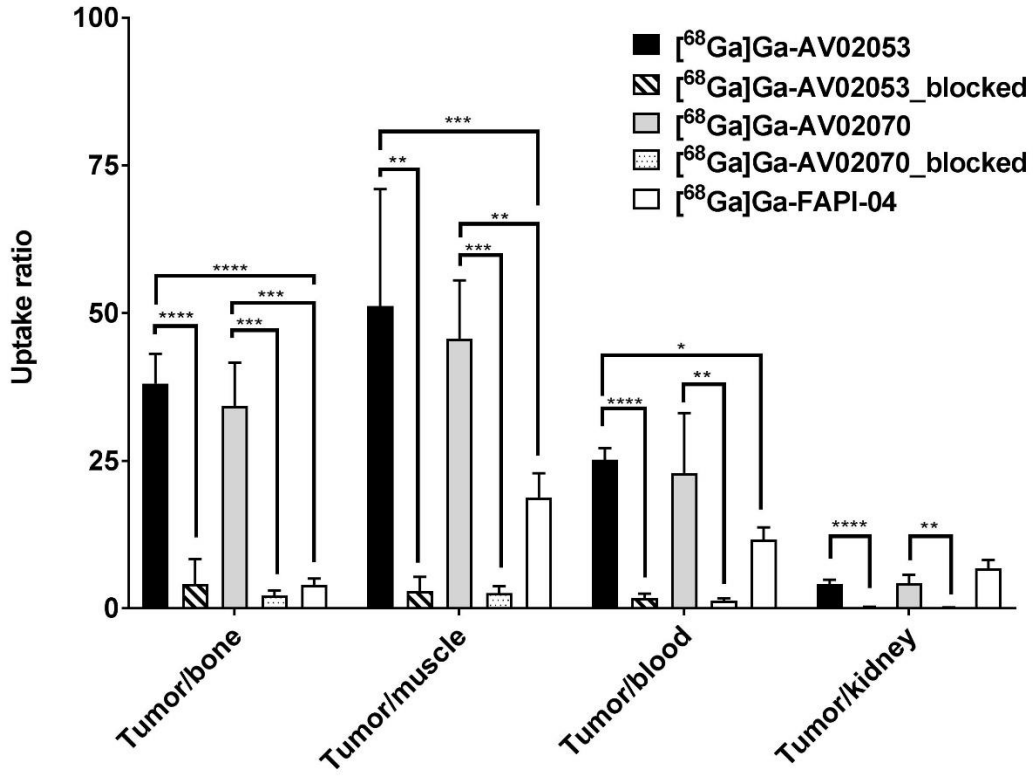

Figure 3.5 Tumor-to-background (bone, muscle, blood and kidney) uptake ratios of [^{68}Ga]Ga-AV02053 and [^{68}Ga]Ga-AV02070 in HEK293T:hFAP tumor-bearing mice (n = 4) at 1 h post-injection with/without co-injection of FAPI-04 (250 µg). The previously published data of [^{68}Ga]Ga-FAPI-04 are presented for comparison[141]. Error bars indicate standard deviation. Statistical significance was calculated using unpaired two-tailed *t*-test with Holm-Sidak method. * $p < 0.05$ ** $p < 0.01$ *** $p < 0.001$**** $p < 0.0001$.

The enzymatic assay (Figure 3.2) revealed that the FAP binding affinity of both Ga-AV02053 (IC_{50} = 187±52.0 nM) and Ga-AV02070 (IC_{50} = 17.1±4.60 nM) is lower than that of Ga-FAPI-04 (IC_{50} = 1.03±0.44 nM). This is consistent with the observations by Jansen and co-

workers that the quinoline-based pharmacophore (4-quinolinoyl)glycyl-(2*S*)-cyanopyrrolidine (IC_{50} = 10.3 nM) is more potent than its pyridine-based analog, (pyridine-4-carbonyl)glycyl-(2*S*)-cyanopyrrolidine (IC_{50} = 63 nM)[111]. We observed that the pyridine-4-carbonyl derived Ga-AV02070 (IC_{50} = 17.1±4.60 nM) is more potent than its pyridine-3-carbonyl-derived analog, Ga-AV02053 (IC_{50} 187±52.0 nM). This is also consistent with the report by Poplawski and co-workers that (pyridine-4-carbonyl)-D-Ala-boroPro derivatives have better FAP binding affinity than their (pyridine-3-carbonyl)-D-Ala-boroPro analogs[113].

The $LogD_{7.4}$ values confirmed that pyridine-based [^{68}Ga]Ga-AV02053 and [^{68}Ga]Ga-AV02070 are more hydrophilic compared to the quinoline-based [^{68}Ga]Ga-FAPI-04 ($LogD_{7.4}$ values = -3.75±0.16, -3.45±0.10 and -1.02±0.35, respectively). The higher hydrophilicity and smaller size of the pyridine-based pharmacophores compared to the quinoline-based pharmacophores could potentially lead to FAP-targeted tracers with faster pharmacokinetics, resulting in lower background uptake and higher tumor-to-background image contrast.

Consistent with the predictions from their binding affinity and smaller molecular size of pharmacophores, PET imaging and biodistribution data (Figures 3.3-3.5 and Table 3.4) revealed that the pyridine-based tracers, [^{68}Ga]Ga-AV02070 (7.93±1.88 %ID/g) and [^{68}Ga]Ga-AV02053 (5.60±1.12 %ID/g), have a lower tumor uptake than the previously reported value of the quinoline-based [^{68}Ga]Ga-FAPI-04 (12.5±2.00 %ID/g) using the same HEK293T:hFAP tumor model[141]. However, the pyridine-based tracers have a lower uptake in muscle and bone, which are the two common off-target organs of FAP-targeted tracers, as observed in the quinoline-based [^{68}Ga]Ga-FAPI-04 (Table 3.4). This leads to significantly higher tumor-to-muscle and tumor-to-bone uptake ratios for [^{68}Ga]Ga-AV02070 and [^{68}Ga]Ga-AV02053 than [^{68}Ga]Ga-FAPI-04. The significantly lower blood uptake of [^{68}Ga]Ga-AV02053 (0.22±0.04 %ID/g) and [^{68}Ga]Ga-AV02070 (0.36±0.05

%ID/g) indicates that both tracers are rapidly cleared from the blood pool. Furthermore, the tumor uptake of both tracers was reduced by ≥ 95% with the co-injection of FAPI-04 (250 µg), demonstrating that tumor uptake of both tracers is FAP-mediated. The highly specific uptake of [^{68}Ga]Ga-AV02070 and [^{68}Ga]Ga-AV02053 in tumors and their superior tumor-to-background contrast suggest that both tracers are promising for clinical translation for cancer imaging.

There are some limitations in our research design: Firstly, the faster pharmacokinetics of pyridine-based FAP-targeted radioligands might limit their applications for radioligand therapy. This is because faster clearance from the blood pool reduces their chances to bind to FAP in tumors and might result in a relatively lower overall tumor uptake. This could be solved by the addition of an albumin binder to the pyridine-based FAP-targeted ligands to extend their blood residence time as similar approaches have been exploited to increase the tumor uptake of radiolabeled quinoline-based FAPI-04 derivatives[129,130]. However, the blood residence time needs to be carefully adjusted as staying to long in blood will result in hematological toxicity. Previously, based on the reported albumin binder 4-(*p*-iodophenyl)butyramide[142], we have discovered a series of albumin binders with a broad range of albumin binding capability by replacing the iodo substituent with Br, Cl, F, H, CH_3, NO_2, OCH_3 and NH_2[122]. These albumin binders could be used to fine-tune the blood residence time of pyridine-based FAP-targeted radioligands to maximize tumor uptake without inducing significant hematological toxicity. Moreover, further biokinetics or pharmacokinetic (PK) studies are needed to confirm the correlation of the tracer structure to the biodistribution observed and to compare the PK with the quinoline-based FAP-targeted tracers. In this paper, we did not include this data, as our main aim is to first evaluate the imaging potential of the novel pyridine-based tracers. In addition, doing PK studies will require the use of more mice, and we think that it would be better to do the study on better compound candidates with

higher binding affinity. In future studies, we could calculate the biokinetics/clearance rate of the tracers by performing the biodistribution and imaging studies in earlier and later time points (30 min, 1 h, 1.5 h, and 2 h).

Secondly, the phenomena observed in the preclinical mouse model might not be representative to what will be observed in the clinic. For example, the high bone uptake of [^{68}Ga]Ga-FAPI-04 in mice is not observed in patients[114]. It will be of interest to compare [^{68}Ga]Ga-FAPI-04 with [^{68}Ga]Ga-AV02070 or [^{68}Ga]Ga-AV02053 in the clinic to investigate if pyridine-based FAP-targeted tracers can still lead to better tumor-to-background contrast, and hence, a better detection sensitivity.

Lastly, the use of *N,N'*-dimethylethylenediamine as the linker between the DOTA chelator and the pyridine moiety of [^{68}Ga]Ga-AV02070 and [^{68}Ga]Ga-AV02053 (Figure 3.2), and the selected position for the linker to attach to the pyridine ring were only due to ease of synthesis and may not be optimal for FAP targeting. Further optimizations on the selection of linker as well as the position for the linker to attach to the pyridine ring might be needed to improve FAP binding affinity, tumor uptake, and maybe even tumor-to-background contrast. A study reported by Lindner and co-workers[135] demonstrated that for the quinoline-based pharmacophores, a piperazine linker and the attachment of linker to the 6- rather than 7-position of the quinoline ring were preferable for FAP targeting. Both traits are preserved for the successful clinical tracers, [^{68}Ga]Ga-FAPI-04 and [^{68}Ga]Ga-FAPI-46. Hence, for future modifications, we will investigate the effects of attaching the linker to the 2- vs 3-position of the pyridine ring, as well as the use of a piperazine linker to potentially further increase binding affinity and tumor uptake.

3.5 Conclusions

Two novel ^{68}Ga-labeled pyridine-based FAP-targeted tracers were successfully synthesized and evaluated using a preclinical tumor model. Despite lower binding affinity and tumor uptake, both [^{68}Ga]Ga-AV02070 and [^{68}Ga]Ga-AV02053 show much higher tumor-to-background (blood, muscle and bone) uptake ratios than [^{68}Ga]Ga-FAPI-04. [^{68}Ga]Ga-AV02070 containing a pyridine-4-carbonyl moiety has better binding affinity and tumor uptake than [^{68}Ga]Ga-AV02053 containing a pyridine-3-carbonyl moiety, making it a promising candidate for the design of FAP-targeted tracers. Future optimization on the selection of linker between the DOTA chelator and the pyridine-based pharmacophores will be explored to increase the tumor uptake while maintaining or even further improving the high tumor-to-background contrast. Furthermore, [^{68}Ga]Ga-AV02070 pharmacophore can be incorporated for the design of PSMA/FAP bispecific tracers to potentially improve the tumor-to-background contrast and tumor uptake.

Chapter 4 : Synthesis and Preclinical Evaluation of Two Novel ^{68}Ga-Labeled Bispecific PSMA/FAP-targeting tracers with 2-Nal-containing PSMA-targeted Pharmacophore and Pyridine-based FAP-targeted Pharmacophore

4.1 Introduction

Previously, our group also has developed three ^{68}Ga-labeled bispecific PSMA/FAP radiotracers which incorporate quinoline-based FAP pharmacophore and anthracene ring-consisting PSMA pharmacophore[141]. We observed a high blood uptake (5-12 %ID/g at 1 h post-injection) in the mouse model with decreased tumor uptake in comparison to the ^{68}Ga-labeled monospecific counterparts, the PSMA-targeting [^{68}Ga]Ga-HTK03041 and the FAP-targeting [^{68}Ga]Ga-FAPI-04. We suspected that the longer blood retention could be caused by the increased lipophilicity of the ligands and potential interaction, such as π–π stacking between the quinoline ring and anthracene ring, which hindered the binding of the tracers to FAP and PSMA, leading to decreased tumor uptake. Our goal in this study is to solve these issues and improve the binding affinity and tumor uptake by replacing the pharmacophores with less lipophilic motifs, such as replacing Ala(9-Anth) in the PSMA-targeting pharmacophore with 2-Nal and replacing the quinoline motif in the FAP-targeting pharmacophore with a more hydrophilic pyridine motif.

Many pyridine-based FAP inhibitors (FAPI) have been reported[111,113], however there are still few reports on the development of pyridine-based FAP-targeted tracers. Previously we synthesized and evaluated two novel ^{68}Ga-labeled pyridine-based FAP-targeted tracers, [^{68}Ga]Ga-AV02053 and [^{68}Ga]Ga-AV02070, and compared their binding affinity and tumor uptake to that of [^{68}Ga]Ga-FAPI-04[143]. We discovered that although [^{68}Ga]Ga-FAPI-04 has higher binding affinity towards FAP and higher tumor uptake, both of our pyridine-based tracers have lower uptake in blood, muscle and bone, leading to a much higher tumor-to-background contrast ratio.

Our results suggest that pyridine-based FAPI is more hydrophilic than quinoline-based FAPI, and has potential to help reduce blood uptake. Furthermore, we found that Ga-AV02070 (Figure 4.1A), which has a carbonyl group at the para position to the pyridine nitrogen, has a better binding affinity to FAP and a higher tumor uptake compared to Ga-AV02053, which has the carbonyl group at the meta- position to the pyridine group. Hence, the pharmacophore of AV02070 is a promising candidate for the design of FAP-targeted tracers.

In this chapter, we report the design, synthesis, and evaluation of two bispecific PSMA/FAP-targeted radiotracers, [^{68}Ga]Ga-AV01084 and [^{68}Ga]Ga-AV01088 (Figure 4.1B). The PSMA binding motif of AV01084 and AV01088 was based on the 2-Nal-containing PSMA-targeted tracer, [^{68}Ga]Ga-PSMA-617[29], and their FAP-targeting motif was derived from our pyridine-based FAP-targeted radiotracer, [^{68}Ga]Ga-AV02070 (Figure 4.1A). The difference between the two tracers is the position of DOTA chelator linked to the lysine, which is the ε-amino group in AV01084 and the α-amino group in AV01088. Their potential for prostate cancer imaging was evaluated by in vitro competition binding assay, PET imaging, and ex vivo biodistribution studies in preclinical PSMA-expressing LNCaP and FAP-expressing HEK293T:hFAP tumor models. The results were then compared with those of corresponding monospecific tracers, [^{68}Ga]Ga-PSMA-617 and [^{68}Ga]Ga-AV02070.

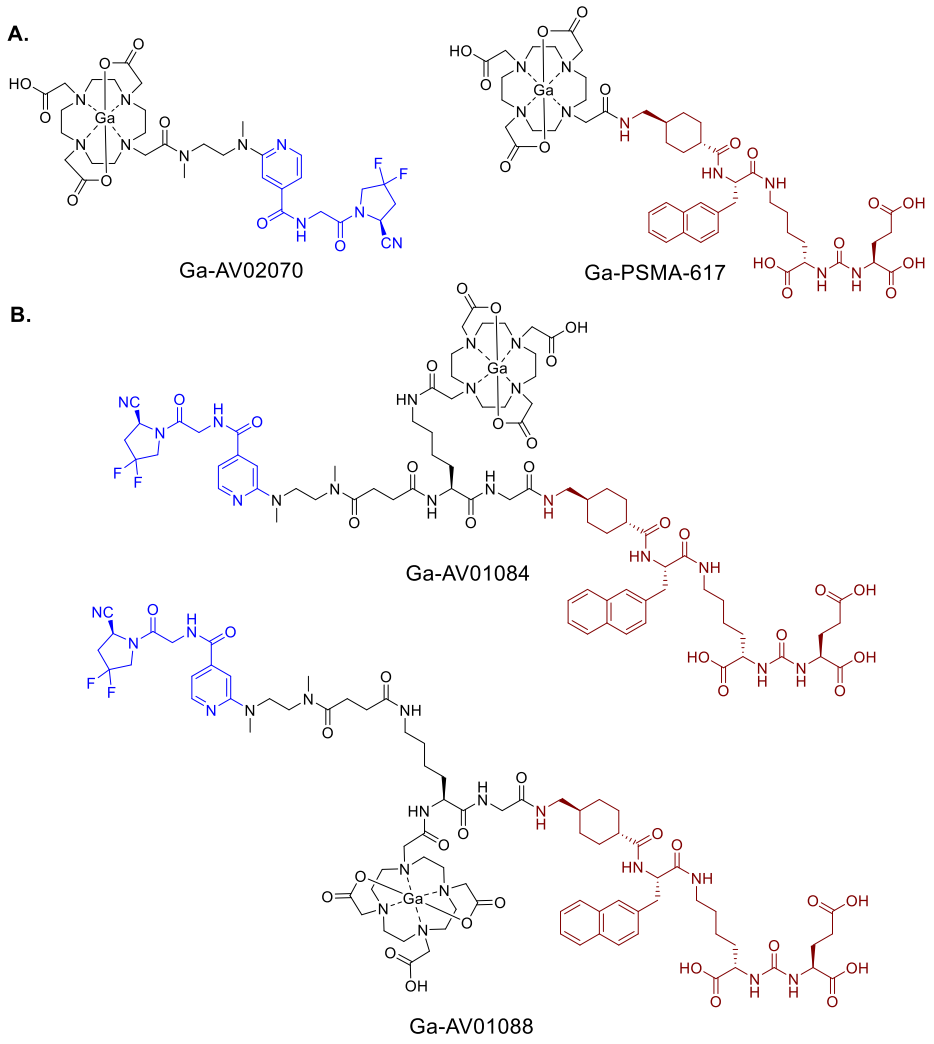

4.2 Materials and Methods

Figure 4.1 Chemical structures of (A) PSMA-targeting [^{68}Ga]Ga-PSMA-617 and FAP-targeting [^{68}Ga]Ga-AV02070; and (B) bispecific PSMA/FAP-targeting ^{68}Ga-labeled AV01084 and AV01088. The PSMA- and FAP- targeting pharmacophores are shown in brown and blue, respectively.

4.2.1 General Methods

1-(1,1-Dimethylethyl) butanedioate (**1**), (S)-N-(2-(2-Cyano-4,4-difluoropyrrolidin-1-yl)-2-oxoethyl)-2-[[2-[[(tert-butoxy)carbonyl]methylamino]ethyl]methylamino]pyridine-4-carboxamide (**3**), AV02070, Ga-AV02070, [^{68}Ga]Ga-AV02070, PSMA-617, Ga-PSMA-617, and

[^{68}Ga]Ga-PSMA-617 were synthesized following literature procedure[111,123,143,144]. All other chemicals and solvents were obtained from commercial sources and used without further purification. Purification and quality control of DOTA-conjugated ligands and their ^{nat}Ga/^{68}Ga-complexed analogs were performed on Agilent (Santa Clara, CA, USA) HPLC systems equipped with a model 1200 quaternary pump, a model 1200 UV absorbance detector (220 nm), and a Bioscan (Washington, DC, USA) NaI scintillation detector. The HPLC columns used were a semi-preparative column (Luna C18, 5 µm, 250 × 10 mm) and an analytical column (Luna C18, 5 µm, 250 × 4.6 mm) purchased from Phenomenex (Torrance, CA, USA). The collected HPLC eluates containing the desired products were lyophilized using a Labconco (Kansas City, MO, USA) FreeZone 4.5 Plus freeze-drier. MS analyses were conducted using the Waters (Milford, MA, USA) Acquity QDa mass spectrometer with the equipped 2489 UV/Vis detector and e2695 Separations module. C18 Sep-Pak cartridges (1 cm^3, 50 mg) were purchased from Waters (Milford, MA, USA). ^{68}Ga was eluted from an ITM Medical Isotopes GmbH (Munich, Germany) generator, and purified according to the previously published procedures using a DGA resin column from Eichrom Technologies LLC (Lisle, IL, USA) [125]. The radioactivity of ^{68}Ga-labeled tracers was measured using a Capintec (Ramsey, NJ, USA) CRC®-25R/W dose calibrator and the radioactivity of mouse tissues collected from biodistribution studies were counted using a Perkin Elmer (Waltham, MA, USA) Wizard2 2480 automatic gamma counter.

4.2.2 Synthesis of the FAP-targeting ligand

The FAP-targeting ligand, (S)-4-((2-((4-((2-(2-cyano-4,4-difluoropyrrolidin-1-yl)-2-oxoethyl)carbamoyl)pyridin-2-yl)(methyl)amino)ethyl)(methyl)amino)-4-oxobutanoic acid (**3**), was synthesized following the steps depicted on Scheme 4.1.

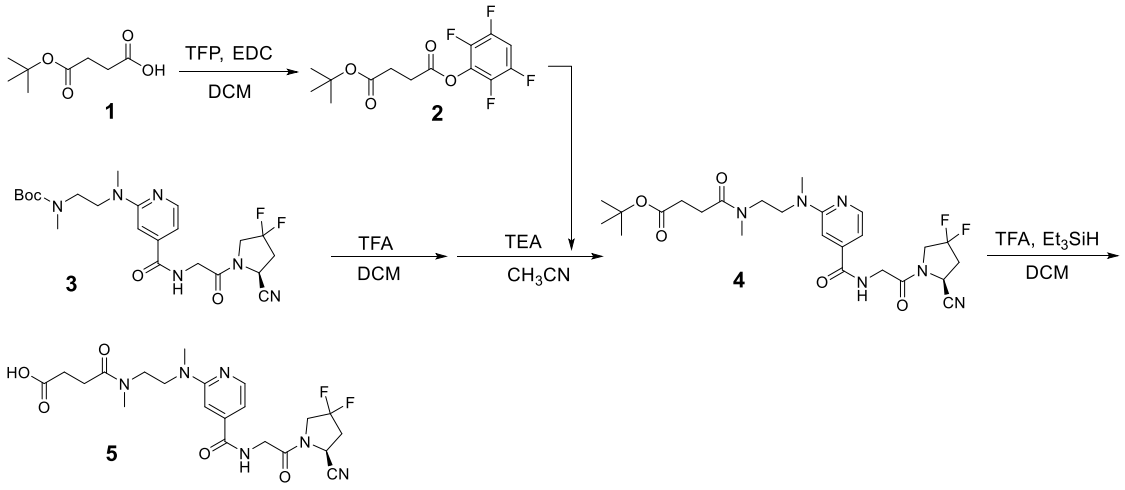

Scheme 4.1 Synthesis of (S)-4-((2-((4-((2-(2-cyano-4,4-difluoropyrrolidin-1-yl)-2-oxoethyl)carbamoyl)pyridin-2-yl)(methyl)amino)ethyl)(methyl)amino)-4-oxobutanoic acid (**5**)

4.2.2.1 Synthesis of of tert-butyl (2,3,5,6-tetrafluorophenyl) succinate (2)

A solution of 1-(1,1-Dimethylethyl) butanedioate (1.87 g, 10.72 mmol) in DCM were added tetrafluorophenol (TFP, 2.32 g, 13.94 mmol) and ethylene dichloride (EDC, 2.26 G, 11.8 mmol) and sittred at room temperature for 20 h. The resulting solution was evaporated under reduced pressure and the residue was dissolved in ethyl acetate (100 mL), washed with H_2O (100 mL x 2). The organic phase was collected, dried over anhydrous $MgSO_4$, filtered, and evaporated under reduced pressure to yield **2** (7.5 mmol, 71% yield) as a light yellow oil. MS (ESI) calculated for $C_{14}H_{14}F_4O_4$ 322.1, found $[M+Na]^+$ 345.1. ^1H NMR (300 MHz, DMSO-d_6) δ 7.94 (tt, J = 11.0, 7.4 Hz, 1H), 3.02 – 2.92 (m, 2H), 2.67 – 2.57 (m, 2H), 1.39 (s, 9H).

4.2.2.2 Synthesis of 2-[[2-[[(*tert*-butoxy)carbonyl]methylamino]ethyl]methylamino] pyridine-4-carboxylic acid (4)

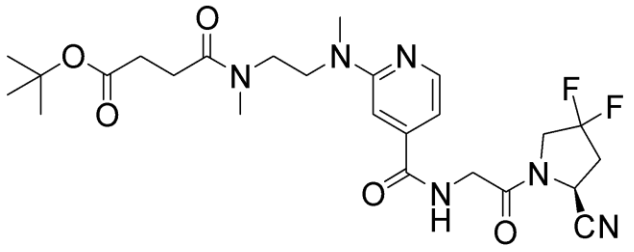

A solution of (S)-N-(2-(2-cyano-4,4-difluoropyrrolidin-1-yl)-2-oxoethyl)-2-[[2-[[(tert-butoxy)-carbonyl]methylamino]ethyl]methylamino]pyridine-4-carboxamide (**3**) (1.49 g, 3.1 mmol) in DCM (20 mL) was added TEA (20 mL) and stirred at room temperature for 2 h. After evaporation, the residue was dissolved in CH_3CN (50 mL), and compound 2 (2.44 g, 7.5 mmol) and triethylamine (TEA, 2.8 mL, 20 mmol) were added. After stirring at 50 °C for 19 h, the volatile solvent was evaporated under reduced procedure, and the residue was purified with flash column chromatography eluted with ethyl acetate (0.6 L), followed by 19:1 (v/v) ethyl acetate/methanol (1.8 L) and 9:1 (v/v) ethyl acetate/methanol (1 L), consecutively. The product eluate fractions were combined and evaporated under reduced pressure to yield **2** as a yellow powder (750 mg, 45% yield). MS (ESI) calculated for $C_{25}H_{34}F_2N_6O_5$ 536.3, found $[M+H]^+$ 537.3. ^{1}H NMR (300 MHz, DMSO) δ 7.39 (d, *J* = 8.1 Hz, 1H), 7.15 (s, 1H), 7.06 (t, *J* = 6.0 Hz, 2H), 6.88 (t, *J* = 6.4 Hz, 1H), 5.07 (dd, *J* = 9.1, 3.0 Hz, 2H), 4.45 (dd, *J* = 9.6, 4.2 Hz, 1H), 4.26 – 3.88 (m, 5H), 3.77 (d, *J* = 6.1 Hz, 4H), 3.70 (dd, *J* = 17.3, 5.6 Hz, 1H), 2.90 (dt, *J* = 14.3, 9.1 Hz, 1H), 2.83 – 2.67 (m, 3H), 1.38 (s, 9H).

4.2.2.3 Synthesis of (S)-4-((2-((4-((2-(2-cyano-4,4-difluoropyrrolidin-1-yl)-2-oxoethyl)carbamoyl)pyridin-2-yl)(methyl)amino)ethyl)(methyl)amino)-4-oxobutanoic acid (5)

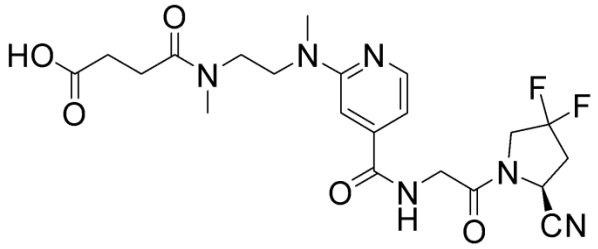

Compound **4** (737 mg, 1.38 mmol) was dissolved in dichloromethane (DCM, 10 mL), and triethylsilane (481 mg, 4.14 mmol) and TFA (10 mL) were added. After stirring for 2 h, the resulting solution was evaporated and the residue was dissolved in ether (250 mL). The ether solution was stirred for 2 hour and the resulting yellow powder was filtered and dried under reduced pressure to yield 670 mg of **5** (100% yield). MS (ESI) calculated for $C_{21}H_{26}F_2N_6O_5$ 480.2, found $[M+H]^+$ 481. 2. ^{1}H NMR (300 MHz, DMSO-d_6) δ 9.03 (dt, *J* = 27.2, 5.8 Hz, 1H), 8.27 – 8.12 (m, 3H), 7.25 (s, 1H), 7.11 – 6.97 (m, 2H), 5.10 (dd, *J* = 9.1, 2.9 Hz, 1H), 4.38 – 4.19 (m, 1H), 4.18 – 4.05 (m, 1H), 3.76 (s, 1H), 3.09 (s, 2H), 2.98 (s, 3H), 2.85 (s, 2H), 2.80 (s, 1H), 2.36 (dd, *J* = 8.7, 4.8 Hz, 3H).

4.2.3 Synthesis of DOTA-conjugated Peptides

AV01084 and AV01088 were synthesized on solid phase using Fmoc peptide chemistry. Fmoc-Lys(ivDde)-Wang resin (0.05 mmol, 0.081 g) was treated with 20% piperidine in DMF to remove the Fmoc protecting group. The isocyanate derivative (3 eq.) of Glu(tBu)-OtBu was synthesized following previously published procedures[77] and was added to the lysine-immobilized resin, with *N*,*N*-diisopropylethylamine (DIEA, 2 eq.) as the base and reacted for 16 h to form the

Lys-urea-Glu moiety. The ivDde-protecting group was then removed with 2% hydrazine in DMF (5 × 5 min). Fmoc-2-Nal-OH (4 eq.), Fmoc-tranexamic acid (3 eq.), Fmoc-Gly-OH, and Fmoc-Lys(ivDde)-OH were pre-activated with HATU (4 eq.) and DIEA (7 eq.) before being sequentially coupled to the resin. Following the removal of Fmoc protecting group, FAP-targeting moiety (compound **3)** or DOTA-tris(*t*-butyl)ester (3 eq.) was pre-activated with HATU (4 eq.) and DIEA (7 eq.) and coupled to the α-amino group of lysine for AV01084 or AV01088, respectively. Finally, the ivDde-protecting group on lysine was removed and coupled with DOTA-tris(*t*-butyl)ester or compound **3** activated with HATU (3 eq.) and DIEA (7 eq.) for AV01084 and AV01088, respectively.

The peptides were deprotected and simultaneously cleaved from the resin with a mixture of trifluoroacetic acid (TFA, 95%), triisopropylsilane (TIS 2.5%) and water (2.5%) for 4 h at room temperature. The cleaved peptides were filtrated and then precipitated by adding cold diethyl ether. The crude peptides were collected by centrifugation and purified with HPLC (semi-preparative column; flow rate: 4.5 mL/min). The eluates containing the desired peptides were collected and lyophilized. The HPLC conditions, retention times, isolated yields and MS confirmations of DOTA-conjugated peptides are provided in the Table 4.1.

4.2.4 Synthesis of Nonradioactive Ga-complexed Standards

The nonradioactive Ga-complexed standards were prepared by reacting the DOTA-conjugated precursors with $GaCl_3$ (5 eq.) in NaOAc buffer (0.1 M, 500 µL, pH 4.2 – 4.5) at 80 °C for 15 min. The reaction mixture was then purified via HPLC (semi-preparative column, flow rate: 4.5 mL/min). The HPLC eluates containing the desired products were collected and lyophilized. The HPLC conditions, retention times, isolated yields and MS confirmations of these nonradioactive Ga-complexed standards are provided in Table 4.2.

4.2.5 Synthesis of ^{68}Ga-labeled Compounds

The radiolabeling experiments were performed according to previously published procedures[126,127]. Purified $^{68}GaCl_3$ in 0.5 mL water was added to a 4-mL glass vial preloaded with 0.7 mL of HEPES buffer (2 M, pH 5.0) and 10 µL precursor solution (1 mM). The radiolabeling reaction was carried out under microwave heating for 1 min, followed by purification using the semi-preparative HPLC column. The eluate fraction containing the radiolabeled product was collected, diluted with water (50 mL), and passed through a C18 Sep-Pak cartridge that was pre-washed with ethanol (10 mL) and water (10 mL). The C18 Sep-Pak cartridge was washed with water (10 mL), and the ^{68}Ga-labeled product was eluted off the cartridge with ethanol (0.4 mL). The eluted product was diluted with PBS for imaging and biodistribution studies. Quality control was performed using the analytical column. The HPLC conditions and retention times are provided in Table 4.3. The tracers were obtained in 27-82% decay-corrected radiochemical yields with ≥56 GBq/µmol molar activity and >95% radiochemical purity.

Table 4.1 HPLC purification conditions and MS characterizations of DOTA-conjugated precursors.

Compound name	HPLC conditions	Retention time (min)	Yield (%)	Calculated mass (m/z)	Found (m/z)
AV01084	26% CH_3CN and 0.1% TFA in H_2O	14.1	12	$[M+2H]^{2+}$ 845.92	$[M+2H]^{2+}$ 845.80
AV01088	26% CH_3CN and 0.1% TFA in H_2O	13.7	7.2	$[M+2H]^{2+}$ 845.92	$[M+2H]^{2+}$ 845.80

Table 4.2 HPLC purification conditions and MS characterizations of nonradioactive Ga-complexed standards.

Compound name	HPLC conditions	Retention time (min)	Yield (%)	Calculated mass (m/z)	Found (m/z)
Ga-AV01084	27% CH_3CN and 0.1% TFA in H_2O	10.8	60	$[M+2H]^{2+}$ 880.28	$[M+2H]^{2+}$ 879.81
Ga-AV01088	26% CH_3CN and 0.1% TFA in H_2O	14.1	21	$[M+2H]^{2+}$ 880.28	$[M+2H]^{2+}$ 879.75

Table 4.3 HPLC conditions for the purification and quality control of ^{68}Ga-labeled tracers.

Compound name	HPLC conditions		Retention time (min)
[^{68}Ga]Ga-AV01084	Semi-Prep	28% CH_3CN and 0.1% TFA in H_2O; flow rate 4.5 mL/min	16.8
	QC	31.5% CH_3CN and 0.1% TFA in H_2O; flow rate 2.0 mL/min	6.3
[^{68}Ga]Ga-AV01088	Semi-Prep	28% CH_3CN and 0.1% TFA in H_2O; flow rate 4.5 mL/min	16.7
	QC	31.5% CH_3CN and 0.1% TFA in H_2O; flow rate 2.0 mL/min	6.3

4.2.6 Cell Culture

The LNCaP cells obtained from ATCC (via Cedarlane, Burlington, Canada) were cultured in RPMI 1640 medium supplemented with 10% FBS, penicillin (100 U/mL) and streptomycin (100 μg/mL) at 37 °C in a Panasonic Healthcare (Tokyo, Japan) MCO-19AIC humidified incubator containing 5% CO_2. The cells were confirmed to be pathogen-free by the IMPACT Rodent Pathogen Test (IDEXX BioAnalytics). Cells were grown until 80-90% confluence and

washed with sterile phosphate-buffered saline (PBS, pH 7.4) and collected after 1 min trypsinization. The cell concentration was counted in triplicate using a hemocytometer and a manual laboratory counter.

The HEK293T:hFAP cells generated in our lab[141] were cultured in DMEM GlutaMAX™ medium supplemented with 10% FBS, penicillin (100 U/mL) and streptomycin (100 µg/mL) at 37 °C in a Panasonic Healthcare (Tokyo, Japan) MCO-19AIC humidified incubator containing 5% CO_2. Cells were grown until 80-90% confluence and washed with sterile phosphate-buffered saline (PBS, pH 7.4) and collected after 1 min trypsinization. The cell concentration was counted in triplicate using a hemocytometer and a manual laboratory counter.

4.2.7 In Vitro PSMA Competition Binding Assay

The PSMA binding assays were conducted following previously published procedures using LNCaP cells and [^{18}F]DCFPyL as the radioligand[122,123,128]. Data analyses of K_i were performed using the nonlinear regression algorithm of GraphPad Prism 7 (San Diego, CA) software. Briefly, LNCaP cells (400,000/well) were plated onto a 24-well poly-D-lysine coated plate for 48 h. Growth media was removed and replaced with HEPES buffered saline (50 mM HEPES, pH 7.5, 0.9% sodium chloride), and the cells were incubated for 1 h at 37 °C. [^{18}F]DCFPyL (0.1 nM) was added to each well (in triplicate) containing various concentrations (10 mM−0.5 pM) of tested compounds (Ga-AV01084 and Ga-AV01088). Nonspecific binding was determined in the presence of 10 µM nonradiolabeled DCFPyL. The assay mixtures were further incubated for 1 h at 37 °C with gentle agitation. Then, the buffer and hot ligand were removed, and cells were washed twice with cold HEPES buffered saline. To harvest the cells, 400 µL of 0.25% trypsin solution was added to each well. Radioactivity was measured on a

PerkinElmer (Waltham, MA) Wizard2 2480 automatic gamma counter. Nonlinear regression analyses and IC_{50} calculations were performed using the GraphPad Prism 7 software.

4.2.8 In Vitro FAP Fluorescence Assay

The half maximal inhibitory concentration (IC_{50}) values of the tested compounds for FAP were measured by in vitro enzymatic assay. The recombinant human FAP (Biolegend; 0.2 µg/mL, 50 µL) was added into costar 96-well plate. PBS and varied concentrations (0.2 pM to 2 µM) of tested nonradioactive Ga-complexed standards were added to each wells (in duplicate) containing the recombinant human FAP. After being incubated for 30 min at 37 °C, 50 µL of Suc-Gly-Pro-AMC (2 µM, Bachem) was added to each well. The fluorescent signals were acquired at 15, 30, 45, and 60 min using FlexStation 3 Multi-Mode Microplate Reader with excitation at 380 nm and emission at 460 nm. The IC_{50}(FAP) was calculated using "nonlinear fit model" built-in model in GraphPad Prism 7.02 software

4.2.9 Ex Vivo Biodistribution and PET/CT Imaging Studies

Imaging and biodistribution studies were performed using male NOD.Cg-Rag1tm1Mom Il2rgtm1Wjl/SzJ (NRG) mice following previously published procedures[129,130]. The experiments were conducted according to the guidelines established by the Canadian Council on Animal Care and approved by Animal Ethics Committee of the University of British Columbia. The mice were briefly sedated by inhalation of 2.5% isoflurane in oxygen, and 100 µL LNCaP (8×10^6 cells) or HEK293T:hFAP (8.5×10^6 cells) cells were inoculated subcutaneously behind the left shoulder. When the tumor grew to 5-8 mm in diameter over 3-4 weeks and 4-5 weeks for HEK293T:hFAP

and LNCaP tumors, respectively, the mice were used for PET/CT imaging and biodistribution studies.

PET/CT imaging experiments were carried out using a Siemens (Knoxville, TN) Inveon micro PET/CT scanner. Each tumor-bearing mouse was injected with ~4-6 MBq of ^{68}Ga-labeled tracer through a lateral caudal tail vein under 2.5% isoflurane in oxygen anesthesia, followed by recovery and roaming freely in its cage during the uptake period. At 50 min post-injection, a 10-min CT scan was conducted first for localization and attenuation correction after segmentation for reconstructing the PET images, followed by a 10-min static PET imaging acquisition.

For biodistribution studies, the mice were injected with the radiotracer (~2-4 MBq) as described above. For blocking study the LNCaP tumor-bearing mice and HEK293T:hFAP tumor-bearing mice were co-injected with 500 μg and 250 μg of FAPI-04, respectively. At 1 h post-injection, the mice were euthanized by CO_2 inhalation. Blood was withdrawn by cardiac puncture, and organs/tissues of interest were collected, weighed and counted using a Perkin Elmer (Waltham, MA) Wizard2 2480 automatic gamma counter.

4.2.10 Statistical Analysis

Data were analyzed with the GraphPad Prism, version 7.02 and Microsoft (Redmond, WA) Excel software. One way ANOVA and multiple t tests were performed for all organs in the biodistribution studies of [^{68}Ga]Ga-AV01084, [^{68}Ga]Ga-AV01088, [^{68}Ga]Ga-PSMA-617, and [^{68}Ga]Ga-AV02070 in LNCaP and HEK293T:hFAP tumor models. A statistically significant difference was considered present when the adjusted *P* value was less than 0.05 using the Holm–Sidak method.

4.3 Results

4.3.1 Synthesis

AV01084 and AV01088 (Figure 4.1B) were synthesized on solid phase. Briefly, Lys(Lys(ivDde)-Gly-tranexamic acid-2-Nal)-urea-Glu(OtBu)-OtBu was first constructed on solid phase, followed by amide coupling of the FAP-targeted motif, compound **5**, and DOTA chelator. To synthesize compound **5** (Scheme 4.1), compound **1** was first coupled with 2,3,5,6-tetrafluorophenol (TFP) to obtain compound **2** in 71% yield. Compound **3** which was synthesized following literature procedures[143] was first Boc-deprotected using trifluoroacetic acid (TFA), followed by coupling with compound **2** to obtain compound **4** in 45% yield. *Tert*-butyl protecting group of compound **4** was removed using TFA and compound **5** was obtained quantitatively.

To synthesize AV01084, compound **5** was coupled to Lys(Lys(ivDde)-Gly-tranexamic acid-2-Nal)-urea-Glu(OtBu)-OtBu, followed by removal of the ivDde group at the Lys side chain and subsequent coupling with the DOTA chelator. To synthesize AV01088, DOTA chelator was first coupled to Lys(Lys(ivDde)-Gly-tranexamic acid-2-Nal)-urea-Glu(OtBu)-OtBu, followed by deprotection of amino group at the Lys side chain and coupling with compound **5**. The DOTA-conjugated ligands were then cleaved off from resin and purified by HPLC (Table S1). AV01084 and AV01088 were obtained in 12% and 7.2% yields, respectively.

Detailed syntheses and characterizations of nonradioactive Ga- and ^{68}Ga-complexed AV01084 and AV01088 are provided in the Supplementary Materials (Tables S2-S3). Nonradioactive Ga-complexed AV01084 and AV01088 were obtained in 60% and 21% yields, respectively, and their ^{68}Ga-labeled analogs were obtained in 33 – 64% decay-corrected radiochemical yields with ≥ 44 GBq/μmol molar activity and > 95% radiochemical purity.

4.3.2 Binding Affinity and Lipophilicity

The binding affinities of Ga-AV01084, Ga-AV01088, and Ga-AV02070 to PSMA were measured by a cell-based binding assay using PSMA-expressing LNCaP prostate cancer cells and were compared to the previously published Ga-PSMA-617 (Ki = 1.23 ± 0.08 nM) [33]. The nonradioactive Ga-complexed standards inhibited the binding of [18F]DCFPyL to LNCaP cells in a dose-dependent manner (Figure 2A). The calculated Ki(PSMA) values for Ga-AV01084, Ga-AV01088, and Ga-AV02070 were 11.6 ± 3.25, 28.7 ± 6.05, and > 1,000 nM, respectively (n = 3).

The binding affinities of Ga-AV01084, Ga-AV01088, and Ga-PSMA-617 to human FAP were measured by an enzyme inhibition assay using Suc-Gly-Pro-AMC as the FAP substrate and were compared to the previously published Ga-AV02070 (IC50 = 17.1 ± 4.6 nM) [31]. The human FAP enzymatic activity on the substrate was inhibited by Ga-complexed standards in a dose dependent-manner (Figure 2B). The calculated IC50 values for Ga-AV01084, Ga-AV01088, and Ga-PSMA-617 were 10.9 ± 0.67, 16.7 ± 1.53 and > 1,000 nM respectively.

The lipophilicity of the ^{68}Ga-labeled AV01084 and AV01088 were calculated using $LogD_{7.4}$ measurement. The $LogD_{7.4}$ values of [^{68}Ga]Ga-AV01084 and [^{68}Ga]Ga-AV01088 were -3.61 ± 0.07 and -3.66 ± 0.25, respectively. The values indicate that the compounds were hydrophilic.

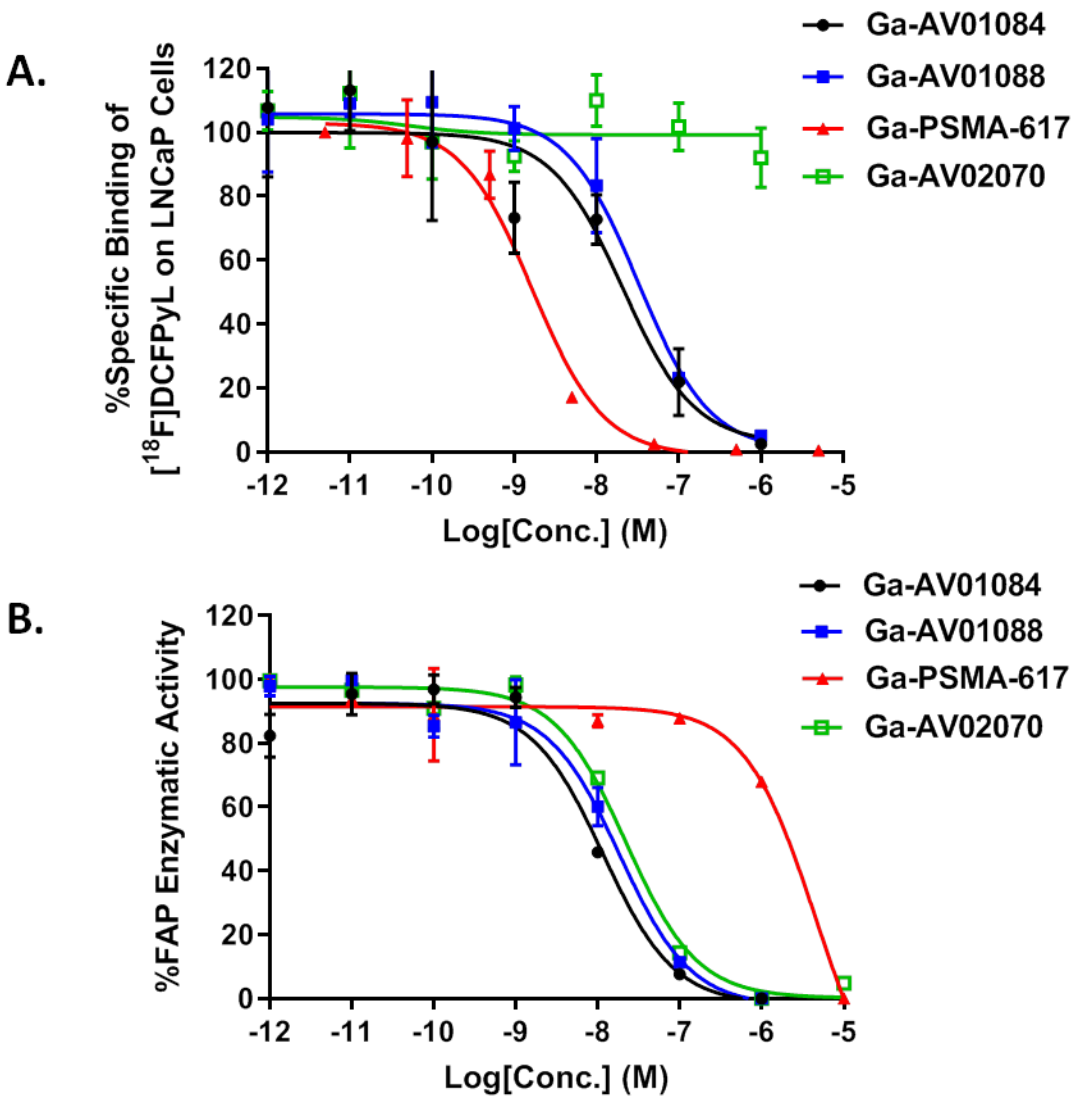

Figure 4.2 (A) Displacement curves of [^{18}F]DCFPyL by Ga-AV01084, Ga-AV01088, Ga-AV02070, and Ga-PSMA-617 generated using PSMA-expressing LNCaP cells; (B) Fluorescence curve of FAP enzymatic activity on Suc-Gly-Pro-AMC substrate with inhibition by Ga-AV01084, Ga-AV01088, Ga-AV02070, and Ga-PSMA-617.

4.3.3 PET Imaging and Ex Vivo Biodistribution

Representative PET images acquired at 1 h post-injection using [^{68}Ga]Ga-AV01084, [^{68}Ga]Ga-AV01088, [^{68}Ga]Ga-PSMA-617 and [^{68}Ga]Ga-AV02070 are provided in Figure 4.3. All the radiotracers were excreted primarily through the renal pathway. LNCaP tumor xenografts

were clearly visualized by [^{68}Ga]Ga-AV01084, [^{68}Ga]Ga-AV01088, and [^{68}Ga]Ga-PSMA-617, but not visualized by [^{68}Ga]Ga-AV02070 (Figure 4.3). HEK293T:hFAP tumor xenografts were clearly visualized by [^{68}Ga]Ga-AV02070, barely visualized by the bispecific tracers ([^{68}Ga]Ga-AV01084 and [^{68}Ga]Ga-AV01088), but not visualized by [^{68}Ga]Ga-PSMA-617 (Figure 4.3). The bispecific tracers have bone and joint uptake, which is commonly observed for FAP-targeting tracers. There was a high kidney uptake in mice injected with the bispecific tracers and [^{68}Ga]Ga-PSMA-617, but not in mice injected with [^{68}Ga]Ga-AV02070. Co-injection of [^{68}Ga]Ga-AV01088 with 2-PMPA (500 µg) in LNCAP tumor xenografts reduced the uptake of [^{68}Ga]Ga-AV01088 in LNCaP to almost background level, confirming the uptake is PSMA mediated. Similarly, co-injection of [^{68}Ga]Ga-AV01088 with FAPI-04 (250 µg) in HEK293T:hFAP tumor xenografts reduced the uptake of [^{68}Ga]Ga-AV01088 in HEK293T:hFAP tumor xenograft to almost background level, confirming the uptake tracers is FAP mediated.

Biodistribution studies were conducted at 1 h post injection with ^{68}Ga-labeled AV01084, AV01088, PSMA-617, and AV02070 in LNCaP tumor-bearing mice (Figure 4.4, Table 4.4). The results were consistent with the observation from their PET images. Tumor uptake values for [^{68}Ga]Ga-AV01084, [^{68}Ga]Ga-AV01088, [^{68}Ga]Ga-PSMA-617 and [^{68}Ga]Ga-AV02070 were 9.05 ± 1.54, 8.85 ± 1.25, 16.71 ± 2.30, and 0.74 ± 0.21 %ID/g, respectively. There was a very low tumor uptake in mice injected with [^{68}Ga]Ga-AV02070, showing very minimal FAP expression in this tumor model. The uptake levels of these tracers on the major organs and tissues are consistent with the trends observed in the PET images of LNCaP tumor-bearing mice.

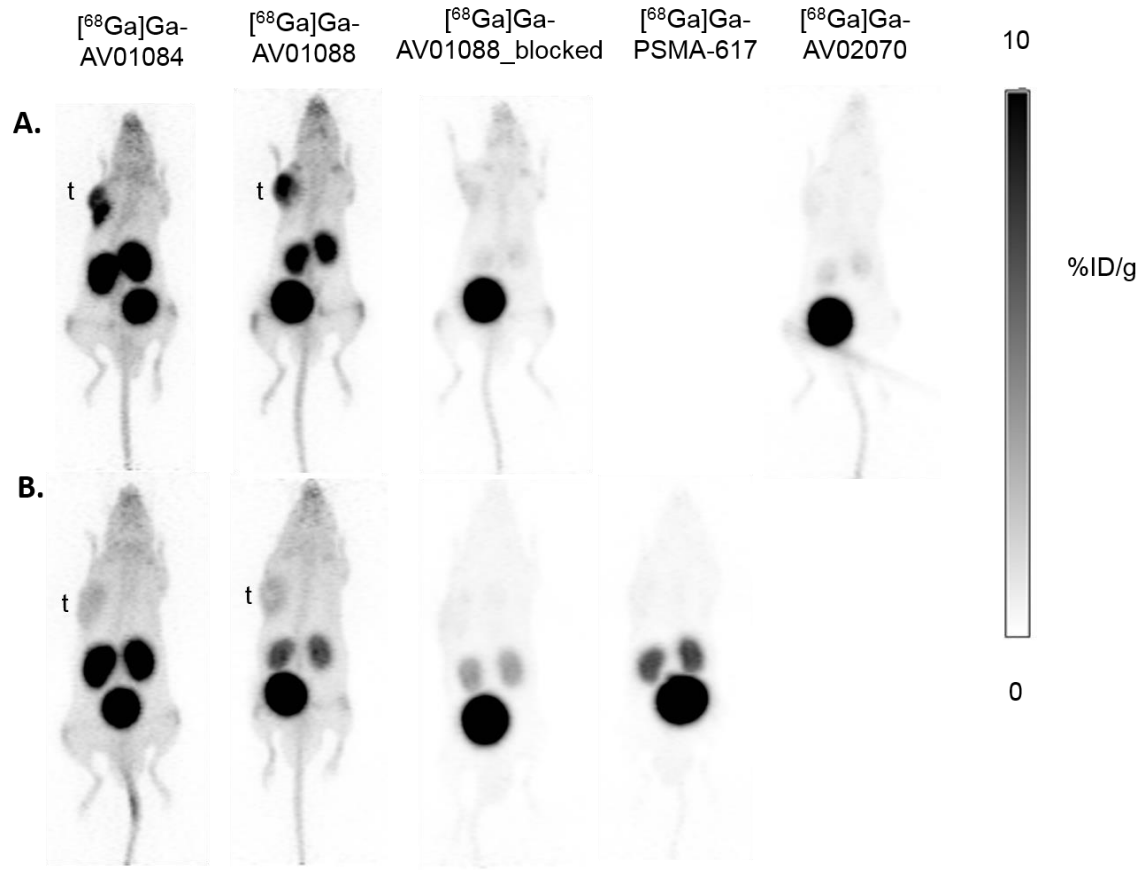

Figure 4.3 Representative maximum intensity projection PET images of [^{68}Ga]Ga-AV01084, [^{68}Ga]Ga-AV01088, [^{68}Ga]Ga-AV01088_blocked, [^{68}Ga]Ga-PSMA-617, and [^{68}Ga]Ga-AV02070 acquired at 1 h post-injection in mice bearing (A) LNCaP tumor xenografts and (B) HEK293T:hFAP tumor xenografts. The blocking with 2-PMPA (in LNCaP tumor xenografts) and FAPI-04 (in HEK293T:hFAP tumor xenografts) decreased the tumor uptake to background level. t: tumor.

The bispecific tracers have significantly higher blood and bone uptake values than the monospecific tracers, [^{68}Ga]Ga-PSMA-617 and [^{68}Ga]Ga-AV02070 (blood uptake: 1.56 - 2.26 vs 0.28-0.75 %ID/g, $p < 0.05$, bone uptake: 0.88-2.47 vs 0.09-0.56 %ID/g, $p < 0.05$), resulting in significantly lower tumor-to-blood ratio (4.09 ± 0.77 for [^{68}Ga]Ga-AV01084 and 4.09 ± 0.77 for [^{68}Ga]Ga-AV01088) compared to [^{68}Ga]Ga-PSMA-617 (27.69 ± 6.28) and lower tumor-to-bone ratio (3.70 ± 0.83 for [^{68}Ga]Ga-AV01084 and 3.75 ± 1.28 for [^{68}Ga]Ga-AV01088) compared to

[^{68}Ga]Ga-PSMA-617 (96.49 ± 47.59). [^{68}Ga]Ga-AV01084 has higher heart, kidney and adrenal glands uptake than [^{68}Ga]Ga-AV01088 ($P < 0.05$).

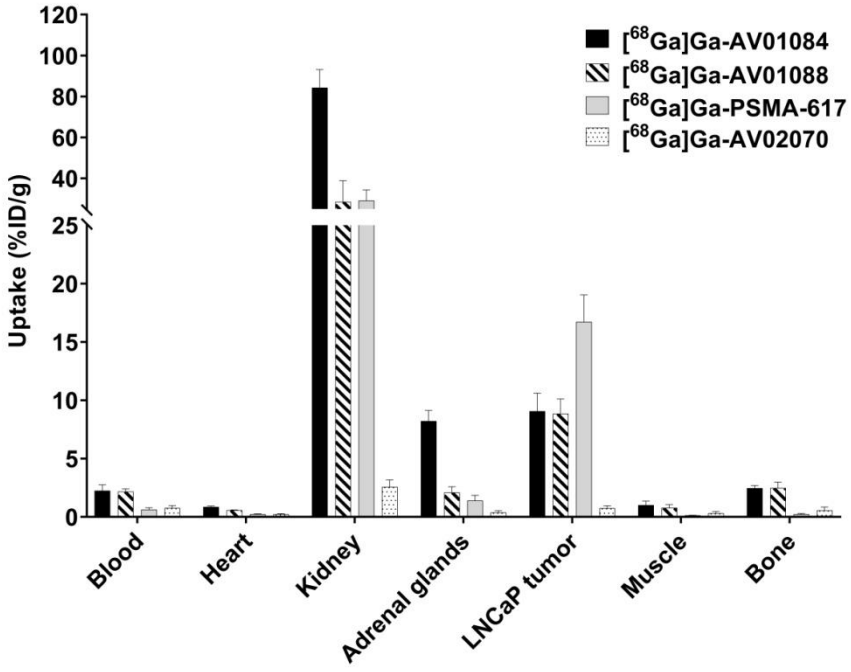

Figure 4.4 Biodistribution of [^{68}Ga]Ga-AV01084, [^{68}Ga]Ga-AV01088, [^{68}Ga]Ga-PSMA-617 and [^{68}Ga]Ga-AV02070 in LNCaP tumor-bearing mice.

Biodistribution studies were also conducted at 1 h post injection with [^{68}Ga]Ga-AV01084, [^{68}Ga]Ga-AV01088, [^{68}Ga]Ga-PSMA-617 and [^{68}Ga]Ga-AV02070 in HEK293T:hFAP tumor-bearing mice (Figure 4.5 and Table 4.5). Tumor uptake values for [^{68}Ga]Ga-AV01084, [^{68}Ga]Ga-AV01088, [^{68}Ga]Ga-PSMA-617 and [^{68}Ga]Ga-AV02070 were 1.9 ± 0.41, 1.2 ± 0.25, 0.26 ± 0.01, and 7.93 ± 1.88 %ID/g, respectively. There was a very low tumor uptake in mice injected with [^{68}Ga]Ga-PSMA-617, showing very minimal PSMA expression in this tumor model. The uptake levels of these tracers on the major organs and tissues are consistent with the trends observed in the PET images of LNCaP tumor-bearing mice (Figure 4.4 and Table 4.4)

Co-injection of 2-PMPA reduced the average uptake of [^{68}Ga]Ga-AV02088 in LNCaP tumor xenografts by 67% (8.85%ID/g down to 2.95%ID/g at 1 h post-injection) confirming the specific uptake of [^{68}Ga]Ga-AV02088 in LNCaP tumor xenografts (Figure 4.6). Co-injection of FAPI-04 reduced the average uptake of [^{68}Ga]Ga-AV02088 in HEK293T:hFAP tumor xenografts by 57% (1.2 ± 0.25 %ID/g down to 0.51 ± 0.14 %ID/g at 1 h post-injection) confirming the specific uptake of [^{68}Ga]Ga-AV02088 in HEK293T:hFAP tumor xenografts.

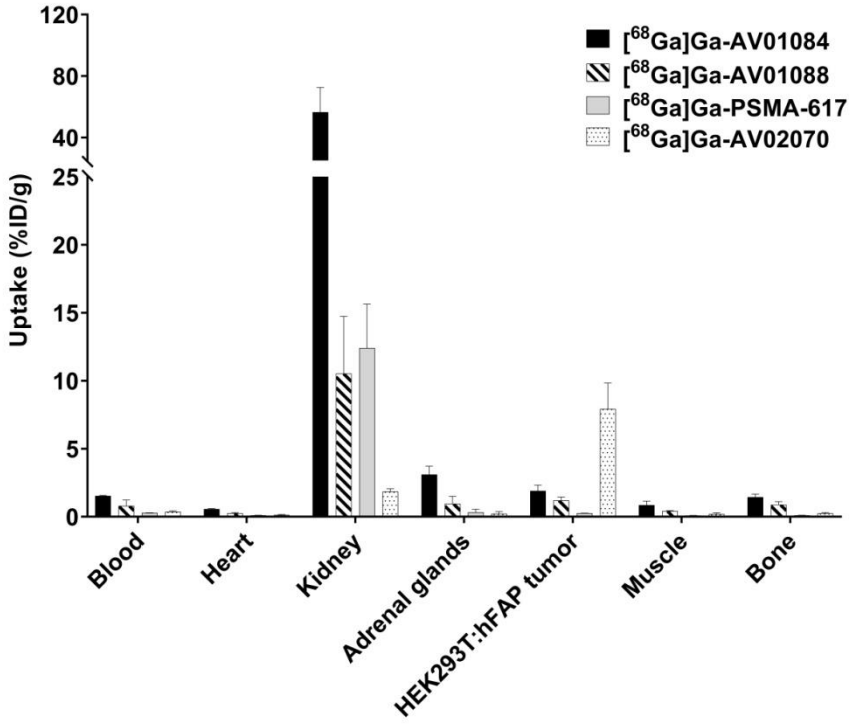

Figure 4.5 Biodistribution of [^{68}Ga]Ga-AV01084, [^{68}Ga]Ga-AV01088, [^{68}Ga]Ga-PSMA-617 and [^{68}Ga]Ga-AV02070 in HEK293T:hFAP tumor-bearing mice.

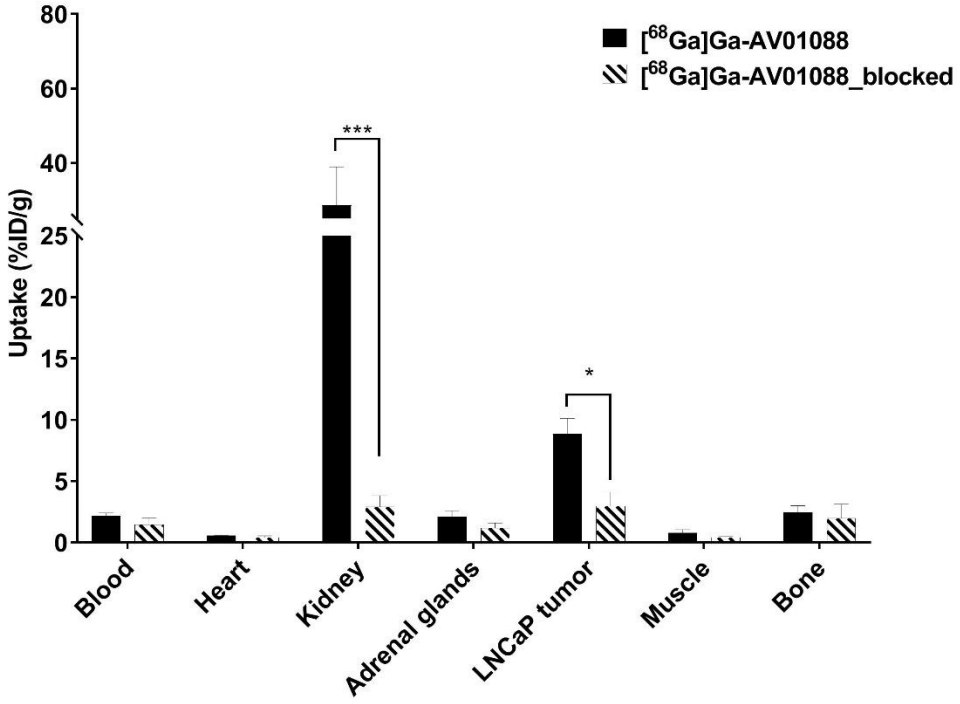

Figure 4.6 Comparison of [^{68}Ga]Ga-AV01088 with/without co-injection of 2-PMPA on the uptake in LNCaP tumor xenografts and major organs/tissues in mice at 1h post-injection. Error bars indicate standard deviation. *$p < 0.05$, ***$p < 0.001$.

4.4 Discussions

Previously, we synthesized three ^{68}Ga-labeled bispecific PSMA/FAP radiotracers, [^{68}Ga]Ga-AV01017, [^{68}Ga]Ga-AV01030, and [^{68}Ga]Ga-AV01038 [141], which incorporate a quinoline-based FAP-targeted pharmacophore and the PSMA-targeted pharmacophore of [^{68}Ga]Ga-HTK03041. The PSMA and FAP in vitro competition binding assays indicated that our bispecific tracers have lower binding affinity to PSMA compared to the monospecific PSMA-targeting ligand, Ga-HTK03041, but maintained a similar binding affinity to FAP when compared to the monospecific FAP-targeted ligand, Ga-FAPI-04. However, the bispecific tracers have higher uptake in major organs (blood, muscle, bone, and heart) and decreased tumor uptake in the mouse models in

Table 4.4 Biodistribution (mean ± SD, n = 4) and uptake ratios of ^{68}Ga-labeled PSMA/FAP bispecific tracers, PSMA-617, and AV02070 in LNCaP tumor-bearing mice. The mice in the blocked group were co-injected with 2-PMPA (500 µg). The biodistribution data of [^{68}Ga]Ga-PSMA-617 have been reported previously by our group[123], and are included here for comparison.

Tissue (%ID/g)	[^{68}Ga]Ga-AV01084	[^{68}Ga]Ga-AV01088		[^{68}Ga]Ga-PSMA-617	[^{68}Ga]Ga-AV02070
	1 h	1 h	1 h_blocked	1 h	1 h
Blood	2.26 ± 0.49	2.18 ± 0.22	1.45 ± 0.53	0.63 ± 0.13	0.75 ± 0.21
Fat	1.44 ± 0.15	0.70 ± 0.36	0.29 ± 0.20	0.25 ± 0.13	0.17 ± 0.16
Testes	0.66 ± 0.06	0.40 ± 0.13	0.34 ± 0.10	0.26 ± 0.06	0.38 ± 0.40
Small intestine	0.63 ± 0.15	0.52 ± 0.06	0.44 ± 0.21	0.31 ± 0.15	0.54 ± 0.17
Stomach	0.23 ± 0.06	0.20 ± 0.02	0.18 ± 0.01	0.08 ± 0.01	0.11 ± 0.05
Spleen	4.35 ± 1.25	1.14 ± 0.16	0.40 ± 0.09	1.18 ± 0.37	0.25 ± 0.07
Liver	0.49 ± 0.01	0.49 ± 0.08	0.40 ± 0.13	0.62 ± 0.15	0.47 ± 0.08
Pancreas	0.99 ± 0.07	0.70 ± 0.04	0.48 ± 0.20	0.19 ± 0.01	0.31 ± 0.21
Adrenal glands	8.22 ± 0.90	2.10 ± 0.48	1.19 ± 0.40	1.20 ± 0.57	0.36 ± 0.17
Kidney	84.3 ± 8.82	28.6 ± 10.4	2.91 ± 0.90	29.2 ± 5.13	2.57 ± 0.58
Lungs	2.09 ± 1.39	0.94 ± 0.64	1.03 ± 0.42	1.03 ± 0.32	0.63 ± 0.22
Heart	0.85 ± 0.08	0.57 ± 0.03	0.40 ± 0.14	0.23 ± 0.04	0.22 ± 0.05
LNCaP tumor	9.05 ± 1.54	8.85 ± 1.25	2.95 ± 1.13	16.7 ± 2.30	0.74 ± 0.21
Muscle	1.00 ± 0.35	0.77 ± 0.27	0.39 ± 0.08	0.12 ± 0.02	0.31 ± 0.14
Bone	2.47 ± 0.22	2.47 ± 0.50	1.97 ± 1.15	0.23 ± 0.05	0.56 ± 0.28
Brain	0.11 ± 0.05	0.06 ± 0.02	0.03 ± 0.01	0.02 ± 0.00	0.03 ± 0.01
Tail	4.49 ± 2.83	3.57 ± 0.78	3.25 ± 2.60	0.52 ± 0.19	1.31 ± 0.58
Tumor/bone	3.70 ± 0.83	3.75 ± 1.28	1.78 ± 0.98	96.5 ± 47.6	1.63 ± 0.95
Tumor/muscle	9.57 ± 2.73	12.7 ± 5.32	7.25 ± 1.77	133 ± 19.5	2.76 ± 1.44
Tumor/blood	4.09 ± 0.77	4.10 ± 0.88	2.06 ± 0.34	27.7 ± 6.28	0.99 ± 0.12
Tumor/kidney	0.10 ± 0.02	0.34 ± 0.13	1.00 ± 0.12	0.63 ± 0.09	0.29 ± 0.08

Table 4.5 Biodistribution (mean ± SD, n = 4) and uptake ratios of ^{68}Ga-labeled PSMA/FAP bispecific tracers in HEK293T:hFAP tumor-bearing mice. The mice in the blocked group were co-injected with FAPI-04 (250 µg). The biodistribution data of [^{68}Ga]Ga-AV02070 have been reported previously by our group [143], and are included here for comparison.

Tissue (%ID/g)	[^{68}Ga]Ga-AV01084	[^{68}Ga]Ga-AV01088		[^{68}Ga]Ga-PSMA-617	[^{68}Ga]Ga-AV02070
	1 h	1 h	1 h_blocked	1 h	1 h
Blood	1.53 ± 0.03	0.79 ± 0.43	0.68 ± 0.25	0.28 ± 0.02	0.36 ± 0.05
Fat	0.78 ± 0.16	0.20 ± 0.05	0.19 ± 0.09	0.09 ± 0.04	0.44 ± 0.81
Testes	0.54 ± 0.05	0.22 ± 0.05	0.33 ± 0.15	0.15 ± 0.03	0.17 ± 0.07
Small Intestine	0.45 ± 0.06	0.20 ± 0.02	0.26 ± 0.07	0.14 ± 0.02	0.42 ± 0.13
Stomach	0.11 ± 0.02	0.08 ± 0.01	0.08 ± 0.03	0.07 ± 0.08	0.08 ± 0.04
Spleen	3.89 ± 1.38	0.81 ± 0.15	0.63 ± 0.28	0.55 ± 0.13	0.25 ± 0.12
Liver	0.46 ± 0.17	0.17 ± 0.01	0.26 ± 0.09	0.11 ± 0.01	0.39 ± 0.05
Pancreas	0.71 ± 0.05	0.31 ± 0.04	0.21 ± 0.07	0.11 ± 0.03	0.34 ± 0.45
Adrenal glands	3.10 ± 0.62	0.96 ± 0.53	0.44 ± 0.06	0.32 ± 0.22	0.22 ± 0.15
Kidney	56.4 ± 16.1	10.5 ± 4.20	8.18 ± 3.98	12.4 ± 3.24	1.85 ± 0.21
Lungs	1.60 ± 0.10	0.55 ± 0.05	0.76 ± 0.26	0.34 ± 0.05	0.34 ± 0.06
Heart	0.56 ± 0.03	0.26 ± 0.04	0.18 ± 0.04	0.10 ± 0.00	0.12 ± 0.03
HEK293T:hFAP tumor	1.90 ± 0.41	1.20 ± 0.25	0.51 ± 0.14	0.26 ± 0.01	7.93 ± 1.88
Muscle	0.85 ± 0.30	0.41 ± 0.03	0.16 ± 0.12	0.08 ± 0.01	0.19 ± 0.10
Bone	1.44 ± 0.21	0.88 ± 0.22	0.20 ± 0.06	0.09 ± 0.02	0.23 ± 0.06
Brain	0.05 ± 0.00	0.40 ± 0.74	0.02 ± 0.01	0.01 ± 0.00	0.02 ± 0.02
Tail	2.33 ± 1.25	1.53 ± 1.38	0.58 ± 0.13	0.35 ± 0.14	0.49 ± 0.04
Tumor/bone	1.02 ± 0.10	1.08 ± 0.31	2.58 ± 0.68	2.95 ± 0.55	34.3 ± 7.35
Tumor/muscle	1.88 ± 0.31	2.44 ± 1.08	4.07 ± 2.13	3.01 ± 0.66	45.7 ± 9.88
Tumor/blood	1.06 ± 0.21	2.26 ± 2.25	0.78 ± 0.09	0.94 ± 0.13	22.9 ± 10.1
Tumor/kidney	0.03 ± 0.02	0.15 ± 0.14	0.06 ± 0.01	0.02 ± 0.00	4.34 ± 1.36

comparison to the ^{68}Ga-labeled monospecific counterparts, [^{68}Ga]Ga-HTK03041 and [^{68}Ga]Ga-FAPI-04.

Therefore, in this report we selected the pharmacophores of [^{68}Ga]Ga-PSMA-617 (in brown, Figure 4.1) and [^{68}Ga]Ga-AV02070 (in blue, Figure 4.1) for the design of our PSMA/FAP bispecific tracers as they are more hydrophilic and have high affinity for PSMA and FAP, respectively. These two pharmacophores are separated by a Lys-Gly linker (Figure 4.1B). The PSMA-targeted pharmacophore (Lys(tranexamic acid-2-Nal)-urea-Glu and the linker (Lys-Gly) was constructed directly on solid phase using the commercially available amino acids. For AV01084, the pyridine-based FAP-targeted ligand and the DOTA chelator were coupled to the α-amino group and side-chain of Lys, respectively. While for AV01088, the DOTA chelator and the pyridine-based FAP-targeted ligand were coupled to the α-amino group and side-chain of Lys, respectively. This allows us to investigate the effect of the position of the DOTA chelator on binding affinity and biodistribution of the bispecific tracers.

The enzymatic assay (Figure 4.2B) confirmed that the FAP binding affinities of Ga-AV01084 (IC_{50} = 10.9 ± 0.67 nM) and Ga-AV01088 (IC_{50} = and 16.7 ± 1.53 nM) were comparable, even slightly better than that of Ga-AV02070 (IC_{50} = 17.1 ± 4.60 nM). To investigate if the PSMA-targeted pharmacophore has any effect on the overall FAP binding of our bispecific ligands, we also measured the FAP binding affinity of Ga-PSMA-617. The very weak binding affinity of Ga-PSMA-617 (IC_{50} > 1,000 nM) suggests that the potent FAP binding affinity of our bispecific ligands is contributed mainly by the AV02070 pharmacophore.

Despite having a lower uptake in the LNCaP tumor compared to [^{68}Ga]Ga-PSMA-617 (16.71 ± 2.30 %ID/g), [^{68}Ga]Ga-AV01084 and [^{68}Ga]Ga-AV01088 (9.05 ± 1.54 and 8.85 ± 1.25

%ID/g, respectively) has better tumor uptake than our previously reported three bispecific PSMA/FAP tracers ([^{68}Ga]Ga-AV01017, [^{68}Ga]Ga-AV01030 and [^{68}Ga]AV01038) (4.25 – 5.17 %ID/g) [141]. Moreover, co-injection of [^{68}Ga]Ga-AV01088 with 2-PMPA decreased the tumor uptake by 67%, indicating that the tumor uptake is specific to PSMA. Moreover, we also observed a significant bone uptake (1.97 ± 1.15 %ID/g) when [^{68}Ga]Ga-AV01088 was co-injected with 2-PMPA, whereas there was a decreased bone uptake to background level (0.20 ± 0.06 %ID/g) when [^{68}Ga]Ga-AV01088 was co-injected with FAPI-04. This indicates that the bone uptake of [^{68}Ga]Ga-AV01088 might be due to specific binding of the FAP-targeted pharmacophore. Uptake of [^{68}Ga]Ga-AV01088 to both LNCaP and HEK293T:hFAP tumor are PSMA- and FAP-mediated, respectively, as demonstrated by the significantly decreased tumor uptake obtained when co-injected with blocking agents.

Unlike the improved uptake in LNCaP tumor xenografts, the uptake of [^{68}Ga]Ga-AV01084 and [^{68}Ga]Ga-AV01088 (1.20-1.90 %ID/g) in HEK293T:hFAP tumor xenografts remains significantly lower than that of the monospecific counterpart, [^{68}Ga]Ga-AV02070 (7.93 ± 1.88 %ID/g, $P < 0.05$). One possible reason is the addition of the succinic acid linker, which might have interfered with the binding of our tracers to FAP, thus decreasing the tumor uptake. Piperazine-based linkers have been shown to be important for maintaining good tumor uptake of FAP-targeted tracers [137]. Therefore, incorporating a piperazine-based linker can also be considered for future modification to improve uptake of PSMA/FAP bispecific tracers to the FAP-expressing tumors.

Compared to the monospecific tracers, the bispecific tracers have higher blood, bone, and muscle uptake. However, the current modified tracers have significantly decreased blood retention (0.79-2.26 %ID/g) when compared to the PSMA/FAP bispecific tracers in our previous report (5.75-11.94 %ID/g) [141]. This leads to better tumor-to-blood contrast ratios for [^{68}Ga]Ga-AV01084

(4.09 ± 0.77) and [^{68}Ga]Ga-AV01088 (4.10 ± 0.88). The decreased blood retention might be contributed by increased hydrophilicity of the new bispecific tracers shown by their low $LogD_{7.4}$ values (< -3.60). This is consistent with previous findings that more hydrophilic radiotracers will have faster pharmacokinetics and clearance, hence, have better tumor-to-background contrast ratio [145]. In addition, there are no significant differences in the tumor uptake or the tumor-to-background contrast ratios between [^{68}Ga]Ga-AV01084 and [^{68}Ga]Ga-AV01088, which indicates that the position of the DOTA chelator to the lysine linker does not have a crucial effect on the pharmacokinetics of the tracers.

Previously, Wang et al. [146] reported a ^{68}Ga-labeled PSMA/FAP bispecific tracer, [^{68}Ga]Ga-FAPI-PSMA (Figure 4.7), consisting of a PSMA-targeted pharmacophore from PSMA-617 (in brown, Figure 4.7) and a FAP-targeted pharmacophore from FAPI-04 (in blue). It would be difficult to directly compare the performance of our bispecific radiotracers with [^{68}Ga]Ga-FAPI-PSMA as different tumor models were used for evaluation: PSMA-expressing LNCaP tumors and FAP-expressing HEK293T:hFAP tumors used in this report; PSMA-expressing 22Rv1 tumors and FAP-expressing U87 MG tumors used by Wang et al. [146]. [^{68}Ga]Ga-FAPI-PSMA was shown to have better tumor uptake (SUVmax = 1.32 and 1.67 for 22Rv1 and U87 MG tumors, respectively) compared to the monospecific tracers, [^{68}Ga]Ga-PSMA-617 (SUVmax = 0.25 for 22Rv1 tumors) and [^{68}Ga]Ga-FAPI-04 (SUVmax = 0.45 for U87 MG tumors). This demonstrates the potential of utilizing PSMA/FAP bispecific tracers to improve the tumor uptake. However, similar to our results, [^{68}Ga]Ga-FAPI-PSMA also had higher background uptake compared to the monospecific tracers.

Replacing the quinoline-based FAP-targeted pharmacophore with a pyridine-based FAP-targeted pharmacophore helps decrease the background uptake (blood, bone, and muscle) of the

bispecific tracers, however it also results in a significantly lower uptake in HEK293T:hFAP tumors. Therefore, future attempts on the use of a pyridine-based FAP-targeted pharmacophore for the design of PSMA/FAP bispecific tracers need to include optimization of linkers such as the use of a piperazine-based linker to further improve FAP binding affinity and tumor uptake.

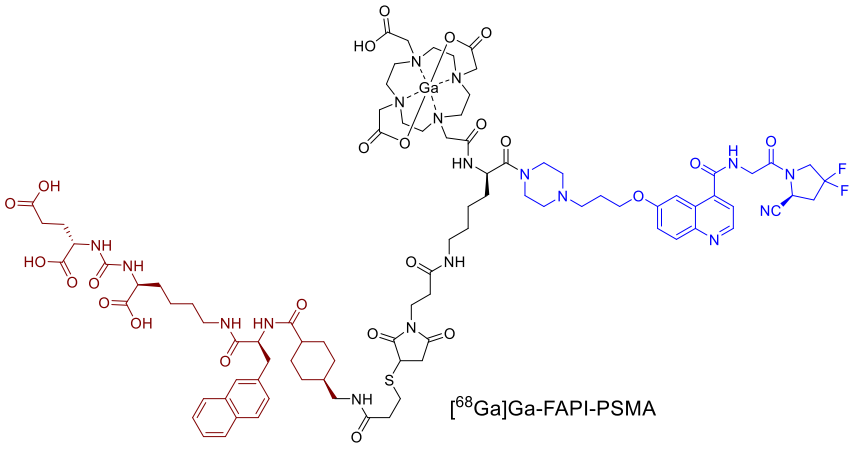

Figure 4.7 Chemical structure of [^{68}Ga]Ga-FAPI-PSMA[146]. The PSMA- and FAP- targeting pharmacophores are shown in brown and blue, respectively.

4.5 Conclusion

Two novel ^{68}Ga-labeled PSMA/FAP bispecific tracers were designed, synthesized, and confirmed to have the ability to bind both PSMA and FAP *in vitro* and *in vivo*. Compared with the monospecific tracers, the bispecific tracers have decreased binding affinities towards PSMA, but retain comparable binding affinities towards FAP. Compared with the three previously reported PSMA/FAP bispecific tracers in chapter 2 ([^{68}Ga]Ga-AV01017, [^{68}Ga]Ga-AV01030, and [^{68}Ga]Ga-AV01038), both [^{68}Ga]Ga-AV01084 and Ga-AV01088 have better PSMA binding affinity, and improved tumor uptake in PSMA-expressing xenografts and tumor-to-background (blood, muscle, and bone) contrast ratios. Further optimization on the selection of linkers should be explored to improve the binding affinity, pharmacokinetics, and tumor uptake of the PSMA/FAP bispecific tracers.

Chapter 5 : Conclusions

5.1 Summary of Findings, Future Directions, and Significance

The research conducted in this thesis is a study to examine the potential of bispecific PSMA/FAP-targeting radiotracers for prostate cancer imaging in comparison with the monospecific PSMA- and FAP-targeted radiotracers. In Chapter 2, we synthesized three bispecific PSMA/FAP-targeted radiotracers, [^{68}Ga]Ga-AV01017, [^{68}Ga]Ga-AV01030 and [^{68}Ga]Ga-AV01038 containing the PSMA pharmacophore of HTK03041[122] and FAP pharmacophore of FAPI-04 with varying linkers' lengths. From this investigation, we found that our bispecific compounds have a significantly higher blood uptake compared to the monospecific tracers, resulting in a lower tumor uptake, higher background uptake, and lower tumor-to-background ratios in both LNCaP and HEK293T:hFAP tumor model. Moreover, when comparing the three tracers, we found that the compound with longest linker has the lowest tumor uptake. We suspected that this phenomenon might be caused by the interaction between the aromatic rings on both pharmacophores and the high lipophilic nature of the compounds. Overall, from this research, we have shown that we have successfully synthesized and evaluated novel bispecific PSMA/FAP-targeted radiotracers. However, pharmacophore and linker modification are still needed to keep improving the binding affinity and tumor uptake. To solve the issue mentioned above, we decided to (1) replace Ala(9-Anth) in the PSMA-targeting pharmacophore with 2-Nal, (2) replace the quinoline motif in the FAP-targeting pharmacophore with a more hydrophilic pyridine motif, and (3) use of less lipophilic linkers.

Since there are not many pyridine-based FAPI tracers that have been developed or published, we decided to develop novel FAP-targeted radiotracers containing a pyridine-based pharmacophore, which is described in Chapter 3. We designed, synthesized, and evaluated two

pyridine-based FAP-targeted tracers, [^{68}Ga]Ga-AV02053 and [^{68}Ga]Ga-AV02070, which are based on the 4,4-difluoro-2-cyanopyrrolidine pharmacophore with linkers mimicking the hydrazine group in [^{99m}Tc]Tc-iFAP[140]. Despite lower FAP binding affinity and tumor uptake when compared with [^{68}Ga]Ga-FAPI-04, the pyridine-based FAP-targeted tracers have much lower background (blood, muscle, and bone) uptake which results in a significantly higher tumor-to-background uptake ratio. The co-injection with the blocking agent, FAPI-04, also decreased their tumor uptake by >95%, but not the background uptake, indicating that they bind specifically to FAP. [^{68}Ga]Ga-AV02070 derived from the pharmacophore with the carbonyl group at the para-position to the pyridine nitrogen, has better tumor uptake and tumor-to-background contrast ratio than [^{68}Ga]Ga-AV02053, making this pharmacophore a promising candidate for the design of FAP-targeted tracers and to be incorporated to the bispecific PSMA/FAP-targeted radiotracers.

Finally, in Chapter 4, we designed 2 novel bispecific PSMA/FAP-targeted radiotracers, [^{68}Ga]Ga-AV01084 and [^{68}Ga]Ga-AV02088 containing the PSMA pharmacophore of PSMA-617 and FAP pharmacophore of the pyridine-based FAP tracer we developed, AV02070. We found that this modification improved the binding affinity to PSMA compared to the first modification reported in Chapter 2, and maintained comparable binding affinity to FAP. Moreover, although still lower in comparison to the monospecific PSMA-targeted tracer, [^{68}Ga]Ga-PSMA-617, both [^{68}Ga]Ga-AV01084 and [^{68}Ga]Ga-AV02088 have significantly better tumor uptake and tumor-to-background ratio compared to the three tracers reported in Chapter 2. However, there is no improvement on the uptake in HEK293T:hFAP tumor model.

There were some limitations in this study: First, we did not perform tests to examine the potential interaction between the pharmacophores which might plays a role in decreasing the tumor uptake. For future research, we would suggest using a molecular docking software to help predict

the intramolecule interactions when designing the new bispecific tracers, so that we can save more time and resources in developing more potential candidates. Second, evaluation by imaging and/or biodistribution studies in tumor bearing mice as in this report is a common practice in the development of radiopharmaceuticals. However, the obtained high tumor-to-background contrast either from imaging or biodistribution data might not be observed in the clinic. In addition, the tumor xenografts used in the imaging and biodistribution studies are often derived from (genetically-modified) cancer cell lines overexpressing the targeted cancer markers, which might not be representative of cancer lesions encountered in the clinic.

For future research, more pharmacophore or linker selections can be explored to improve the uptake in FAP-expressing tumor xenografts. Some modifications that can be considered are (1) incorporating piperazine-based linkers which have been shown to be important for maintaining good tumor uptake of FAP-targeting tracers; (2) Incorporating different linkers that have been previously used for the design of bispecific radiotracers that showed good tumor uptake and binding affinity[119–121]. To minimize the number of mice used, we could construct and use PSMA/FAP-expressing cell line and tumor xenograft. The development of this cell line is under way in our lab.

Overall, this thesis shed light on of the process and feasibility of developing novel bispecific PSMA/FAP-targeted radiotracers. Our data shows that the bispecific PSMA/FAP-targeted tracers were able to bind to both target, PSMA and FAP. Moreover, modifying the pharmacophore and linker selection is found to have an effect on the tumor and background uptake in vivo, with more hydrophilic linkers and pharmacophores leading to better imaging results. The findings reported in this thesis can build a foundation and give more understanding on parameters to be considered in designing bispecific PSMA/FAP-targeted tracers.

5.2 Concluding Remarks

In this thesis, we hypothesized that the bispecific PSMA/FAP radiotracers can bind to both PSMA and FAP, and will have comparable or even higher binding affinity and tumor uptake than the respective monospecific radiotracers. From the data, we found that this hypothesis is partially acceptable. The binding affinity data and biodistribution data show that the bispecific PSMA/FAP radiotracers have specific binding to both targets. However, when compared to the monospecific tracers, our bispecific compounds have lower binding affinity to PSMA, and comparable binding affinity to FAP. Moreover, our bispecific compounds have significantly lower tumor uptake in PSMA- and FAP-expressing tumors and lower tumor-to-background contrast ratio. We suspected that this lower tumor uptake may be caused by longer blood retention due to the interaction between both pharmacophores and lower hydrophilicity of the bispecific compounds. Furthermore, we successfully improved the binding affinity to PSMA, tumor uptake in PSMA-expressing tumor, and tumor-to-background contrast ratio of the PSMA/FAP bispecific tracers by increasing the hydrophilicity through changing the pharmacophores and linkers, shown in chapter 4.

Although we have not achieved our goal in designing a bispecific PSMA/FAP radiotracer with comparable or even higher tumor uptake compared to the monospecific radiotracers, we successfully achieved all of our aims. The first aim is to design, synthesize, and evaluate novel bispecific PSMA/FAP radiotracers for prostate cancer imaging. We successfully designed 5 novel PSMA/FAP radiotracers and evaluated them in vitro and in vivo. We also completed the second aim by comparing the binding affinity, tumor uptake, and biodistribution of the bispecific radiotracers with the respective monospecific radiotracers. In addition, we successfully synthesized and demonstrated the potential of pyridine-based FAPI tracers in Chapter 3, which

opens a new path for FAP-targeted radiotracer development. Further research is required to keep improving the binding affinity, tumor uptake, and tumor-to-background uptake ratios of the bispecific PSMA/FAP radiotracers by considering the pharmacophore selection, linker's length and selection, and hydrophilicity of the compounds.

Bibliography

1. Tafti D, Banks KP. Nuclear Medicine Physics. In: *StatPearls*. StatPearls Publishing; 2023. Accessed June 2, 2023. http://www.ncbi.nlm.nih.gov/books/NBK568731/

2. Chen ZY, Wang YX, Lin Y, et al. Advance of Molecular Imaging Technology and Targeted Imaging Agent in Imaging and Therapy. *BioMed Res Int*. 2014;2014:819324. doi:10.1155/2014/819324

3. Pysz MA, Gambhir SS, Willmann JK. Molecular Imaging: Current Status and Emerging Strategies. *Clin Radiol*. 2010;65(7):500-516. doi:10.1016/j.crad.2010.03.011

4. Vermeulen K, Vandamme M, Bormans G, Cleeren F. Design and Challenges of Radiopharmaceuticals. *Semin Nucl Med*. 2019;49(5):339-356. doi:10.1053/j.semnuclmed.2019.07.001

5. Weissleder R, Pittet MJ. Imaging in the era of molecular oncology. *Nature*. 2008;452(7187):580-589. doi:10.1038/nature06917

6. Lu FM, Yuan Z. PET/SPECT molecular imaging in clinical neuroscience: recent advances in the investigation of CNS diseases. *Quant Imaging Med Surg*. 2015;5(3):433-447. doi:10.3978/j.issn.2223-4292.2015.03.16

7. Hwang BH, Kim MH, Chang K. Molecular Imaging of High-Risk Atherosclerotic Plaques: Is It Clinically Translatable? *Korean Circ J*. 2011;41(9):497. doi:10.4070/kcj.2011.41.9.497

8. Čolović M. *Radiofluorinated Amino Acids for Oncological Positron Emission Tomography Imaging*. University of British Columbia; 2019. doi:10.14288/1.0387567

9. Rahmim A, Zaidi H. PET versus SPECT: strengths, limitations and challenges. *Nucl Med Commun*. 2008;29(3):193-207. doi:10.1097/MNM.0b013e3282f3a515

10. Langer A. A systematic review of PET and PET/CT in oncology: A way to personalize cancer treatment in a cost-effective manner? *BMC Health Serv Res*. 2010;10:283. doi:10.1186/1472-6963-10-283

11. Buck AK, Herrmann K, Stargardt T, Dechow T, Krause BJ, Schreyögg J. Economic Evaluation of PET and PET/CT in Oncology: Evidence and Methodologic Approaches. *J Nucl Med*. 2010;51(3):401-412. doi:10.2967/jnumed.108.059584

12. Gallamini A, Zwarthoed C, Borra A. Positron Emission Tomography (PET) in Oncology. *Cancers*. 2014;6(4):1821-1889. doi:10.3390/cancers6041821

13. Farwell MD, Pryma DA, Mankoff DA. PET/CT imaging in cancer: Current applications and future directions. *Cancer*. 2014;120(22):3433-3445. doi:10.1002/cncr.28860

14. Basu S, Kwee TC, Surti S, Akin EA, Yoo D, Alavi A. Fundamentals of PET and PET/CT imaging. *Ann N Y Acad Sci*. 2011;1228(1):1-18. doi:10.1111/j.1749-6632.2011.06077.x

15. Vaquero JJ, Kinahan P. Positron Emission Tomography: Current Challenges and Opportunities for Technological Advances in Clinical and Preclinical Imaging Systems. *Annu Rev Biomed Eng*. 2015;17:385-414. doi:10.1146/annurev-bioeng-071114-040723

16. Franquet E, Park H. Molecular imaging in oncology: Common PET/CT radiopharmaceuticals and applications. *Eur J Radiol Open*. 2022;9:100455. doi:10.1016/j.ejro.2022.100455

17. Roh JL, Yeo NK, Kim JS, et al. Utility of 2-[18F] fluoro-2-deoxy-D-glucose positron emission tomography and positron emission tomography/computed tomography imaging in the preoperative staging of head and neck squamous cell carcinoma. *Oral Oncol*. 2007;43(9):887-893. doi:10.1016/j.oraloncology.2006.10.011

18. Ng SH, Yen TC, Chang JTC, et al. Prospective study of [18F]fluorodeoxyglucose positron emission tomography and computed tomography and magnetic resonance imaging in oral cavity squamous cell carcinoma with palpably negative neck. *J Clin Oncol Off J Am Soc Clin Oncol*. 2006;24(27):4371-4376. doi:10.1200/JCO.2006.05.7349

19. Li J, Xiao Y. Application of FDG-PET/CT in Radiation Oncology. *Front Oncol*. 2013;3:80. doi:10.3389/fonc.2013.00080

20. Rahman WT, Wale DJ, Viglianti BL, et al. The impact of infection and inflammation in oncologic 18F-FDG PET/CT imaging. *Biomed Pharmacother Biomedecine Pharmacother*. 2019;117:109168. doi:10.1016/j.biopha.2019.109168

21. Jacobson O, Weiss ID, Szajek L, Farber JM, Kiesewetter DO. 64Cu-AMD3100—A novel imaging agent for targeting chemokine receptor CXCR4. *Bioorg Med Chem*. 2009;17(4):1486-1493. doi:10.1016/j.bmc.2009.01.014

22. Lindner T, Loktev A, Altmann A, et al. Development of Quinoline-Based Theranostic Ligands for the Targeting of Fibroblast Activation Protein. *J Nucl Med*. 2018;59(9):1415-1422. doi:10.2967/jnumed.118.210443

23. Hennrich U, Eder M. [68Ga]Ga-PSMA-11: The First FDA-Approved 68Ga-Radiopharmaceutical for PET Imaging of Prostate Cancer. *Pharmaceuticals*. 2021;14(8):713. doi:10.3390/ph14080713

24. Gleason GI. A positron cow. *Int J Appl Radiat Isot*. 1960;8(2):90-94. doi:10.1016/0020-708X(60)90052-1

25. Martiniova L, Palatis LD, Etchebehere E, Ravizzini G. Gallium-68 in Medical Imaging. *Curr Radiopharm*. 9(3):187-207.

26. Braune A, Oehme L, Freudenberg R, et al. Comparison of image quality and spatial resolution between 18F, 68Ga, and 64Cu phantom measurements using a digital Biograph Vision PET/CT. *EJNMMI Phys*. 2022;9(1):58. doi:10.1186/s40658-022-00487-7

27. Marganiec-Gałązka J, Nähle OJ, Kossert K. Activity determination of 68Ge/68Ga by means of 4πβ(Č)-γ coincidence counting. *Appl Radiat Isot*. 2018;134:240-244. doi:10.1016/j.apradiso.2017.06.027

28. Wadas TJ, Wong EH, Weisman GR, Anderson CJ. Coordinating Radiometals of Copper, Gallium, Indium, Yttrium and Zirconium for PET and SPECT Imaging of Disease. *Chem Rev*. 2010;110(5):2858-2902. doi:10.1021/cr900325h

29. Benešová M, Schäfer M, Bauder-Wüst U, et al. Preclinical Evaluation of a Tailor-Made DOTA-Conjugated PSMA Inhibitor with Optimized Linker Moiety for Imaging and Endoradiotherapy of Prostate Cancer. *J Nucl Med Off Publ Soc Nucl Med*. 2015;56(6):914-920. doi:10.2967/jnumed.114.147413

30. Yandrapalli S, Puckett Y. SPECT Imaging. In: *StatPearls*. StatPearls Publishing; 2023. Accessed July 18, 2023. http://www.ncbi.nlm.nih.gov/books/NBK564426/

31. Sarikaya I, Povoski SP, Al-Saif OH, et al. Combined use of preoperative 18F FDG-PET imaging and intraoperative gamma probe detection for accurate assessment of tumor recurrence in patients with colorectal cancer. *World J Surg Oncol*. 2007;5:80. doi:10.1186/1477-7819-5-80

32. Berrocal J, Saperstein L, Grube B, et al. Intraoperative Injection of Technetium-99m Sulfur Colloid for Sentinel Lymph Node Biopsy in Breast Cancer Patients: A Single Institution Experience. *Surg Res Pract*. 2017;2017:5924802. doi:10.1155/2017/5924802

33. Sartor O, de Bono J, Chi KN, et al. Lutetium-177–PSMA-617 for Metastatic Castration-Resistant Prostate Cancer. *N Engl J Med*. 2021;385(12):1091-1103. doi:10.1056/NEJMoa2107322

34. Huizing FJ, Garousi J, Lok J, et al. CAIX-targeting radiotracers for hypoxia imaging in head and neck cancer models. *Sci Rep*. 2019;9:18898. doi:10.1038/s41598-019-54824-5

35. Chen Y, Pullambhatla M, Foss CA, et al. 2-(3-{1-Carboxy-5-[(6-[18F]Fluoro-Pyridine-3-Carbonyl)-Amino]-Pentyl}-Ureido)-Pentanedioic Acid, [18F]DCFPyL, a PSMA-Based PET Imaging Agent for Prostate Cancer. *Clin Cancer Res*. 2011;17(24):7645-7653. doi:10.1158/1078-0432.CCR-11-1357

36. Salih S, Elliyanti A, Alkatheeri A, AlYafei F, Almarri B, Khan H. The Role of Molecular Imaging in Personalized Medicine. *J Pers Med*. 2023;13(2):369. doi:10.3390/jpm13020369

37. Srivastava SC. Paving the Way to Personalized Medicine: Production of Some Promising Theragnostic Radionuclides at Brookhaven National Laboratory. *Semin Nucl Med*. 2012;42(3):151-163. doi:10.1053/j.semnuclmed.2011.12.004

38. Mandrekar SJ, Sargent DJ. Predictive biomarker validation in practice: lessons from real trials. *Clin Trials Lond Engl*. 2010;7(5):567-573. doi:10.1177/1740774510368574

39. Bussink J, Kaanders JHAM, van der Graaf WTA, Oyen WJG. PET-CT for radiotherapy treatment planning and response monitoring in solid tumors. *Nat Rev Clin Oncol*. 2011;8(4):233-242. doi:10.1038/nrclinonc.2010.218

40. Beylergil V, Morris PG, Smith-Jones PM, et al. Pilot study of 68Ga-DOTA-F(ab′)2-trastuzumab in patients with breast cancer. *Nucl Med Commun*. 2013;34(12):1157-1165. doi:10.1097/MNM.0b013e328365d99b

41. Gebhart G, Lamberts LE, Wimana Z, et al. Molecular imaging as a tool to investigate heterogeneity of advanced HER2-positive breast cancer and to predict patient outcome under trastuzumab emtansine (T-DM1): the ZEPHIR trial. *Ann Oncol Off J Eur Soc Med Oncol*. 2016;27(4):619-624. doi:10.1093/annonc/mdv577

42. Sharma R, Aboagye E. Development of radiotracers for oncology – the interface with pharmacology. *Br J Pharmacol*. 2011;163(8):1565-1585. doi:10.1111/j.1476-5381.2010.01160.x

43. Eder M, Schäfer M, Bauder-Wüst U, et al. 68Ga-complex lipophilicity and the targeting property of a urea-based PSMA inhibitor for PET imaging. *Bioconjug Chem*. 2012;23(4):688-697. doi:10.1021/bc200279b

44. Bottoni G, Fiz F, Puntoni M, et al. Diagnostic effectiveness of [18F]Fluoroestradiol PET/CT in oestrogen receptor-positive breast cancer: the key role of histopathology. Evidence from an international multicentre prospective study. *Eur J Nucl Med Mol Imaging*. 2023;50(8):2477-2485. doi:10.1007/s00259-023-06173-9

45. Treglia G, Sadeghi R, Del Sole A, Giovanella L. Diagnostic performance of PET/CT with tracers other than F-18-FDG in oncology: an evidence-based review. *Clin Transl Oncol Off Publ Fed Span Oncol Soc Natl Cancer Inst Mex*. 2014;16(9):770-775. doi:10.1007/s12094-014-1168-8

46. Mannweiler S, Amersdorfer P, Trajanoski S, Terrett JA, King D, Mehes G. Heterogeneity of Prostate-Specific Membrane Antigen (PSMA) Expression in Prostate Carcinoma with Distant Metastasis. *Pathol Oncol Res*. 2009;15(2):167-172. doi:10.1007/s12253-008-9104-2

47. Isik EG, Has-Simsek D, Sanli O, Sanli Y, Kuyumcu S. Fibroblast Activation Protein–Targeted PET Imaging of Metastatic Castration-Resistant Prostate Cancer Compared With 68Ga-PSMA and 18F-FDG PET/CT. *Clin Nucl Med*. 2022;47(1):e54. doi:10.1097/RLU.0000000000003837

48. Lundmark F, Abouzayed A, Mitran B, et al. Heterodimeric Radiotracer Targeting PSMA and GRPR for Imaging of Prostate Cancer-Optimization of the Affinity towards PSMA by Linker Modification in Murine Model. *Pharmaceutics*. 2020;12(7):614. doi:10.3390/pharmaceutics12070614

49. Li ZB, Wu Z, Chen K, Ryu EK, Chen X. 18F-labeled BBN-RGD heterodimer for prostate cancer imaging. *J Nucl Med Off Publ Soc Nucl Med*. 2008;49(3):453-461. doi:10.2967/jnumed.107.048009

50. Sung H, Ferlay J, Siegel RL, et al. Global Cancer Statistics 2020: GLOBOCAN Estimates of Incidence and Mortality Worldwide for 36 Cancers in 185 Countries. *CA Cancer J Clin*. 2021;71(3):209-249. doi:10.3322/caac.21660

51. Siegel RL, Miller KD, Wagle NS, Jemal A. Cancer statistics, 2023. *CA Cancer J Clin*. 2023;73(1):17-48. doi:10.3322/caac.21763

52. Hoogendam A, Buntinx F, de Vet HC. The diagnostic value of digital rectal examination in primary care screening for prostate cancer: a meta-analysis. *Fam Pract*. 1999;16(6):621-626. doi:10.1093/fampra/16.6.621

53. Lau J, Rousseau E, Zhang Z, et al. Positron Emission Tomography Imaging of the Gastrin-Releasing Peptide Receptor with a Novel Bombesin Analogue. *ACS Omega*. 2019;4(1):1470-1478. doi:10.1021/acsomega.8b03293

54. Mottet N, Bellmunt J, Bolla M, et al. EAU-ESTRO-SIOG Guidelines on Prostate Cancer. Part 1: Screening, Diagnosis, and Local Treatment with Curative Intent. *Eur Urol*. 2017;71(4):618-629. doi:10.1016/j.eururo.2016.08.003

55. Han S, Woo S, Kim YJ, Suh CH. Impact of 68Ga-PSMA PET on the Management of Patients with Prostate Cancer: A Systematic Review and Meta-analysis. *Eur Urol*. 2018;74(2):179-190. doi:10.1016/j.eururo.2018.03.030

56. Zhou C, Tang Y, Deng Z, et al. Comparison of 68Ga-PSMA PET/CT and multiparametric MRI for the detection of low- and intermediate-risk prostate cancer. *EJNMMI Res*. 2022;12(1):10. doi:10.1186/s13550-022-00881-3

57. Zhou J, Gou Z, Wu R, Yuan Y, Yu G, Zhao Y. Comparison of PSMA-PET/CT, choline-PET/CT, NaF-PET/CT, MRI, and bone scintigraphy in the diagnosis of bone metastases in patients with prostate cancer: a systematic review and meta-analysis. *Skeletal Radiol*. 2019;48(12):1915-1924. doi:10.1007/s00256-019-03230-z

58. Regula N, Kostaras V, Johansson S, et al. Comparison of 68Ga-PSMA PET/CT with fluoride PET/CT for detection of bone metastatic disease in prostate cancer. *Eur J Hybrid Imaging*. 2022;6(1):5. doi:10.1186/s41824-022-00127-4

59. Carter RE, Feldman AR, Coyle JT. Prostate-specific membrane antigen is a hydrolase with substrate and pharmacologic characteristics of a neuropeptidase. *Proc Natl Acad Sci U S A*. 1996;93(2):749-753.

60. Tiffany CW, Lapidus RG, Merion A, Calvin DC, Slusher BS. Characterization of the enzymatic activity of PSM: Comparison with brain NAALADase. *The Prostate*. 1999;39(1):28-35. doi:10.1002/(SICI)1097-0045(19990401)39:1<28::AID-PROS5>3.0.CO;2-A

61. Pinto JT, Suffoletto BP, Berzin TM, et al. Prostate-specific membrane antigen: a novel folate hydrolase in human prostatic carcinoma cells. *Clin Cancer Res Off J Am Assoc Cancer Res*. 1996;2(9):1445-1451.

62. Silver DA, Pellicer I, Fair WR, Heston WD, Cordon-Cardo C. Prostate-specific membrane antigen expression in normal and malignant human tissues. *Clin Cancer Res Off J Am Assoc Cancer Res*. 1997;3(1):81-85.

63. Spatz S, Tolkach Y, Jung K, et al. Comprehensive Evaluation of Prostate Specific Membrane Antigen Expression in the Vasculature of Renal Tumors: Implications for Imaging Studies and Prognostic Role. *J Urol*. 2018;199(2):370-377. doi:10.1016/j.juro.2017.08.079

64. Wernicke AG, Varma S, Greenwood EA, et al. Prostate-specific membrane antigen expression in tumor-associated vasculature of breast cancers. *APMIS Acta Pathol Microbiol Immunol Scand*. 2014;122(6):482-489. doi:10.1111/apm.12195

65. Wright GL, Haley C, Beckett ML, Schellhammer PF. Expression of prostate-specific membrane antigen in normal, benign, and malignant prostate tissues. *Urol Oncol*. 1995;1(1):18-28. doi:10.1016/1078-1439(95)00002-y

66. Ross JS, Sheehan CE, Fisher HAG, et al. Correlation of primary tumor prostate-specific membrane antigen expression with disease recurrence in prostate cancer. *Clin Cancer Res Off J Am Assoc Cancer Res*. 2003;9(17):6357-6362.

67. Yao V, Berkman CE, Choi JK, O'Keefe DS, Bacich DJ. Expression of prostate-specific membrane antigen (PSMA), increases cell folate uptake and proliferation and suggests a novel role for PSMA in the uptake of the non-polyglutamated folate, folic acid. *The Prostate*. 2010;70(3):305-316. doi:10.1002/pros.21065

68. Kaittanis C, Andreou C, Hieronymus H, et al. Prostate-specific membrane antigen cleavage of vitamin B9 stimulates oncogenic signaling through metabotropic glutamate receptors. *J Exp Med*. 2017;215(1):159-175. doi:10.1084/jem.20171052

69. Gordon IO, Tretiakova MS, Noffsinger AE, Hart J, Reuter VE, Al-Ahmadie HA. Prostate-specific membrane antigen expression in regeneration and repair. *Mod Pathol Off J U S Can Acad Pathol Inc*. 2008;21(12):1421-1427. doi:10.1038/modpathol.2008.143

70. Sodee DB, Malguria N, Faulhaber P, Resnick MI, Albert J, Bakale G. Multicenter ProstaScint imaging findings in 2154 patients with prostate cancer11A complete list of the ProstaScint Imaging Centers is provided in the Appendix. *Urology*. 2000;56(6):988-993. doi:10.1016/S0090-4295(00)00824-4

71. Liu H, Moy P, Kim S, et al. Monoclonal Antibodies to the Extracellular Domain of Prostate-specific Membrane Antigen Also React with Tumor Vascular Endothelium1. *Cancer Res*. 1997;57(17):3629-3634.

72. Taneja SS. ProstaScint® Scan: Contemporary Use in Clinical Practice. *Rev Urol*. 2004;6(Suppl 10):S19-S28.

73. Wurzer A, Parzinger M, Konrad M, et al. Preclinical comparison of four [18F, natGa]rhPSMA-7 isomers: influence of the stereoconfiguration on pharmacokinetics. *EJNMMI Res*. 2020;10:149. doi:10.1186/s13550-020-00740-z

74. Langbein T, Wang H, Rauscher I, et al. Utility of 18F-rhPSMA-7.3 positron emission tomography for imaging of primary prostate cancer and pre-operative efficacy in N-staging of unfavorable intermediate to very high-risk patients validated by histopathology. *J Nucl Med*. Published online January 1, 2022. doi:10.2967/jnumed.121.263440

75. Chen Y, Foss CA, Byun Y, et al. Radiohalogenated prostate-specific membrane antigen (PSMA)-based ureas as imaging agents for prostate cancer. *J Med Chem*. 2008;51(24):7933-7943. doi:10.1021/jm801055h

76. Hillier SM, Maresca KP, Femia FJ, et al. Preclinical Evaluation of Novel Glutamate-Urea-Lysine Analogues That Target Prostate-Specific Membrane Antigen as Molecular Imaging Pharmaceuticals for Prostate Cancer. *Cancer Res*. 2009;69(17):6932-6940. doi:10.1158/0008-5472.CAN-09-1682

77. Benešová M, Bauder-Wüst U, Schäfer M, et al. Linker Modification Strategies To Control the Prostate-Specific Membrane Antigen (PSMA)-Targeting and Pharmacokinetic Properties of DOTA-Conjugated PSMA Inhibitors. *J Med Chem*. 2016;59(5):1761-1775. doi:10.1021/acs.jmedchem.5b01210

78. Bu T, Zhang L, Yu F, et al. 177Lu-PSMA-I&T Radioligand Therapy for Treating Metastatic Castration-Resistant Prostate Cancer: A Single-Centre Study in East Asians. *Front Oncol*. 2022;12. Accessed July 17, 2023. https://www.frontiersin.org/articles/10.3389/fonc.2022.835956

79. Cardinale J, Schäfer M, Benešová M, et al. Preclinical Evaluation of 18F-PSMA-1007, a New Prostate-Specific Membrane Antigen Ligand for Prostate Cancer Imaging. *J Nucl Med Off Publ Soc Nucl Med*. 2017;58(3):425-431. doi:10.2967/jnumed.116.181768

80. Ceci F, Castellucci P, Graziani T, et al. 68Ga-PSMA-11 PET/CT in recurrent prostate cancer: efficacy in different clinical stages of PSA failure after radical therapy. *Eur J Nucl Med Mol Imaging*. 2019;46(1):31-39. doi:10.1007/s00259-018-4189-7

81. Zacherl MJ, Gildehaus FJ, Mittlmeier L, et al. First Clinical Results for PSMA-Targeted α-Therapy Using 225Ac-PSMA-I&T in Advanced-mCRPC Patients. *J Nucl Med Off Publ Soc Nucl Med*. 2021;62(5):669-674. doi:10.2967/jnumed.120.251017

82. Paschalis A, Sheehan B, Riisnaes R, et al. Prostate-specific Membrane Antigen Heterogeneity and DNA Repair Defects in Prostate Cancer. *Eur Urol*. 2019;76(4):469-478. doi:10.1016/j.eururo.2019.06.030

83. Michalski K, Ruf J, Goetz C, et al. Prognostic implications of dual tracer PET/CT: PSMA ligand and [18F]FDG PET/CT in patients undergoing [177Lu]PSMA radioligand therapy. *Eur J Nucl Med Mol Imaging*. 2021;48(6):2024-2030. doi:10.1007/s00259-020-05160-8

84. Goldstein LA, Ghersi G, Piñeiro-Sánchez ML, et al. Molecular cloning of seprase: a serine integral membrane protease from human melanoma. *Biochim Biophys Acta BBA - Mol Basis Dis*. 1997;1361(1):11-19. doi:10.1016/S0925-4439(97)00032-X

85. Rosenblum JS, Kozarich JW. Prolyl peptidases: a serine protease subfamily with high potential for drug discovery. *Curr Opin Chem Biol*. 2003;7(4):496-504. doi:10.1016/S1367-5931(03)00084-X

86. Park JE, Lenter MC, Zimmermann RN, Garin-Chesa P, Old LJ, Rettig WJ. Fibroblast Activation Protein, a Dual Specificity Serine Protease Expressed in Reactive Human Tumor Stromal Fibroblasts *. *J Biol Chem*. 1999;274(51):36505-36512. doi:10.1074/jbc.274.51.36505

87. Fitzgerald AA, Weiner LM. The role of fibroblast activation protein in health and malignancy. *Cancer Metastasis Rev*. 2020;39(3):783-803. doi:10.1007/s10555-020-09909-3

88. Collins PJ, McMahon G, O'Brien P, O'Connor B. Purification, identification and characterisation of seprase from bovine serum. *Int J Biochem Cell Biol*. 2004;36(11):2320-2333. doi:10.1016/j.biocel.2004.05.006

89. Edosada CY, Quan C, Tran T, et al. Peptide substrate profiling defines fibroblast activation protein as an endopeptidase of strict Gly(2)-Pro(1)-cleaving specificity. *FEBS Lett*. 2006;580(6):1581-1586. doi:10.1016/j.febslet.2006.01.087

90. Keane FM, Nadvi NA, Yao TW, Gorrell MD. Neuropeptide Y, B-type natriuretic peptide, substance P and peptide YY are novel substrates of fibroblast activation protein-α. *FEBS J*. 2011;278(8):1316-1332. doi:10.1111/j.1742-4658.2011.08051.x

91. Christiansen VJ, Jackson KW, Lee KN, McKee PA. Effect of Fibroblast Activation Protein and α2-Antiplasmin Cleaving Enzyme on Collagen Types I, III and IV. *Arch Biochem Biophys*. 2007;457(2):177-186. doi:10.1016/j.abb.2006.11.006

92. Lee KN, Jackson KW, Christiansen VJ, Chung KH, McKee PA. A novel plasma proteinase potentiates α2-antiplasmin inhibition of fibrin digestion. *Blood*. 2004;103(10):3783-3788. doi:10.1182/blood-2003-12-4240

93. Lee KN, Jackson KW, Christiansen VJ, Lee CS, Chun JG, McKee PA. Antiplasmin-cleaving enzyme is a soluble form of fibroblast activation protein. *Blood*. 2006;107(4):1397-1404. doi:10.1182/blood-2005-08-3452

94. Dunshee DR, Bainbridge TW, Kljavin NM, et al. Fibroblast Activation Protein Cleaves and Inactivates Fibroblast Growth Factor 21. *J Biol Chem*. 2016;291(11):5986-5996. doi:10.1074/jbc.M115.710582

95. Fan MH, Zhu Q, Li HH, et al. Fibroblast Activation Protein (FAP) Accelerates Collagen Degradation and Clearance from Lungs in Mice. *J Biol Chem*. 2016;291(15):8070-8089. doi:10.1074/jbc.M115.701433

96. Garin-Chesa P, Old LJ, Rettig WJ. Cell surface glycoprotein of reactive stromal fibroblasts as a potential antibody target in human epithelial cancers. *Proc Natl Acad Sci U S A*. 1990;87(18):7235-7239.

97. Tillmanns J, Hoffmann D, Habbaba Y, et al. Fibroblast activation protein alpha expression identifies activated fibroblasts after myocardial infarction. *J Mol Cell Cardiol*. 2015;87:194-203. doi:10.1016/j.yjmcc.2015.08.016

98. Jung YY, Lee YK, Koo JS. Expression of cancer-associated fibroblast-related proteins in adipose stroma of breast cancer. *Tumor Biol*. 2015;36(11):8685-8695. doi:10.1007/s13277-015-3594-9

99. Iwasa S, Jin X, Okada K, Mitsumata M, Ooi A. Increased expression of seprase, a membrane-type serine protease, is associated with lymph node metastasis in human colorectal cancer. *Cancer Lett*. 2003;199(1):91-98. doi:10.1016/S0304-3835(03)00315-X

100. Shi M, Yu DH, Chen Y, et al. Expression of fibroblast activation protein in human pancreatic adenocarcinoma and its clinicopathological significance. *World J Gastroenterol*. 2012;18(8):840-846. doi:10.3748/wjg.v18.i8.840

101. Kesch C, Yirga L, Dendl K, et al. High fibroblast-activation-protein expression in castration-resistant prostate cancer supports the use of FAPI-molecular theranostics. *Eur J Nucl Med Mol Imaging*. 2021;49(1):385-389. doi:10.1007/s00259-021-05423-y

102. Dolznig H, Schweifer N, Puri C, et al. Characterization of cancer stroma markers: in silico analysis of an mRNA expression database for fibroblast activation protein and endosialin. *Cancer Immun*. 2005;5:10.

103. Teichgräber V, Monasterio C, Chaitanya K, et al. Specific inhibition of fibroblast activation protein (FAP)-alpha prevents tumor progression in vitro. *Adv Med Sci*. 2015;60(2):264-272. doi:10.1016/j.advms.2015.04.006

104. Santos AM, Jung J, Aziz N, Kissil JL, Puré E. Targeting fibroblast activation protein inhibits tumor stromagenesis and growth in mice. *J Clin Invest*. 2009;119(12):3613-3625. doi:10.1172/JCI38988

105. Balaziova E, Vymola P, Hrabal P, et al. Fibroblast Activation Protein Expressing Mesenchymal Cells Promote Glioblastoma Angiogenesis. *Cancers*. 2021;13(13):3304. doi:10.3390/cancers13133304

106. Ji D, Jia J, Cui X, Li Z, Wu A. FAP promotes metastasis and chemoresistance via regulating YAP1 and macrophages in mucinous colorectal adenocarcinoma. *iScience*. 2023;26(6):106600. doi:10.1016/j.isci.2023.106600

107. Henry LR, Lee HO, Lee JS, et al. Clinical Implications of Fibroblast Activation Protein in Patients with Colon Cancer. *Clin Cancer Res*. 2007;13(6):1736-1741. doi:10.1158/1078-0432.CCR-06-1746

108. Tran T, Quan C, Edosada CY, et al. Synthesis and structure–activity relationship of N-acyl-Gly-, N-acyl-Sar- and N-blocked-boroPro inhibitors of FAP, DPP4, and POP. *Bioorg Med Chem Lett*. 2007;17(5):1438-1442. doi:10.1016/j.bmcl.2006.11.072

109. Rüger R, Tansi FL, Rabenhold M, et al. In vivo near-infrared fluorescence imaging of FAP-expressing tumors with activatable FAP-targeted, single-chain Fv-immunoliposomes. *J Control Release Off J Control Release Soc*. 2014;186:1-10. doi:10.1016/j.jconrel.2014.04.050

110. Xin L, Gao J, Zheng Z, et al. Fibroblast Activation Protein-α as a Target in the Bench-to-Bedside Diagnosis and Treatment of Tumors: A Narrative Review. *Front Oncol*. 2021;11. Accessed March 28, 2022. https://www.frontiersin.org/article/10.3389/fonc.2021.648187

111. Jansen K, Heirbaut L, Verkerk R, et al. Extended Structure–Activity Relationship and Pharmacokinetic Investigation of (4-Quinolinoyl)glycyl-2-cyanopyrrolidine Inhibitors of Fibroblast Activation Protein (FAP). *J Med Chem*. 2014;57(7):3053-3074. doi:10.1021/jm500031w

112. Jansen K, Heirbaut L, Cheng JD, et al. Selective Inhibitors of Fibroblast Activation Protein (FAP) with a (4-Quinolinoyl)-glycyl-2-cyanopyrrolidine Scaffold. *ACS Med Chem Lett*. 2013;4(5):491-496. doi:10.1021/ml300410d

113. Poplawski SE, Lai JH, Li Y, et al. Identification of Selective and Potent Inhibitors of Fibroblast Activation Protein and Prolyl Oligopeptidase. *J Med Chem*. 2013;56(9):3467-3477. doi:10.1021/jm400351a

114. Kratochwil C, Flechsig P, Lindner T, et al. 68Ga-FAPI PET/CT: Tracer Uptake in 28 Different Kinds of Cancer. *J Nucl Med*. 2019;60(6):801-805. doi:10.2967/jnumed.119.227967

115. Giesel FL, Kratochwil C, Lindner T, et al. 68Ga-FAPI PET/CT: Biodistribution and Preliminary Dosimetry Estimate of 2 DOTA-Containing FAP-Targeting Agents in Patients with Various Cancers. *J Nucl Med*. 2019;60(3):386-392. doi:10.2967/jnumed.118.215913

116. Baum RP, Schuchardt C, Singh A, et al. Feasibility, Biodistribution, and Preliminary Dosimetry in Peptide-Targeted Radionuclide Therapy of Diverse Adenocarcinomas Using 177Lu-FAP-2286: First-in-Humans Results. *J Nucl Med*. 2022;63(3):415-423. doi:10.2967/jnumed.120.259192

117. Wegen S, Roth KS, Weindler J, et al. First Clinical Experience With [68Ga]Ga-FAPI-46-PET/CT Versus [18F]F-FDG PET/CT for Nodal Staging in Cervical Cancer. *Clin Nucl Med*. 2023;48(2):150. doi:10.1097/RLU.0000000000004505

118. Ballal S, Yadav MP, Kramer V, et al. A theranostic approach of [68Ga]Ga-DOTA.SA.FAPi PET/CT-guided [177Lu]Lu-DOTA.SA.FAPi radionuclide therapy in an end-stage breast cancer patient: new frontier in targeted radionuclide therapy. *Eur J Nucl Med Mol Imaging*. 2021;48(3):942-944. doi:10.1007/s00259-020-04990-w

119. Ma X, Wang M, Wang H, et al. Development of Bispecific NT-PSMA Heterodimer for Prostate Cancer Imaging: A Potential Approach to Address Tumor Heterogeneity. *Bioconjug Chem*. 2019;30(5):1314-1322. doi:10.1021/acs.bioconjchem.9b00252

120. Boinapally S, Lisok A, Lofland G, et al. Hetero-bivalent agents targeting FAP and PSMA. *Eur J Nucl Med Mol Imaging*. 2022;49(13):4369-4381. doi:10.1007/s00259-022-05933-3

121. Hu K, Li L, Huang Y, et al. Radiosynthesis and Preclinical Evaluation of Bispecific PSMA/FAP Heterodimers for Tumor Imaging. *Pharmaceuticals*. 2022;15(3):383. doi:10.3390/ph15030383

122. Kuo HT, Lin KS, Zhang Z, et al. 177Lu-Labeled Albumin-Binder-Conjugated PSMA-Targeting Agents with Extremely High Tumor Uptake and Enhanced Tumor-to-Kidney Absorbed Dose Ratio. *J Nucl Med Off Publ Soc Nucl Med*. 2021;62(4):521-527. doi:10.2967/jnumed.120.250738

123. Kuo HT, Pan J, Zhang Z, et al. Effects of Linker Modification on Tumor-to-Kidney Contrast of 68Ga-Labeled PSMA-Targeted Imaging Probes. *Mol Pharm*. 2018;15(8):3502-3511. doi:10.1021/acs.molpharmaceut.8b00499

124. North AJ, Karas JA, Ma MT, et al. Rhenium and Technetium-oxo Complexes with Thioamide Derivatives of Pyridylhydrazine Bifunctional Chelators Conjugated to the Tumour Targeting Peptides Octreotate and Cyclic-RGDfK. *Inorg Chem*. 2017;56(16):9725-9741. doi:10.1021/acs.inorgchem.7b01247

125. Lin KS, Pan J, Amouroux G, et al. In vivo radioimaging of bradykinin receptor b1, a widely overexpressed molecule in human cancer. *Cancer Res*. 2015;75(2):387-393. doi:10.1158/0008-5472.CAN-14-1603

126. Zhang C, Zhang Z, Lin KS, et al. Preclinical Melanoma Imaging with 68Ga-Labeled α-Melanocyte-Stimulating Hormone Derivatives Using PET. *Theranostics*. 2017;7(4):805-813. doi:10.7150/thno.17117

127. Kuo HT, Lin KS, Zhang Z, et al. What a difference a methylene makes: replacing Glu with Asp or Aad in the Lys-urea-Glu pharmacophore of PSMA-targeting radioligands to reduce kidney and salivary gland uptake. *Theranostics*. 2022;12(14):6179-6188. doi:10.7150/thno.76571

128. Kuo HT, Lepage ML, Lin KS, et al. One-Step 18F-Labeling and Preclinical Evaluation of Prostate-Specific Membrane Antigen Trifluoroborate Probes for Cancer Imaging. *J Nucl Med*. 2019;60(8):1160-1166. doi:10.2967/jnumed.118.216598

129. Meng L, Fang J, Zhao L, et al. Rational Design and Pharmacomodulation of Protein-Binding Theranostic Radioligands for Targeting the Fibroblast Activation Protein. *J Med Chem*. 2022;65(12):8245-8257. doi:10.1021/acs.jmedchem.1c02162

130. Ding J, Xu M, Chen J, et al. 86Y-Labeled Albumin-Binding Fibroblast Activation Protein Inhibitor for Late-Time-Point Cancer Diagnosis. *Mol Pharm*. 2022;19(9):3429-3438. doi:10.1021/acs.molpharmaceut.2c00579

131. Pereira BA, Vennin C, Papanicolaou M, et al. CAF Subpopulations: A New Reservoir of Stromal Targets in Pancreatic Cancer. *Trends Cancer*. 2019;5(11):724-741. doi:10.1016/j.trecan.2019.09.010

132. Stock K, Steinestel K, Wiesch R, et al. Neovascular Prostate-Specific Membrane Antigen Expression Is Associated with Improved Overall Survival under Palliative Chemotherapy in Patients with Pancreatic Ductal Adenocarcinoma. *BioMed Res Int*. 2017;2017:2847303. doi:10.1155/2017/2847303

133. Poels TT, Vuijk FA, de Geus-Oei LF, Vahrmeijer AL, Oprea-Lager DE, Swijnenburg RJ. Molecular Targeted Positron Emission Tomography Imaging and Radionuclide Therapy of Pancreatic Ductal Adenocarcinoma. *Cancers*. 2021;13(24):6164. doi:10.3390/cancers13246164

134. Kessel K, Seifert R, Weckesser M, et al. Prostate-specific membrane antigen and fibroblast activation protein distribution in prostate cancer: preliminary data on immunohistochemistry and PET imaging. *Ann Nucl Med*. 2022;36(3):293-301. doi:10.1007/s12149-021-01702-8

135. Lindner T, Loktev A, Altmann A, et al. Development of Quinoline-Based Theranostic Ligands for the Targeting of Fibroblast Activation Protein. *J Nucl Med*. 2018;59(9):1415-1422. doi:10.2967/jnumed.118.210443

136. Yang Y, Ji S, Liu S. Impact of Multiple Negative Charges on Blood Clearance and Biodistribution Characteristics of 99mTc-Labeled Dimeric Cyclic RGD Peptides. *Bioconjug Chem*. 2014;25(9):1720-1729. doi:10.1021/bc500309r

137. Imlimthan S, Moon ES, Rathke H, et al. New Frontiers in Cancer Imaging and Therapy Based on Radiolabeled Fibroblast Activation Protein Inhibitors: A Rational Review and Current Progress. *Pharm Basel Switz*. 2021;14(10):1023. doi:10.3390/ph14101023

138. Lukas Kessler, Justin Ferdinandus, Nader Hirmas, et al. Pitfalls and Common Findings in ^{68}Ga-FAPI PET: A Pictorial Analysis. *J Nucl Med*. 2022;63(6):890. doi:10.2967/jnumed.121.262808

139. Gündoğan C, Güzel Y, Can C, Alabalik U, Kömek H. False-Positive 68Ga-Fibroblast Activation Protein-Specific Inhibitor Uptake of Benign Lymphoid Tissue in a Patient With Breast Cancer. *Clin Nucl Med*. 2021;46(8):e433-e435. doi:10.1097/RLU.0000000000003594

140. Trujillo-Benítez D, Luna-Gutiérrez M, Ferro-Flores G, et al. Design, Synthesis and Preclinical Assessment of 99mTc-iFAP for In Vivo Fibroblast Activation Protein (FAP) Imaging. *Molecules*. 2022;27(1):264. doi:10.3390/molecules27010264

141. Verena A, Zhang Z, Kuo HT, et al. Synthesis and Preclinical Evaluation of Three Novel 68Ga-Labeled Bispecific PSMA/FAP-Targeting Tracers for Prostate Cancer Imaging. *Molecules*. 2023;28(3):1088. doi:10.3390/molecules28031088

142. Müller C, Struthers H, Winiger C, Zhernosekov K, Schibli R. DOTA conjugate with an albumin-binding entity enables the first folic acid-targeted 177Lu-radionuclide tumor therapy in mice. *J Nucl Med Off Publ Soc Nucl Med*. 2013;54(1):124-131. doi:10.2967/jnumed.112.107235

143. Verena A, Kuo HT, Merkens H, et al. Novel 68Ga-Labeled Pyridine-Based Fibroblast Activation Protein-Targeted Tracers with High Tumor-to-Background Contrast. *Pharm Basel Switz*. 2023;16(3):449. doi:10.3390/ph16030449

144. Wünsch M, Schröder D, Fröhr T, et al. Asymmetric synthesis of propargylamines as amino acid surrogates in peptidomimetics. *Beilstein J Org Chem*. 2017;13:2428-2441. doi:10.3762/bjoc.13.240

145. Nguyen AT, Kim HK. Recent Developments in PET and SPECT Radiotracers as Radiopharmaceuticals for Hypoxia Tumors. *Pharmaceutics*. 2023;15(7):1840. doi:10.3390/pharmaceutics15071840

146. Wang P, Wang S, Liu F, et al. Preclinical Evaluation of a Fibroblast Activation Protein and a Prostate-Specific Membrane Antigen Dual-Targeted Probe for Noninvasive Prostate Cancer Imaging. *Mol Pharm*. 2023;20(2):1415-1425. doi:10.1021/acs.molpharmaceut.2c01000

Appendices

Appendix A: Mass Spectra of Intermediates and Compounds

A.1 Mass Spectra of Intermediates and Compounds in Chapter 2

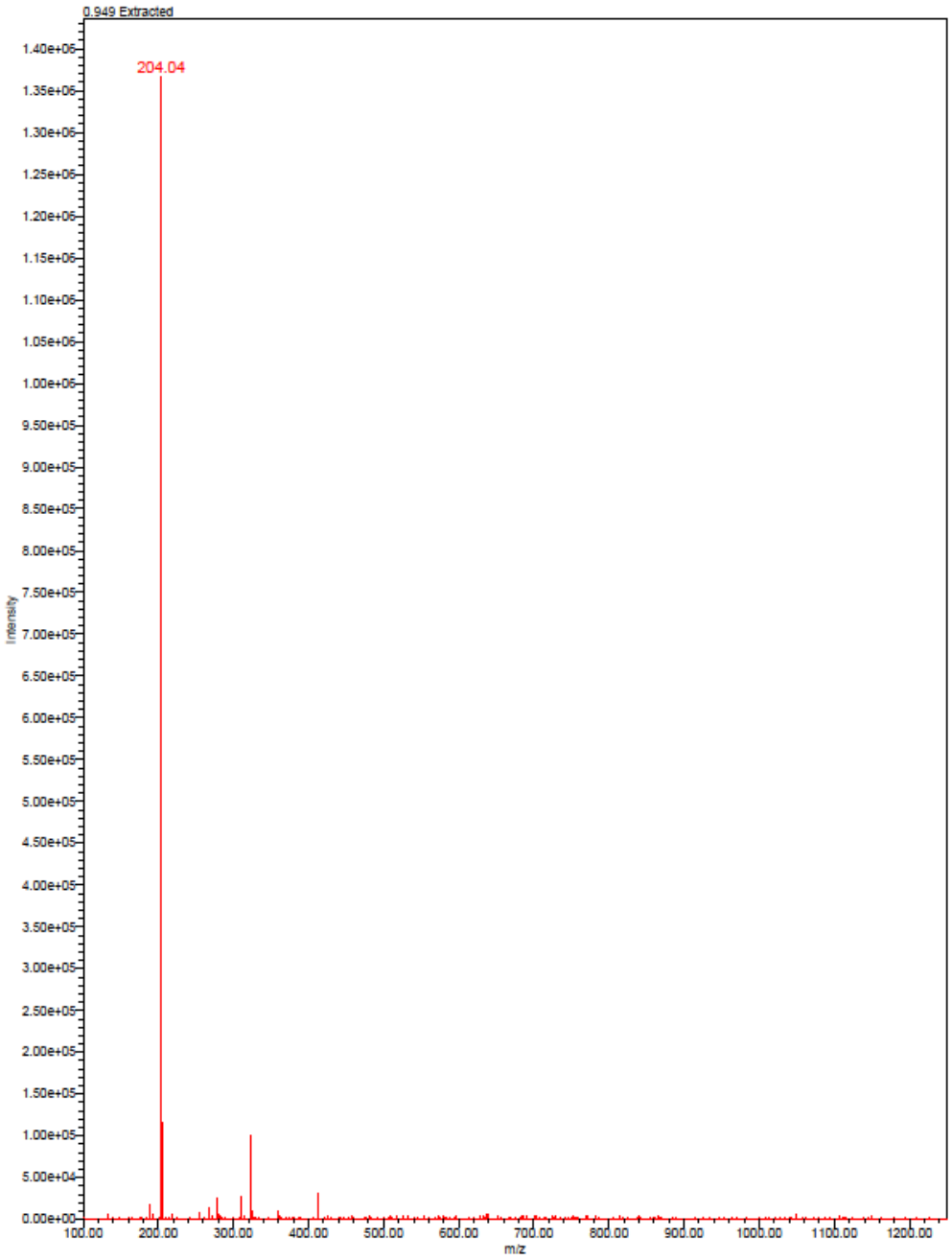

methyl 6-hydroxyquinoline-4-carboxylate (1)

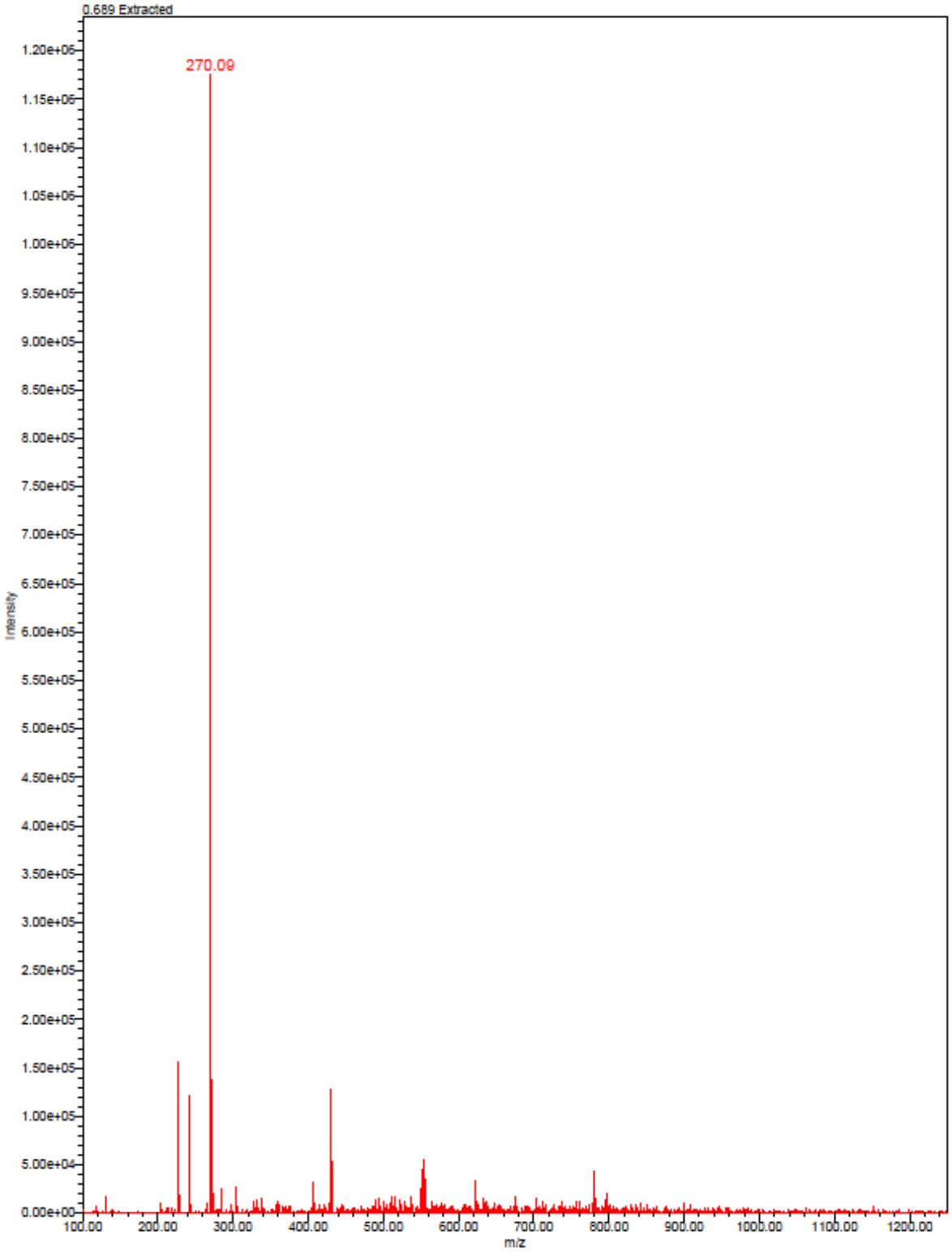

methyl 6-(pent-4-yn-1-yloxy)quinoline-4-carboxylate (2)

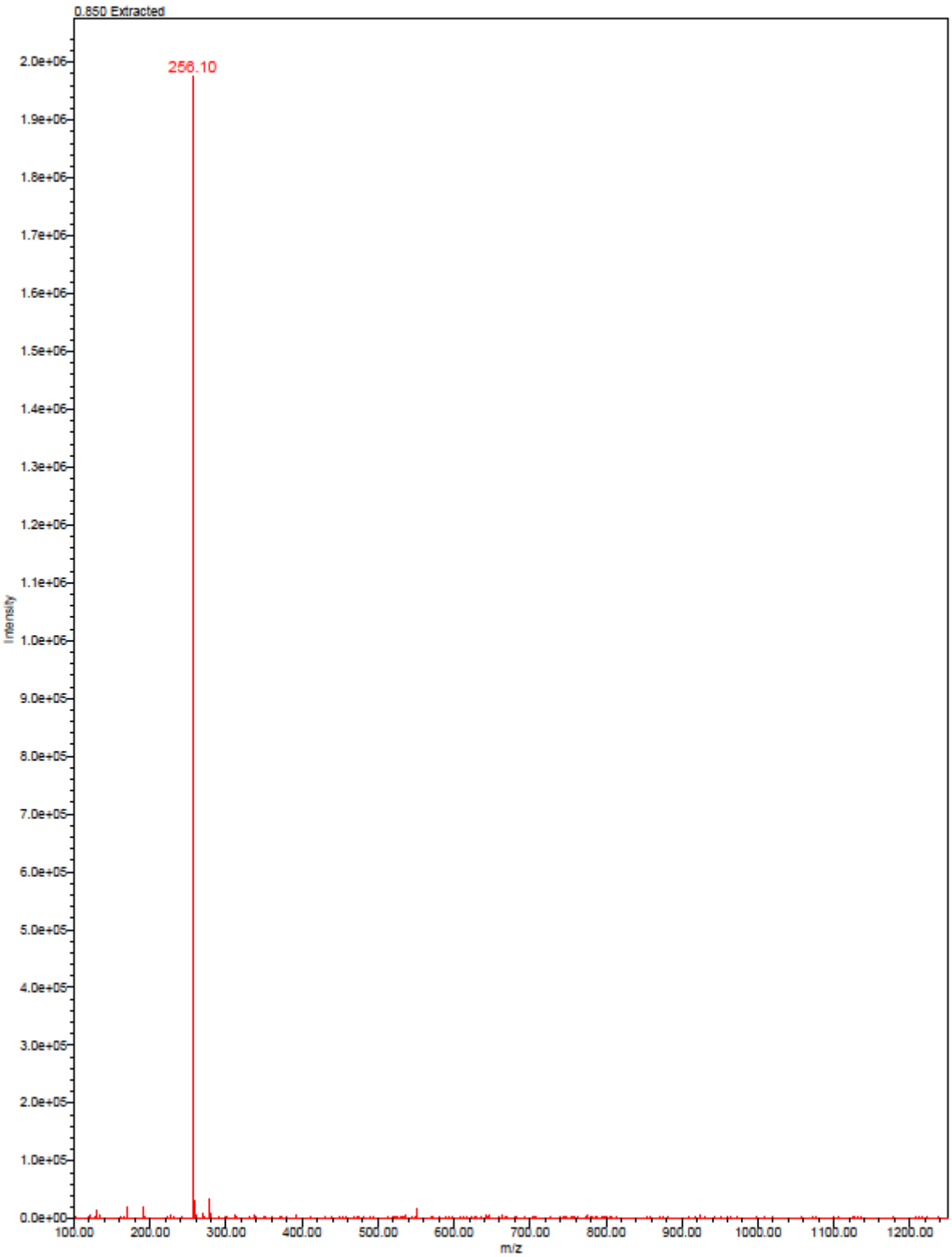

6-(pent-4-yn-1-yloxy)quinoline-4-carboxylic acid (3)

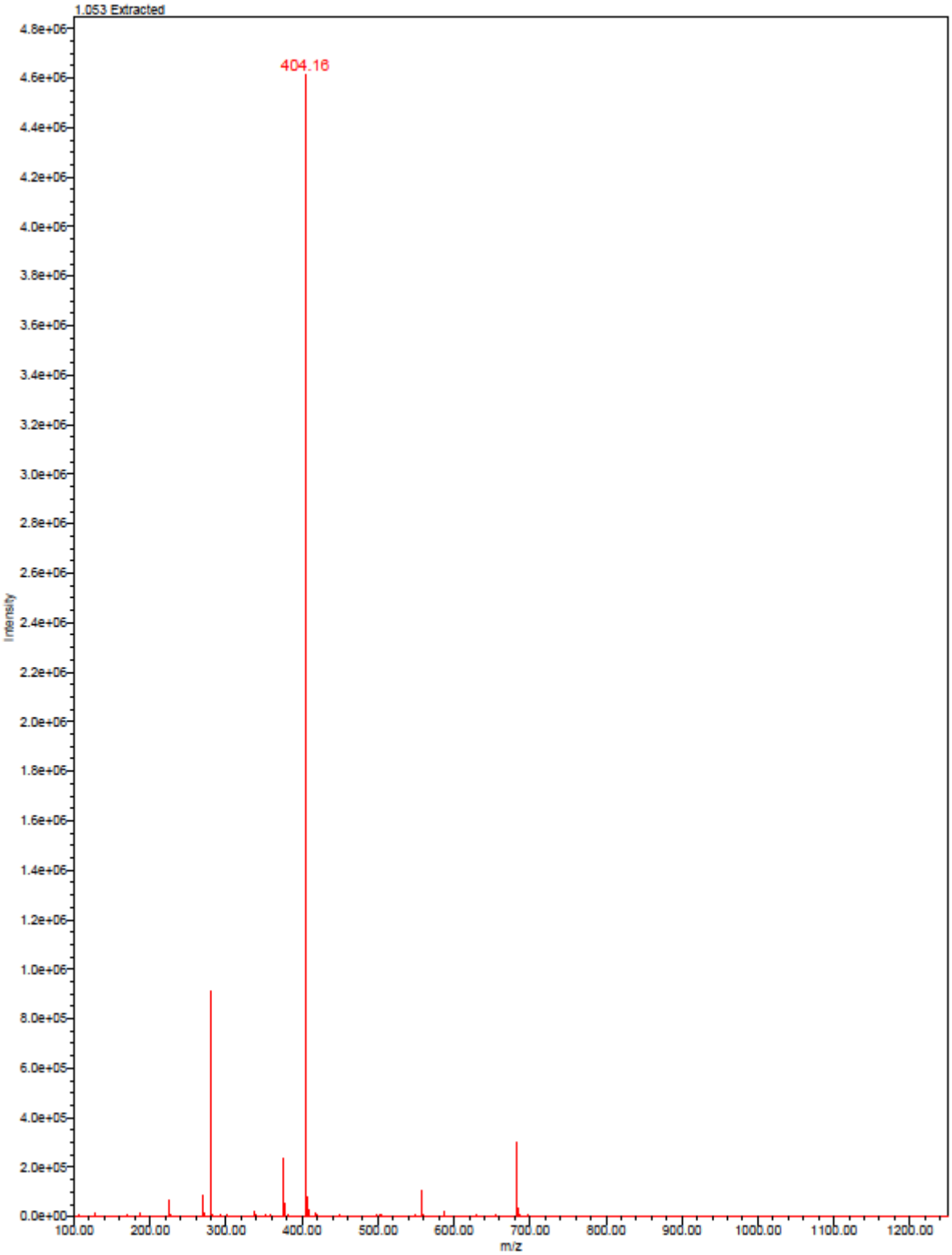

2,3,5,6-tetrafluorophenyl 6-(pent-4-yn-1-yloxy)quinoline-4-carboxylate (4)

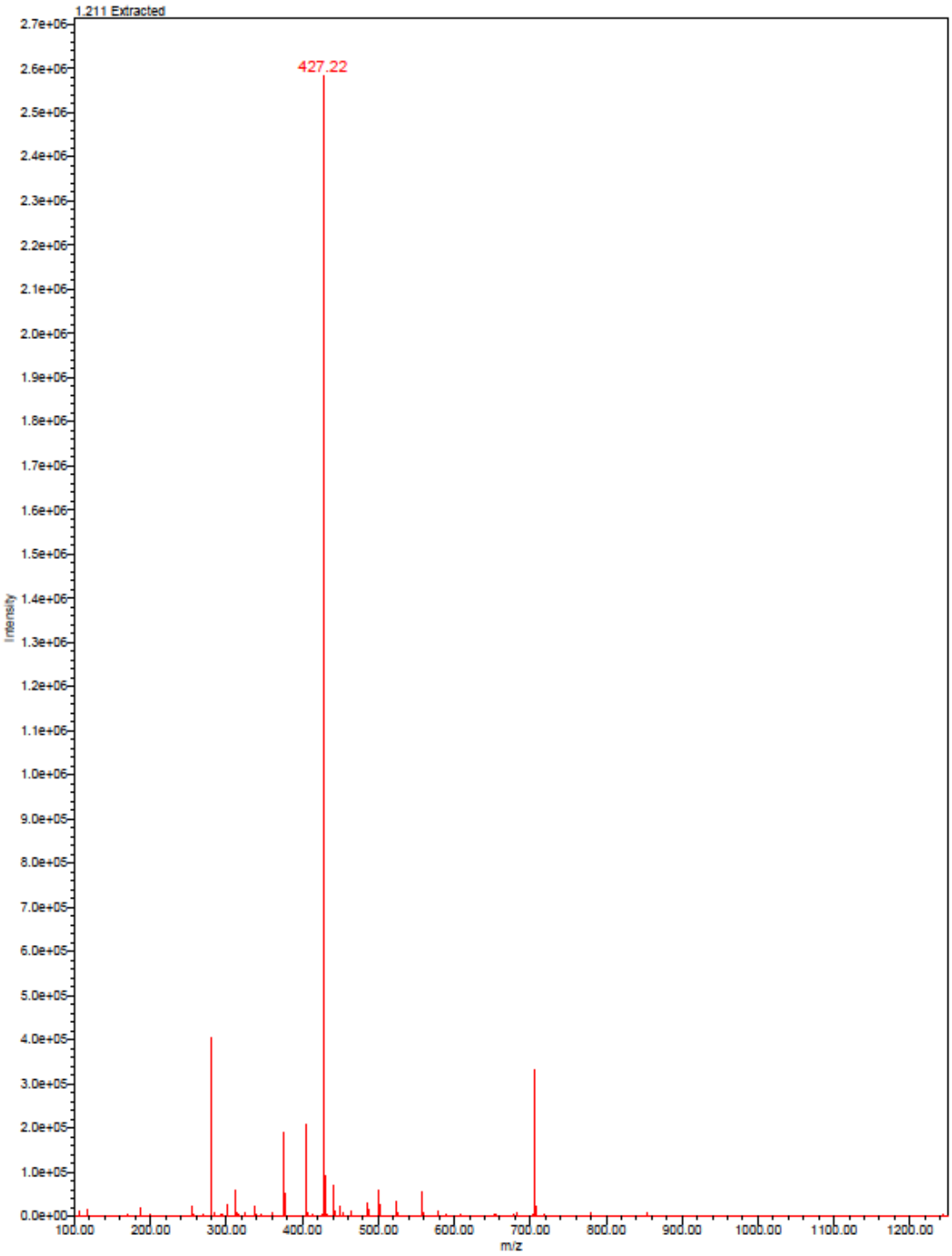

(S)-N-(2-(2-cyano-4,4-difluoropyrrolidin-1-yl)-2-oxoethyl)-6-(pent-4-yn-1-yloxy)quinoline-4-carboxamide (5)

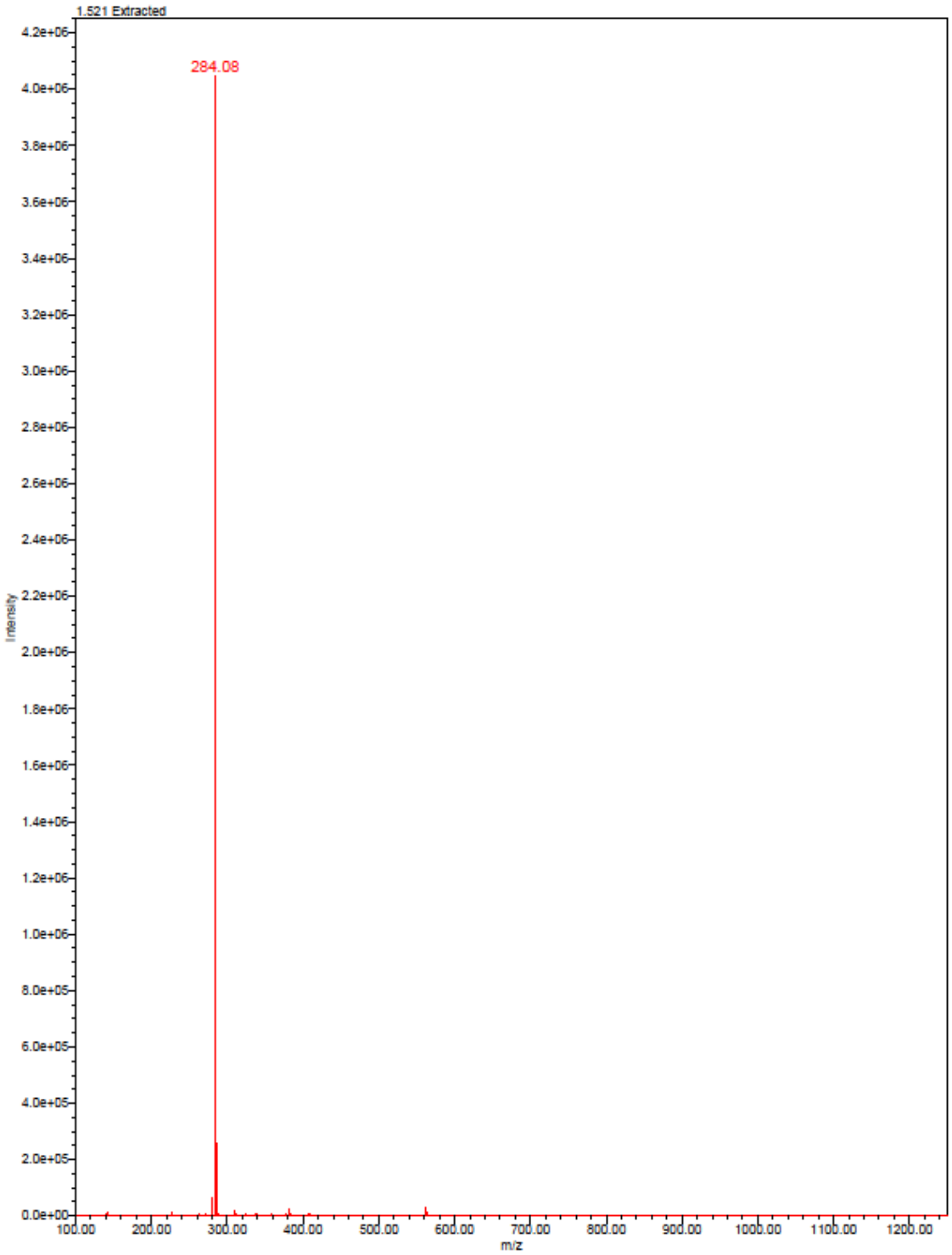

methyl 6-(2-(trimethylsilyl)ethynyl)quinoline-4-carboxylate (6)

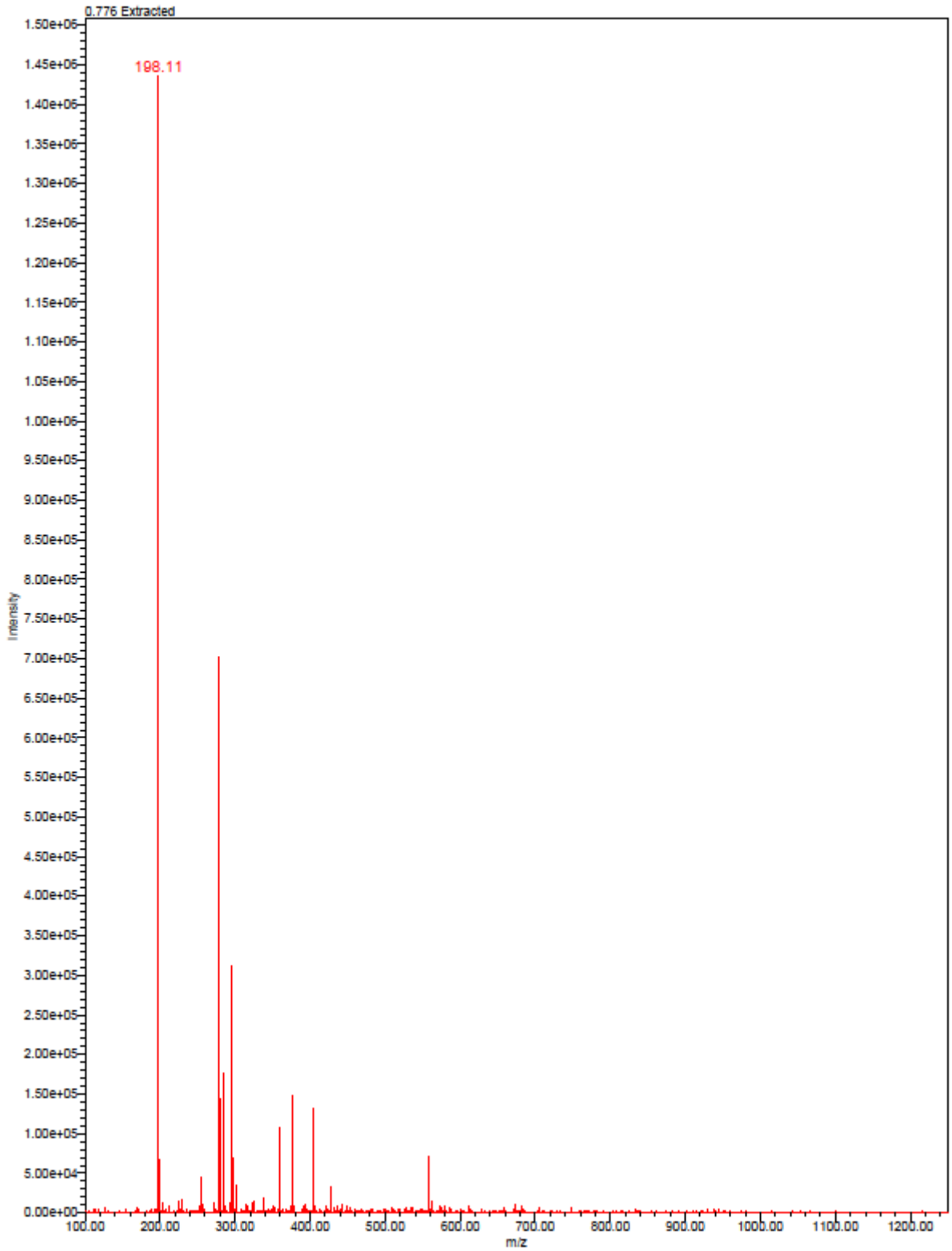

6-ethynylquinoline-4-carboxylic acid (7)

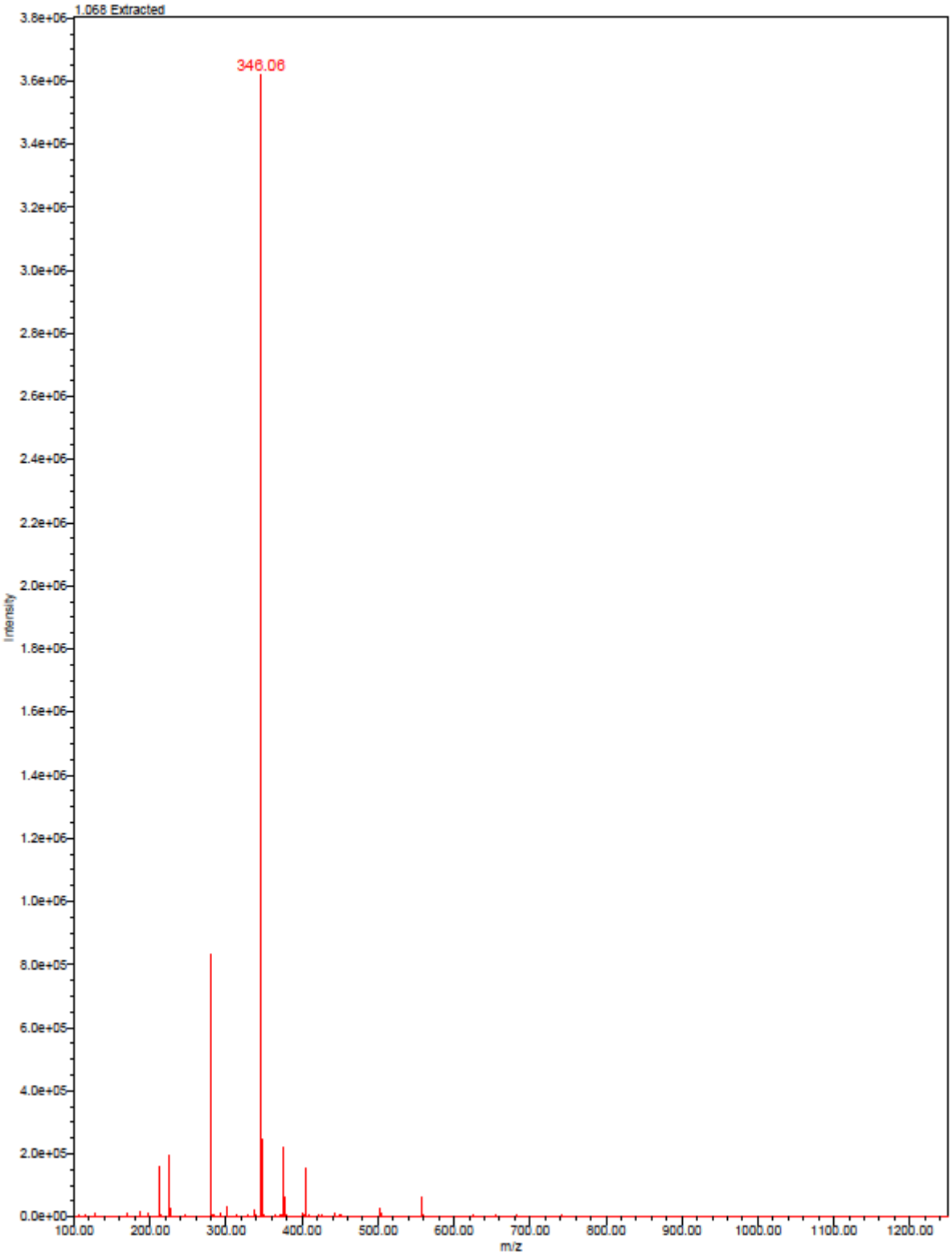

2,3,5,6-tetrafluorophenyl 6-ethynylquinoline-4-carboxylate (8)

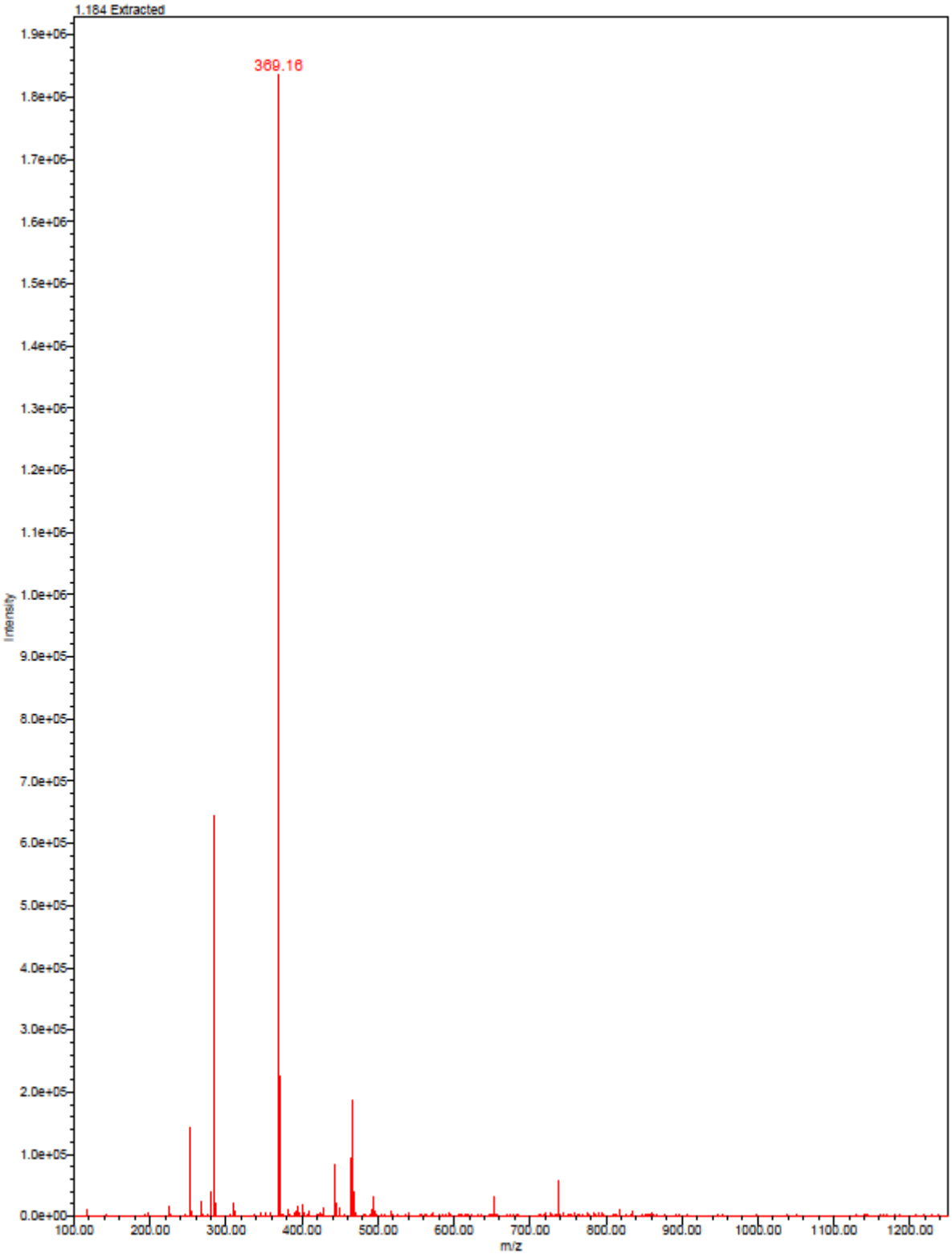

(S)-N-(2-(2-cyano-4,4-difluoropyrrolidin-1-yl)-2-oxoethyl)-6-ethynylquinoline-4-carboxamide (9)

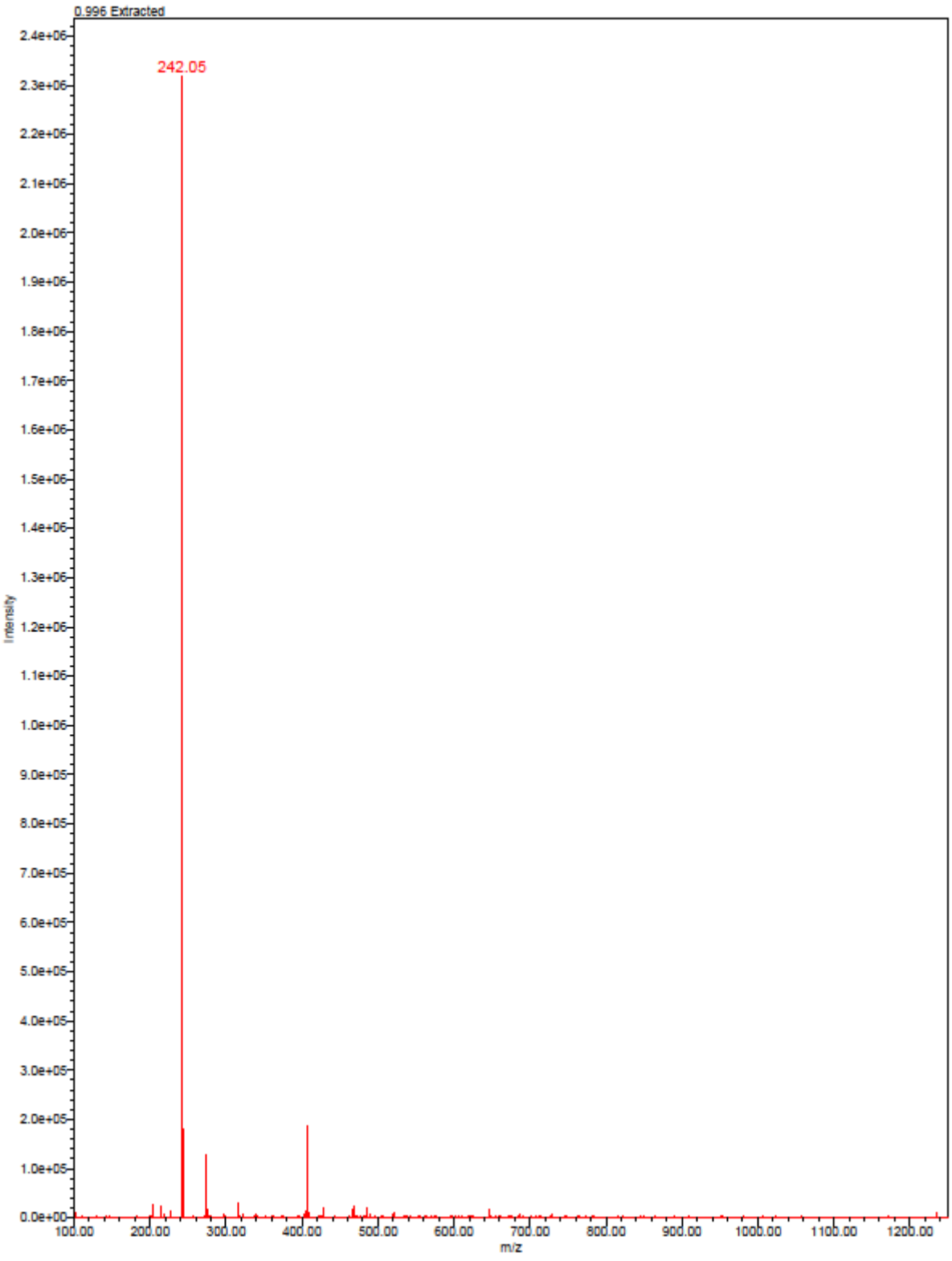

methyl 6-(prop-2-yn-1-yloxy)quinoline-4-carboxylate (10)

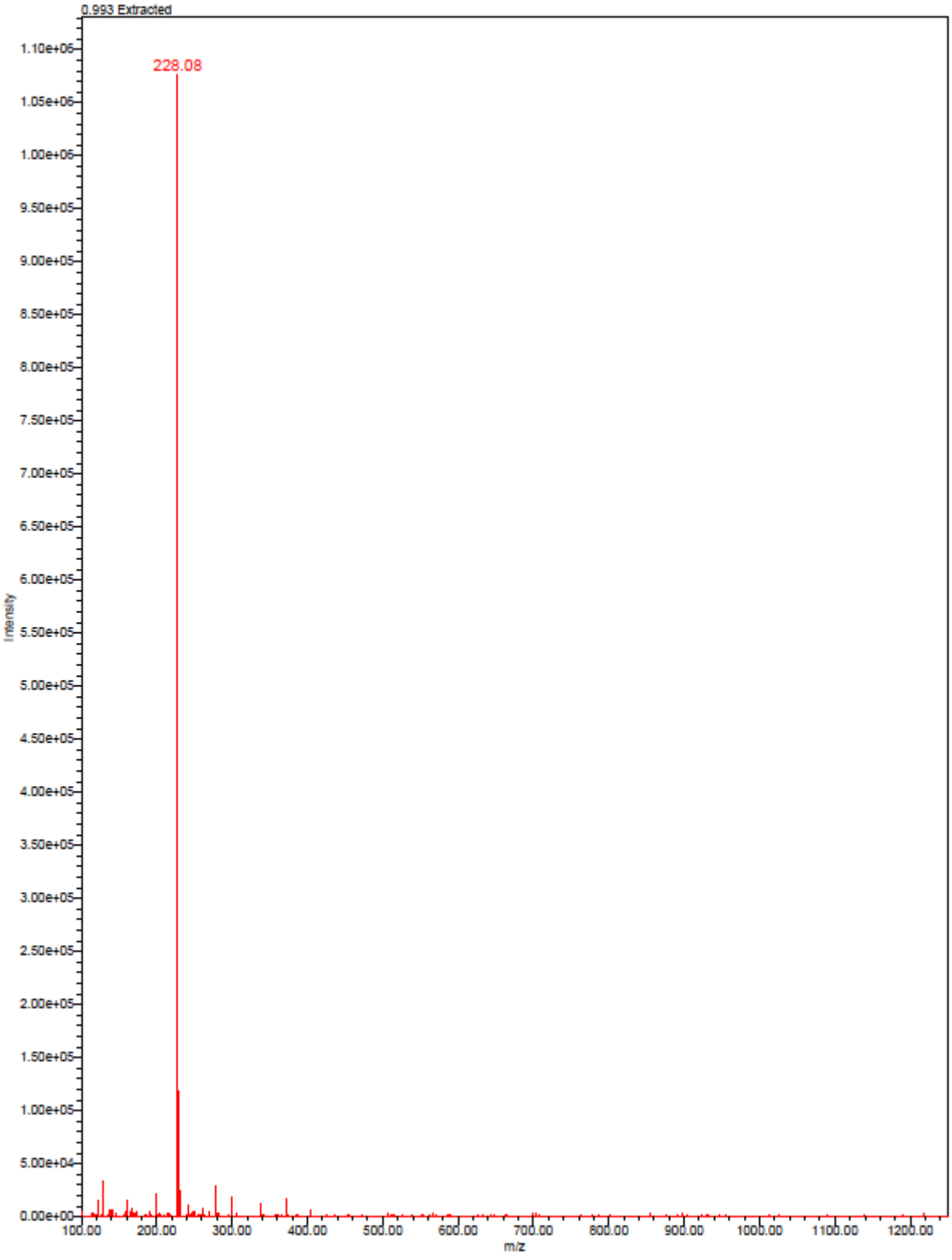

6-(prop-2-yn-1-yloxy)quinoline-4-carboxylic acid (11)

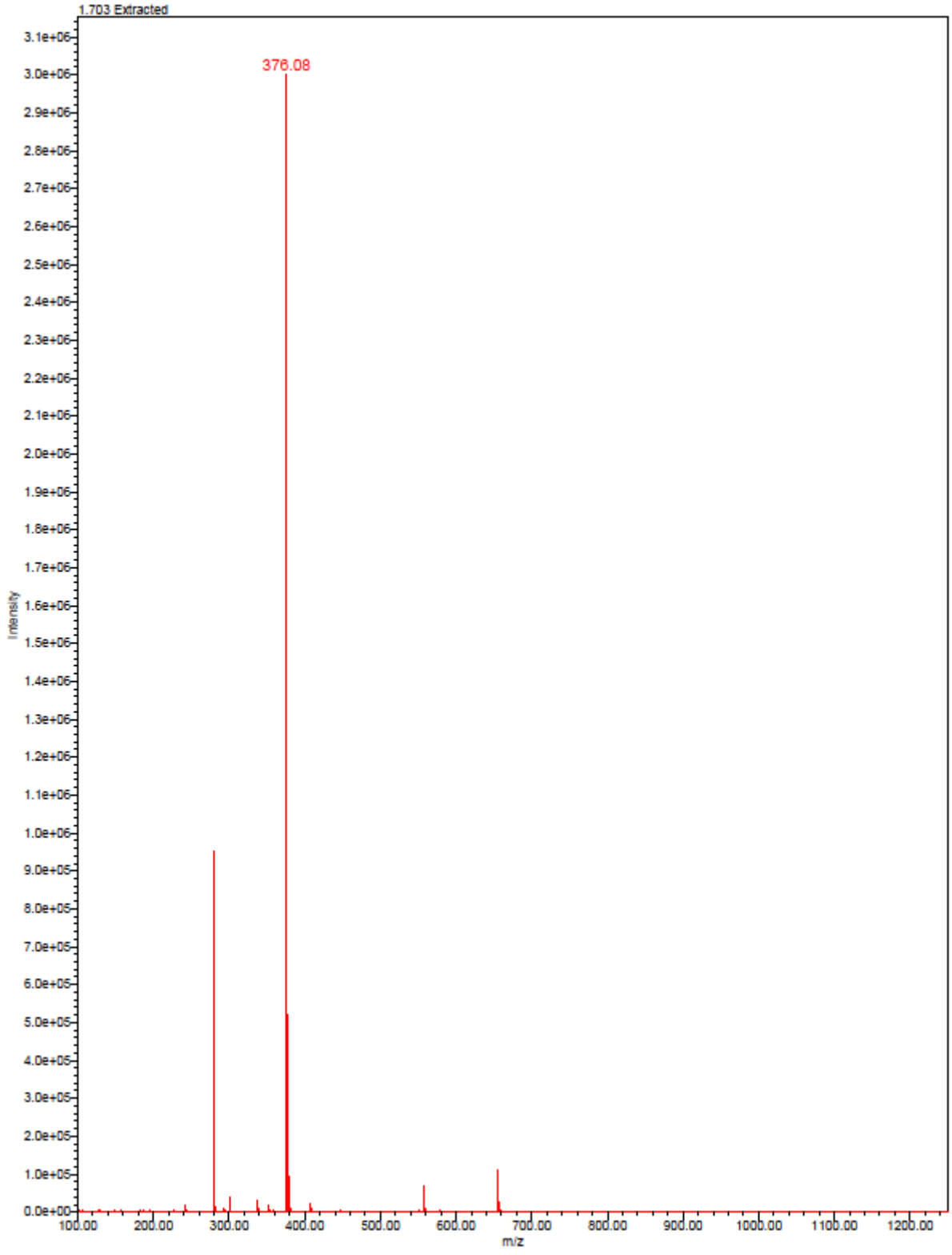

2,3,5,6-tetrafluorophenyl 6-(prop-2-yn-1-yloxy)quinoline-4-carboxylate (12)

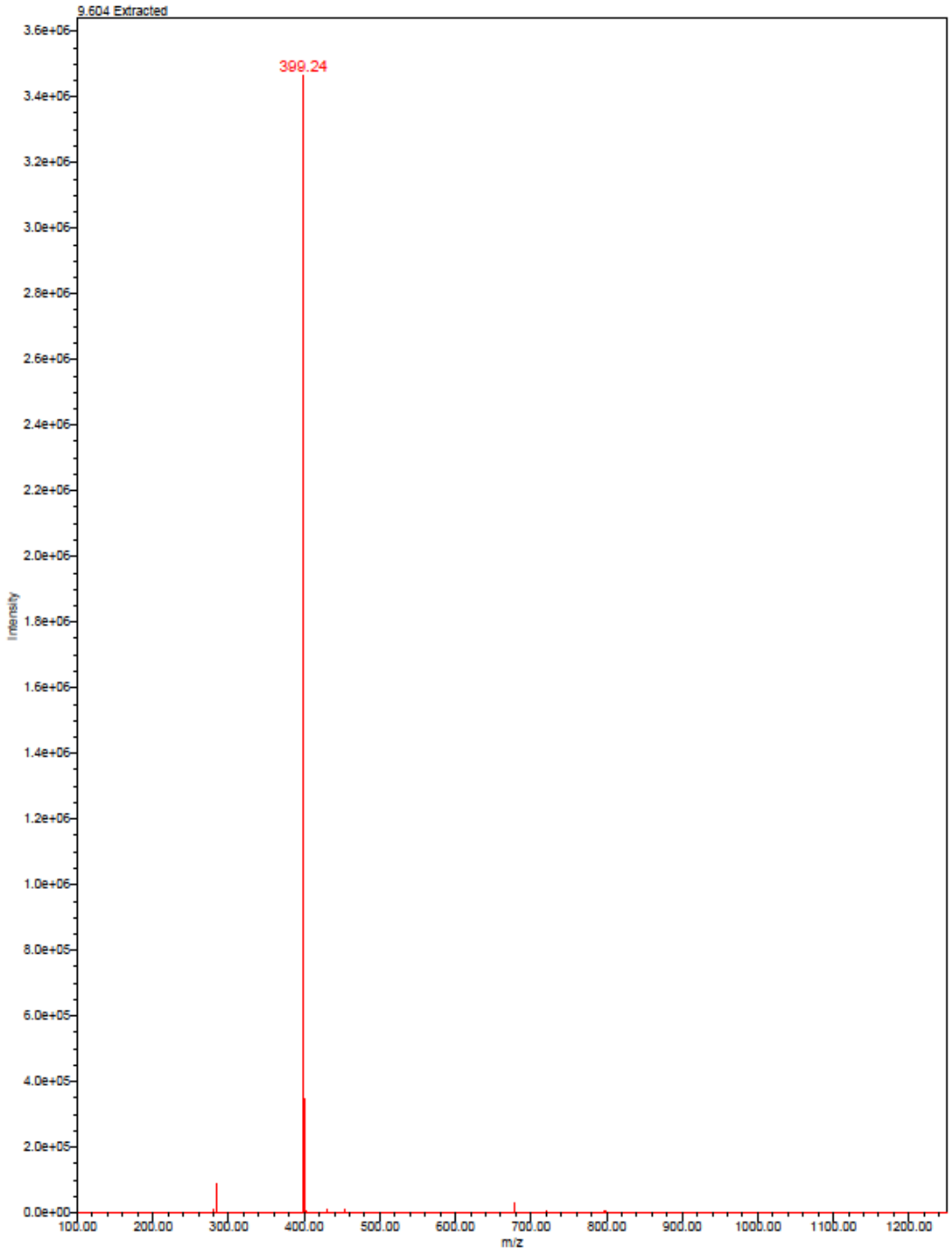

(*S*)-*N*-(2-(2-cyano-4,4-difluoropyrrolidin-1-yl)-2-oxoethyl)-6-(prop-2-yn-1-yloxy)quinoline-4-carboxamide (13)

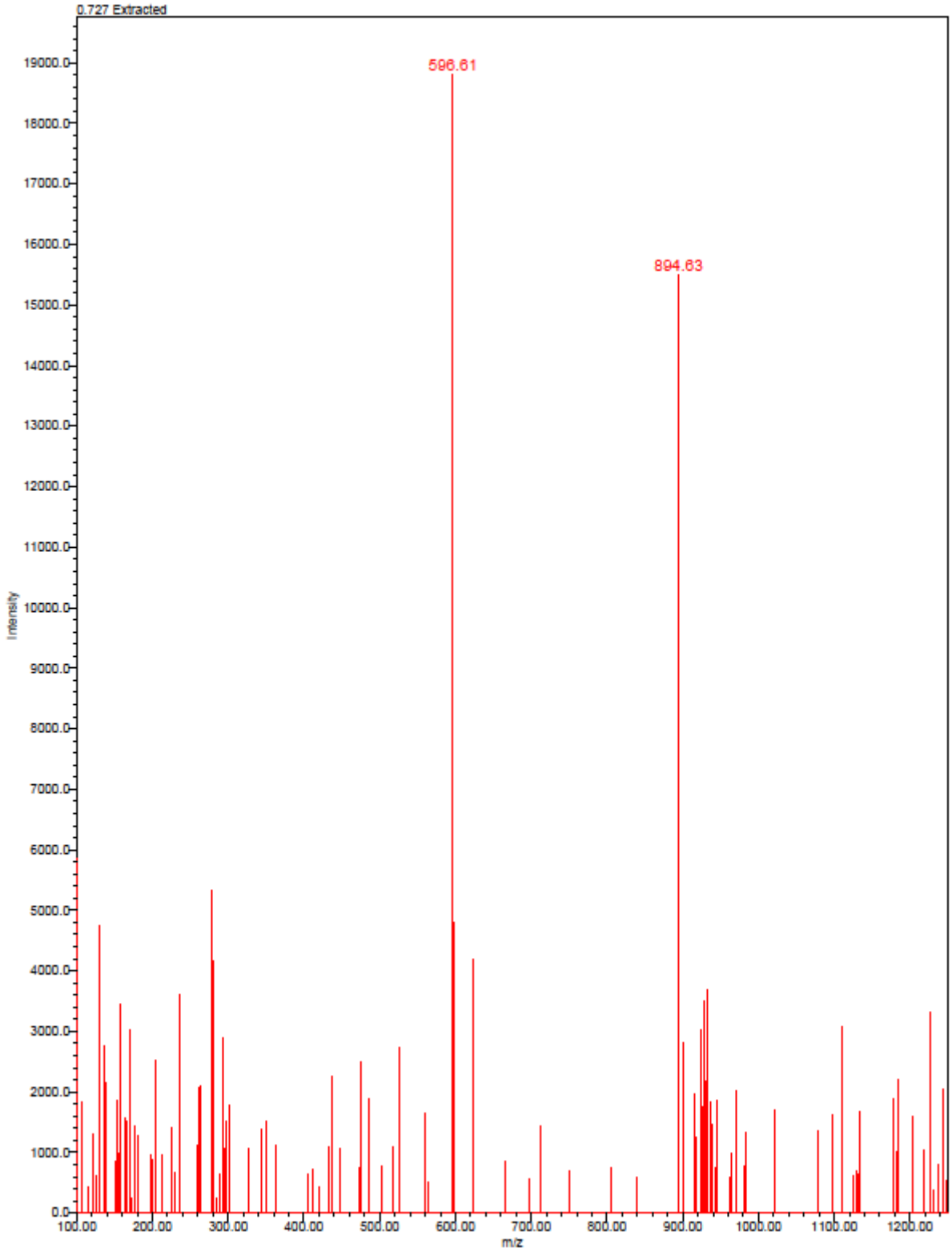

AV01017

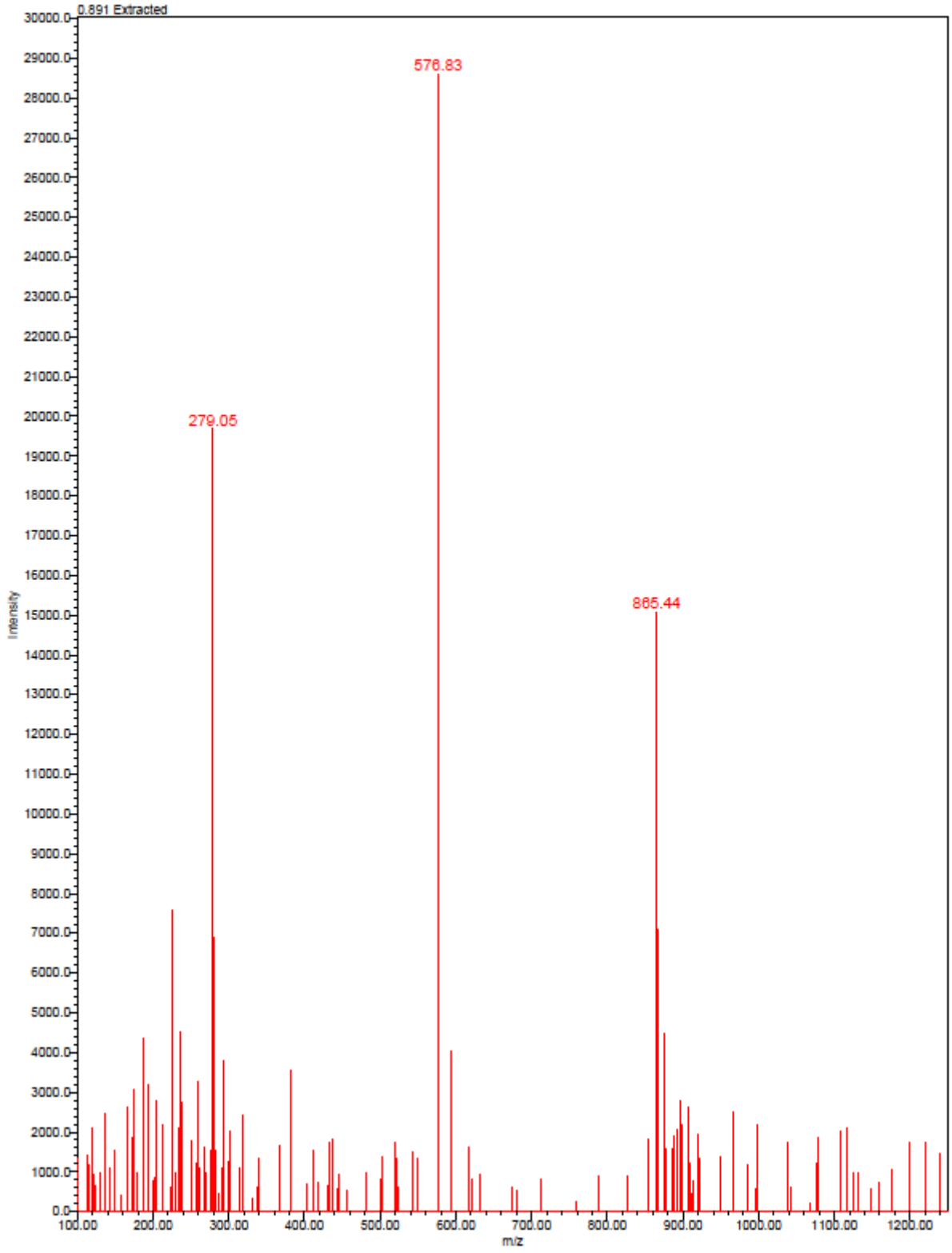

AV01030

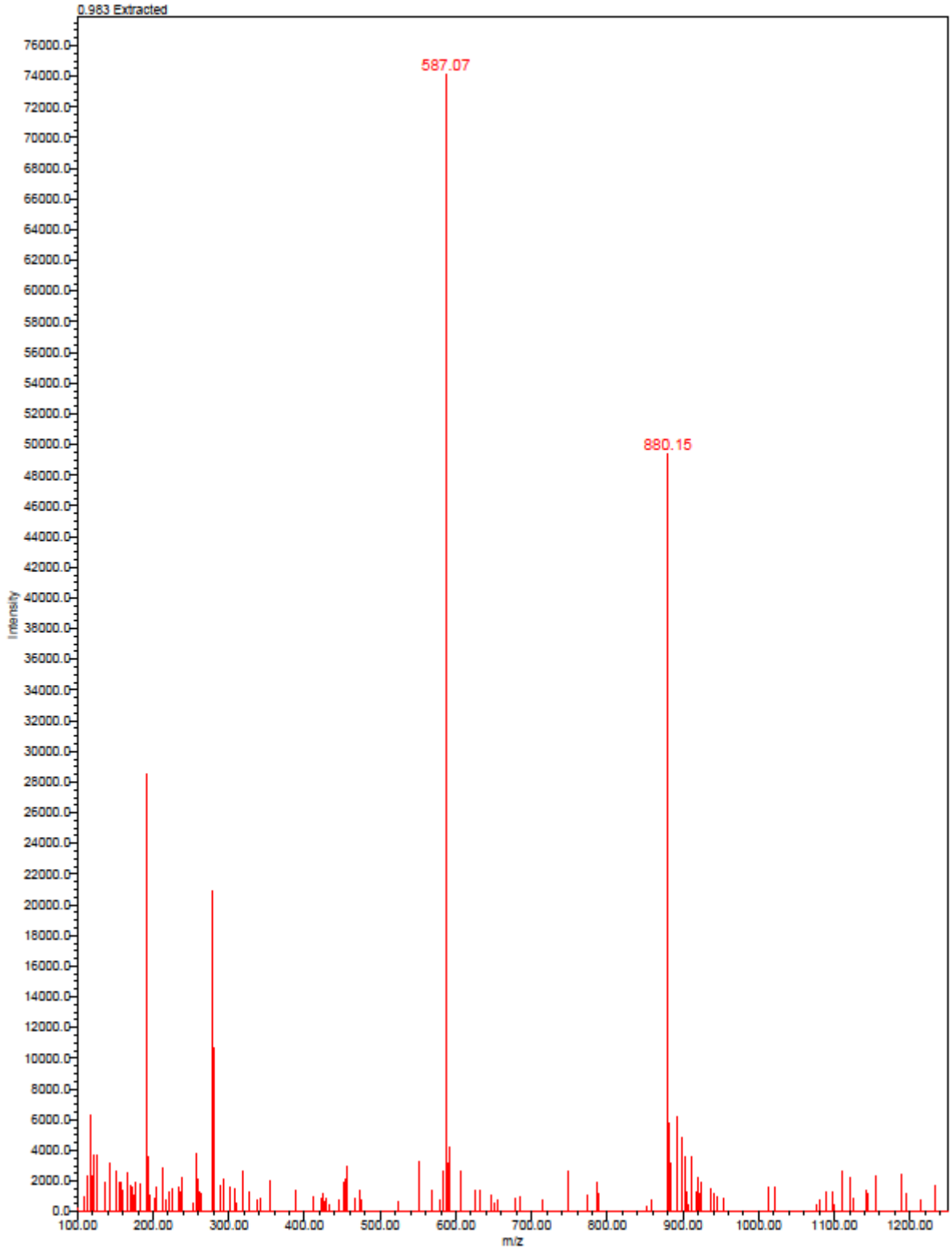

AV01038

A.2 Mass Spectra of Intermediates and Compounds in Chapter 3

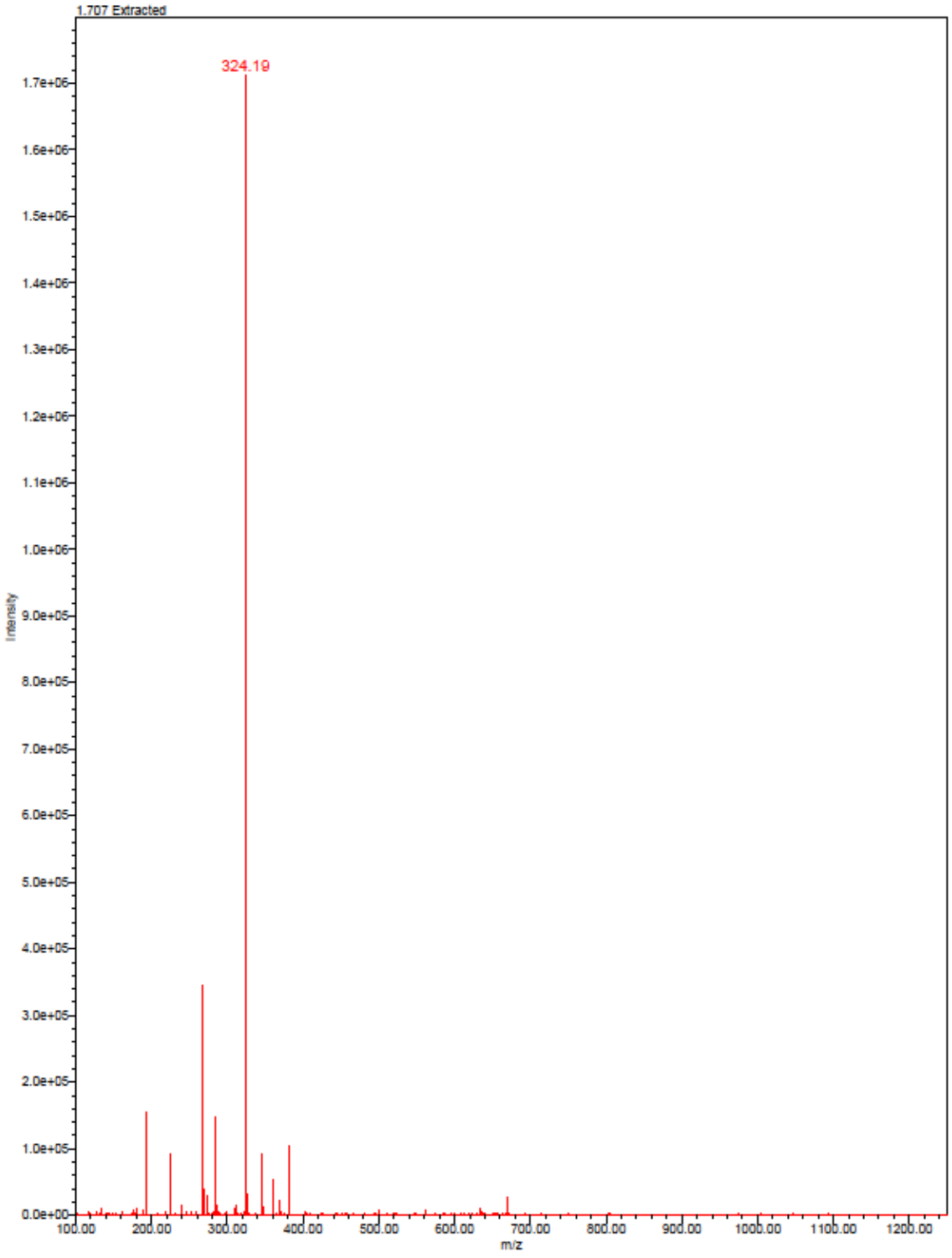

methyl 6-[[2-[[(tert-butoxy)carbonyl]methylamino]ethyl]methylamino] pyridine-3-carboxylate (1)

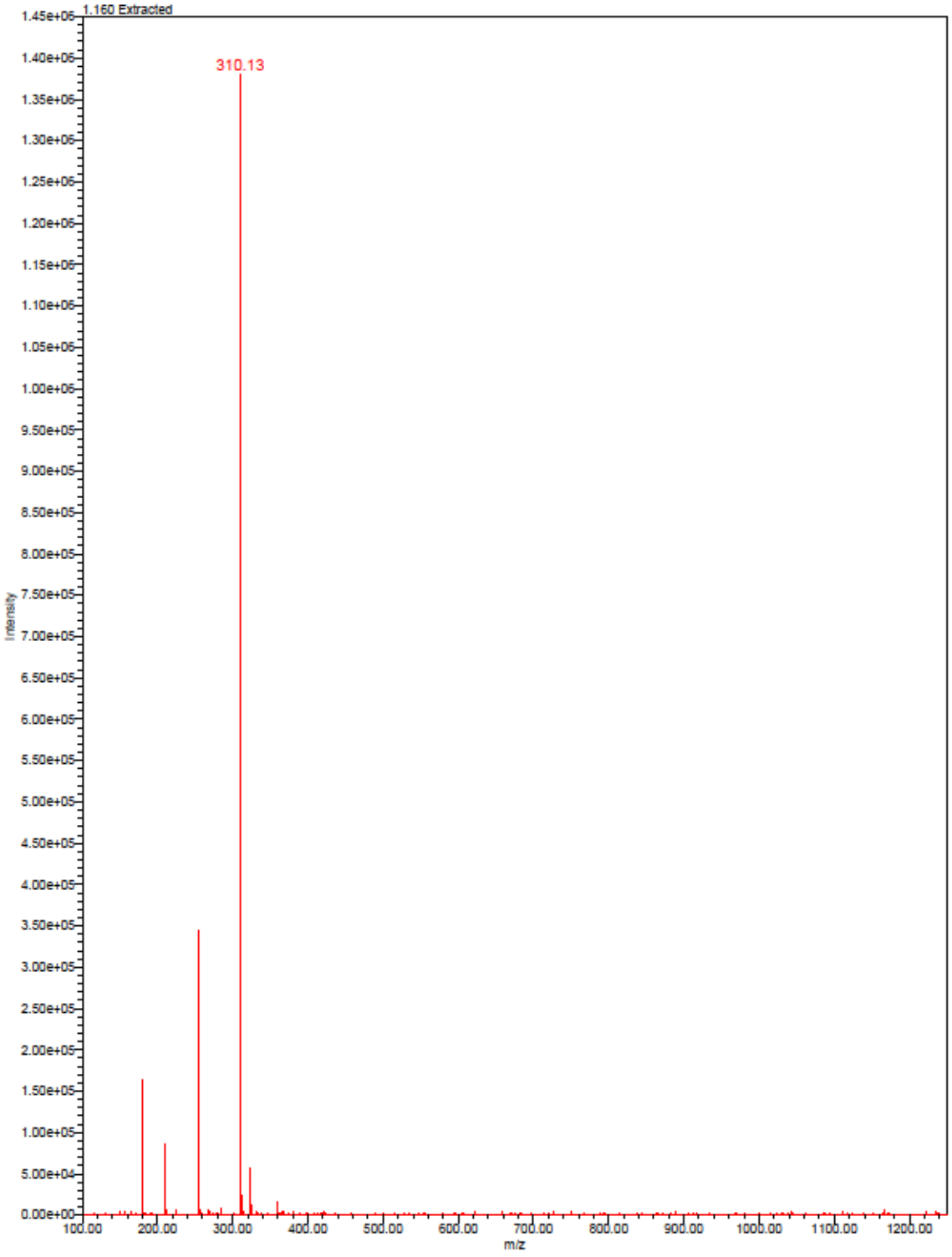

6-[[2-[[(*tert*-butoxy)carbonyl]methylamino]ethyl]methylamino]pyridine -3-carboxylic acid

(2)

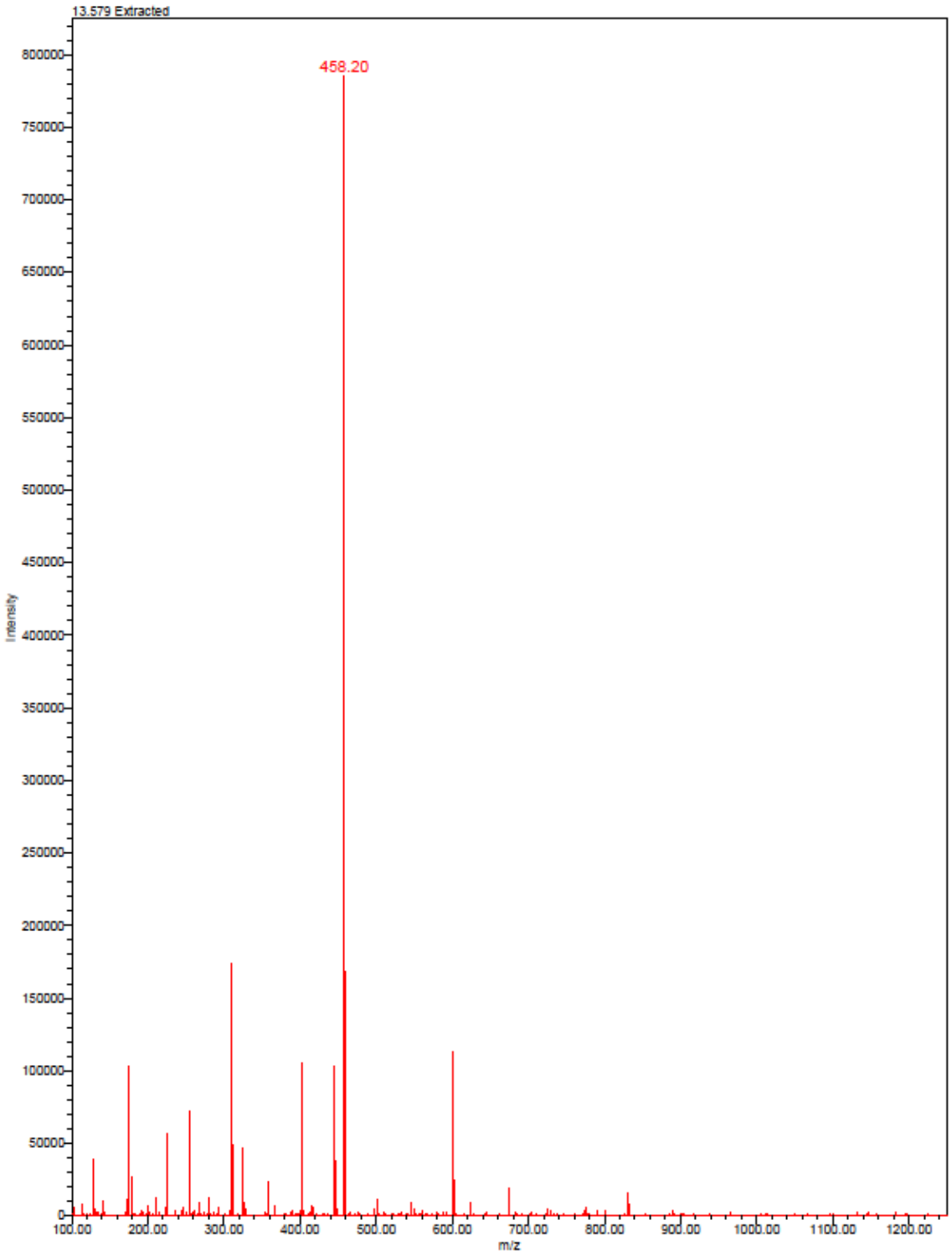

2,3,5,6-tetrafluorophenyl 6-[[2-[[(*tert*-butoxy)carbonyl]methylamino] ethyl]methylamino]pyridine-3-carboxylate (3)

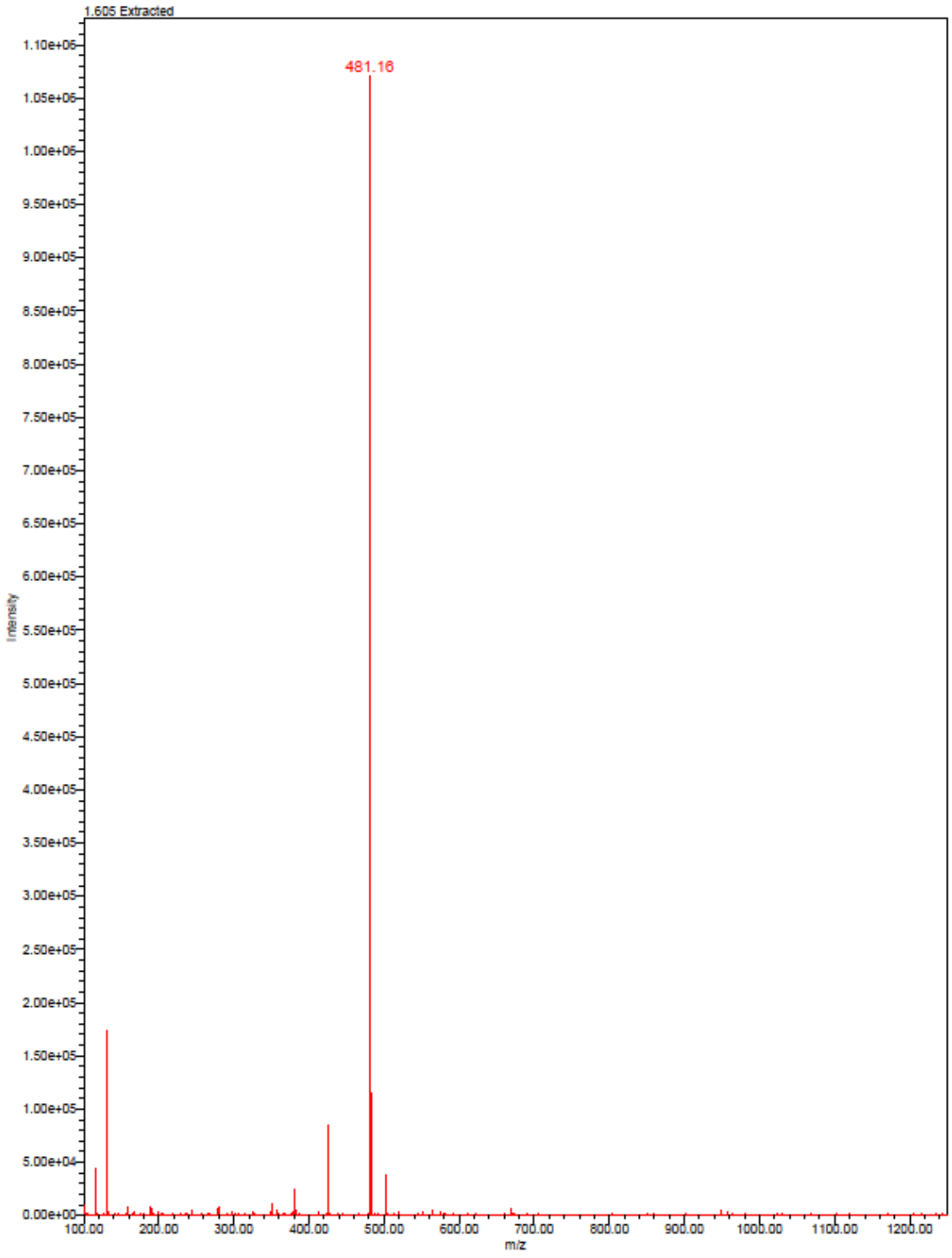

(S)-N-(2-(2-cyano-4,4-difluoropyrrolidin-1-yl)-2-oxoethyl)-6-[[2-[[(*tert*-butoxy)-carbonyl]methylamino]ethyl]methylamino]pyridine-3-carboxamide (4)

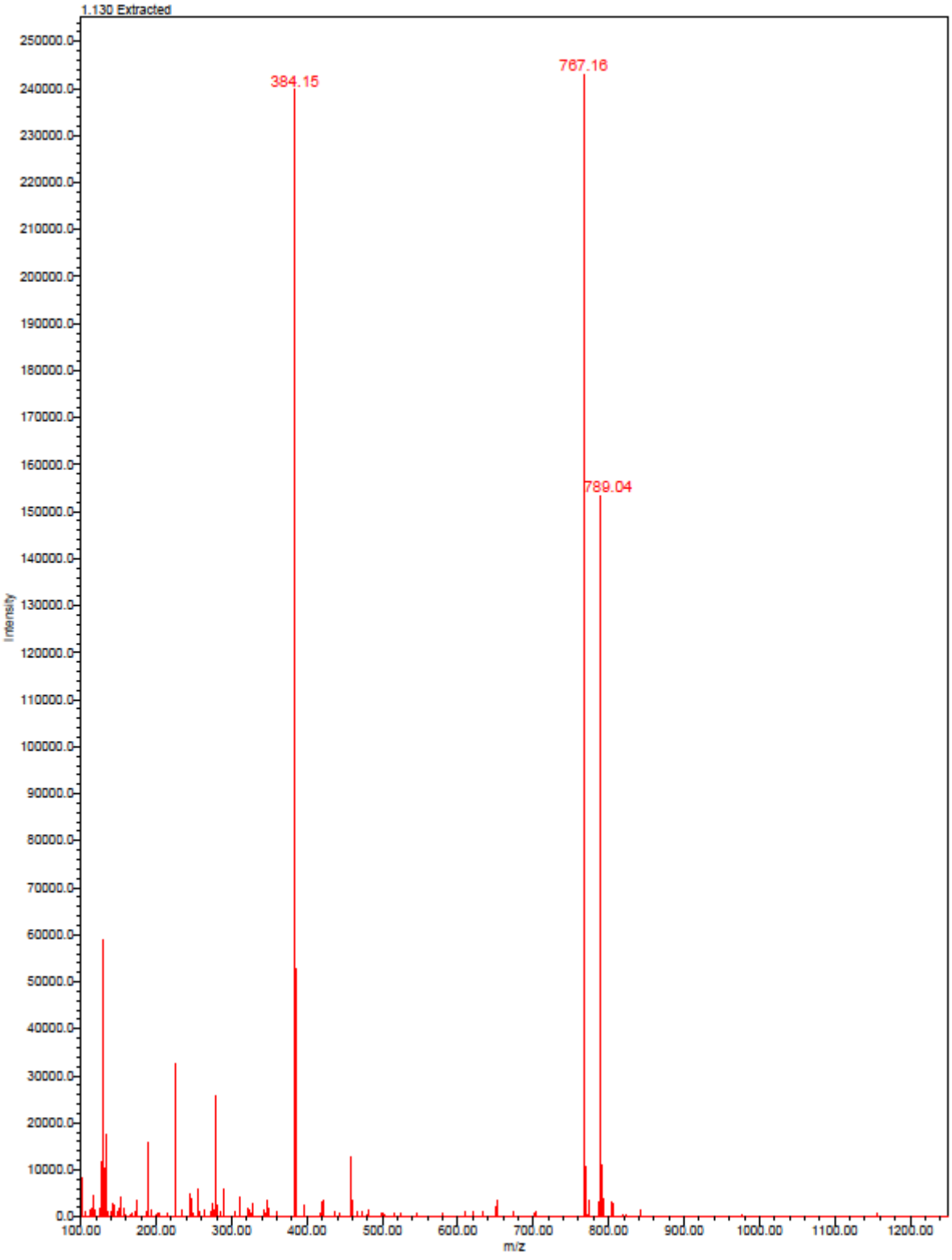

AV02053

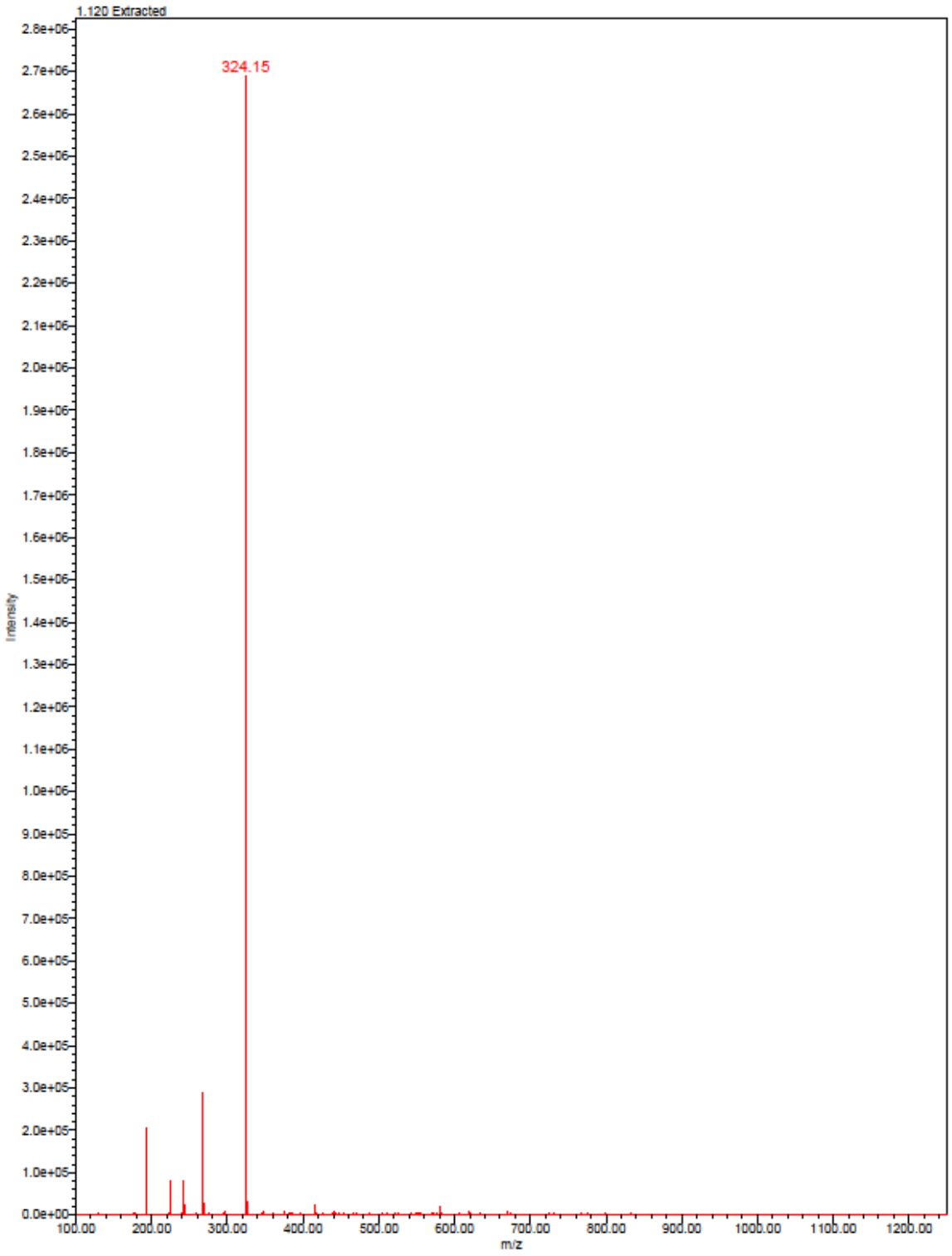

methyl 2-[[2-[[(*tert*-butoxy)carbonyl]methylamino]ethyl]methylamino] pyridine-4-carboxylate (5)

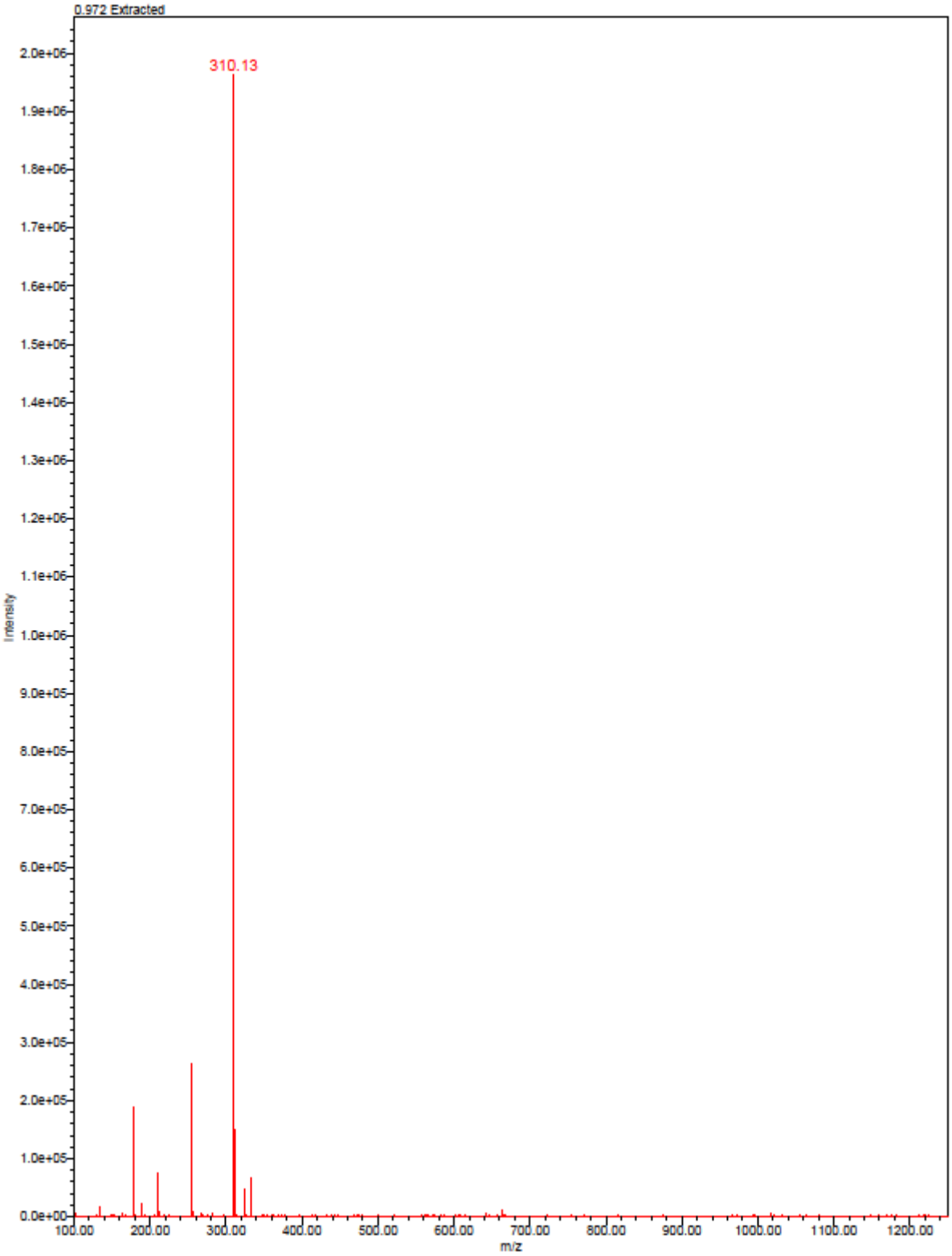

2-[[2-[[(*tert*-butoxy)carbonyl]methylamino]ethyl]methylamino]pyridine-4-carboxylic acid (6)

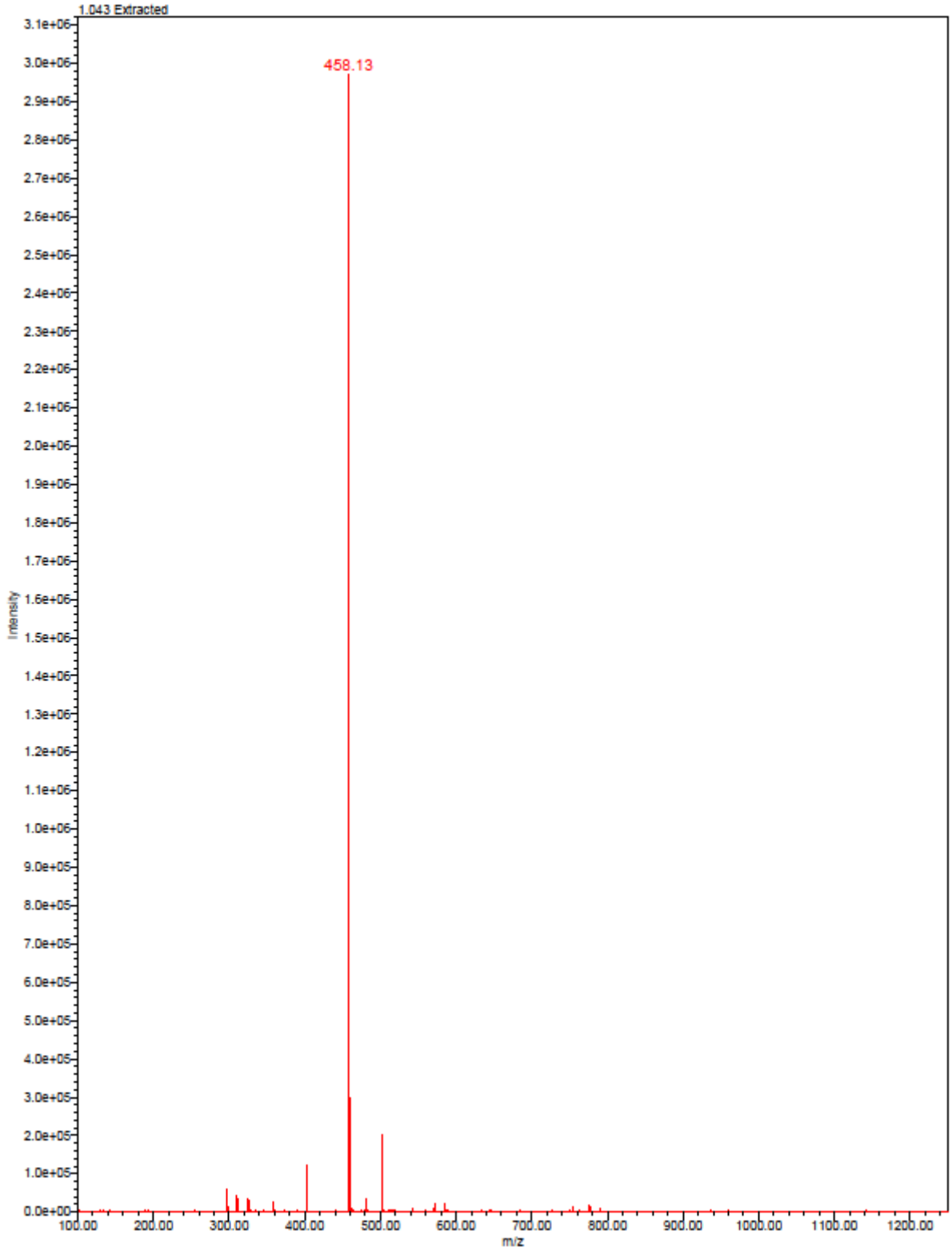

2,3,5,6-tetrafluorophenyl 2-[[2-[[(tert-butoxy)carbonyl]methylamino] ethyl]methylamino]pyridine-4-carboxylate (7)

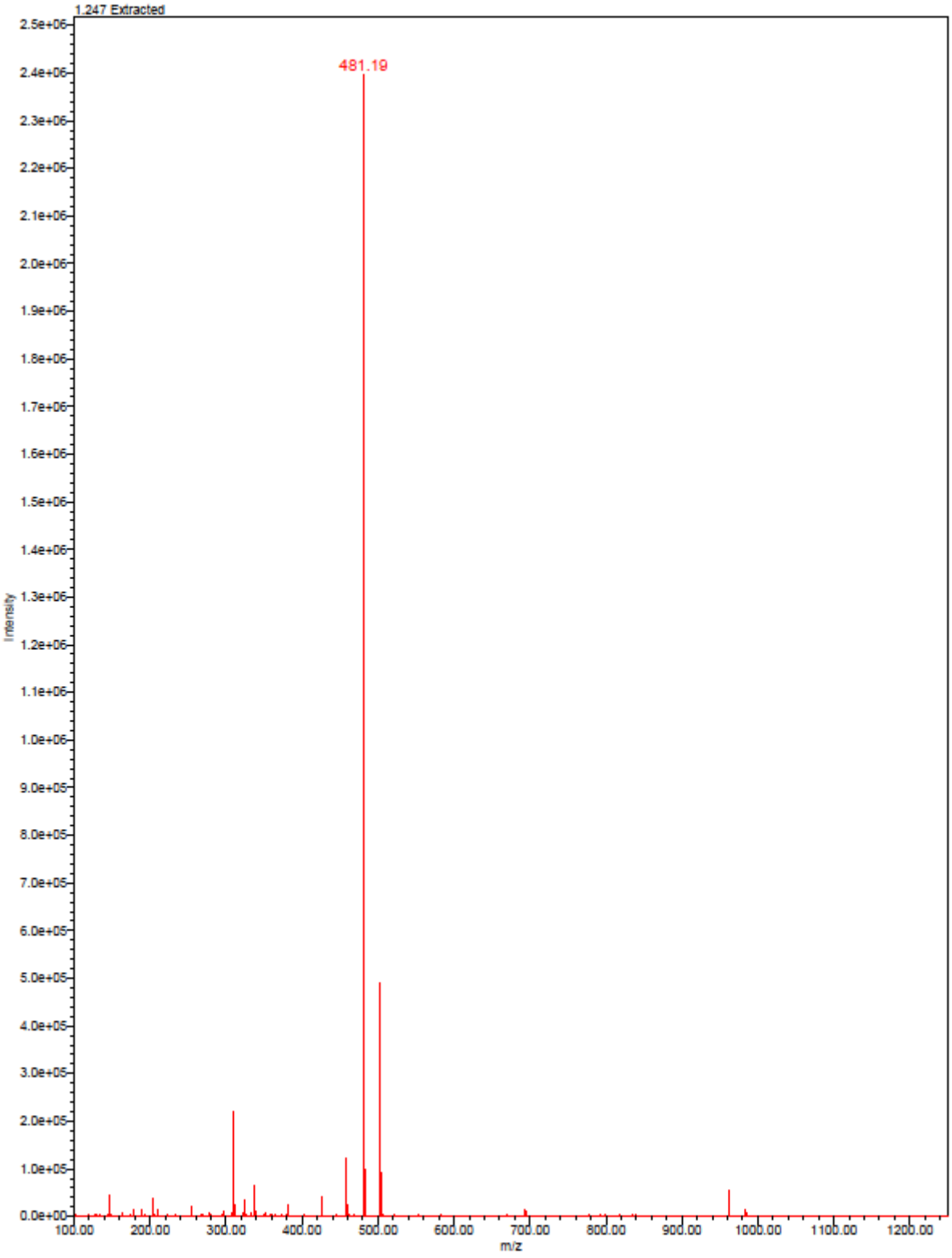

(S)-N-(2-(2-cyano-4,4-difluoropyrrolidin-1-yl)-2-oxoethyl)-2-[[2-[[(*tert*-butoxy)-carbonyl]methylamino]ethyl]methylamino]pyridine-4-carboxamide (8

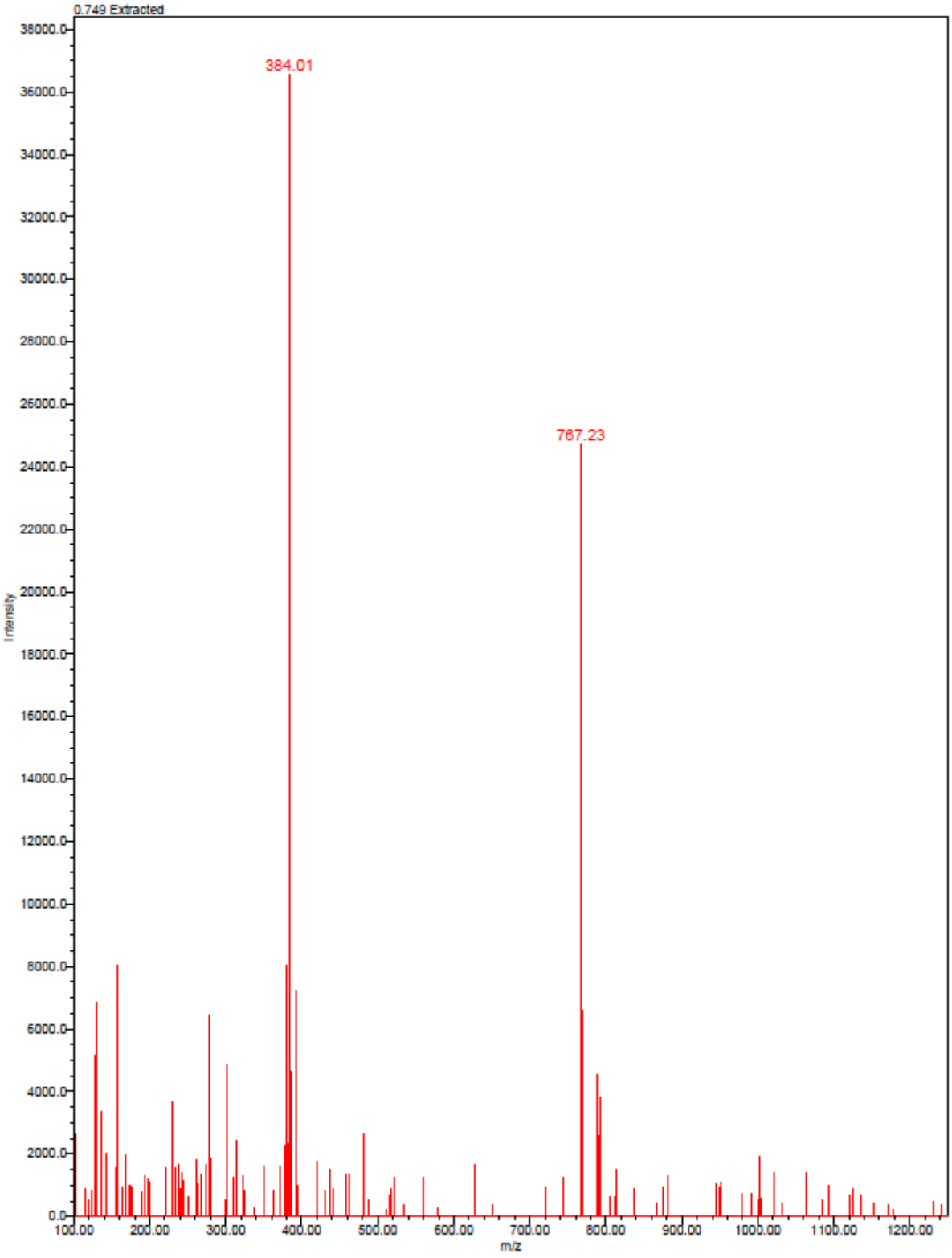
0.749 Extracted
384.01
767.23
Intensity
m/z
38000.0
36000.0
34000.0
32000.0
30000.0
28000.0
26000.0
24000.0
22000.0
20000.0
18000.0
16000.0
14000.0
12000.0
10000.0
8000.0
6000.0
4000.0
2000.0
0.0
100.00
200.00
300.00
400.00
500.00
600.00
700.00
800.00
900.00
1000.00
1100.00
1200.00

AV02070

A.3 Mass Spectra of Intermediates and Compounds in Chapter 4

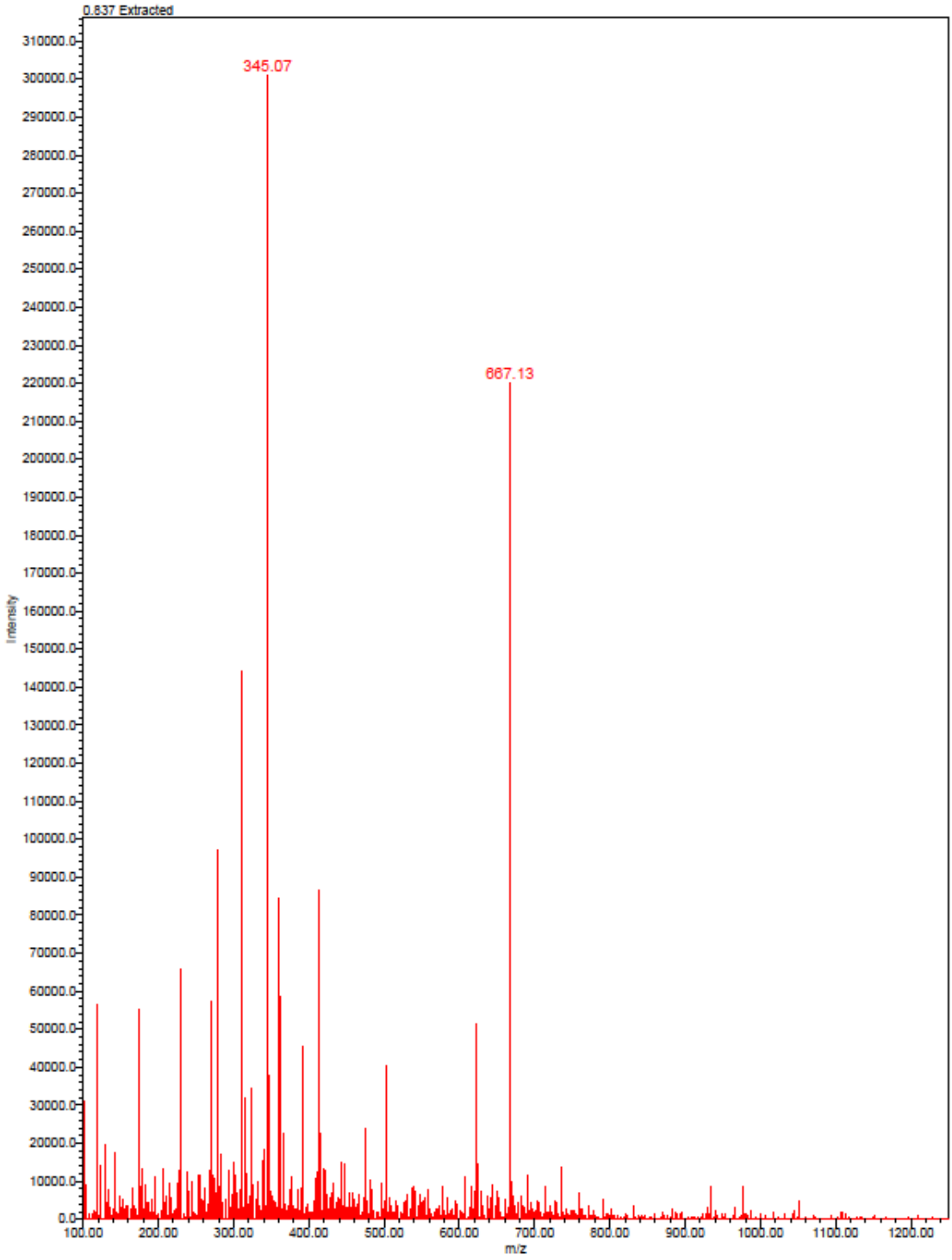

tert-butyl (2,3,5,6-tetrafluorophenyl) succinate (2)

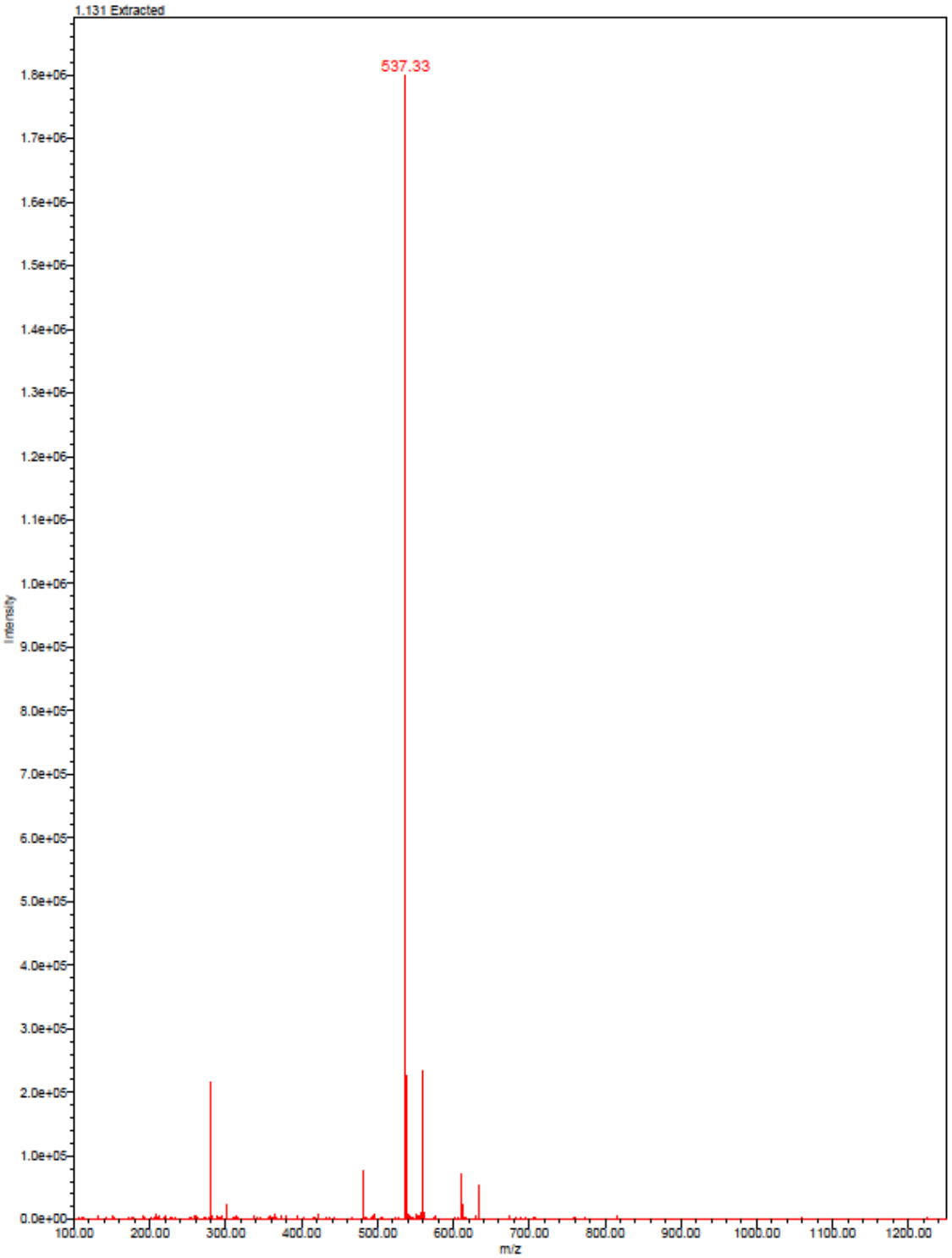

2-[[2-[[(tert-butoxy)carbonyl]methylamino]ethyl]methylamino] pyridine-4-carboxylic acid (4)

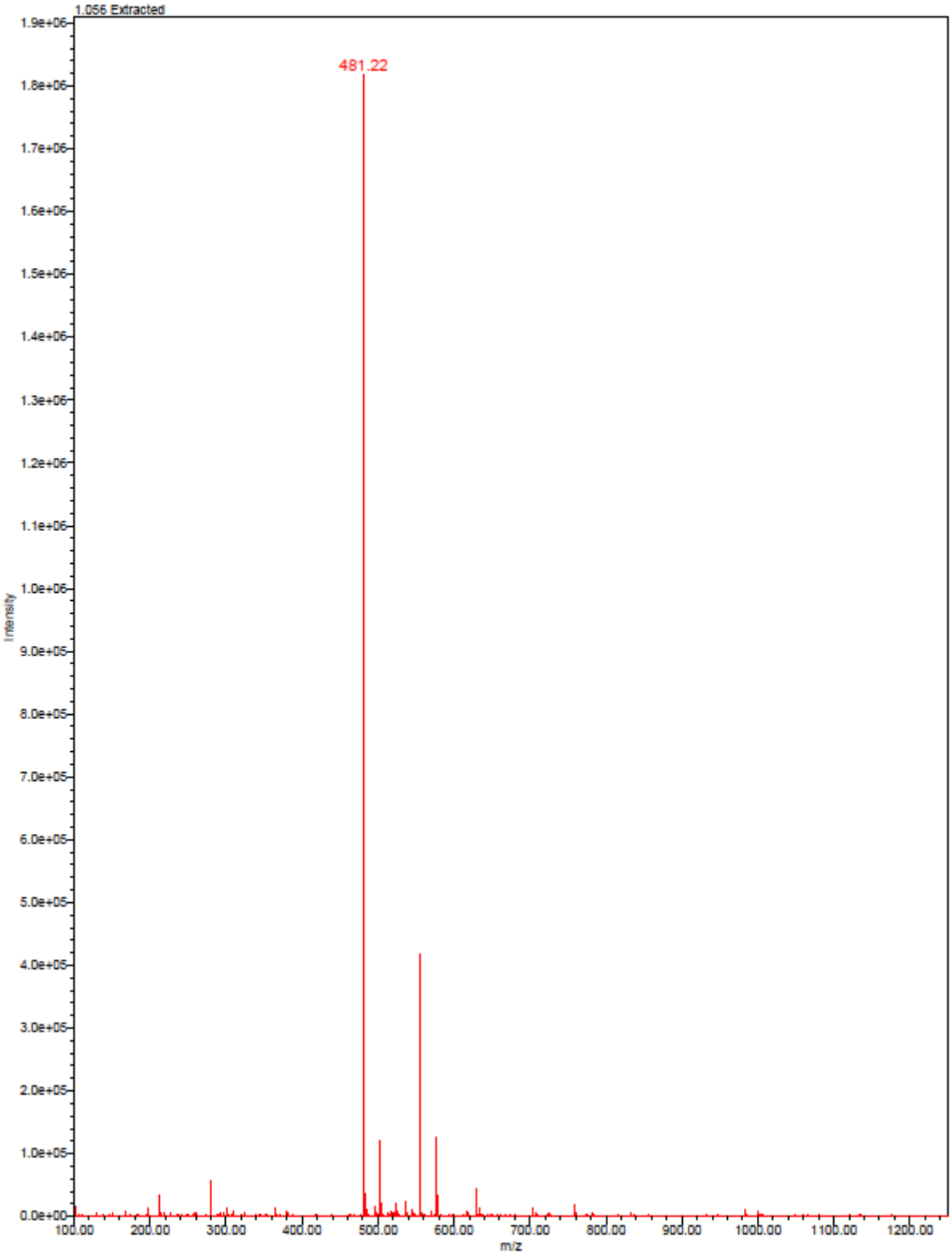

(S)-4-((2-((4-((2-(2-cyano-4,4-difluoropyrrolidin-1-yl)-2-oxoethyl)carbamoyl)pyridin-2-yl)(methyl)amino)ethyl)(methyl)amino)-4-oxobutanoic acid (5)

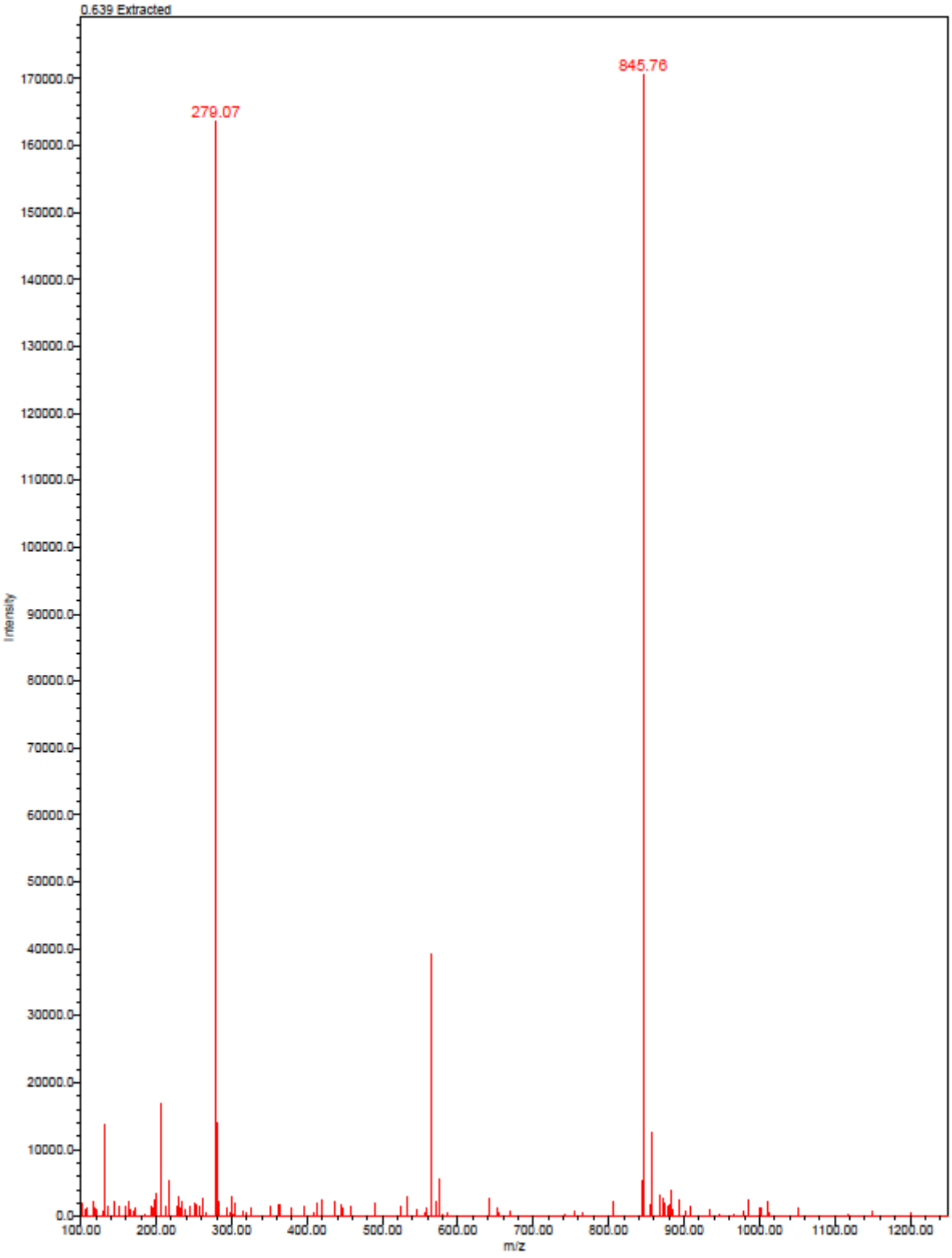

AV01084

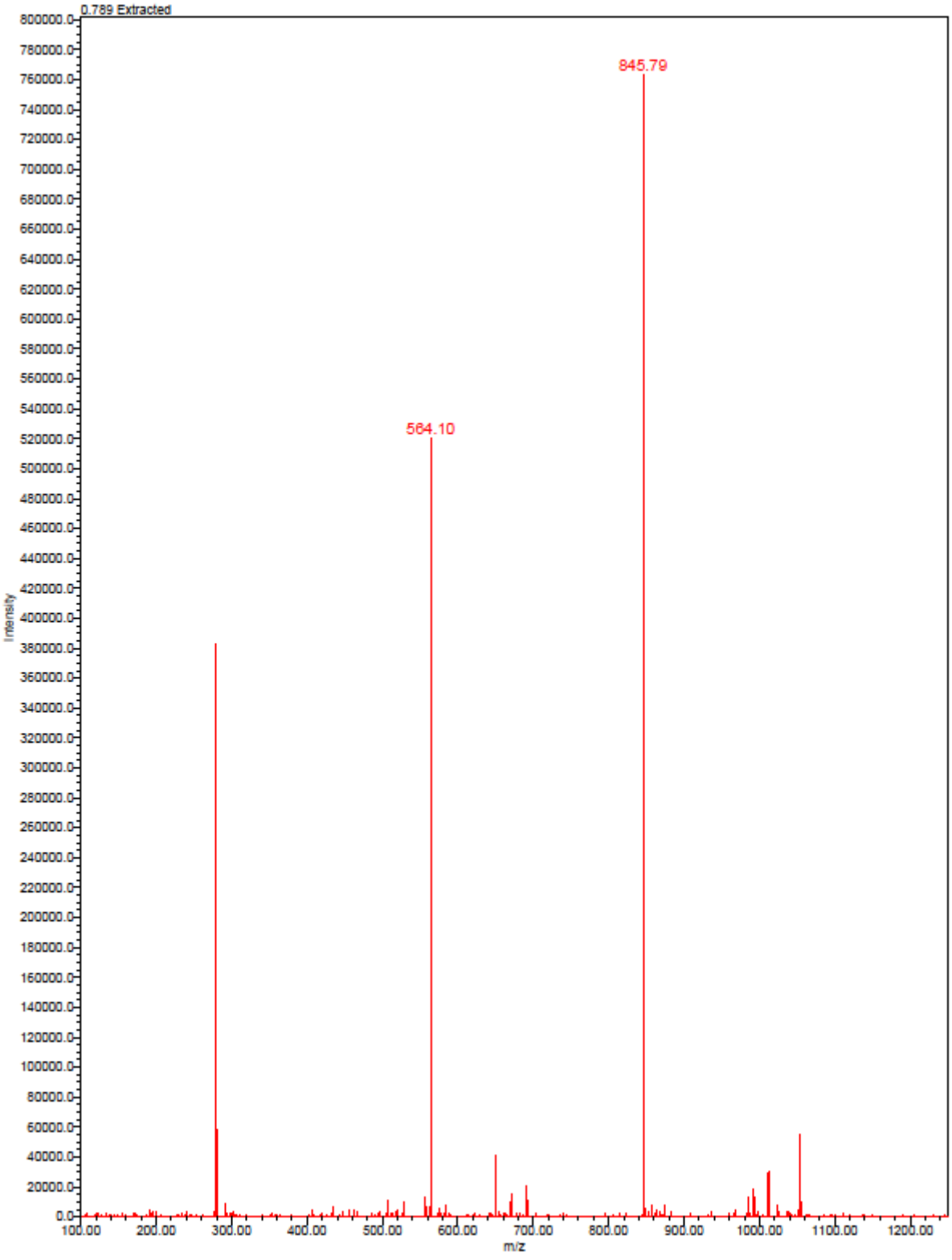

AV01088